Computational Microscopy at 5 Meters using Symmetric Fourier Sampling

by

K. J. Nowicki

B.S., University of Alaska Fairbanks, 2001

M.S., University of Colorado Boulder, 2015

A thesis submitted to the

Faculty of the Graduate School of the

University of Colorado in partial fulfillment

of the requirements for the degree of

Doctor of Philosophy

Department of Electrical, Computer and Energy Engineering

2018

This thesis entitled:
Computational Microscopy at 5 Meters using Symmetric Fourier Sampling
written by K. J. Nowicki
has been approved for the Department of Electrical, Computer and Energy Engineering

Prof. Kelvin H. Wagner

Carly Howett

Robert Cormack

Date

The final copy of this thesis has been examined by the signatories, and we find that both the content and the form meet acceptable presentation standards of scholarly work in the above mentioned discipline.

Nowicki, K. J. (Ph.D., Electrical Engineering)

Computational Microscopy at 5 Meters using Symmetric Fourier Sampling

Thesis directed by Prof. Kelvin H. Wagner

Robotic planetary exploration relies upon a suite of scientific instruments to measure and record the environment under study, with the most ubiquitous instrument being some form of imager. This work describes the development of a microscope that can be mounted to the mast of planetary rover and obtain images with 10 μm spatial resolution at an unprecedented 5 meter distance. Rather than using traditional optics to generate images on a 2D focal plane array, this "remote microscope" uses a computation imaging technique to reconstruct images of targets. A set of four electronically programmable, frequency-shifted collimated laser beams that are symmetric about the axis of the optical system are projected to overlap at a distance of 5 meters and generate moving interference fringes which are used to probe the matched spatial Fourier components of the 2D intensity reflectivity function of the target surface. By probing and collecting a large set of these Fourier measurements, an image of the target is reconstructed using Fourier synthesis. This document provides a detailed description of the optical designs, electronic control requirements, opto-mechanical structures, operational conditions and algorithmic techniques used to generate a functioning computational remote microscope.

I describe and analyze a novel optical design capable of achieving the operational requirements of the system and derive the optical parameters and relevant aberrations. A novel optical surface testing technique useful for high departure aspheres is derived and demonstrated with experimental measurements. I describe in detail the optical procedures and electronics components of the laboratory implementation of the computational microscope. I report the images obtained using the microscope of scattering and reflective targets. Finally, calculation of the effects of a turbulent atmosphere on the operation of the microscope are derived and demonstrated with experimental data, and a new approach to measuring the turbulent atmosphere was developed.

Dedication

The original version of this work is dedicated to those who suspect that the feral truth of an idea, scientific or otherwise, is more powerfully and veraciously presented in an obvious and delightfully pernicious exaggeration than in a sea of dry facts lost in the vertiginous pursuit of soporific pedantry.

The final version of this document submitted to the public record is dedicated to all the people who feel they are too old to return to school. They're probably right.

Acknowledgements

Thank you to my committee members Bob Cormack, Bob McLeod, Brian Hynek, Carly Howett and Kelvin Wagner for taking the time to read this. It was painful enough to write, I can't really comprehend how someone could read it with only decency and compassion to push through.

This work was partially funded at the University of Colorado, Boulder by NASA grant NNX12AI40G, and partially by support from the Southwest Research Institute.

A conditional thank you to my family and friends who thought it was a good idea for me to keep on keeping on and finish this. I fully intend to make you all pay dearly and repeatedly for your horrible advice. I'm looking at you Christopher, Laurie and Scott.

Full appreciation goes to my mother who was the one that understood best what I was attempting to do, why I would do it, and what it truly cost.

To Jonathan Pfieffer and Stephanie Swartz, your companionship and mutual suffering made this easier to bear.

My thanks to Alyssa for her persistent and frequent attempts to convince me to quit everything and go travel.

Tara, thank you for your understanding, kindness, support and patience.

And finally, this work would not have been possible without my advisor Kelvin. I'm sincerely grateful for the humor, the candid conversations and the acknowledgement of a shared perspective of trying to make sense out of the mess of research and life in general.

Contents

Chapter

Tables

Table

Figures

Figure

Chapter 1

Introduction

1.1 Microscopic imagers and NASA

Since the inception of NASA, every spacecraft that has landed on the surface of another body in the solar system has been equipped with at least one imaging system. Imagers are used in a range of mission vital activities including observing the surface during descent and landing to avoid hazards, providing panoramic views of the landing site after spacecraft deployment, generating stereoscopic scenes during rover navigation, and producing high resolution images of the surface for geologic and biological investigations. Early *in situ* surface imagers had relatively poor optical performance and were primarily used to provide geologic context and identify targets for more detailed analysis using the other instruments onboard.

The vanguard of the exploratory forces, named Viking 1 and 2 (Fig 1.1 A), which landed on the surface of Mars in 1976, were equipped with two scan-line cameras called the Lander Imaging Experiment [128, 101]. These cameras produced high resolution (0.04 degrees/pixel) black and white and lower resolution (0.12 degrees/pixel) color images by scanning each "TV line" of a picture at a time and directing the light with a rotating mirror onto a photodetector. The image was transmitted directly to Earth for achiving and viewing by the mission operators. The two cameras were mounted on a mast 1.3 m above the ground and horizontally separated by 80 cm to provide stereoscopic pairs, and they could be directed to look at a range of angles from -60 to +32 degrees with respect to the horizon and focus from 1.7m to infinity. Upon its arrival, Viking 1 provided the first *in situ* images of the surface of the planet with millimeter-scale spatial resolution.

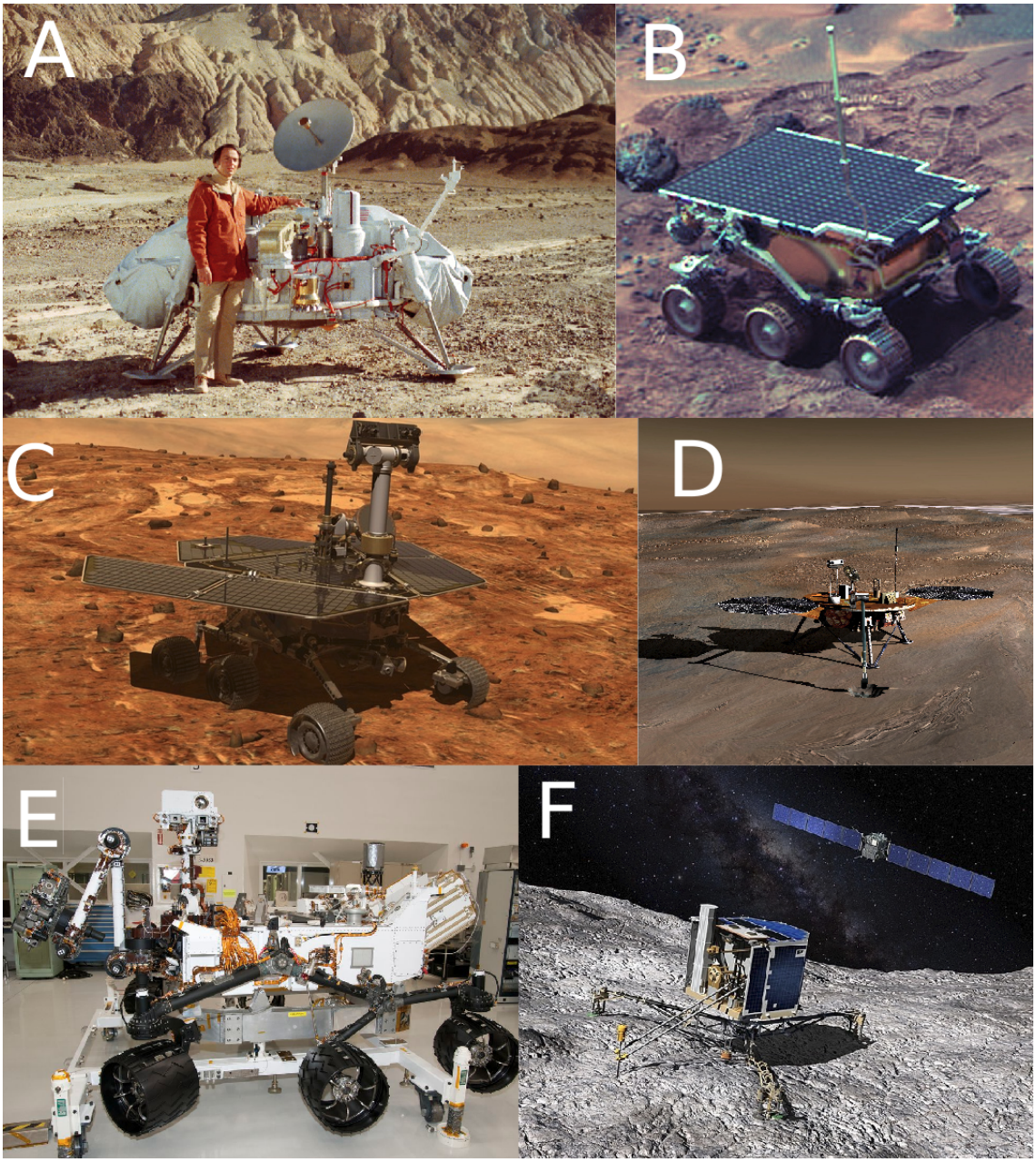

Figure 1.1: (A) The legendary astronomer Carl Sagan standing next to a replica of the Viking 1 lander. (B) The Pathfinder Sojourner. (C) MER Opportunity; one of the two twin rovers launched in 2003. (D) The Phoenix lander (E) Mars Science Laboratory (F) The Rosetta Philae lander pictured in what must seem in hindsight to be a comically optimistic landing position. (All images provided by NASA.)

It was clear, even in this first successful landed mission that having a good context and investigation imager was a scientific necessity.

It would be 20 years before the next mission, Pathfinder (Fig 1.1 B), landed on the surface of Mars in 1997. The Pathfinder mission included a small remote-controlled-car-sized rover called Sojourner, the first of its kind, that would venture from the landing site and explore the surrounding terrain. Pathfinder, like the Viking missions before it, was equipped with two cameras capable of making stereoscopic pairs called the Imager for Mars Pathfinder (IMP). These cameras were significantly more advanced than their predecessors in that they contained 12 spectral filters spanning 440 nm to 1000 nm (in comparison to Viking's 6 filters) and used a frame-based CCD for the detector [143]. They improved the depth-of-field range to focus up to 0.6 m and were able to achieve a spatial resolution of just over 1.5 mm/pixel at that range. Sojourner was equipped with three imagers, two black and white forward-looking cameras that imaged the diode laser lines projected for navigation and one back-looking color camera that provided geologic context for targets of the alpha proton x-ray spectrometer housed onboard. Due to the limited resources available to the rover, these imagers were limited in their optical capabilities with a maximum spatial resolution of 0.2 degrees/pixel (2.4 mm/pixel) [113]. The Pathfinder mission showed that the exploration of planets using semi-autonomous rovers was feasible and opened a new field of possible investigations, but producing high quality imagers for the rovers became a high priority for future NASA missions.

The next mission consisted of two vehicles the size of golf-carts, the Mars Exploration Rovers (MER) (Fig 1.1 C), which landed on Mars in 2003 armed with a larger arsenal of scientific instruments. The two identical rovers Spirit and Opportunity, were sent to two different locations on the planet for independent investigation without a base station as the Viking and Pathfinder missions had. Each rover had two imaging systems; the PanCam was the latest iteration of the popular stereoscopic ranging and navigational camera, and for the first time, a camera dedicated to small spatial scale images, the microscopic imager (MI). The MI was mounted at the end of an actuating arm that brought the camera close to the surface being investigated and used natural light for illumination. Using a CCD detector and a fixed-focus Cooke triplet lens design, it produced images with $30\mu m$ spatial resolution at the best focus (69 mm) over the visible spectral region [75].

The Phoenix lander arrived in 2008 (Fig 1.1 D). Again, stereo images were provided by

the mast-mounted Stero Surface Imager (SSI) and another microscopic imager, the Robotic Arm Camera (RAC) used a double-Gauss adjustible focus imaging train and was able to achieve $23\mu m$ resolution images [96]. NASA equipped the RAC with its own illumination source containing 104 visible spectrum spanning LED lamps. In addition to being a useful stand-alone instrument that provided morphological and contextual images to surface scientists, the RAC also was used as a support instrument for the Microscopy, Electrochemistry, and Conductivity Analyzer (MECA). Samples for analysis by MECA were primarily chosen using criteria based on the visual data provided by the RAC.

The latest investigation to the red planet was the Mars Science Laboratory (MSL) in 2012 (Fig 1.1 E). MSL, the size of an early 2000s sport utility vehicle, also named Curiosity, was supplied with three imaging systems and a powerful onboard computer capable of processing the significant amount of data generated. The MastCams were a far more sophisticated stereoscopic system capable of spectral analysis, sun imaging and video. The Mars Descent Imager (MARDI) was dedicated to hazard avoidance during the complicated and risky landing of such a large vehicle. The imager most used for close scientific study, the Mars Hand Lens Imager (MAHLI) was a small camera at the end of the robotic arm capable of taking images with $15\mu m$ spatial resolution at 25 mm distance. Owing much to the designs of cameras in public use on Earth, MAHLI has focus and autofocusing capability, video acquisition, LED illumination and a Bayer pattern filter for color imaging [47]. The optical design consists of three sets of triplets, two of which are stationary, and onboard data processing electronics for digital processing and compression.

In 2020, the serendipitously named Mars 2020 mission will deliver yet another large rover to the planet's surface. Again, amongst the scientific instruments will be another microscopic imager called SuperCam whose technical specifications are not yet published. Obviously, Mars is not the only body in the solar system to which we've sent robotic investigations armed with microscopes. In 2014, the Rosetta mission sent an orbiter and lander named Philae (Fig 1.1 F) to the comet 67P/Churyumov-Gerasimenko. In addition to the cameras on the orbiter, the Philae lander was equipped with 6 "micro cameras" capable of $7\mu m$ resolution images at closest focus [14].

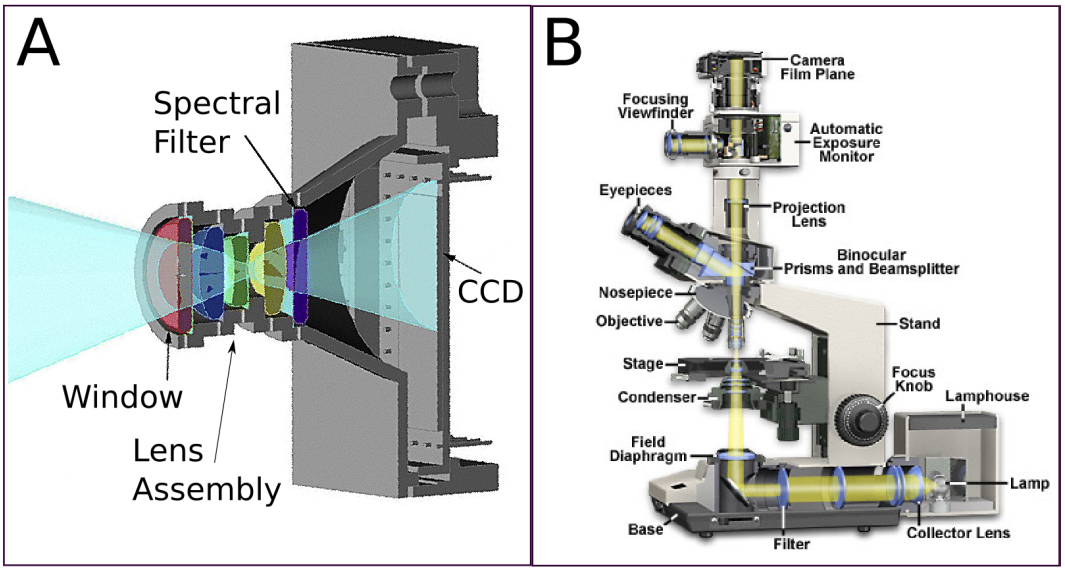

Figure 1.2: (A) The CAD drawing of the Microscopic Imager (MI) on the Mars Exploration Rovers showing a simple window, three-element imaging lens assembly, a spectral filter and CCD detector (adapted from [75]). (B) Standard laboratory optical microscope with parts labeled.

1.1.1 Conventional Imagers as 2D Spatial Samplers

Not withstanding their many technical successes and the scientific investigations they have enabled, the microscopic imagers used for planetary exploration have some significant operational limitations due in part to fundamental physics and in part to the basic anatomical constraints imposed by space travel. Other than the Viking imager, which I'll return to in a moment, the imagers on the NASA missions referenced above, as well as the vast majority of cameras from non-US space efforts not referenced herein, use a variant of the familiar camera construction shown in Fig 1.2 panel A. A set of lenses project a spatially-magnified (either larger or smaller) image of a scene onto a 2D detection array such as a charge-coupled-device (CCD) or a complementary-metal-oxide-semiconductor (CMOS) sensor after passing through optional spectral filters, turning mirrors and flat windows. This process is what most people think of when discussing the collection of images with traditional cameras. Every detector pixel has a 1:1 mapping to a location of the scene and a surrounding unresolvable area. The pixel collects the spatially-integrated intensity of the light emanating from the totality of that unresolvable area. In the ideal unaberrated geometrical

optical model, excluding the effects of diffraction, the spatial resolution of the ideal image (r) is a simple function of the spatial extent of the field-of-view (FOV in m^2), the magnification of the optical system (M) and the number of pixels (N) across the image on the 2D detector according to the following geometric relationship.

$$r = \frac{FOV \cdot M}{N} \tag{1.1}$$

In order to collect higher resolution data, the magnification is increased. To gain a wider field-of-view without losing resolution, more and smaller pixels are crammed into the detector plane. In short, all pixels are created equal and the relevant tradeoff is the balance of resource use vs quantity of pixels being measured, stored, processed and transmitted. The basic camera architecture would seem to have little in common with the modern laboratory optical microscope (Fig 1.2 panel B), but in actuality, the structural differences derive from changing the delivery of illumination to the target and molding the system into a form that is conducive to human interface.

The optical designs of nearly all of the imagers sent to other planets follow this imaging philosophy from panoramic cameras to the imagers used as microscopes. The exception to this was the Viking imaging system, which is worthwhile to describe because it has an operational technique that will be useful for comparison later. The CCD was invented in 1969 and was first used in commercial products in 1974 [18]. The other common 2D detector for visible light, CMOS active-pixel-sensors (APS) didn't come into use until the mid 1980s. Other technologies providing 2D imagery were widely used in the 50's - 70's but were not robust enough for uncrewed spacecraft. The effort to design and construct the Viking landers predates both of these sensors and as a result, Viking 1 and 2 didn't have solid state 2D focal plane arrays as an option to collect images of the surface of Mars. The primary option to collect 2D images was to use a line-scanning imaging system that used a rotating mirror and single-pixel detector. The optical system for the Vikings had a small FOV that matched the resolution of the "pixel" they were synthesizing at any moment. In essence, they built up the image one pixel at a time. The physics of the image collection process was still essentially the same as applies to the imagers used in later missions, but scanning systems also

suffer from being photon inefficient. There are two main tradeoffs that encumber the engineering choices of conventional imagers; the coupling of the working distance to the resolution of the optical system and the coupling of resolution to the depth-of-field.

1.1.2 Limitations and Tradeoffs: Working Distance and Resolution

In traditional microscopy, like any other optical system using lenses to form images, the highest achievable spatial resolution is most commonly described using the maximum half-angle (θ_{max}) at which the system can accept light that started at the object being imaged (as shown in Fig 1.3 panel A). This acceptance angle is described as f-number ($f/\#$) to photographers and as numerical aperture (NA) to microscopists through the following equations:

$$f\# = \cot(\theta_{max}) = \frac{f}{D} \tag{1.2}$$

$$NA = n\sin(\theta_{max}) = n\sin\left(\arctan\left(\frac{D}{2f}\right)\right) \tag{1.3}$$

$$\approx \frac{nD}{2f} \tag{1.4}$$

where n is the index of refraction of the medium, f is the focal length of the lens and D is the diameter of the lens. In the paraxial limit, we may safely make the approximation in the final equation above. Using these definitions, the highest achievable spatial resolution of an optical system described in terms of the smallest resolvable feature d is defined by the Abbe diffraction limit equation [5].

$$d = \frac{\lambda}{2NA} \approx \frac{f\lambda}{nD} \tag{1.5}$$

where λ is the wavelength of light. I'll be discussing the numerical aperture and this equation in more depth in Chapter 2. For any given n and λ, the smallest resolvable feature can be decreased (and θ_{max} is thereby increased) by either decreasing the distance (f) to the target or increasing the diameter D of the lens as depicted in Fig 1.3 panel A.

It is an important and often understated requirement that to achieve the diffraction limit with traditional imaging systems it is necessary to use imaging optics with sufficiently high surface precision to limit wavefront errors. As asserted by Lord Rayleigh in 1879, "*An optical instrument*

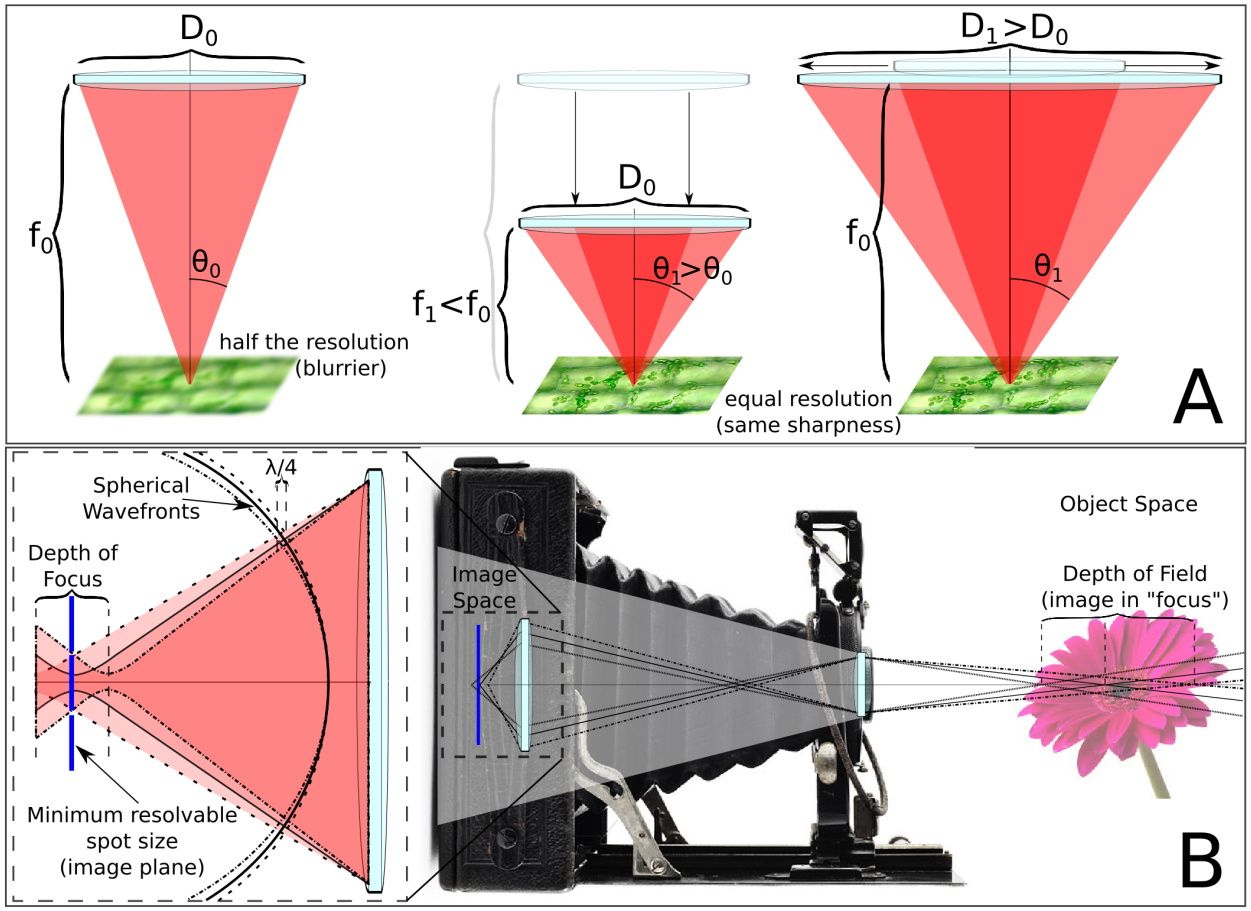

Figure 1.3: (A) The smallest resolvable feature size is inversely proportional to the numerical aperture defined as $NA = n\sin(\theta)$ where θ is the angle at which light can enter the system. Increasing the numerical aperture requires either bringing the lens closer to the object, or increasing the diameter of the lens. (B) Depth of *Field* is the range in the distance from the camera that objects are qualitatively "in focus". This range can vary from a few microns for high NA microscopes to many thousands of meters for standard cameras focused at infinity stopped down to a very low NA. Depth of *Focus* is the range in the locations of the foci of converging spherical wavefronts that differ by $\pm\ \lambda/4$.

would not fall seriously short of the performance possible with an absolutely perfect system if the distance between the longest and shortest paths leading to a selected focus did not exceed one-quarter of a wavelength" [130]. He was referring to the two concepts of optical pathlength (OPL) and optical pathlength difference (OPD). The OPL is defined as the effective pathlength of a route through a system defined as

$$OPL = \sum_{j=1}^{m} n_j d_j \tag{1.6}$$

where n_j is the index of refraction of the jth portion of the path and d_j is the measured distance within that material. The OPD is just the difference between the values of the OPL of two unique paths. Since the OPD must also be the sum across all optical surfaces in the system, in order to achieve the admittedly qualitative Rayleigh criterion requires all surfaces to individually greatly surpass the criterion. In practice, this means that marginal-quality surfaces are precise to $\lambda/4$ across the entire surface, while high-quality surfaces for use in multi-component systems should be better than $\lambda/20$. The consequence of all of this is that in order to resolve small features at large distances, Equation 1.5 demands a mirror or lens with a large diameter, while the Rayleigh criterion demands that those large mirrors have *high optical quality*, which drastically increases manufacturing cost. It is far cheaper, lighter and more convenient to use a smaller lens at a closer distance, as in the case of a traditional laboratory microscope (Fig. 1.2 panel C). Although laboratory microscope objectives are not cheap, and in fact have some of the best imaging lenses in commercial use, they use very small optics that would be astronomically expensive (and in most circumstances physically impossible) to design and manufacture with apertures large enough to enable imaging at a large working distance.

Returning to the discussion of spaceflight instruments, as each generation of the microscopic imagers used on planetary exploration rovers has increased their spatial resolution over the decades from the Viking era to the Curiosity rover today, the working distance has proportionally decreased according to Eq. 1.5. Although this mathematical relationship still holds for the remote microscope presented in this work, the presumed requirement of high-precision optical surfaces that binds traditional imagers will be significantly relaxed by the techniques introduced here. I'll explain the reasons for this crucial design advantage and how it is exploited in the following chapters.

1.1.3 Limitations and Tradeoffs: Resolution and Depth of Field

The second tradeoff in operational characteristics of traditional imaging systems is the coupling of resolution to the depth-of-field. Before continuing, I must explicitly address a matter of common confusion. Due to an unfortunate choice of nomenclature and a strong relationship

between the concepts, the depth-of-*field* and the depth-of-*focus* are terms whose definitions are commonly swapped, confused or equated for convenience. Depth-of-*field* is the range in the distance from the objective of an imaging system to the target objects where images of those objects meet the subjective threshold of a person saying that they are "in focus". This definition is a bit of a word salad and makes more sense by examining Figure 1.3 panel B. The camera is at some set f-stop value and is taking a picture of the flower. When the camera is close to the flower, the center of the flower will be in focus while the closer and farther parts of the flower are out of focus. The depth-of-field is just the range of distances in "object space" where the portions of the flower are crisp in the image and can range from microns for microscopes to millimeters for close-up images to many kilometers for landscapes.

Depth-of-*focus* is a quantity that is relevant inside the camera and is sometimes referred to as "image space". It has a more rigorous definition, but it is still productive to return to the illustration in Figure 1.3 panel B. Three points on the flower at successively increasing distances from the camera (dashed, solid and dash-dotted, respectively) emit spherical wavefronts that enter the camera. The spherical wavefront that enters the system is bounded by the rays drawn on the camera and flower. Zooming into the detector region of the camera (image space) we see a sagittal slice of three cones of light converging near the detector at different distances. Overlaid on these triangular slices are the spherical wavefronts as dashed, solid and dash-dotted circles. The depth-of-focus is defined as the range of focal distance for the spherical wavefronts that have a maximum OPD variation of $\lambda/4$, thereby meeting the Rayleigh criterion. The practical application of this criterion is that all of the light in these converging waves will be absorbed into the minimum resolvable spot size on the detector plane. Beyond this wavefront deviation threshold, a portion of the cone of light will fall on an adjacent pixel and the resulting image will be "out of focus". As a result of the spatial scales of images and the lenses that form them, depth-of-focus values are typically measured in microns.

Now that I have spent this effort presenting distinct conceptual definitions for the depth-of-field and depth-of-focus, I will conform to the custom of the microscopy community and use these

two terms interchangably and refer to these concepts simply as "DOF". The reason that these two terms are somewhat dismissively equated is because in microscopy both of these depths are measured in microns. To bring a portion of the object into focus with the "focus" knob, the stage or stand typically move a similar distance as would be necessary to move the focal plane if the optical system were designed to allow it. As a result, the depth-of-field and depth-of-focus become irrelevantly differentiated concepts in this context.

The obfuscation of the DOF in microscopy extends beyond the conceptual definition to the mathematical formula used to calculate it as there is no universal consensus. A wave-optics analysis, first described by Abbe using the Rayleigh criterion [58] yields a DOF (Δz) of:

$$\Delta z_{Abbe} = \lambda\Big(\frac{n}{NA}\Big)^2 \tag{1.7}$$

Although this formulation has a basis in simple physical principles, the microscopy community has long argued that it is a poor match to the observed DOF in many microscopes and has inspired others to construct more complex formulas that better match specific applications [141, 100]. Without delving into the justification for the formulations from the publications just referenced, their derived equations which they claim are better matches to the DOF of microscopic images are stated below.

$$\Delta z_{shillaber} = \frac{\lambda\sqrt{n^2-(NA)^2}}{(NA)^2} \tag{1.8}$$

$$\Delta z_{kingslake} = \frac{\lambda}{4n\Big(1-\sqrt{1-\frac{NA}{n}}\Big)^2} \tag{1.9}$$

Clearly, everyone agrees that the DOF is linearly dependent upon wavelength, but otherwise it seems the dependence on numerical aperture and index of refraction are up for grabs. That being said, the differences amongst the calculated values of DOF using these equations are on the order of a few percent for plausible values of NA, n, and wavelength. Others prefer to define the DOF in terms of the hyperfocal distance d_H which is defined as the diameter of the entrance pupil divided

by the maximum acceptible angular blur [116]. Again, the values computed using the hyperfocal distance are congruent with the values obtained by the other DOF equations. I will adhere to using the physical quantities of NA, n and λ and avoid definitions based on arbitrary quality thresholds. This discussion is simply a long-winded summation and dismissal of the arguments of how to quantify the DOF in traditional systems. What is important is that although the methods differ in their derivations, the values obtained all agree to at least the second significant digit. As a result, I will rely on Abbe's formulation. In the case where the object is in air, the DOF defined in Equation 1.7 is simplified to the well known rule-of-thumb equation:

$$\Delta z = \frac{\lambda}{(NA)^2} \tag{1.10}$$

From Equation 1.5 we know that the smallest resolvable feature (d) is inversely proportional to NA, and Equation 1.10 states that the DOF is inversely proportional to the square of the NA. Substituting equation 1.5 into this equation gives the relationship that directly couples resolution with DOF for traditional imaging systems.

$$\Delta z = \frac{4d^2}{\lambda} \tag{1.11}$$

For a resolvable feature of $d = 10\ \mu m$ at visible wavelengths ($\lambda = 500$ nm) the DOF is 800 μm and the corresponding NA of the optical system is 0.025. I'll return to this nominal system performance for comparison several times in future sections.

In addition to the two tradeoffs discussed above, there are drawbacks to conventional microscopic imagers that are evident from experience. *Cost*: The development of high quality cameras over the years that have yielded increasingly better image quality has come at a significant monetary cost and lens designs of sublime complexity with components that are difficult to manufacture. *Data volume*: An increase in resolution has also demanded a similar increase in the amount of data being stored, processed and transferred. Except in the case of compressive sensing (Sec 2.2.11), the data cubes acquired by high-resolution cameras can be breathtakingly large from an interplanetary data transfer bandwidth perspective. *Lighting*: Finally, the imagers either need to rely upon

ambient lighting or must supply a light source that, in general also needs to get close to the object being imaged. Each of these restictions and how they are alleviated in the implementation of the remote microscope are discussed in following chapters.

1.2 Imaging techniques by imparting more information into a measurement

A little historical narrative is useful before I introduce the imaging technique used in this thesis. There have been multitudinous technological paths explored in the last half-century to achieve better spatial resolution in imaging systems, or to achieve imaging in cases that would be intractible with traditional optical systems. This is particularly true in the fields of microscopy and telescopy where the edge of scientific knowledge is fundamentally limited by the resolution limit. A goodly proportion of these techniques achieve their enhanced performance by imparting more information into the measurement, or equivalently by restricting the information that can possibly be measured. I'm going to introduce a few of these that are seminal to this work and provide perspective and contrast for future discussions. The three techniques that are most relevant are structured illumination microscopy, Fourier microscopy and Fourier telescopy.

1.2.1 Structured illumination microscopy

Structured illumination microscopy (SIM) is a wide-field imaging technique, variants of which use both coherent and incoherent light for optical sectioning, super-resolution and phase imaging [135]. For the case of optical sectioning, a well-characterized spatially-varying pattern, typically consisting of sinusoidal fringes, is superimposed on the target through a traditional microscope by placing a physical amplitude transmission grating (for the incoherent case) at a conjugate image plane in front of the illumination source as in Fig 1.4 (reproduced from [135]). The grating is placed on a movable stage and is positioned with a precise piezo-electric drive moving perpendicular to the lines of constant transmission in the plane of the grating. Images of the object are collected with the grating pattern positioned at three different phases, minimally sampling a sinusoid across the field of view. With spatially incoherent illumination passing through the microscope objective, and

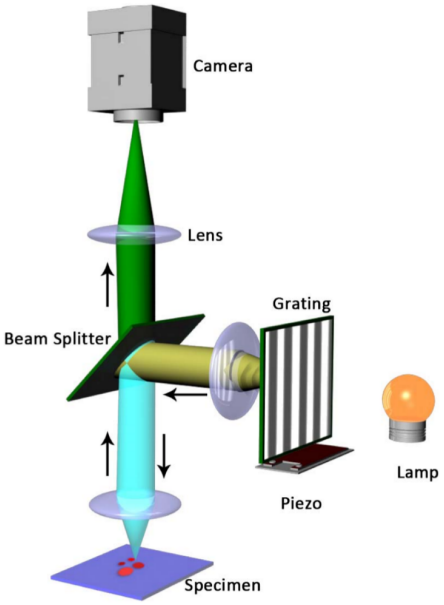

Figure 1.4: In structured illumination microscopy, an amplitude transmission grating is imaged onto a sample. Images of the object are acquired with the grating positioned in at least three phase locations Reproduced from [135].

using a thin grating, the image pattern is only in focus over a very small depth of field according to Equation 1.7. At any of the three phases (θ_{SIM}) the imaged grating produces the structured illumination light field described by:

$$I_{SIM} = I_0(1 + \frac{m}{2}\cos(2\pi k_x x + \theta_{SIM})) \tag{1.12}$$

where I_0 is the average intensity of the illumination field, x is the spatial dimension, k_x is the spatial frequency in the x-direction, and m is the modulation depth. The intensity of the image at every (x,y) location is the product of the 2D SIM field with the 2D structure of the object S_{obj} convolved with the intensity point spread function $|h|^2$.

$$I(x,y) = I_{SIM} S_{obj} \circledast |h|^2 \tag{1.13}$$

By demodulating the images with three phases, the sinusoidal pattern is computationally removed and an image of a very thin section of the sample is extracted from a larger 3D volume. Multiple 2D sections at different depths may be measured by moving the sample in the focus in the direction of the beam.

1.3 Fourier-based imaging techniques

Manipulating the Fourier representation of a dataset is fundamental to many processing algorithms used throughout the physical and computer sciences. However, data sets are generally collected in the space that the measurement is desired, a transformation is applied to bring them into Fourier space where they may be filtered or manipulated and then are returned to their original basis. An extention of Fourier-space sampling, albeit with a more complex instrumental, mathematical and operational setup, is applied to techniques in imaging, such as tomographic imagers, a familiar example of which is the magnetic resonance Fourier imager [50, 115] and the computational tomography (CT) scan which are used in medical imaging to computational reconstruct images of structure inside an optically-opaque volume using either x-rays or nuclear magnetic resonance (NMR). Concepts pertinent to tomographic imaging will be presented in Chapter 2. The work in this thesis is deeply related to two other Fourier-based techniques called Fourier microscopy and Fourier telescopy which generate images of the surface of a target in a very different manner than a traditional lens.

1.3.1 Fourier microscopy

A patent from 1986 (US 4584484 A) describes an early variant of implementing structured illumination in microscopy to actively probe the Fourier components of a target [86]. The basic layout of the claim of the invention can be seen in Figure 1.5 Panel A. A laser is directed toward a sample at angle θ_i. One half of the beam illuminates the object while the other half is reflected off a 90-degree mirror and illuminates the same portion of the target creating linear interference fringes. By changing θ_i the period d of the fringes changes according to the equation:

$$d = \frac{\lambda}{\sin(2\theta_i)} \tag{1.14}$$

The reflected light from the target is collected with a lens onto a single-pixel "bucket" detector as a time series while the incidence angle of the laser $\theta_i$is changed from some low to high limit. This time series is a type of time domain Fourier transform of the sequentially sampled spatial frequencies

of the target and constitutes what is called a "Fourier slice", a line of Fourier components in the complex Fourier plane. The sample is rotated and another slice is collected at each rotation step, thereby filling the 2D Fourier representation of the object. A 2D Fourier transform of this data reconstructs an image of the object.

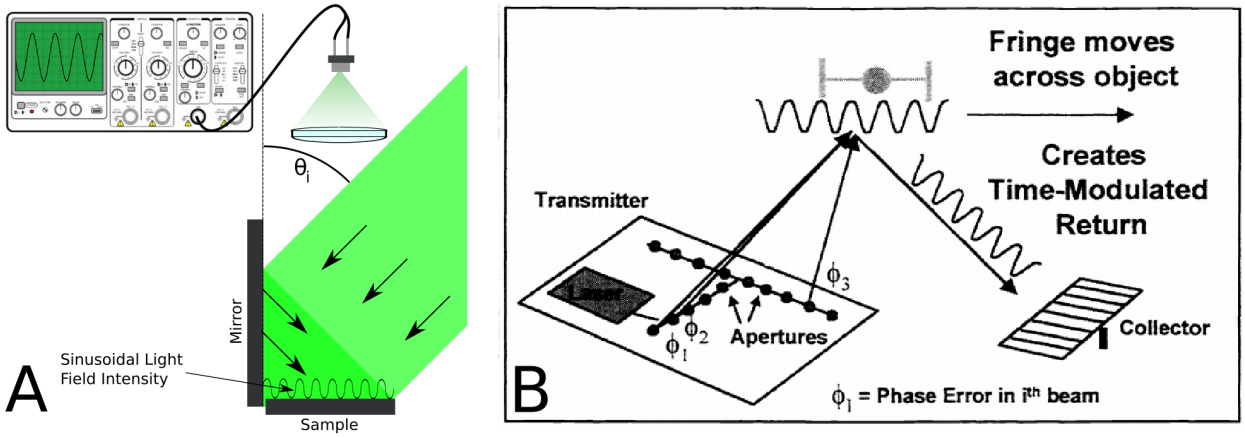

Figure 1.5: A. The patented idea of Fourier microscopy directs a laser at some incidence angle θ_i at a target and a vertical mirror. The interference fringes generated on the target are collected by a wide angle bucket detector and digitized as a time series. A range of spatial frequencies are probed by changing the angle of incidence θ_i. B. Fourier telescopy uses arrays of laser transmitters to illuminate an Earth-orbiting satellite with multiple mutually-coherent beams. These beams interfere at the target and generate fringes across which the object moves. The telescope on the ground collects the spatially-integrated time-modulated intensity. Reproduced from [79].

Probably because the patent isnot a scientific paper, a significant amount of technical detail and mathematical background is omitted. Nevertheless, the patent outlines several important observations concerning this type of imaging system. The patent claim asserts, "The scattered light collecting optical members may be of a low optical quality relative to the final resolution of the image to be reproduced. This is in contrast to the use of high quality optical components in prior art viewing devices such as microscopes." A second unsubstantiated and unquantified claim states that the system is, "capable of producing high resolution with a large depth of field without precision optical components." I'll clarify both of these claims in Chapter 2 since they both happen to be true and they also apply to the system described in this thesis. Although this patent was ostensibly the first occurrence of designing a system that uses coherent illumination to probe Fourier

components of a microscopic target, the implementation seems to have never been commercialized and other high-resolution computational imaging techniques became standard industry practice. Despite being something of an intellectual dead-end, it is claimed as partial inspiration of a similar technique for deep space imaging called Fourier telescopy.

1.3.2 Fourier telescopy

Fourier telescopy applies the same measurement philosophy as Fourier microscopy to a system designed to image objects in Earth's orbit [78, 79]. An array of coherent transmitters are laid out in a 2D spatial distribution as is commonly used for radio telescopic arrays as shown in Fig 1.5 Panel B. In the simplest case, any two of these transmitting apertures can project light onto the orbiting target where they interfere and produce a spatially-varying sinusoidal intensity grating. Either the object moves across the fringes or the fringes are made to move across the stationary object by frequency shifting one of the beams to probe the 1D Fourier component. The reflected light temporally oscillates in intensity at the frequency difference and is collected by a "bucket detector". Different spatial frequencies are probed by choosing different pairs of transmitting apertures which have different spatial separation and orientation as in panel B. As with a conventional aperture, the resolution of the reconstructed image is limited by the maximum separation of the discrete transmitting apertures.

Fourier telescopy suffers from computational complications that are often negligible in most microscopy applications, phase offsets between the sub-apertures and phase errors as a result of atmospheric turbulence. Phase closure, a process that allows the calibration of the phase offsets between apertures, is accomplished using all possible triplets of beams whose sum of pairwise phase differences must be zero, yielding equations that can be solved for all unwanted phase offsets. In order to limit the effects of atmospheric turbulence corrupting the phase across the beam, the transmitter apertures are designed to be smaller than the scale length of the atmospheric scintillation so the technique suffers only from the varying piston phase which can be corrected with phase closure[78]. An obvious drawback is that hardware implementation of Fourier telescopy

is not easily scalable to a smaller form factor to allow it to be used in lieu of a traditional imager. Which brings us to the subject of this thesis.

1.4 The $\mathcal{F}$-BASIS imaging technique

The remote microscope developed in this thesis does not acquire images in the traditional sense, but instead uses a computational imaging technique developed over the last decade with strong intellectual ties to Fourier microscopy and telescopy called Fourier-basis agile structured illumination sensing ($\mathcal{F}$-BASIS) and previously referred to as Doppler Encoded Excitation Patterning (DEEP) [53, 54, 55, 56]. In $\mathcal{F}$-BASIS imaging, the Fourier components of a target are selectively probed using traveling-wave sinusoidal-intensity illumination patterns projected onto the target surface, as shown in Fig 1.6 panel A. Each sinusoidally varying intensity pattern probes the corresponding spatial frequency of an object's intensity reflectivity (or flourescent response). One of the characteristic of $\mathcal{F}$-BASIS that sets it apart from the other Fourier-based techniques is that the light field patterns are generated rapidly and with high fidelity using acousto-optic deflectors. A collimated laser beam is directed through an acousto-optic deflector (AOD) which, in the simplest case when driven by two RF tones (f_1, f_2), generates two first-order diffracted, Doppler frequency-shifted beams which are recombined using a 4-f imaging system at the surface of a target where they coherently interfere producing a traveling-wave sinusoidal spatial fringe illumination. A portion of the fluoresced or scattered light from the illuminated field of view is spatially-integrated by collection optics and relayed to a high-temporal-bandwidth single-pixel detector where it is collected as a time series that oscillates at the frequency difference ($\delta f = f_2 - f_1$) as the sinusoidal pattern moves across the surface (panel B). The phase and amplitude of this temporal oscillation provides a precise measurement of the phase and amplitude of the spatial Fourier component of the sample that matches the spatial frequency of the illumination field. By probing many spatial frequencies, an image of the sample surface can be reconstructed using Fourier synthesis. In Chapter 2, I will explore in detail the mathematical foundations and operation of the $\mathcal{F}$-BASIS technique. Some significant strengths of the $\mathcal{F}$-BASIS technique are that it can be implemented

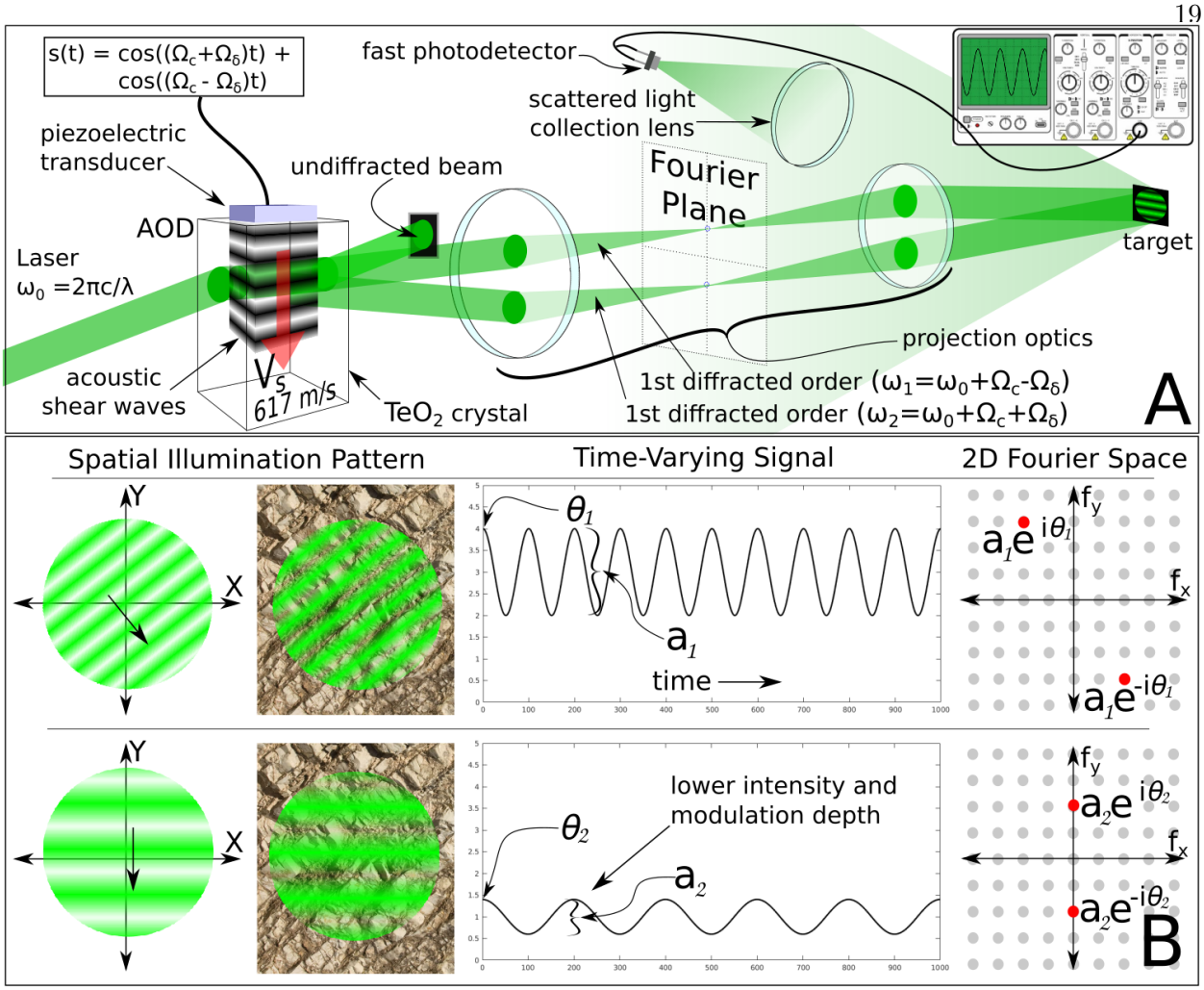

Figure 1.6: (A) A laser passes through an acousto-optic deflector and is split into the 0th-order undiffracted beam and two 1st-order diffracted beams upshifted by frequencies $\omega_0+\omega_1$ and $\omega_0-\omega_1$. The 1st-order beams are sent through a 4-f optical system to project them onto the surface of the target where they are recombined to generate the fringe pattern. Scattered light is spatially integrated using a lens and focused onto a fast single-pixel detector and the resulting sinusoidal signal is recorded on an oscilloscope. (B) A sinusoidal intensity pattern travels across the surface of a target. The amplitude and modulation depth change as a function of the strength of the Fourier component of the sample. The time-varying signal is Fourier transformed to calculate the complex 2D spatial Fourier components which are then placed into the approriate locations on a 2D grid (red dots at coordinates $a_k e^{i\theta_k}$ and $a_k e^{-i\theta_k}$).

with a small form factor; it provides fast electronic frequency addressing; there are no moving parts, and it is compatible with traditional microscopes and cameras but may also be used with dedicated low-optical-quality optics to produce diffraction limited images by using phase-closure calibration and by exploiting system symmetries.

An early implementation of what would become the $\mathcal{F}$-BASIS technique demonstrated a proof of concept by producing 1-D image reconstructions of a flat target through a microscope objective [57]. A laser was directed into a single AOD driven by a double-sided RF chirp which swept across the spatial frequencies. The resulting beams were directed through a polarizing beamsplitter (PBS) then a Nikon microscope objective onto the sample. The microscope objective also acted as the collection optics, directing the reflected light through the PBS and onto a single-pixel detector (Fig 1.7 panel a). The resulting waveform was converted into a 1-D reconstruction by de-chirping - a process that performs a Fourier transform and adds quadratic phase. To reconstruct a two dimensional image via Fourier sampling, the 2D Fourier plane must be at least partially filled, and a single AOD can produce fringes that vary in spatial frequency only in one dimension. A mechanically-rotating right-angle prism allowed the 1D slices to be rotated with respect to the sample and the first 2D image reconstructions of Ronchi rulings were made using a standard tomographic filtered back-projection algorithm (illustrated in the panel d of the reproduced Fig 1.8) [93]. In *Feldkhun and Wagner, (2010)*, they used this system to demonstrate a 4mm DOF by generating 2D reconstructions of resolution targets at different depths shown in Fig 1.7 panel d (reproduced). Each image was generated using 500 Fourier slices over 180^o each with a measurement interval of 10 ms. They were able to resolve 2 μm features throughout the entire DOF for a specularly reflective USAF resolution target, which is nearly $1000\times$ larger than the DOF of a conventional microscope with this resolution.

In later work, they implemented an optics-table mounted reflective illumination delivery system consisting of a 165 mm diameter diamond-turned concave ellipsoidal primary mirror and a 25 mm diameter near-paraboloid reflective-coated aspheric lens, the design and picture of which are shown in Fig 1.9 a and d respectively. Using a single frequency-chirped AOD and a high-precision rotating stage, they reconstructed the same USAF resolution target as in prior work with a FOV of 400 μm, but at a working distance of 213 mm which is about two orders of magnitude larger than what is possible with a conventional microscope objective. In addition to the experimental results, an improvement over the single AOD projector was designed (shown in the reproduced panel b

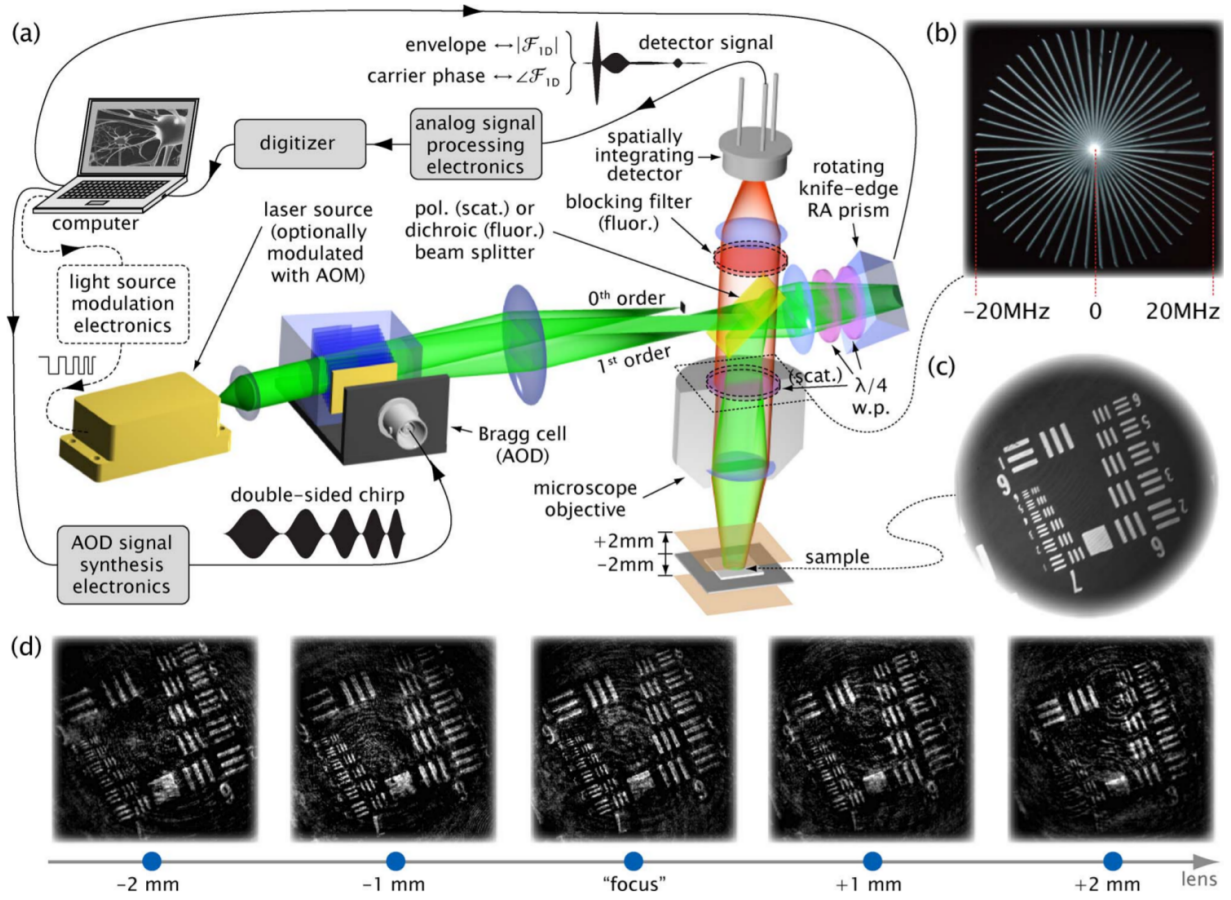

Figure 1.7: The initial work performed to demonstrate the $\mathcal{F}$-BASIS technique in *Feldkhun and Wagner, (2010)*. (a) A single AOD steps through spatial frequencies and diffracts the incoming laser beam in the horizontal plane, which are then rotated using a prism as a wavefront rotator to probe Fourier slices of the object. These beams are directed onto the surface of a target with a microscope objective. (b) The Fourier slices are filtered and projected using standard tomographic back-projection algorithms to generate a reconstruction of (c) the airforce resolution target used as a sample. (d) The target was probed at several distances and the reconstructions remain in focus over a 4 mm DOF. Reproduced from [54].

of Fig 1.9) containing a pair of crossed AODs used in series [55]. This design has the significant benefits of containing no moving parts and fully electronically addressable spatial frequencies on a 2D cartesian grid appropriate for FFT processing instead of the prior polar grid.

The most recent implementation of the 2D acousto-optic pattern projector simplifies the optical path and eliminates wavefront aberrations that existed in the previous design (Fig 1.10). Laser light enters the pattern projector as a horizontally-polarized collimated beam. It is injected at

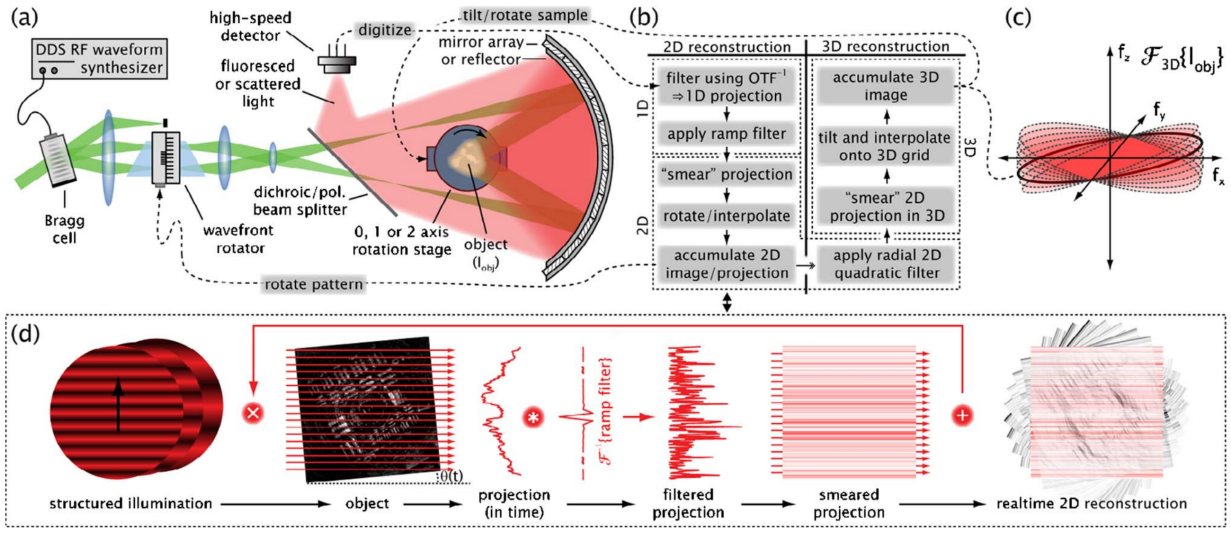

Figure 1.8: Continued development of the technique reported in *Feldkhun and Wagner, (2010)*. (a) A single AOD steps through spatial frequencies in the horizontal plane. The beams are reflected off an ellipsoidal mirror onto a rotating stage containing the sample to be imaged. The rotating stage takes the place of the right angle mirror. (b-c) The data is filtered and projected using standard tomographic back-projection algorithms (d) A pictorial view of the data collection and processing sequence. Reproduced from [54].

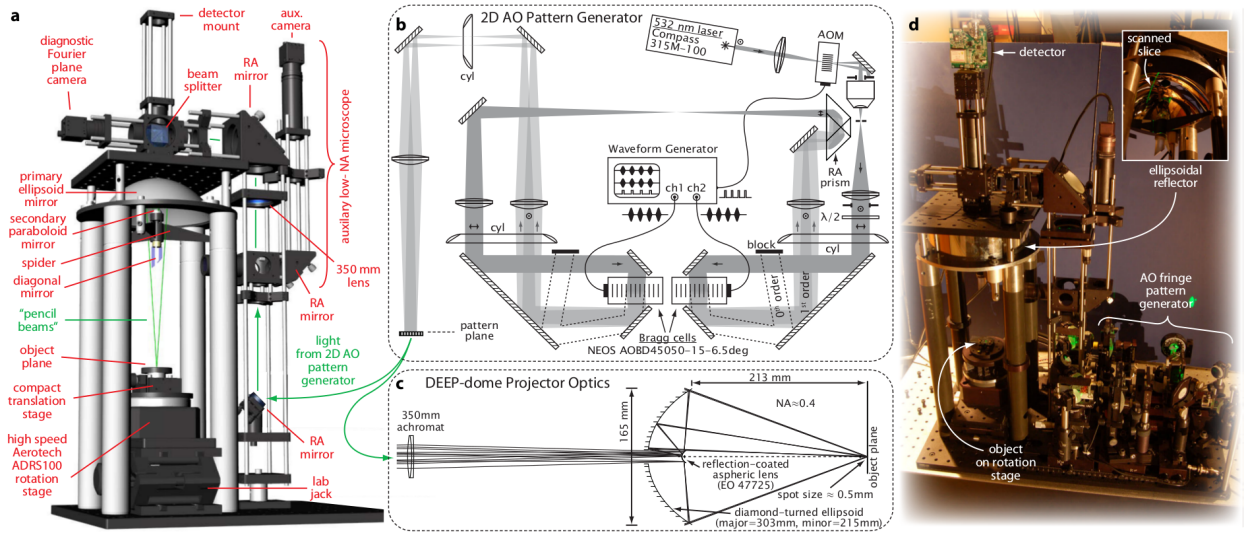

Figure 1.9: (a) Optomechanical design of the DEEP dome system using a reflective mode of $\mathcal{F}$-BASIS . (b) The pattern projector eliminates the need for a mechanically turning mirror by using crossed AODs. (c) The optical design of the mirror set. (d) A picture of the experimental hardware.

the Bragg angle of the first AOD which is driven by two tones $\omega_0+\omega_1$ and $\omega_0-\omega_1$ and generates two

collimated beams whose polarization is switched to vertical and are horizontally-deflected according to the equations 2.5 and 2.6. The undiffracted light is blocked by a beam dump. These beams are focused by the first lens in a 4-f imaging system and are subsequently rotated 90 degrees to be vertically-oriented by a wavefront rotator consisting of a mirror and a right-angle prism. Due to the double reflection in the wavefront rotator, the beams are polarized in the horizontal direction. After passing through focus, the beams are collimated again with the second lens of the 4-f set. The two collimated beams are recombined in space to form a 90^o-rotated image of the first AOD incident at the Bragg-angle inside the active aperture of the second AOD. This second AOD is driven with the RF tones $\omega_0+\omega_2$ and $\omega_0-\omega_2$ which again generates two horizontally-deflected beams for each of the two vertically-deflected input beams from the first AOD, resulting in four beams with horizontal and vertical symmetry of angular deflection. Another 4-f imaging set relays the combined image of the active apertures of the AODs to the output port of the pattern generator.

The $\mathcal{F}$-BASIS technique was expanded into three-dimensional imaging by retrofitting a laboratory microscope to receive the illumination patterns generated by the 2-D AO generator shown in Figure 1.10. Instead of relying upon probing single spatial frequencies or chirping across a range, the work pioneered the use of separable crossed non-redundant beam arrays with 23 beams on a side to sample 128,524 simultaneous Fourier samples [56]. They further expanded the technique by obtaining fluorescence images of fluorophore beads with a 3D spatial distribution. A single 7.44 ms waveform was used to probe the frequencies and resolve the 4 μm fluorescent beads in a 200 x 200 x 500 μm cube.

To summarize the previous work, the $\mathcal{F}$-BASIS technique has been demonstrated in modalities that expanded upon the DOF, the working distance and used with scattered, specularly reflected and fluoresced light. The earlier work demonstrated a DOF of 4 mm at a working distance of $\sim$1 cm resolving $2\mu m$ features. The optical-bench reflective system demonstrated a working distance of 21 cm resolving a 2 μm feature. Coupling the 2D pattern projector into a conventional microscope and utilizing spatio-temporal non-redundant arrays resulted in the resolved measurement of 4 μm fluorescent beads being measured through a depth of 500 μm.

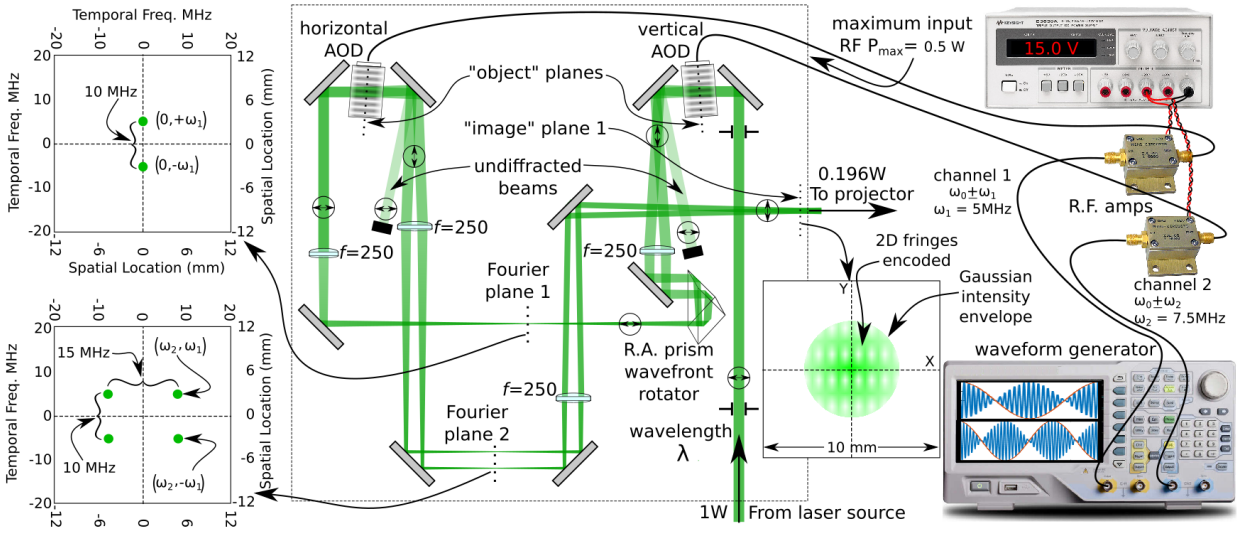

Figure 1.10: The acousto-optic pattern generator uses two orthogonal AODs driven by arbitrary waveform generators to produce symmetric pairs of horizontal and vertical programmable beams. From the laser source (below figure), the single beam passes through first AOD and is diffracted horizontally into multiple first-order beams. Two 4-f imaging optical trains form the image of the first AOD in the active aperture of the second AOD and relay this doubly encoded image to the output port. Each of the Fourier planes show the beams and temporal frequencies of the beams that are overlapped. Orthogonality between the two AODs is produced by a 90-degree double-reflection wavefront rotation using a right-angle prism at 45^o. The multiple beams overlap at the exit port (on the right of the dotted box) and are sent to the remote microscope optical assembly.

1.5 Scope of this research

Stated simply, the goal of this research was to design and build an imager that uses the $\mathcal{F}$-BASIS technology that is capable in form and function to operate on the mast of a planetary exploration rover and use it to acquire images with $\sim 10\mu m$ lateral spatial resolution. The tasks required to achieve this goal spanned a number of disciplines including mechanical engineering, manufacture processing, traditional optical design and modeling, manufacturing optical testing, algorithm development, laser science, acousto-optic physics and signal processing. It is important, here at the beginning of this document, to clarify what research was original to this effort and what portions were inherited. To this end, I want to make clear that the illumination pattern projector used in this research is the same as was used in the prior $\mathcal{F}$-BASIS development effort ([55, 56]), and this thesis is a natural continuation and extention of the body of work therein. The

remainder of this thesis, except in cases of obvious theoretical expositions of established background physics and mathematics, represents original research. The remote microscope optical assembly for imaging optics at 5m was designed as a portion of this work and it consists of a low precision ellipsoidal-paraboloidal two mirror 0.025 NA set and accompanying relay and aberration-correction optics to complete a 4-f imaging system. Unlike the most recently published $\mathcal{F}$-BASIS work that used non-redundant spatial frequencies to collect many simultaneous Fourier samples [56], I sequentially sample the object's spatial Fourier components and do so symmetrically about the optical axis thereby foregoing assymmetric spatial frequency measurements. By only sampling spatial frequencies that are axially symmetric, this instrument is insensitive to radially-symmetric phase errors and the DOF extends the entire length of the overlapping volume of the beams ($\sim$10 cm). The second difference from prior work is that I reduce the collection interval to the minimum necessary to measure the four Fourier components being simultaneously probed. This fast sampling cadence allows me to acquire high spatial-frequency data in the presence of short time-constant phase-error-inducing atmospheric turbulence. A phase-closure technique is proposed using highly redundant phase measurements of the horizontal and vertical Fourier components. The acousto-optics allows me to offset the DC location in the exit pupil thereby removing low spatial frequency losses due to a central hole in the optical train and providing a mechanism to get lower resolution binocular images. Previously, the $\mathcal{F}$-BASIS technique has been demonstrated with a 20-cm working distance, high resolution microscopic imaging system [55]; this work extends this technique to acquire images with 11 μm spatial resolution at 5 m, a DOF defined in centimeters rather than microns, all with a low-precision optical assembly.

1.6 Guide to this thesis

This document may be viewed as a "how-to" manual for constructing a remote microscope that uses the $\mathcal{F}$-BASIS technique with a path to spaceflight. The chapters that follow will provide detailed descriptions of all of the mechanical, optical, electronic, operational and algorithmic considerations that must be addressed when producing such a system. Several mathematical trea-

tises are peppered throughout the document when necessary to provide a theoretical foundation and conceptual framework for seminal subfields. The thesis is organized with the intent that each chapter addresses a different engineering discipline within the broader narrative but acts as a stand alone document as much as possible.

Chapter 2: *The Mathematical Foundations of $\mathcal{F}$-BASIS* begins with a review of a limited selection of Fourier analysis concepts necessary to understand the operation of the microscope and its differences from standard imaging systems. This is immediately followed by a thorough derivation of the mathematical foundation of the $\mathcal{F}$-BASIS technique. I derive the illumination field due to the interference of two ideal plane wave beams and the resulting signal at the detector and expand this analysis to include a Gaussian intensity distribution. The chapter ends with a discusson of several aspects of the $\mathcal{F}$-BASIS system that are not intuitively obvious, including the calculation of the depth-of-field, tolerance to some aberrations, limitations due to the time-bandwidth product, applications for compressive sensing collection schemes, and sensitivity to atmospheric turbulence.

Chapter 3: *Opto-mechanical Design* discusses the necessary mechanical and opto-mechanical requirements and engineering solutions for constructing a rover-mast-mounted remote microscope. The opto-mechanical performance with respect to gravitational deformation, vibration and thermal gradients of a light-weighted aluminum primary mirror are modeled using finite element analysis. This is followed by a discussion of the techniques and considerations for manufacturing a monolithic aluminum mirror that meets the optical requirements of the remote microscope. I outline the approach to the engineering of the opto-mechanical support spider assembly and again explore its mechanical performance using finite element analysis. I detail the precision requirements for the position of optical components and the resulting error tolerance.

Chapter 4: *Remote Microscope Optical Design* constitutes a significant portion of the research of this effort. I begin with the notional optical requirements for the microscope and describe specific approach and design used in this research, including an exploration of the candidate mirror sets and the trade-offs involved. The relevant optical concepts of finite image conjugation and telecentrism are introduced. This is followed by a targeted derivation of the aberrations of two-mirror systems,

calculating the optical prescription of those mirrors and the curvature of the focal surface between them. I concentrate on the third-order aberrations of astigmatism and field curvature, explore the inter-relationship between them, and demonstrate their importance to the optical train. Using this perspective, I outline the task of correcting the geometric aberrations of the optical design using an altered Cooke-triplet based zoom lens assembly. I end the chapter with the results of simulations of the performance of the microscope optical assembly, and the limits of use as a zoom system.

Chapter 5: *Optical Form Testing* introduces the subject of practical optical surface testing using phase-shifting interferometry. During this work, a new technique was developed for testing aspheric surfaces using paraboloidal-parameterized annular sub-apertures. I derive the mathematical foundation of the technique, compare it with the standard technique used in the field today, and demonstrate it to measure the surface error of my mirrors.

Chapter 6: *Remote Microscope Laboratory Experiment* describes in detail the experimental setup used in the laboratory. A diagram of the experimental layout acts as the guide for the narrative. I state the commercial instruments used in the experiment and call out relevant operational characteristics. The distances between components, laser beam collimation and polarization characteristics and optical power at fiducials are all specified. I differentiate the response of the system with respect to the reflective characteristics of the target, namely in the specular and Lambertian scattering regimes. The control electronics and data acquisition train are described in detail. This chapter ends with a report on the measured laser powers at important fiducial points for different reflectivities of targets.

Chapter 7: *Remote Microscope Alignment, Errors and Image Reconstructions* describes the three alignment procedures needed to construct and use the microscope. I explore the sources and effects of error in the system including mirror deformation, optical train wavefront error, bulk temperature evolution effects on laser pointing, atmospheric turbulence and electronic timing error. I introduce the consequences of turbulence on the system, the prior art of measuring turbulence, and how these effects can lead to a deeper understanding of atmospheric processes. I analyze the contributions of turbulence to the microscope's received time-signal, providing verification through

multiple methods. I present the interplay between temporal and spatial frequencies in the structured illumination field to provide clarity when describing the measurement schemes that utilize time sequences to sample spatial frequencies of the target. The detection equation and phase error terms are written in explicit form. Specularly-reflective resolution targets are used to demonstrate the maximum performance characteristics of the remote microscope. Reconstructions of scattering paper targets with partial and negligible polarization retention are compared. I present the techniques that best sample and reconstruct images and propose a new phase closure technique for the remote microscope and a final reconstruction algorithm. I present the reasons behind and process for collecting data using stepped axially-symmetric minimalized Fourier sampling.

Chapter 8: *Conclusions* presents a report on the lessons learned from each of the tasks from the preceding chapters. I complete this work with a description of the state of the art of the remote microscope and possible routes for future work.

Chapter 2

The Mathematical Foundations of $\mathcal{F}$-BASIS

2.1 Concepts of Imaging in Fourier Space

2.1.1 The Fourier Transform

In 1822, Joseph Fourier wrote his mathematical treatise on decomposing certain functions into a complete basis of sinusoids [61]. He showed that functions that meet three conditions could always be decomposed, that is to say, they can be exactly represented by a summation of a series of sinusoids with independent spatial period, amplitude and phase. The conditions for Fourier decomposition are:

(1) The function must be integrable at all points

(2) It must have at most a finite number of discontinuities and extrema

(3) It must have no discontinuities where the value of the function reaches infinity

The mathematical operation that decomposes functions into a sinusoidal basis set is called the Fourier transform and is a homomorphic transformation, meaning that it doesn't change any of the values of the function, but rather casts the information contained within the waveform into a different basis set. The decomposition of the function into a series of sinusoids changes the basis set from defining the curve using one y-value per x pixel location to a series of coefficients specifying the amplitude and phase of a complete basis set of sinusoidal waveforms.

Now, the reason I've gone on what could justly be described as a "self-indulgent tour of somebody else's house" is that I now get to introduce a point of confusion that will be particularly important in the operations that will be repeatedly discussed in the remainder of this thesis. The Fourier transform can be applied to any signal from any arbitrary source in any conceptual space that meets the above criteria. So, it can be applied to a waveform consisting of spatial height measurements such as profilometry or the amount of blue in a single row of a 2D RGB image or a signal that varies in time (temporal) such as laser intensity illuminating a surface or an RF signal being measured at an antenna. I am over-emphasizing this because in the work that follows, I perform many Fourier transforms sometimes on spatial distributions of optical intensity or intensity reflectivity or on 2-D variations of optical fields and sometimes on 1D temporal waveforms. In the algorithms for this $\mathcal{F}$-BASIS microscope the temporal representations and physical space are coupled together and it is often confusing. Once one gets familiar with this work it becomes second nature to throw Fourier transforms around with acrobatic nonchalance, but if you're reading this thesis in the hopes of using it to construct a $\mathcal{F}$-BASIS microscope then the differentiation of the various Fourier transform operations and what each is accomplishing is one of the top five concepts that must eventually be understood. So, keeping this in mind, I will now proceed to the subject of the notational construction of the mathematical operation of the Fourier transform that I will use in this thesis.

In cartesian coordinates, a one-dimensional spatial Fourier Transform of the real function g(x) is expressed as:

$$G(f_x) = \mathcal{F}_x\{g(x)\} = \int_{-\infty}^{\infty} g(x)e^{-i2\pi f_x x}dx \tag{2.1}$$

where f_x is the spatial frequency in units m^{-1} in the x dimension, and I designate the Fourier transform integral operator $\mathcal{F}_x$. My notation extends into two spatial dimensions in Cartesian coordinates via:

$$G(f_x, f_y) = \mathcal{F}_{xy}\{g(x,y)\} = \int_{-\infty}^{\infty}\int_{-\infty}^{\infty} g(x,y)e^{-i2\pi(f_x x + f_y y)}dxdy \tag{2.2}$$

Similarly, the 1-D transform is applied to a temporal signal g(t) via the operation expressed as:

$$G(f) = \mathcal{F}_t\{g(t)\} = \int_{-\infty}^{\infty} g(t)e^{-i2\pi ft}dt \tag{2.3}$$

where the temporal frequency is designated as f in units of s^{-1}.

2.1.1.1 The Abbe Theory of Image Formation and Spatial Frequencies

Ernst Abbe, along with Karl Zeiss, was one of the founders of modern optics and is responsible for a hefty portion of our understanding of traditional imaging systems including concepts of numerical aperture, the resolution limit of a microscope, depth-of-field and more [5]. In his work on the optics of microscopes, Abbe formulated a theory of image formation using the concept of spatial frequencies which is fundamental to constructing an intuitive operational model of the $\mathcal{F}$-BASIS remote microscope. Abbe stated that only a portion of the diffracted orders of coherent light from a surface would pass through the finite aperture of the entrance pupil of an optical system as shown in panel A of Figure 2.1. The low diffracted orders are near the center of the aperture while the components lost at high angle contain the high spatial frequencies. Although Abbe formulated this model using coherent light, the mapping of spatial frequencies to angle applies to all illumination and imaging systems. This is one of the most important conceptual images for the $\mathcal{F}$-BASIS technique, and I'll be returning to it several times for reference in my descriptions. Panel B of Figure 2.1 illustrates the basic mechanics of how the spatial frequencies of the object are probed with the $\mathcal{F}$-BASIS remote microscope using collimated beams of light and demonstrates the conceptual similarity to the Abbe theory of imaging. The beams recombine on the surface of the target, interfere to produce fringes which are then used to probe the spatial Fourier components of the object. An important visualization to keep in mind is the fact that the lower spatial frequencies are probed using beams near the center of the optical system and higher spatial frequencies are probed using beams at higher angle. Eventually, in the chapter 7, I'll describe how I can bend the rules somewhat with regard to this conceptual construct.

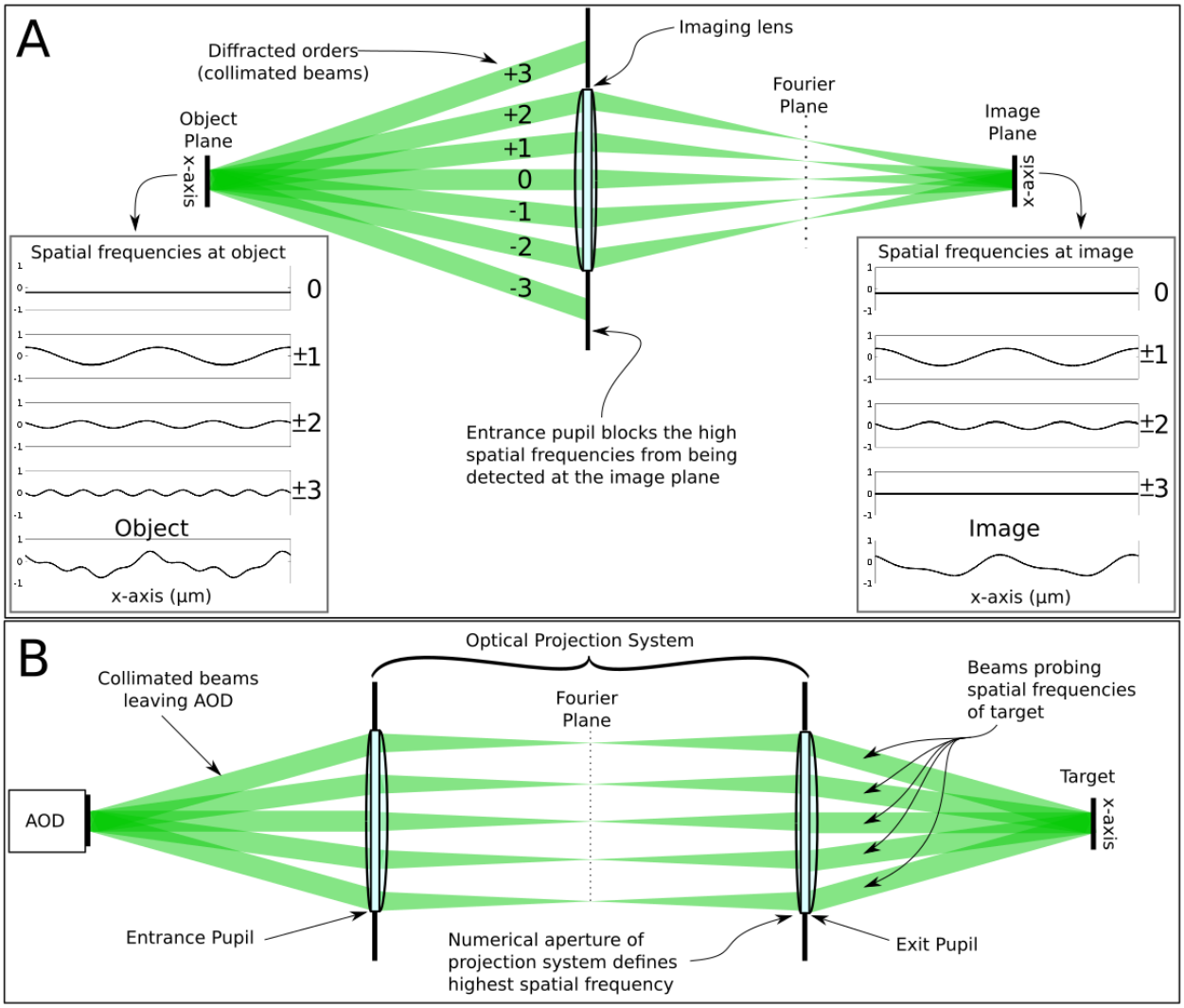

Figure 2.1: A) Abbe theory of coherent image formation. Diffracted orders mapped as spatial frequencies at the object diffract at angles proportional to the frequency. The zeroth order beam, the DC component, is undiffracted and travels down the center of the aperture. An entrance pupil to the optical system places an upper limit on the spatial frequencies that can be collected to generate the image. B) The operating principal of $\mathcal{F}$-BASIS imaging. The collimated beams exiting the acousto-optic deflector are redirected by the optical projection system to overlap on the surface of the target. The beams probe the spatial frequencies in the same manner as described in A, limited by the numerical aperture of the optics of the projector.

2.2 Mathematical Background of the $\mathcal{F}$-BASIS Technique

2.2.1 Plane Wave Illumination Field

The sinusoidal illumination patterns used in $\mathcal{F}$-BASIS are generated using devices called acousto-optic deflectors (AOD) (known as Bragg cells), that consist of a piezoelectric transducer mounted to one face of a crystal with specific acoustic and optical properties which I describe in later chapters, typically tellurium dioxide (TeO_2). In the simplest case (Fig 1.6 panel A), the transducers are driven with a temporal waveform $s(t)$ containing a pair of RF tones centered at angular frequency $\Omega_0 = 2\pi f_o$ upshifted and downshifted by the deflection frequency $\Omega_d = 2\pi f_d$.

$$s(t) = \cos\left((\Omega_0 + \Omega_d)t\right) + \cos\left((\Omega_0 - \Omega_d)t\right) = \frac{1}{2}(e^{i(\Omega_0+\Omega_d)t} + e^{i(\Omega_0-\Omega_d)t} + cc) \tag{2.4}$$

Typical AODs have center frequencies around $f_c = 100$ MHz and support octave bandwidths $B = 2f_c/3$. When driven with this waveform, the transducer launches a temporal beat-frequency shear acoustic wave with power envelope modulated at $2\Omega_d$ into the crystal that travels at the anomalously slow shear-wave velocity in TeO_2 ($v_s = 617$ m/s) and locally varies the off-axis dielectric tensor of the crystal via shearing deformation producing an anisotropic polarization switching volumetric traveling diffraction grating. When a collimated laser beam is sent through the AOD at the appropriate Bragg angle θ_B, a portion of the light is diffracted into two 1st-order beams that are deflected at small angles (at most a couple of degrees) defined by the equations:

$$\theta_{(+d)} = \cos^{-1}\left(\frac{n_o}{n_e}\right) + \sin^{-1}\left(\frac{\lambda f_d}{n_o v_a}\right) \tag{2.5}$$

$$\theta_{(-d)} = \cos^{-1}\left(\frac{n_o}{n_e}\right) + \sin^{-1}\left(\frac{\lambda f_{-d}}{n_o v_a}\right) \tag{2.6}$$

where λ is the wavelength of the laser, v_a is the acoustic velocity, n_o and n_e are the ordinary and extraordinary indices of refraction of the acousto-optic crystal respectively. In addition to being angularly deflected, the angular frequencies of the 1st-order beams (ω_1, ω_2) are also Doppler-shifted

by the RF frequencies driving the AOD.

$$\omega_1 = 2\pi\frac{c}{\lambda} + \Omega_0 + \Omega_d \tag{2.7}$$

$$\omega_2 = 2\pi\frac{c}{\lambda} + \Omega_0 - \Omega_d \tag{2.8}$$

Using a 4-f imaging system, these collimated beams are recombined on the surface of a target where they interfere to produce the traveling planar fringes. Within the circumference of the beam, the simplest model for the wavefront of the diffracted laser beam is a plane wave, the electric field of which is defined by the complex field:

$$E(\vec{r},t) = \frac{A(\vec{r})}{2}(e^{i(\vec{k}\cdot\vec{r}-\omega t)} + cc) \tag{2.9}$$

where $\vec{k} = 2\pi/\lambda\hat{k}$ is the wave vector pointing in the direction of beam propagation, and ω is the temporal frequency of the monochromatic beam. The field intensity (W/m^2) is:

$$I(\vec{r},t) = \frac{E(\vec{r},t)\cdot E(\vec{r},t)^*}{2\eta_0} = \frac{\left|E(\vec{r},t)\right|^2}{2\eta_0} \tag{2.10}$$

where the * denotes a complex conjugate, $\eta_0 = 377\Omega$ is the impedance of free space, and the constant factor of $2\eta_0$ will be dropped in the following. The intensity generated by the interference of two temporally coherent plane waves is the square of the sum of the electric field vector phasors of the two beams.

$$I(\vec{r},t) = \left|E_1(\vec{r},t) + E_2(\vec{r},t)\right|^2 \tag{2.11}$$

$$= \left|\frac{A_1(\vec{r})}{2}(e^{i(\vec{k_1}\cdot\vec{r}-\omega_1 t)} + cc) + \frac{A_2(\vec{r})}{2}(e^{i(\vec{k_2}\cdot\vec{r}-\omega_2 t)} + cc)\right|^2 \tag{2.12}$$

Multiplying these out and substituting in Equation 2.10 gives:

$$I_{12}(\vec{r},t) = I_1(\vec{r},t) + I_2(\vec{r},t) + E_1(\vec{r},t)\cdot E_2(\vec{r},t)^* + E_2(\vec{r},t)\cdot E_1(\vec{r},t)^* \tag{2.13}$$

Expanding the third term:

$$E_1(\vec{r},t)\cdot E_2(\vec{r},t)^* = \frac{A_1(\vec{r})}{2}e^{i(\vec{k_1}\cdot\vec{r}-\omega_1 t)} \cdot \frac{A_2^*(\vec{r})}{2}e^{i(\vec{k_2}\cdot\vec{r}+\omega_2 t)} \tag{2.14}$$

$$= \frac{A_1 A_2^*}{4}e^{i((\vec{k_1}-\vec{k_2})\cdot\vec{r}-(\omega_1-\omega_2)t)} \tag{2.15}$$

Expanding out the fourth term in Equation 2.13 produces an analogous result:

$$E_2(\vec{r},t)\cdot E_1(\vec{r},t)^* = \frac{A_2A_1^*}{4}e^{-i(\vec{k}_{12}\cdot\vec{r}-\omega_{12}t)} \tag{2.16}$$

Combining with its complex conjugate allows us to use Euler's Formula to recast the equation in trigonometric terms so that the intensity is then:

$$I_{12}(\vec{r},t) = I_1(\vec{r},t) + I_2(\vec{r},t) + \frac{2}{4}\big|A_1A_2\big|\cos\big((\vec{k_1}-\vec{k_2})\cdot\vec{r}-(\omega_1-\omega_2)t+\phi_1-\phi_2\big) \tag{2.17}$$

Observing that A is the square root of the intensity I, and that $I_1 + I_2$ is the average intensity I_0 at every location, the last equation can be rewritten into a familiar form:

$$\begin{aligned} I_{12}(\vec{r},t) &= I_o(\vec{r})\Big(1+\frac{m}{2}\cos\big((\vec{k_1}-\vec{k_2})\cdot\vec{r}-(\omega_1-\omega_2)t\big)\Big) \\ &= I_o(\vec{r})\Big(1+\frac{m}{2}\cos\big((\vec{K}_g\cdot\vec{r}-\Omega_g t)\big)\Big) \end{aligned} \tag{2.18}$$

where $m = \sqrt{I_1I_2}/(I_1+I_2)$ is the "modulation depth", a quantity from 0 to 1 ratioing the strength of the sinudoidal oscillation to the maximum value in the field. I've also substituted the two wave vectors and temporal frequencies of the two diffracted beams with the wave vector K_g and angular frequency Ω_g of the traveling grating. This is the expression for the intensity of the light field inside the FOV of the $\mathcal{F}$-BASIS imaging system.

2.2.2 Detected Signal with Plane Wave Illumination

At any moment in time, the traveling wave sinusoidal spatial intensity illumination pattern interacts with the target surface (as shown on the surface of a rock face in Fig 1.6 panel B) and a portion is either specularly reflected or scattered depending upon the spatial variation of the intensity reflectivity of the surface, or the laser activates fluorescence in the material which isotropically radiates a temporally-modulated wavelength-shifted emission. Taking the case of a Lambertian scattering surface with a position-dependent intensity reflectivity coefficient $R_{obj}(\vec{r})$ (which is fundamentally the quantity we are attempting to measure), a portion of the hemisphere of reflected light will be collected by the limiting aperture of the collection optics Γ_{aper} and relayed

with some optical efficiency η_{opt} to a high-speed single-pixel detector. If the reflectivity function is unity everywhere as would be the case with a featureless ideal scattering target, then the amplitude of the photocurrent i_0 that is generated at the detector is:

$$i_0 = I_{inc} \cdot \eta_{AO}^2 \cdot \eta_{opt} \cdot \frac{\Gamma_{aper}}{2\pi} \cdot Q_E \tag{2.19}$$

where I_{inc} is the incident laser beam intensity measured at the output port of the laser, η_{AO} is the diffraction efficiency of one AOD, and Q_E is the quantum efficiency of the detector.

When considering real targets that contain spatial variation of their reflectivity coefficient $R_{obj}(\vec{r})$, this photocurrent amplitude is modulated by the interaction of the light with this spatially-varying reflectivity. As time progresses, the sinusoidal intensity illumination pattern will move across the target, interacting with the matched sinusoidal reflectivities at the shifted spatial position until a point in time when the fringes have moved a distance of one spatial period and the detected signal will repeat (time varying signal in Fig 1.6). The time sequence of the photoelectrical current $i_{pc}(t)$ generated by the detector from the power of the detected light can then be expressed as:

$$i_{pc}(t) = i_0 \iint_{FOV} R_{obj}(\vec{r}) \Big[1 + \frac{m}{2} \cos\Big(\vec{K}_g \cdot \vec{r} - \Omega_g t\Big)\Big] d\vec{r} \tag{2.20}$$

Casting the sinusoidal intensity illumination pattern in exponential notation:

$$1 + \frac{m}{2}\cos(\vec{K}_g \cdot \vec{r} - \Omega t) = 1 + \frac{m}{4}\Big(e^{i2\pi(\vec{K}_g \cdot \vec{r} - \Omega t)} + cc\Big) \tag{2.21}$$

$$= 1 + \frac{m}{4}\Big(e^{i2\pi(f_{gx}x + f_{gy}y - \Omega t)} + cc\Big) \tag{2.22}$$

where f_{gx} and f_{gy} are the spatial frequencies of the interference grating produced. Expressing the real spatially dependent intensity reflectivity function of the object using its Hermitian Fourier representation symbolized by $\mathcal{R}_{obj}$:

$$R_{obj}(\vec{r}) = \iint_{-\infty}^{\infty} \mathcal{R}_{obj}(f_x, f_y) e^{i2\pi(f_x x + f_y y)} df_x df_y \tag{2.23}$$

Recasting Equation 2.20 in these terms we get:

$$i_{pc}(t) = i_0 \iint_{-\infty}^{\infty} \left[\iint_{-\infty}^{\infty} \mathcal{R}_{obj}(f_x, f_y) e^{i2\pi(f_x x + f_y y)} df_x df_y \right] \Big(1 + \frac{m}{4}\big(e^{i2\pi(f_{gx}x + f_{gy}y - \Omega_g t)} + cc\big)\Big) dx dy \tag{2.24}$$

Since these two integrals are over different variables, we can swap the order of integration.

$$\begin{aligned} i_{pc}(t) &= i_0 \iint_{-\infty}^{\infty} \left[\iint_{-\infty}^{\infty} \mathcal{R}_{obj}(f_x, f_y) df_x df_y \right] dx dy \\ &+ i_0 \frac{m}{4} e^{-i\Omega_g t} \iint_{-\infty}^{\infty} \mathcal{R}_{obj}(f_x, f_y) \left[\iint_{-\infty}^{\infty} \left(e^{i2\pi((f_x+f_{gx})x+(f_y+f_{gy})y)} + cc \right) dx dy \right] df_x df_y \end{aligned} \tag{2.25}$$

The first term is the integral of all spatial frequencies over the entire field of view. This is just the average reflected energy of the object, this is otherwise known as the DC component of the reflectivity $\mathcal{R}_{obj}(0,0)$. The term within the brackets of the second line is just the definition of a delta function in Fourier space at the frequency $(f_x = -f_{jx}, f_y = -f_{jy})$, and the complex conjugate is likewise the delta function at $(f_x = f_{jx}, f_y = f_{jy})$.

$$i_{pc}(t) = i_0 \Big[\mathcal{R}_{obj}(0,0) + \frac{m}{4} \big(e^{-i\Omega_g t} \big) \iint_{-\infty}^{\infty} \mathcal{R}_{obj}(f_x, f_y) \big(\delta(f_x + f_{gx}, f_y + f_{gy}) + \delta(f_x - f_{gx}, f_y - f_{gy}) \big) df_x df_y \Big] \tag{2.26}$$

By the sifting property of the delta function, the integral of the complex valued function $\mathcal{R}_{obj}$ multiplied by a delta function is just the function itself at the frequency of the delta function, so that the detector signal current is:

$$i_{det}(t) = i_0 \Big[\mathcal{R}_{obj}(0,0) + \frac{m}{4} \big(e^{-i\Omega_g t} \big) \mathcal{R}_{obj}(f_{gx}, f_{gy}) + cc \Big] \tag{2.27}$$

What this says is that the detected signal is the average reflectivity within the illuminated FOV plus the Fourier component of the reflectivity times a sinusoidal temporal waveform times the efficiency and modulation depth terms. The first term is just an offset value in the detected signal and an AC-coupled detector won't measure it, so we can set it to zero in the analysis except when determining its shot noise contribution.

This derivation assumes plane waves interfering to make sinusoidal illumination patterns with uniform spatial intensity across the illuminated FOV. By looking for a specific temporal frequency in the signal waveform and by knowing the system efficiency response function i_0 we can measure the spatial Fourier component at frequency (f_{gx}, f_{gy}) of the object. The 2D (or indeed 3D) Fourier representation of an object can be reconstructed by measuring many such spatial frequencies.

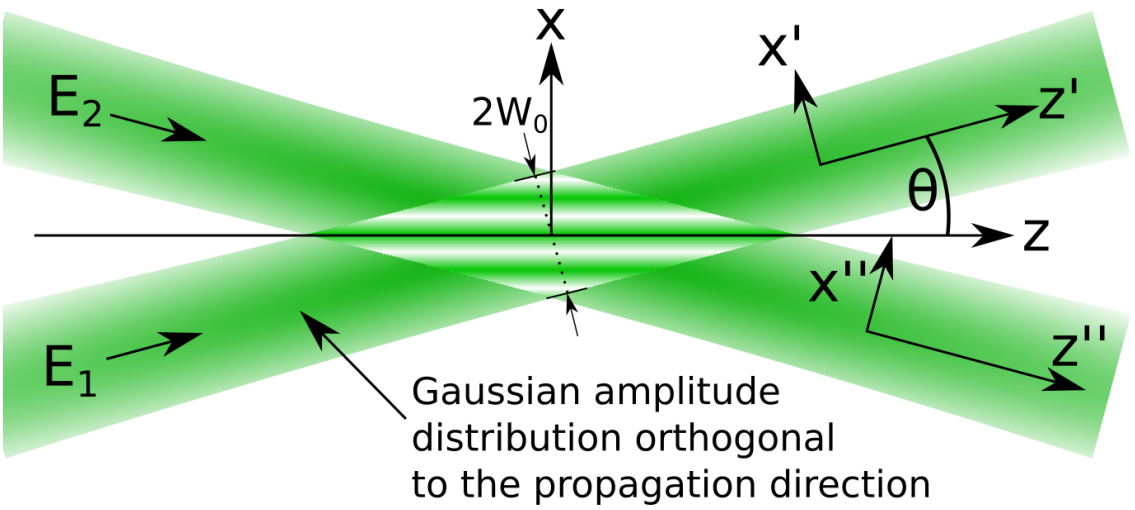

Figure 2.2: The interference of two Gaussian beams. The two beams E_1 and E_2 are propagating in the $x-z$ plane at symmetric angles $+\theta$ and $-\theta$ from the z-axis respectively so that their propagation vectors are now z' and z''. The volume of interference occurs at the mutual waists of the two beams centered at $z = 0$.

2.2.3 Detected Signal with Gaussian Beam Illumination

In reality, the laser beams are not uniform intensity plane waves of infinite spatial extent illuminating the surface, they have some field amplitude distribution function across a finite cross-sectional area. The interference of two Gaussian beams intersecting at an angle 2θ is shown graphically in Figure 2.2. In the ideal case when optical aberrations are sufficiently suppressed, the beam has been optimally spatially-filtered and the active aperture of the acousto-optic deflector is assumed to be homogeneous, each beam can be modeled as having a complex Gaussian amplitude distribution according the following equations.

$$E_1(x', y', z', t) = E_0 \frac{q_0}{q(z')} \left(e^{\left(-ik\frac{\rho'^2}{2q(z')}\right)} e^{-i(kz'-\omega_1 t)} + cc \right) \hat{\rho}' \tag{2.28}$$

$$E_2(x'', y'', z'', t) = E_0 \frac{q_0}{q(z'')} \left(e^{\left(-ik\frac{\rho''^2}{2q(z'')}\right)} e^{-i(kz''-\omega_2 t)} + cc \right) \hat{\rho}'' \tag{2.29}$$

where (x', y', z') and (x'', y'', z'') represent the coordinate systems of each beam rotated from the (x, z) axis by $+\theta$ and $-\theta$ respectively. The axial position $z = 0$ is the location of the mutual center of the waist of both beams. For all $'$, $''$ and unrotated coordinate systems, $\rho^2 = x^2 + y^2$. The inverse of the so-called q-parameter of the beam $q(z) = z + iz_0$ can be broken into real and imaginary parts

by defining two functions that express the beam width $W(z)$ and radius of curvature of the Gaussian wavefront $R(z)$:

$$W(z) = W_0\sqrt{1+(\frac{z}{z_0})^2} \tag{2.30}$$

$$R(z) = z\Big[1+(\frac{z_0}{z})^2\Big] \tag{2.31}$$

where $z_0 = \pi W_o/\lambda^2$ is the Rayleigh range for a beam with minimum waist half-width of W_0. Using these definitions, the inverse q-parameter is expressed as:

$$\frac{1}{q(z)} = \frac{1}{R(z)} - i\frac{\lambda}{\pi W^2(z)} \tag{2.32}$$

In order to express the equation for interference in a single coordinate system, the Equations 2.28 and 2.29 must be cast in the unrotated coordinates. The prime coordinates (x', z') and (x'', z'') are related to the original coordinates (x, z) via a coordinate rotation about θ.

$$x' = x\cos\theta - z\sin\theta \tag{2.33}$$

$$z' = x\sin\theta + z\cos\theta \tag{2.34}$$

$$x'' = x\cos\theta + z\sin\theta \tag{2.35}$$

$$z'' = -x\sin\theta + z\cos\theta \tag{2.36}$$

Since the beams are tilted in the $x-z$ plane $y' = y'' = y$. Substituting the rotated coordinate values into Equations 2.28 and 2.29 casts the equations for the beams in the (x, z) coordinate system.

$$E_1(x,y,z,t) = \frac{E_0 i z_0}{(iz_0 + z\cos\theta + x\sin\theta)} e^{-i\left(k\frac{(x\cos\theta - z\sin\theta)^2+y^2}{2(iz_0+z\cos\theta+x\sin\theta)} + k(z\cos\theta + x\sin\theta) - \omega_1 t\right)} + cc \tag{2.37}$$

$$E_2(x,y,z,t) = \frac{E_0 i z_0}{(iz_0 + z\cos\theta - x\sin\theta)} e^{-i\left(k\frac{(x\cos\theta + z\sin\theta)^2+y^2}{2(iz_0+z\cos\theta-x\sin\theta)} + k(z\cos\theta - x\sin\theta) - \omega_2 t\right)} + cc \tag{2.38}$$

Plugging these into Equation 2.13 and employing the shorthand $c = \cos\theta$ and $s = \sin\theta$ for readability, yields the following equation for the interference of the two beams.

$$I_{12}(x,y,z,t) = |E_1|^2 + |E_2|^2 + E_1E_2^* + E_1^*E_2 \tag{2.39}$$

$$= I_0 + \frac{I_0(m/2)z_0^2}{(zc+xs+iz_0)(zc-xs-iz_0)} e^{-i(2kxs-(\omega_1-\omega_2)t)} e^{-ik\frac{x^2c^2-2xczs+z^2s^2+y^2}{2(zc+xs+iz_0)} - \frac{x^2c^2+2xczs+z^2s^2+y^2}{2(zc-xs-iz_0)}} + cc$$

$$= I_0 + \frac{I_0(m/2)z_0^2}{z^2c^2 - x^2s^2 + z_0^2 + 2ixsz_0} e^{-i(2kxs-(\omega_1-\omega_2)t)} e^{-ik\frac{x^2c^2-2xczs+z^2s^2+y^2}{2(zc+xs+iz_0)} - \frac{x^2c^2+2xczs+z^2s^2+y^2}{2(zc-xs-iz_0)}} + cc$$

For nearly collimated beams, the radius of curvature $R(z) = \infty$, the amplitude and Guoy phase in the denominator can be neglected, and the real part of the $q(z)$ goes to zero so that the following relation is true.

$$q(z) = q(z') = q(z'') = q_0 = iz_0 \tag{2.40}$$

This simplifies the interference equation to:

$$I_{12}(x,y,z,t) = I_0\Big(1 + \frac{mz_0^2}{-2z_0^2} e^{-i(2kxs-\Omega_g t)}\big(e^{\frac{-ik(x^2c^2+z^2s^2-2xzcs+y^2)}{2iz_0}} e^{\frac{ik(x^2c^2+z^2s^2+2xzcs+y^2)}{-2iz_0}}\big) + cc\Big) \tag{2.41}$$

where the difference in the temporal frequencies of the interfering beams $(\omega_1 - \omega_2)$ has been substituted with Ω_g. The $2x\sin\theta z\cos\theta$ terms in the two exponentials cancel leaving

$$I_{12}(x,y,z,t) = I_0\Big(1 - \frac{m}{2} e^{-i(2kxs-\Omega_g t)} e^{-k\frac{(x^2c^2+z^2s^2+y^2)}{2z_0}} + cc\Big) \tag{2.42}$$

But $k/2z_0 = 2\pi/\lambda = 1/W_0^2$ so

$$I_{12}(x,y,z,t) = I_0\Big(1 - \frac{m}{2}\cos(2kx\sin\theta - \Omega_g t) e^{-\frac{x^2\cos^2\theta + z^2\sin^2\theta + y^2}{W_0^2}}\Big) \tag{2.43}$$

The exponential term is a real Gaussian intensity distribution across the intersection area of the beam, and the cosine term describes the same sinusoidal oscillation as in the plane wave case. The spatial Fourier component of the object is encoded into the sinusoidal temporal waveform, but the contribution across the field of view is no longer constant and instead has a Gaussian intensity distribution which slightly blurs the object Fourier spectrum.

2.2.4 Optical Consequences of the $\mathcal{F}$-BASIS Technique

As should be clear from the discussion leading up this point, the $\mathcal{F}$-BASIS technique has considerable optical and operational differences from traditional imaging systems. Traditional imagers have 2D detectors and a relatively simple optical train whose only purpose is to form an image on the focal plane array, whereas the $\mathcal{F}$-BASIS system uses a simpler single-pixel detector at the cost of a much more complex optical system which produces and projects structured illumination, receives the reflected light and mathematically processes the acquired signal to construct an "image". In

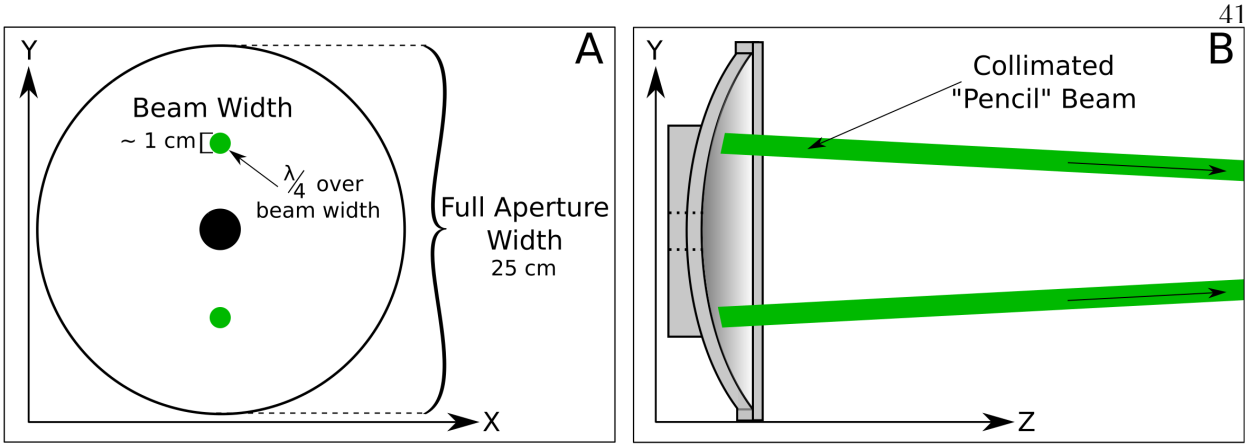

Figure 2.3: A: The full aperture pupil function of the optical system used in this thesis is shown face on as seen across the optical axis. Two beams intersect with the objective optic with a circular cross-section with a width of w_b. The wavefronts of two beams may have a maximum difference of $\lambda/4$ to generate diffraction limited fringes at the target. B: The optical system is shown in cross-section. The two beams reflect from the large mirror as collimated "pencil-like" cylinders with flat, near-planar wavefronts.

addition to these more obvious differences between the $\mathcal{F}$-BASIS and traditional imaging systems, there are subtler but important advantages and liabilities that warrant explicit exposition.

2.2.5 Low Optical Quality Tolerance

The acousto-optic pattern projector produces thin (∼5 mm diameter), pencil-like beams that are collimated when they interfere on the surface of the target. In the simplest case of two interfering beams, the portion of the projection optics that is used to probe a single Fourier component is just the two cross sections of the lens or mirror with each of two pencil beams as shown in Figure 2.3. Unlike in a traditional optical system where a large-aperture mirror would need to be a high-optical-quality surface with variations less than $\lambda/4$ (approximately 100 nm) across the entire aperture as discussed in section 1.1.1, the optical surface of a large aperture mirror used for the $\mathcal{F}$-BASIS technique only needs to meet the optical $\lambda/4$ threshhold over the width of any one pencil beam to project straight fringes. Differences in the average phase of two beams may exceed multiple wavelengths since they will wrap to a 0 - 2π range which is easily measured and corrected in the calibration of the system. This means that a large aperture mirror may have large deformations

that would make it unusable for traditional imaging, but if it varies less than a quarter wavelength over the area of one beam it is sufficient for diffraction-limited imaging in the $\mathcal{F}$-BASIS scheme.

This requirement applies only to the projection function of the optical system. We use the same optics to acquire the reflected light as we do to project the beams. In this "collection mode", we use the entire aperture of the optical system just as a traditional optical system does. However, for $\mathcal{F}$-BASIS, the optical surface for collection needs to be precise to $\lambda/4$ of the *equivalent spatial wavelength of the RF temporal signal*. The maximum temporal frequencies used are on the order of 100 MHz, and at the speed of light this corresponds to a wavelength slightly greater than 3 meters. So, the collection optics needs to have a maximum OPD across the entire aperture of 75 cm - a threshhold that would require significant imagination and dedication *not* to meet. Since large-aperture optics for traditional imaging systems are difficult and expensive to manufacture almost exclusively due to the demanding surface-quality constraints, similarly sized optics manufactured for $\mathcal{F}$-BASIS systems can be far less expensive and are far more tolerant to light-weighting design efforts.

2.2.6 Coherent and Incoherent Transfer Functions of the System

In the ray optics view, the performance of an imaging system is quantified using point-spread functions, resolution metrics and measures of aberrations such as Seidel and Zernike coefficients. The Fourier optics method of analyzing and characterizing the performance of a traditional optical system entails the use of transfer functions, which quantify the ability of the system to pass spatial frequencies. Although these functions are extraordinarily powerful and useful to those who understand them, the fact of the matter is that they're easily misinterpreted. Their enigma is compounded by the similarity of the labels and the concepts throughout standard introductions of the subject; subtleties are understandably lost. The conventional wisdom is reduced to a platitude; namely that optical systems using coherent illumination are governed by the coherent transfer function (CTF) while systems using incoherent light are analysed with the optical transfer function (OTF). In truth, the analysis of the the $\mathcal{F}$-BASIS microscope requires the use of both transfer

functions.

First, some definitions are needed. The CTF is the mathematical function describing the transformation of the amplitude and phase of the spatially coherent *electromagnetic (EM) field* of the illumination as it passes through an optical system. It is important to remember that the CTF defines what an optical system does to an EM wave and says absolutely nothing about *how that EM wave is detected.* I'll return to this point a couple of times. The CTF, represented mathematically as $H_c(f_x, f_y)$ is defined point-wise for every pair of spatial frequencies f_x, f_y and is intimately related to two other functions, the pupil function of the optical system and the coherent impulse response of the optical system.

The pupil function $P(x, y)$ is the aperture that limits the angle at which rays may enter the optical system; typically this is the entrance or exit pupil. The pupil function is most intuitively understood by re-examining the diagram showing the $\mathcal{F}$-BASIS operating principle in Panel B of Figure 2.1. The collimated beams of light are emitted from the AOD, the entrance pupil of the system (the first lens) limits the angle at which these beams deviate from the optical axis and still make it through the imaging system. Despite the fact that the pupil function obviously has some relation to the angle of the beams, it is defined only in terms of spatial coordinates. The angular dependency is mapped into the impulse response function (h) by realizing that the impulse response is the Fraunhofer diffraction pattern of the pupil function [64].

$$h(x_i, y_i) = \frac{A}{\lambda z_i} \iint_{\infty}^{\infty} P(x, y) e^{-i\frac{2\pi}{\lambda z_i}\left[(x_i - Mx_o)x + (y_i - My_o)y\right]} dxdy \tag{2.44}$$

The image magnification of the optical system relates the spatial coordinates of the image to the object according to the relation $x_i = Mx_o$, and z_i is the distance from the exit pupil to the image. The impulse response (also called the point spread function) is used in geometric optical analysis to remove aberrations and diffraction effects from images by deconvolving point-by-point the image with h as the kernel. The impulse response contains all of the information contained within the CTF and it can be shown that the CTF is the Fourier transform of the impulse response [64]. Applying a Fourier transform to Equation 2.44 and reducing terms yields the relationship between

the coherent transfer function and the pupil function.

$$H_c(f_x, f_y) = \frac{A}{\lambda z_i} P(-\lambda z_i f_x, -\lambda z_i f_y) \tag{2.45}$$

Where now, the pupil function is inverted, the optical intensity is scaled according to $A/\lambda z_i$ and the spatial coordinates of the pupil P(x,y) are replaced with spatial frequencies scaled by $-\lambda z_i$. The coherent transfer function of the optical system may be completely described by the complex pupil function.

The optical transfer function (OTF) describes the transformation of spatial frequencies of the intensity pattern at the object to the intensity pattern of the image. The intensity of the image is the convolution of the square of the point spread function with the intensity distribution of the object, so the system is linear in intensity.

$$\begin{aligned} I_{image}(x_i, y_i) &= \iint_{-\infty}^{\infty} |h(x_i - x_o, y_i - y_o)|^2 I_{object}(x_o, y_o) dx_o dy_o & (2.46) \\ &= |h(x_i, y_i)|^2 \circledast I_{object}(x_o, y_o) & (2.47) \end{aligned}$$

where $\circledast$ is the symbol for 2-D convolution and the real-valued point spread function $|h(x_i, y_i)|^2$ is the mod-squared of the complex impulse response. When this exact relationship is converted into spatial frequencies it shows that the OTF ($\mathcal{H}_i$) is the normalized auto-correlation of the CTF [64].

$$\begin{aligned} \mathcal{H}_i &= \frac{\iint_{-\infty}^{\infty} H_c(g_x + f_{cx}, g_y + f_{cy}) H^*(g_x - f_{cx}, g_y - f_{cy}) dg_x dg_y}{\iint_{\infty}^{\infty} |H(g_x, g_y)|^2 dg_x dg_y} & (2.48) \\ &= \frac{H_c \star H_c}{\iint_{-\infty}^{\infty} |H_c(g_x, g_y)|^2 dg_x dg_y} & (2.49) \end{aligned}$$

The variables of integration g_x, g_y are spatial frequencies while f_{cx}, f_{cy} are the coherent spatial frequencies in the x and y directions and the $\star$ symbolizes the 2-D autocorrelation function. The denominator term normalizes the value so that the OTF has a maximum value of unity at the DC location.

A pictorial explanation of the 1D CTF and OTF calculated for a traditional system is shown in Figure 2.4. Panel A shows the CTF in dark green of the band-limited system with cut-off frequency of f_c. Panel B demonstrates the operation of the autocorrelation whereby one copy of

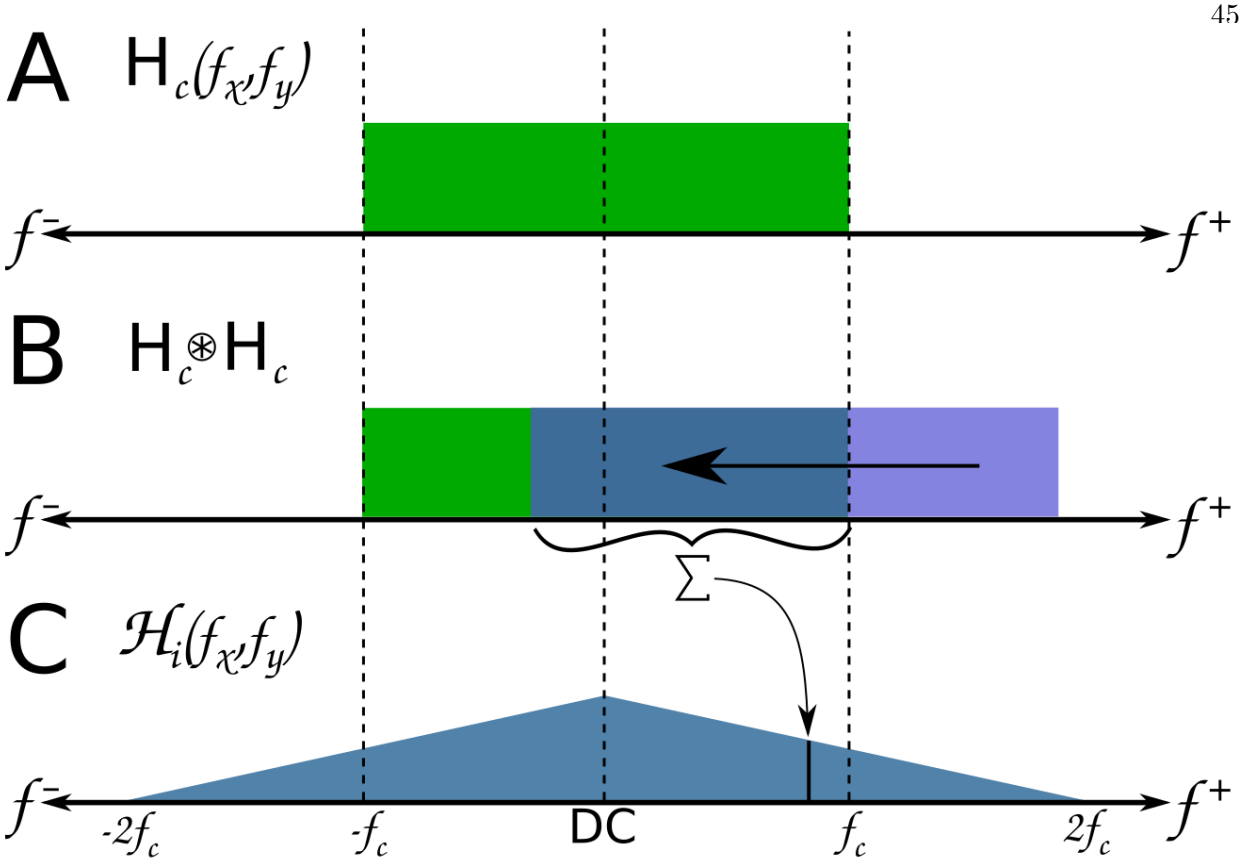

Figure 2.4: Representation of the 1D CTF and OTF for a traditional optical system. (A) The CTF (H_c) is band-limited by the pupil function to a maximum spatial frequency of f_c which in turn is limited by the exit pupil. (B) The OTF is computed by the normalized autocorrelation of the CTF. The autocorrelation is easily visualized as sliding one copy of the CTF across another and summing the area under within the intersection. (C) The 1D OTF ($\mathcal{H}_i$) shows a unity frequency transmission response at DC and a linear decrease as the frequency increases to twice the maximum frequency transmitted through the exit pupil.

the CTF is slid past another to compute the overlapping region. Panel C shows the completed OTF of the optical system with a maximum value at the DC component and a linear drop off that reaches zero at twice the coherent cutoff frequency.

The differences between the OTF and CTF can not be stated too strongly; the OTF deals with the spatial distribution of the intensity of light which can only be positive-valued while the CTF is only relevant to the electromagnetic field which contains complex values. The intensity pattern $I(x,y)$ produced from an EM field $E(x,y)$ obeys the relationship $I = |E|^2$, and the geometric identity $\cos(\theta)^2 = 1/2 + \cos(2\theta)/2$. In short, a sinusoidal spatial distribution of the electromagnetic

field with spatial frequency f_c produces an intensity pattern with spatial frequency $f_i = 2f_c$. This is an important point that textbooks often muddle by using obfuscating descriptions. They give the impression that somehow the spatial frequencies of an incoherent imaging system are magically double those of the coherent system, which is exactly analogous to measuring distances in lengths of individual shoes (incoherent) rather than *pairs* of shoes (coherent). The spatial frequencies *transmitted through* a system should just be thought of in terms of EM frequencies and can *never* be doubled, while the spatial frequencies you *measure* depend upon *the method of detection*. If your detector is capable of measuring the phase of the electromagnetic field, then you are measuring the coherent spatial frequency and to continue the analogy, you are able to determine whether it is a left shoe or right shoe. If you only detect the intensity of the light, then you lose the phase information from the EM field and you detect the incoherent spatial frequency which is just the number of shoes and you have no idea whether it is a lefty or righty. Measuring the phase of the EM field with a detection mechanism capable of determining phase loses *none* of the information from a system, it just requires twice the number of samples per spatial frequency as does the incoherent detector. You can use an incoherent detector with coherent illumination (as I do) and by so doing, you are limited to measuring incoherent spatial frequencies. Finally and most importantly, from an experimental implementation point of view, an optical intensity detector is far easier and most of the time is the only practical detector to use.

I can now address the CTF and OTF of the system described in this thesis. An $\mathcal{F}$-BASIS optical system is fundamentally both a coherent and an incoherent imaging system. It is a coherent system during the projection of laser beams and their interference at a target and an incoherent detection system when it is collecting the scattered light encoded with the Fourier components of a target, and it makes the most sense to analyze the two functions independently. Furthermore, the OTF of the remote microscope (in the detection function) is constructed very differently from traditional imaging systems.

The projection function of the system is represented by panel B of Figure 2.1. The plane of overlap on the target is the image of the AODs that will be relayed by the optical system.

The maximum angle at which the collimated beams may exit the optical system is limited by the entrance/exit pupil $P(x, y)$. As I said before, the general pupil function is complex-valued and explicitly defines any reductions in amplitude at every spatial point within the aperture of the system and any offsets in phase of the band-limited transmitted spatial frequencies. Typically, when the aberrations are small, the phase component of the pupil function is ignored and the amplitude transmittance is modeled as unity over the 2D passband and zero everywhere else, but in $\mathcal{F}$-BASIS, it is necessary to maintain accurate book-keeping of the entire complex nature of the pupil function for system calibration and image reconstruction. Since the beams interfering at the target are coherent light, the amplitude attenuation and phase offsets of the interference fringes of the *electromagnetic field* at the surface are defined by the coherent transfer function (CTF).

The phase component of the pupil function is a point-wise summation of the OPD and the relevant phase contributions due to optical aberrations. I'll be discussing the contributions due to aberrations and their consequences on the measurement of spatial frequencies and image reconstructions in following sections. The amplitude component which represents the square root of the *optical intensity* transmittance across the pupil is almostly completely unaffected by the uniform transparency of the physical optical train. Rather, it is dominated by the acousto-optic diffraction efficiency of the AODs which is a function of acoustic frequency and thereby mapped linearly to (x,y) position in the pupil for the two crossed AODs. Unlike in cases where a coherent light field fills the exit pupil and the object is illuminated from all portions of the optical system at once, the simplest case of the $\mathcal{F}$-BASIS microscope uses two beams as described in the previous section. The wavefronts of these beams are multiplied by the intersecting area of the pupil function before interfering on the surface of the target. Mapping out the phase and amplitude transformation of the pupil function is the goal of the system calibration procedure, and multiplying the measurement results by the conjugate of the pupil function removes all systematic errors in the reconstructions. Once this process is applied, the corrected coherent transfer function becomes the idealized CTF with unity within the passband and zero elsewhere.

Once the beams have interfered and have been partially reflected by the relevant Fourier

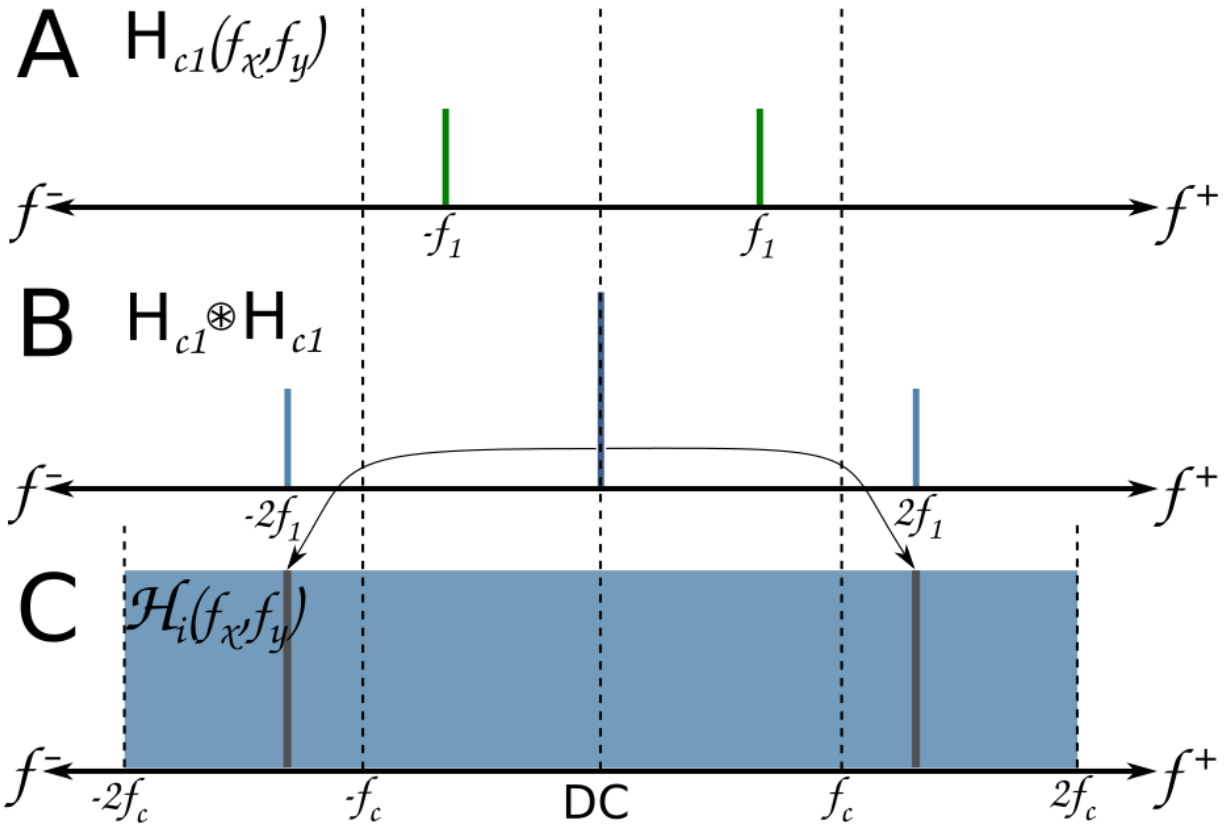

Figure 2.5: Representation of the 1D CTF and OTF for an $\mathcal{F}$-BASIS system. (A) The CTF for one pair of beams generating the frequency $f_1 < f_c$ (the coherent cutoff frequency). (B) The autocorrelation of this pair of delta functions in Fourier space generates a set of delta functions with twice the spatial frequency from the CTF at $2f_1$ and a DC component that we measure with the optical system. (C) Attributing the DC component to the appropriate location in the OTF and summing the contributions of all the DC components from every pair of sampled beams, the synthetic OTF is constructed and exhibits no attenuation of high spatial frequencies.

component of the target, the system ceases to act as a coherent imaging system. It no longer matters what the phase of the electromagnetic field is, only the phase of the intensity fringes on the target, and this backscattered intensity oscillates at the coherent temporal beat frequency Ω_g generated by the two beams. However, the construction of the $\mathcal{F}$-BASIS OTF is significantly different from traditional systems. At any moment in time, there is a single spatial frequency component being probed and is described by two delta functions at the coherent spatial frequency f_1 as shown in Figure 2.5, Panel A. The autocorrelation of these two delta functions is shown in Panel B. This operation generates two delta functions at twice the spatial frequency of the coherent

frequency, as we expect, and there is a DC value with twice the amplitude of the other components. For specular targets, this produces a beam that travels back down the center of the optical system (in the case of two beams that are centered about the optical axis). For diffuse scattering targets, a hemisphere of light is scattered in all directions containing speckle and oscillating in time at Ω_g and with modulation depth described in Equation 2.18.

At this point, the description of the transfer functions for $\mathcal{F}$-BASIS systems deviates significantly from the traditional narrative. In $\mathcal{F}$-BASIS systems, we are probing a spatial Fourier component of the target by measuring a temporal oscillation. As the interference intensity sinusoid moves across the target, the intensity of the hemisphere of reflected light will oscillate at the temporal beat frequency Ω_g with an amplitude proportional to the modulation depth of the measured spatial Fourier component of the reflectivity function. Therefore, all that is needed to measure the amplitude and phase of a probed Fourier component is to collect the oscillation of any portion of the hemisphere of light scattered from the target rather than collecting a large enough cone of light that would be needed to resolve the spatial frequency being probed as in traditional imaging. What this means is that although we need a large mirror to project collimated beams at wide angular separations in order to produce high spatial frequency interference fringes at the target, we can *measure* the strength of that Fourier component with a detector of any arbitrary angular size since measuring an arbitrarily small portion of the hemisphere of scattered light places no demands on the numerical aperture of the collection system. In traditional imaging systems, the DC component of the Fourier transform of the intensity reflectivity reponse of the target is a constant additive value that provides no information about spatial frequency to the detector. In $\mathcal{F}$-BASIS, since the instantanous phase of the spatial frequency is encoded into a temporal waveform, the temporal variation in the hemisphere of scattered light contains all the relevant *Fourier* information. To construct the synthetic OTF of the $\mathcal{F}$-BASIS system, the DC component of the autocorrelation of each pair of delta-functions (at f_1 and $-f_1$) from the CTF is attributed to the appropriate location (at $2f_1$ and $-2f_1$) in the synthetic OTF. This produces a top-hat synthetic OTF with no roll off as the frequency approaches the incoherent cutoff frequency $2f_c$ as shown in Panel C.

2.2.7 Extended DOF

The DOF of traditional optical systems is coupled to the resolution according to Equation 1.11. Taking the previously used example from section 1.1.1 of a traditional optical system capable of resolving 10 μm features at a wavelength of $\lambda = 500nm$, the DOF (in the z-direction) is 0.85 mm and the NA necessary to achieve these values is 0.025. This DOF is identical across the FOV (x, y) due to the fact that it is defined for the assemblage of all spatial frequencies being measured by the optical system. By definition, in the absence of astigmatism or field curvature, venturing beyond the DOF in z will result in an isometrically increasingly blurry image.

The DOF in $\mathcal{F}$-BASIS is not bound by the same limits as are traditional systems because the spatial information is not being measured as a summation of all spatial frequencies simultaneously at a single location (pixel) in image space. The beams of the $\mathcal{F}$-BASIS system needed to resolve 10 microns will be tilted at an angle of $\pm 1.43°$ from the optical axis. The DOF in z for any two beams is a 2D function of x and y across the intersection of the beam orthogonal to the optical axis. The overlap of two cylinders of arbitrary diameter at arbitrary angles requires a hypergeometric series or elliptical integrals to compute and renders the task of determining the xy function of the DOF of the overlapping volume painfully difficult [84]. However, if we limit the analysis to two cylinders of the same diameter (panel A of Figure 2.6) that intersect so that no ray can pass through any part of one beam without passing through that intersecting volume, then the problem reduces to a simpler geometric form. Rather than being a radially symmetric function, the overlapping volume of two cylinders is a 3D shape (panel B) that has an y-z cross section of an elongated ellipse, a x-y cross section of a mild ellipse and a x-z cross section of a parallelogram, the upper halves of which are illustrated in panel C and D. The y-z and x-z cross sections become more elongated as the angle between the intersecting cylinders approaches zero, while the x-y cross section approaches a circle. However, we can see from the plots that the axis orthogonal to the plane (Y=0) of the intersection of the beams retains a higher DOF across the aperture, while the in-plane slice (X=0) drops off linearly with radius from the center. For the system quantities described above and assuming that

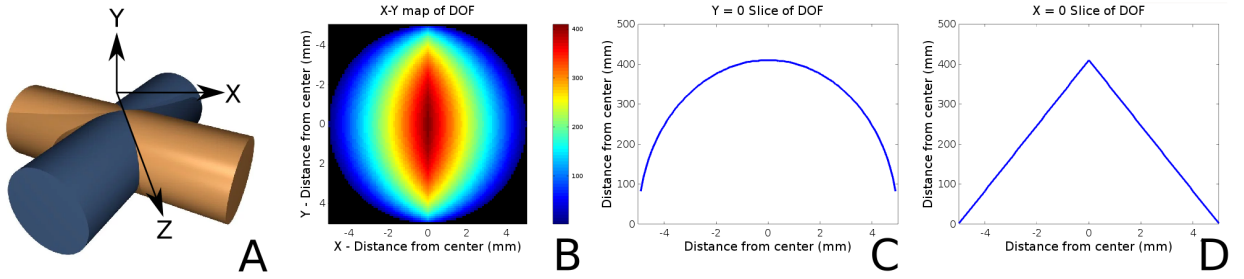

Figure 2.6: (A) Two 1-cm wide cylindrical beams cross in the X-Z plane at angle θ with respect to the z-axis. (B) The numerically-computed DOF map parallel to the average direction of the beams is nearly circular in extent but shows a bi-modal symmetry along the x and y axis. (C) A cross-section of the DOF map along the Y-Z plane shows the DOF of an elongated ellipse. (D) The X-Z slice where the DOF is a parallelogram.

the beams are 5 mm in diameter, along the optical axis the overlapping region has a maximum extent of 200 mm, a greater than 235x increase over the DOF of the traditional imaging system. By another measure, the DOF for these two beams is greater than 50 mm (58x gain) over 80 percent of the radius and 64 percent of the FOV. Finally, the average DOF across the entire FOV for these parameters is 175 mm (206x gain).

The DOF is defined independently for each pair of beams and will increase in depth at lower spatial frequencies due to smaller angles and a more elongated overlapping volume. At the small angular deflections induced by AODs, geometric inspection shows that the DOF in the center of the FOV for small angular separations θ is:

$$\Delta z_{max} = \frac{D}{tan(\theta)} \approx \frac{D}{\theta} \tag{2.50}$$

where D is the diameter of one of the identical overlapping beams and θ is the beam deflection from the optical axis in radians. This value also happens to be the semi-major axis of the ellipse defining the X-Z slice of the DOF. Every x-y location of the DOF function illustrated in Fig 2.6 may be calculated by taking the normalized DOF function and scaling it by the maximum value of the DOF computed from the beam angles.

2.2.8 Beam Wavefront Topology and Aberration Tolerance

The two beams used to probe one spatial Fourier component need to produce straight fringes at the target to within $\lambda/4$, and I showed in section 2.2 that beams with planar wavefronts generate these ideal fringes and that sufficiently collimated Gaussian beams will achieve the same result, albeit with some modulation depth variation across the FOV. The question is what happens when we have other wavefront shapes within the beams. It is a standard exercise in undergraduate and graduate optics textbooks to mathematically derive the fringes that are generated from the interference of plane waves with spherical waves and when two spherical waves interfere, primarily because these problems are tractible enough to solve analytically [11, 133, 64]. Nevertheless, a quick review of the second case is useful for illustrative purposes mainly because it is the *most likely* fringe topology produced from a mis-alignment of the $\mathcal{F}$-BASIS remote microscope optical assembly.

In spherical coordinates a wave emanating from a point source has the complex amplitude:

$$E(\vec{\rho},t) = \frac{A}{R}e^{i(kR-\omega t)} = \frac{A}{R}e^{i(k\sqrt{\rho^2+z^2}-\omega t)} \tag{2.51}$$

In this notation, the spherical wave has a radius $R = \sqrt{x^2+y^2+z^2}$ and the orthogonal distance on the observation plane $\rho = \sqrt{x^2+y^2}$. The instantaneous phase of the fringes generated by the interference of two spherical waves of the same optical frequency ($\omega_1 = \omega_2$) (shown in Figure 2.7) at a plane that is an equidistant in z from the source points ($z_1 = z_2 = 0$) is defined by the separation of the source points from the observation point according to the following equation.

$$\begin{aligned} \phi_{interfere} &= \frac{2\pi}{\lambda}\Big(\sqrt{(R-R_1)^2} - \sqrt{(R-R_2)^2}\Big) \\ &= \frac{2\pi}{\lambda}\Big(\sqrt{(x-x_1)^2+(y-y_1)^2+z^2} - \sqrt{(x-x_2)^2+(y-y_2)^2+z^2}\Big) \end{aligned} \tag{2.52}$$

This equation describes a family of 3D hyperbolae, a 2D cross section of which is plotted in the upper right of Figure 2.7. In the condition that the observation plane is very far away from the source points, expanding out the square roots as Taylor series and only taking the first two terms,

gives:

$$\begin{aligned}\phi_{interfere} &\approx \frac{2\pi}{\lambda} z\Big(1+\frac{(x-x_1)^2+(y-y_1)^2}{2}-1-\frac{(x-x_2)^2+(y-y_2)^2}{2}\Big) \\ &= \frac{2z\pi}{2\lambda}\Big(x^2-2xx_1+x_1^2-x^2+2xx_2-x_2^2+y^2-2yy_1+y_1^2-y^2+2yy_2-y_2^2\Big) \\ &= \frac{z\pi}{\lambda}\Big(2((xx_2-xx_1)+(yy_2-yy_1))+((x_1^2-x_2^2)+(y_1^2-y_2^2))\Big)\end{aligned} \tag{2.53}$$

The dependence on x^2 and y^2 cancels, and the squared terms are all constants set by the locations of the two source points. The phase of the interference pattern is expressed in terms of the lateral distance from the two source points in X-Y plane which describes the standard sinusoidal fringe pattern.

At this juncture, it helps to define some reference locations in the coordinate system to aid descriptions (upper left panel of Figure 2.7). Let's assume that the two points sources are located on two points of the X-axis and Y=0. The X-Z plane is a plane containing the point sources that is parallel to any observation plane. The observation plane is some distance away and contains the areas of observation which correspond to the FOV of the $\mathcal{F}$-BASIS imager. The bisector plane is a Y-Z plane at X=0 on either side of which the 3D fringes are symmetric. Every point on the bisector plane is equidistant from the two point sources. If the optical frequencies are identical, the illumination pattern has no temporal component and remains fixed in space. The wavefronts of the interference hyperbolae are orthogonal to the surface of a 3D ellipsoid whose two foci are the source points; it is only on this ellipsoid that the fringes are equidistant and contain no phase or frequency evolution. A flat object placed on the observation plane, or indeed any object that has a 3D surface that doesn't match the ellipsoid will have fringe curvature in at least one direction.

Within some range of distance near the bisector plane, the fringes are straight(ish) as with the planar wave interference but are diverging away from the source points so that the fringe period is shorter at one end of a FOV than the other (rectangular selections A and B in the figure). This divergence is one form of deviation from planar fringes that will degrade the $\mathcal{F}$-BASIS technique if the phase evolution across the FOV is greater than $\lambda/4$. The images in Figure 2.7 illustrate point sources that are close to the observation plane. As the point sources move farther away, the

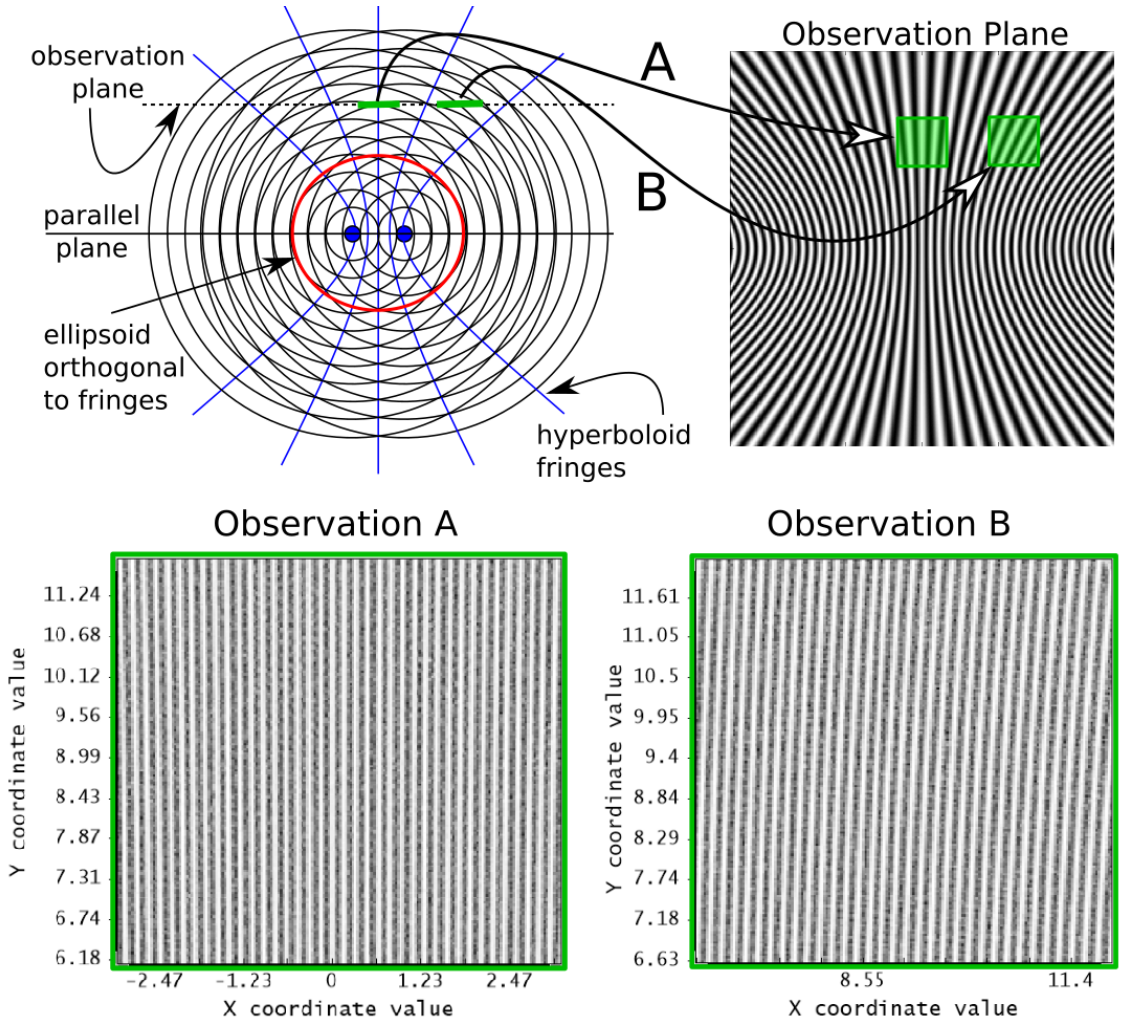

Figure 2.7: (Upper left) An X-Z planar cross section of two spherically diverging wavefronts interfering in 3D space. Two observations (A and B) surfaces are marked at the observation plane. The blue lines are cross sections of a family of hyperboloids marking the locations of fringe peaks in this plane. (Upper right) An interference simulation showing the fringe evolution over the entire observation plane and the locations of the two fields of possible observations. (Lower left) Observation area A is located equidistant from the point sources creating the spherical waves, but positioned laterally from the normal vector to the observation plane. A Zemax simulation of the fringes exhibit different spatial frequencies in X at the bottom and top of the observation area. (Lower right) Observation area B is off axis and not equidistant from the point sources. A Zemax simulation of the fringes show frequency and phase evolution both in X and Y and can be seen by counting the fringes that intersect the edges of the observation square.

evolution of the period of the fringes across the FOV will decrease. In order for diverging beams to be usable, the source points must be very far away, which if taken to the limit of infinity brings them back to planar waves. Near the parallel plane, the fringes curve and distort so that both

the relative phase and period changes across the FOV. This fringe distortion is also reduced as the point sources recede from the observation plane. Simply stated, the $\mathcal{F}$-BASIS technique can only accommodate very large spherical radii R as measured in distance away from the target.

The fringe distortion within the FOV causes only a portion of the beam to match the spatial frequency that is desired to be measured. Figure 2.8 shows the results of two different fringe curvatures of the illumination field on the temporal signal detected. The spatial frequency of the object that we wish to measure is shown in panel A. Panel B shows the fringe curvature with the upper row containing fringes with $\lambda/4$ maximum curvature across the FOV and the lower row with 1.5λ. In the upper row, the illumination and the object spatial frequency match to within a quarter fringe period over the entire FOV, while the overlap in the lower row is designated by the yellow box in Panel D. The temporal signal for the fringes with more curvature shows a lower maximum and a lower modulation depth. Modulation depth does not drop to zero however; a portion of the illumination field will match the targeted spatial frequency over a decreasing fraction of the area out to many waves of curvature as shown in panel E. However, this is only one part of the reduction in efficacy with fringe curvature. The FOV will contain a range of spatial frequencies distributed in the f_x, f_y Fourier plane (Panel C). As a result only the portion of the beam that contains an illumination field that varies from the expected planar fringes by less than $\lambda/4$ will beneficially contribute to the temporal signal at the detector. The remainder of the FOV will probe a range of frequencies that can constructively or destructively interfere with the temporal signal at the same temporal frequency and cannot be disambiguated with Fourier decomposition.

Although spherical waves are one of the most common forms of wavefront error due to optical misalignment in the remote microscope (e.g. misfocus), the wavefront errors that are generated from the off-axis aberrations coma, distortion and field curvature can now be included in the remainder of this analysis. If the beams are symmetric about the optical axis, each beam will contain equal but opposite aberration contributions which will cancel out at the target and still produce straight fringes in some portion of the FOV just as in the case of the spherical waves (albeit with lower modulation depth in the temporal waveform). The spatial distribution of the

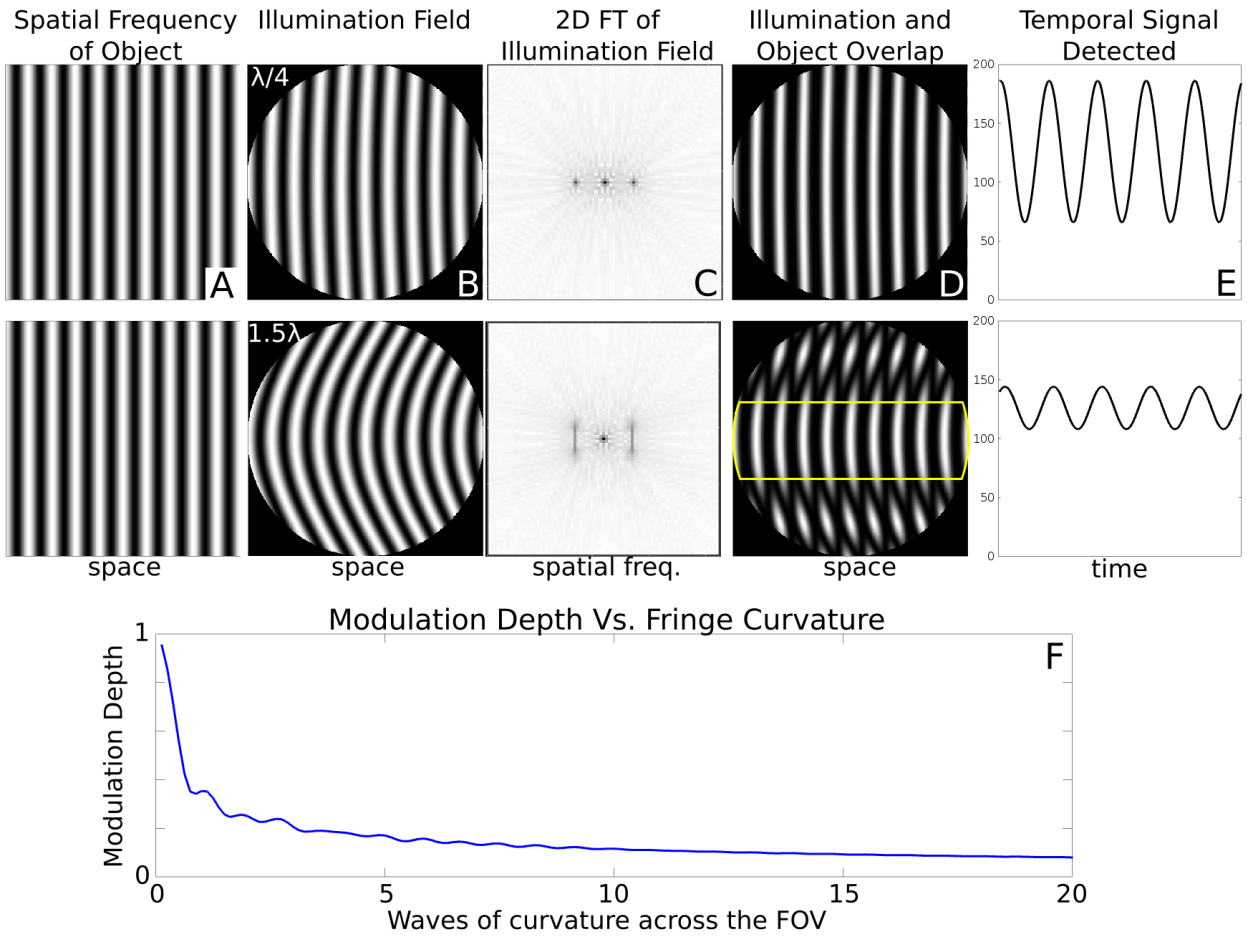

Figure 2.8: The effects of fringe curvature ($\lambda/4$ on top and 1.5λ on bottom) on the temporal signal detected. (A) The spatial frequency of the object to be measured. (B) The illumination field used to probe the spatial frequency with the indicated fringe curvature. (C) The 2D Fourier transform of the illumination field. (D) The overlap of the illumination field with the object. (E) The detected temporal waveform showing a decrease in maximum amplitude and modulation depth with an increase in fringe curvature. The yellow box shows the portion of the FOV where the illumination field matches the spatial frequency to $\lambda/4$. (F) The modulation depth of the temporal signal as a function of the waves of curvature of the fringes across the FOV.

fringe degradation due to aberrations is a complex function of the position of the beam through the optical system. A quantification of all of these sources of fringe degradation is most simply expressed in the instrument response function and compensated during system calibration. It is important to note that these aberrations would degrade the resolution of an image produced by a traditional imager along with the degradation due to axial aberrations such as defocus and spherical and chromatic aberration which do not affect this technique. Defocus is a mismatch of phases across

spatial components resulting in a blur; since we are gathering spatial frequencies one at a time, defocus can only occur by ignorantly or purposefully attributing incorrect phases during image reconstruction. Spherical aberration will only result in an axial shift of the working distance with spatial frequency; however, since the DOF is so large, it would be difficult or impossible to generate sufficient spherical aberration to matter. Finally, this system is immune to chromatic aberration due to its use of monochromatic illumination.

2.2.9 Active Illumination and Large Light Bucket

Traditional imagers use ambient lighting or lamps to illuminate the FOV. Generally speaking, those lamps are spatially incoherent broadband sources and are incapable of concentrating all of their light only onto the subject of investigation. As the distance R to the target increases, the intensity of the reflected light falls off as R^2. The lasers used to probe the target in $\mathcal{F}$-BASIS are also the only needed (and desired) illumination to construct an image. Furthermore, since the laser beams are collimated, the intensity in the FOV remains constant irrespective of distance and *only* the FOV is illuminated.

2.2.10 The Bandwidth Products and Temporal Limitations

The limit of the information content in an image taken with a traditional imaging system is defined by the space-bandwidth product of the system [64]. Clearly, all images are finite in spatial dimensions and are therefore space-limited, i.e. they have a finite length L in cartesian coordinates (x, y) such that $(\frac{-L_x}{2} \leq x \leq \frac{+L_x}{2}, \frac{-L_y}{2} \leq y \leq \frac{+L_y}{2})$. The Fourier transform tells us that functions that are perfectly space-limited can not be bandwidth-limited, however, it says nothing of the *relevancy* of the frequency values needed to construct the space-limited function. The Abbe theory of image formation tells us that an image contains only a finite amount of spatial frequency content of the scene and is limited by the entrance aperture of the optical system. In truth, the high spatial frequencies beyond some finite threshold $(\frac{-f_{Xmax}}{2} \leq f_x \leq \frac{+f_{Xmax}}{2}, \frac{-f_{Ymax}}{2} \leq f_y \leq \frac{+f_{Ymax}}{2})$ that are needed to spatially limit the rectangular function $g(x, y)$ that perfectly defines an image of finite

extent says nothing of the *content* of the image, but rather just the *shape* of the image boundary. The total relevant information content of the image is the product of the spatial dimensions and the bandwidth dimensions called the space-bandwidth product (SB = $f_{Xmax} f_{Ymax} L_x L_y$).

There are two temporal limitations that govern the measurement scheme of an $\mathcal{F}$-BASIS system; the first relates to Nyquist sampling of a temporal frequency and the second stems from the transit time for an acoustic wave to traverse the active aperture of the acousto-optic device. Devices that multiplex the measurement of frequencies in the time domain rather than the space domain, such as the AODs used in the $\mathcal{F}$-BASIS technique, have an information limitation analogous to the space-bandwidth product called the time-bandwidth product (TB). A sound wave propagating across the active aperture of the AOD takes approximately 20 μs to cross the crystal. The AODs used in this work support a bandwidth of 40 MHz producing a 1D TB of 800. In practical terms, this means that the AOD can support 800 Rayleigh-resolved temporal frequencies across the acousto-optic bandwidth, where the spacing is 40 MHz/800 = 50 kHz. The Nyquist limit defines the minimum required temporal sampling to resolve these frequencies as twice the temporal frequency to be measured. So, to utilize the maximum supported bandwidth of the AOD and resolve 800 temporal frequencies, we need to collect at least 20 μs of data at 50 kHz sampling. If we assume that the horizontal and vertical AODs are identical and that the limiting aperture of the optical system can support the transmission of all available spatial frequencies produced by the AODs, this constitutes $800 \times 800 = 160{,}000$ unique spatial frequencies at 20 μs each for a total of 3.2 seconds of data if the samples are collected sequentially.

The second limitation on sample acquisition time of the $\mathcal{F}$-BASIS system results from the previously mentioned 20 μs transit time for a sound wave to cross the aperture of the AOD, called the acousto-optic access time (t_{AO}). As the boundary of one temporal frequency to another is passing the aperture of the AOD, a spatial portion of the laser beam passing through the device will be diffracted at a different angle than the remainder of the beam. In addition to this, the boundary between temporal frequencies is not a hard cutoff, but rather consists of a spread of frequencies unrelated to the those targeted for sampling. In sequential sampling, as is being used

in this work, it is required to wait for the boundary between one temporal frequency and another to pass beyond the aperture. This presents one of great drawbacks of sequential sampling in $\mathcal{F}$-BASIS implementation. Adding both of these temporal requirements onto the measurement time, each of the 160,000 Fourier components capable of being sampled by the optical system require a minimum of 40 μs to acquire, bringing the minimum time for the acquisition of a complete data set to 6.4 seconds. There are measurement schemes that overcome this lower limit by eliminating the losses from the access time and by acquiring many spatial frequency samples at once, although they come at significant operational costs [55, 56].

2.2.11 Compressive Sensing

The space-bandwidth product assumes that all information within an image is equally useful. This is demonstrably not true in the vast majority of cases. The only image which requires the entire space-bandwidth product to be accurately represented is a point-by-point random image such as Gaussian noise. Images of real objects have been shown to be sparse, that is, they can be faithfully represented by only a small subset of the spatial frequencies supported by the pixels of the image. Familiar image compression algorithms, both lossy and lossless, use this property of real images to reduce the sizes of data files in post-processing. Compressive-sensing is the term used for measurement techniques that attempt to exploit the sparsity of the information content in a multi-dimensional measurement to collect a number of samples that is smaller than is demanded by the Nyquist limit. Since the $\mathcal{F}$-BASIS technique does not passively collect spatial information but instead requires consciously choosing which spatial frequencies to probe, the number of Fourier components and their distribution in Fourier space is left to the user. Each component is fully represented by a single complex number which quantifies the amplitude and phase of the sinusoid, and the order in which these values are collected is arbitrary. This opens the opportunity to utilize compressive sensing algorithms, or even to operationally limit the resolution of images generated or change the frequency sampling of the image just by selecting a subset of the frequencies probed. The consequence is that a user may implement a purposeful and controlled reduction in data

content and volume, which has significant utility from a interplanetary data bandwidth transfer perspective.

2.2.12 Monochromatic

This technique uses a continuous-wave (CW) monochromatic laser to illuminate the surface and it collects the scattered light on a single pixel detector, as a result gray-scale images are produced. A seemingly natural extension of the technique would be to use multiple wavelengths or a broadband source to generate color images, but implementation of this is more difficult than is immediately obvious and requires signficant consideration for the optical design of the relay and projection optics.

2.2.13 Turbulence and Compensation

There are differences between this technique and traditional imaging systems that don't strictly qualify as either a benefit or a drawback but still have consequences on operations. For example, $\mathcal{F}$-BASIS uses an interferometric process to generate the fringes at the target, which like any interferometer is far more sensitive to instantaneous (rather than time-averaged) atmospheric turbulence than traditional imagers, particularly at high spatial frequencies. Luckily, the effects of turbulence are minimized by the fact that any single Fourier sample only needs on the order of 100 μs to be collected, which is generally much shorter than the time constants of eddies in the atmosphere. Furthermore, the phase errors due to the change in index of refraction of a parcel of air in the path of the lasers will be larger for higher spatial frequencies. A model of atmospheric turbulence and a technique for compensation with regards to the remote microscope is described in detail in Chapter 7.

Chapter 3

Opto-mechanical Design

3.1 Mechanical Design Introduction

Reconstruction of 2D images with microscopic resolution using the $\mathcal{F}$-BASIS technique had already been demonstrated in the laboratory with components mounted on floating optical tables before this project to construct a remote microscope for operation on a Mars rover had been initiated. The largest working distance that was previously achieved with the DEEP-dome system, which had a reflective projection optical assembly containing a 165 mm diamond-turned monolithic ellipsoidal aluminum mirror with a working distance of 213 mm shown in panel D of Figure 1.9. The mirror was manufactured without consideration of mass constraints, and as a result the optical surface was supported by a thick substrate to avoid any optical form errors due to surface deformation resulting from mounting stresses, thermal expansions during diamond turning or gravitational loads. All $\mathcal{F}$-BASIS implementations pursuing fluorescence images used a standard laboratory microscope with the requisite working distances and opto-mechanical structure.

The explicit goal of the research in this thesis was to produce images with microscopic resolution at 5 meters, both in the laboratory and in a proposed field demonstration campaign with the entirety of the instrumental hardware mounted to the mast of the Jet Propulsion Laboratory (JPL) Athena research rover. This research was funded by a NASA Planetary Instrument Definition and Development Program (PIDDP) grant, the purpose of which is to raise the technological readiness level (TRL) of candidate instrument technologies so that those instruments can subsequently be proposed for use on NASA planetary exploration missions. The TRL scale is a value

ranging from 1 to 9 wherein a TRL of 1 designates a technology that has been theorized to work but has not been experimentally demonstrated (known colloquially in the aerospace community as "vaporware"), and a TRL of 9 which denotes an instrument that has already been used in space for scientific investigations and is said to have "space-flight heritage". At the beginning of my PhD, the $\mathcal{F}$-BASIS remote microscope stood at a high TRL 2: the basic principles of the component technologies have been shown to work in laboratory experiments or with simulations. The $\mathcal{F}$-BASIS technique was well-established, but no hardware usable for planetary exploration had been constructed. The design and manufacture of the opto-mechanical hardware necessary to achieve the imaging goal was a significant portion of the effort of my PhD. Concisely stated, I needed to produce an opto-mechanical assembly that met the two competing mechanical design requirements:

(1) Retain rigidity for optical figure and system alignment stability

(2) Have a form-factor and a sufficiently low mass to be plausibly used as an instrument mounted to an analog planetary exploration lander in field testsm for use in planetary exploration applications.

The first physical property which has a quantifiable effect on the performance of the remote microscope and needed to be investigated before manufacturing is the coefficient of thermal expansion (CTE). The CTE defines the fractional expansion or contraction of a material with a change in temperature. The CTE of aluminum is a strong function of temperature, however unlike some other metals that have directionally-dependent coefficients, expansion of aluminum is isometric [77]. The entire projection optical assembly of the remote microscope is made out of 6061 alumimum and there are two consequences of changes in temperature of the assembly that were evaluated. The first was the change in the optical form of individual reflective components as a function of temperature with respect to the maximum possible temperature change and gradient across the surface that would yield acceptible optical performance. The second consequence of the CTE was the change in the inter-component distances and alignment with bulk temperature change of the entire assembly [127].

The second physical deformation of the optical components I evaluated was the deformation due to gravity. The property that quantifies the relationship between stress (force/area) and strain (deformation) of a material is Young's modulus. In the case of mirrors, the greater Young's modulus is the less the optical form will change due to gravitational stress. Again, there wasn't any real choice for the selection of any other material besides aluminum for the prototype mirror, but beryllium and magnesium have been used in space applications and a proposed mission to other planets could afford to use other materials. I evaluated aluminum and beryllium deformations in the finite element analysis in Section 3.4.2. The inter-component spacings due to gravitional stress both on Earth and Mars and thermal changes are investigated in Section 3.5.1.

3.2 Mirror lightweighting

The term "lightweighting" refers to minimizing the mass of the substrate body of a mirror without detrimentally affecting its optical performance or structural integrity. In fact, appropriate lightweighting has been shown to be beneficial to optical performance since it removes mass that doesn't add structural rigidity but does add to gravitational stress and deformation [138]. There have been many publications that discuss "optimal" lightweight designs under specific ideal circumstances such as large-aperture temperature-controlled low-induced-stress concave astronomical mirrors [140], midsize-aperture portable concave astronomical mirrors [30], space-based mirrors that operate in zero-gravity [98], and flat turning mirrors for spaceflight applications [44], but each of these implementations utilize their own set of assumptions for mirror support, orientation and operation and aren't easily transferable to other applications. For example, the large astronomical mirrors are assumed to be supported by a large metal substructure used to point the telescope inside an observatory. As a result, the mirror need only keep sufficient rigidity under the conditions of evenly distributed support by the rigid metal substructure.

There is a wide selection of techniques to manufacture lightweight mirrors, however the basic concept is universal; a mesh of ridges of substrate material supports a thin solid shell containing the optical surface, but there have been many variations pursued. Some of the more popular

geometries are the square mesh, regular triangular mesh, irregular triangular mesh, pie-slice ribs and hexagonal mesh. There is also variation in the construction techniques where the support patterns are machined out of the substrate, constructed of epoxy-bonded struts and fused cells and others [95]. All of these techniques in the published literature are intended to achieve the expectation of $\lambda/4$ (or less) deviation over the entire optical surface. There is practically no comprehensive discussion of lightweight designs that have softer performance goals in the optical regime - only curtailed admissions of techniques that failed to produce usable mirrors with satisfactory optical performance. As the intended operational spectral range of the optical assembly shifts into longer wavelengths, the optical tolerances measured in distances (mm, μm, etc.) become less stringent even while the optical forms relative to the wavelength remain comparable, i.e. $\lambda/4$ for 10 μm wavelength thermal infrared light demands an accuracy of only 2.5 μm.

3.2.1 Remote microscope lightweight mirror design

One of the major differences between the remote microscope mirror and the majority of the lightweighted mirrors used in astronomical applications was the fact that the remote microscope mirror is intended to be used at a range of orientations from -20 degrees to +60 degrees where 0 degrees denotes a horizontal direction. Most of the reported lightweight designs assumed that the weight of the mirror would be on top of the support structure even if at some high orientation angle. In the remote microscope case, the lightweight design needs to support the mirror from three mounting bolts in any spatial orientation. In addition to this, like all of the published techniques for manufacturing lightweight optical surfaces, the lightweighting process of removing material needed to be completed before the optical surface was cut. As a result, the lightweight design had the requirement of retaining rigidity during the diamond lathing process. Unfortunately, neither Nipro Optics, who manufactured the mirror, nor I were certain of how much material could be removed without risking failure during the lathing of the surface, and so we committed to an iterative and collaborative approach to the design.

A cross-section and back view of the final design of the primary mirror showing relevant

dimensions is shown in Figure 3.1. The lightweight design that I chose for the remote microscope primary mirror used pie-slice ribs and concentric support rings. A primary reason for this was to reduce machining costs. Several of my initial design concepts containing many thin ribs with deep cuts increased manufacturing time significantly. The tradeoff put an upper limit on the number and depth of the support ribs. The optical surface of the mirror is 250 mm in diameter and the entirety of the optical surface is supported by a constant substrate thickness of 3 mm. Initial simulations showed that an unsupported mirror that is 3 mm thick would suffer too much deformation under gravitational stress and so I iterated on a light-weight design containing support ribs and rings. The internal ring is approximately 6 mm in height and 7.5 mm in width in order to support the mirror around the central 23 mm hole and contains 24 4-40 tapped holes onto which Thorlabs cage system rods could be threaded. The principle support ring at 60% of the mirror radius was machined with a radial thickness of 9 mm and a height of approximately 2 cm to accommodate 24 equidistant tapped 1/4-20 mounting holes three of which would be used to mount the mirror to the support assembly. A set of 6 rotationally symmetric ribs approximately 6 mm in height were left between the inner and outer ring to provide support for the shell. Twelve more ribs were left outside of the principle support ring for the remainder of the shell radius. On the circumference of the optical surface, a 1 cm wide, 5 mm thick flat ring with a 3 mm wide 7 mm tall lip was left to support the outer optical surface. The circumferential ring contains another set of 24 equidistant 1/4-20 tapped holes for the mounting of a proposed but never realized dust-shield in front of the mirror. The finite element analysis of the deformation due to gravity of the final design is shown in Section 3.4.2.

3.3 Primary Mirror Manufacturing

A significant part of this effort was spent developing a manufacturing technique for the lightweighted primary aluminum mirror since the manufacturer had never fabricated one before that met the unorthodox optical requirements of the remote microscope. The ellipsoidal primary mirror and paraboloidal secondary mirror were both manufactured by Nipro Optics. Three attempts were

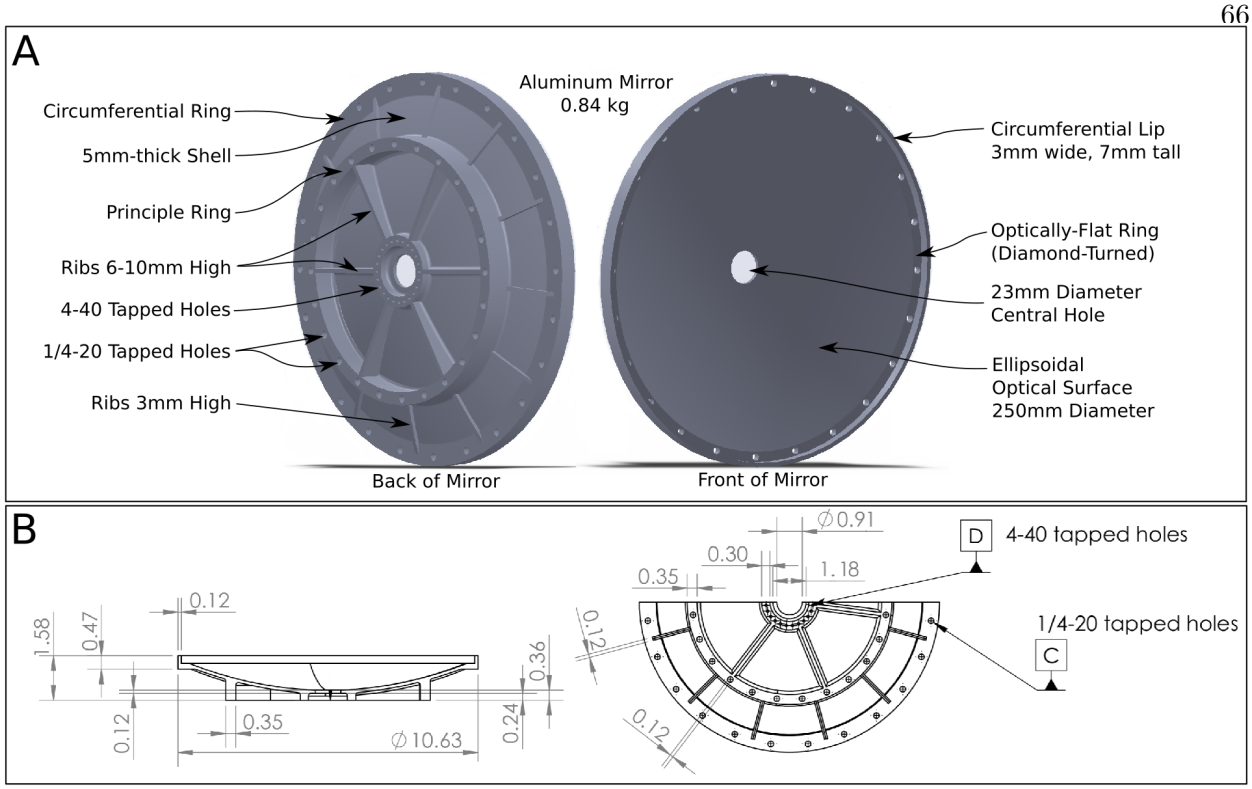

Figure 3.1: Design of the primary mirror of the remote microscope. A. The light-weighted back and front sides of the mirror are shown. The total weight of the ideal mirror design was 0.84 kg although the manufactured mirror came in somewhat higher that this at 1.03 kg (within our specified manufacturing tolerances). B. The dimensional drawing of the cross section of the primary mirror showing the relevant dimensions for manufacture.

made to manufacture the mirror due to failures of the process to produce a surface of sufficient quality. The first step of the manufacture of the primary mirror involved machining the light-weighted structure into the back of the mirror. Starting with a 6.3 cm thick, 30 cm diameter cylindrical billet of extruded 6061 aluminum, a standard end-mill was used to remove material leaving the ribs and rings needed to support the optical surface. The 1/4-20 tapped mounting holes in the principle ring and the circumferential lip, and 4-40 tapped holes in the inner ring were machined prior to working on the other side. Once the structure in the back of the mirror was complete, the majority of the material inside the cavity of the optical surface was removed using a standard machining lathe. What would become the optical surface was left to a thickness of slightly less than 4 mm to accommodate machining error and loss of material due to cutting the optical

surface. Without light-weighting, once the concavity of the primary mirror is roughed out, it can be moved from the standard lathe to the diamond lathe for high-precision optical surface cutting.

Diamond lathes have been in use since the 1960s to produce reflective surfaces for optical components. There are two types of diamond lathes which either hold the component steady and assign all movements to the diamond tool allowing freeform surfaces, or the diamond tool is moved along cartesian coordinates while the object rotates about its axis to produce rotationally symmetric surfaces. Fundamentally, the difference between these models is just which company receives the payment; manufacturers of machines with both modalities claim the same precision in output. For the manufacture of the remote microscope primary mirror, Nipro optics used a diamond lathe that holds the object steady against a fixture plate. As with many optical mounting problems, there is a tradeoff between holding the material steady enough to ensure a precise optical surface cut without slippage, and inducing stresses in the material with the mounting bolts. The fixture plates used by Nipro Optics contain optically flat surfaces on plates sufficiently thick to eliminate stress deformation, however the back of the remote microscope mirror was machined to a tolerance of 1/2 mil $\approx 13\mu m$. In addition to this, the end mill is only able to ensure flatness with respect to the table of the end mill when the part is secured to it. Once the part leaves the end mill, any residual stresses induced or released by the machining process will warp the nominally flat machined surface. As a result, the assumption that the machined surface is approximately optically flat with a roughness spatial distribution that averages to zero is a poor one. Nipro used three equally-spaced stainless steel 1/4-20 bolts to affix the back of the mirror using the principle ring to the fixture plate. The diamond lathe cut the ellipsoidal reflective surface from the roughed out concave surface of the mirror blank. The pressure of the diamond tool causes a small amount of elastic deformation of the surface, which can be ignored when the surface is supported by a thick substrate, but will result in optical surface form errors if the elastic deformation varies across the surface without compensating with cutting pressure. In general, this compensation is a complex process which is only practical in cases of smooth and simple material thickness variation which was not the case in the primary mirror of the remote microscope. To alleviate the pressure deformation, Nipro proposed a minimum

shell thickness of 3 mm and they reduced their cutting speed to the minimum sufficient to cut the aluminum thereby minimizing point pressure on the shell. In addition to the ellipsoidal surface, Nipro used the diamond tool to cut an optically flat surface into the portion of the circumferential lip whose surface normal vector is parallel with the optical axis. Although this wasn't called out for in the specifications of the mirror design, it turned out that including this feature provided a serendipitous simplification of the surface testing and system alignment procedure which I describe in Chapter 4.

When the first mirror was delivered, my initial surface form tests using a Fizeau interferometric tester showed severe and asymmetric warping of the optical surface far beyond the threshold of the interferometric tester to measure. Working stresses build up in aluminum (and other ductile metals) during machining which can partially relax in hours to weeks under ambient conditions [73]. After a few tests by Nipro demonstrating that the stresses weren't significantly induced during the diamond turning process, we decided to add a heat-treating step to relieve bulk stresses remaining from the machining process. Heat-treating is a generic term to describe a repetitive process of heating and cooling a metal to accelerate the spontaneous relaxation of material stresses or reset the hardness of the metal to pre-worked conditions. This term is sometimes sloppily referred to as "annealing", but in actuality annealing is one type of heat-treatment and is not strictly synonymous. Heat treatment of softer metals such as aluminum, copper, berylium, silver, etc. do not need to approach their melting points to relieve stress, as is required in the process of annealing which also resets the ductility of hardened metals such as most ferrous alloys [94]. Another consequence of annealing is to increase the rate of oxidation and the resultant oxidation layer, which in the case of aluminum would generate a thicker shell of the much harder aluminum oxide which must be cut through to produce the optical surface and which can induce unwanted pitting and scratches during diamond turning. Whereas in ambient conditions this layer is less than 0.5 nm thick, it can double when annealing at 500 ^{o}C in an oxygen environment, and can cause pitting at temperatures above 1000 ^{o}C when exposed to limitless oxygen [168].

Starting from scratch, Nipro roughed out a billet identically to the first mirror then sent

Step Number	Action	Duration
1.	Start at ambient 70^o F	
2.	Cool to -70^o F	over 90 min
3.	Hold at -70^o F	for 60 min
4.	Heat to 70^o F	over 60 min
5.	Hold at 70^o F	for 30 min
6.	Heat to 350^o F	over 90 min
7.	Hold at 350^o F	for 60 min
8.	Cool to 70^o F	in 60 min
9.	Hold at 70^o F	for 30 min
10.	Repeat 1-9	2 more times

Table 3.1: Heat treatment procedure followed to relieve work-induced stresses in the third aluminum mirror blank used to fabricate the final remote microscope mirror. American manufacturing specifications use the Imperial system.

the roughed mirror blank to me. Using a research-grade Tenny Junior temperature test chamber at the Southwest Research Institute, I processed the mirror blank according to a heat treatment procedure similar to one prescribed by Nipro Optics and utilized commercially shown in Table 3.1 with a nitrogen purge attached to the oven during thermal cycling. After heat-treatment, the mirror blank was returned to Nipro Optics for diamond turning. The resultant mirror showed no surface deformation during interferometric testing and exhibited no evidence of relaxation in subsequent tests or use during experimentation.

3.4 Finite Element Analysis of Remote Microscope

3.4.1 Finite Element Analysis

In the design phase of constructing the remote microscope, I used the finite element analysis (FEA) functionality of the CAD software SolidWorks to simulate the response of each of the candidate architectures of the primary mirror to load stresses and quantified the deformations due to gravity and thermal expansion from a uniform rise in bulk temperature. In finite element analysis, the response of an object is modeled as a collection of numerous contiguous and inter-connected elements. Although there are many implementations and algorithms, the general concept is that when a force is applied to the object each element is apportioned an amount scaled to the volume

or mass of the element. The equations are solved to determine the total force on each element in bulk and then the semi-continuous response of the entire object is constructed by applying the boundary conditions between all adjacent elements [45]. In simple models such as deformation of I-beams to gravity, FEA is robust and requires very little attention from the user to accurately model realistic physics and the choice of number of elements is somewhat arbitrary. However, the more complex a system becomes, the easier it is for the user to request models of physically impossible circumstances. As the number of elements is increased, the FEA model can show significantly different results and in most cases, without a sufficiently large number of elements the model will fail to converge to any meaningful result at all. Generally, the rule of thumb is that you increase the number of elements until the results of the model cease to change between simulations. Another soft failure mode of FEA is inaccurate coupling between components of complex systems. In the case of the remote microscope primary mirror, the FEA analysis runs could be significantly different depending upon how I modeled the coupling of the primary mirror to the support structure. The stresses induced by the three bolts used to affix the primary mirror are not easily modeled and the simplistic demand that surfaces on the coupling boundaries are best modeled as immovable and unwarpable is clearly a sophomoric expectation. That being said, gross failures of the model are clear when a simulation generates a nonsensical response. In my application of FEA, I wasn't trying to simulate a physical response that matched reality to a high precision, I was looking for order-of-magnitude deformation responses of optical components.

3.4.2 Primary Mirror Finite Element Analysis Results

The primary drivers of static deformation of the primary mirror are mounting stresses and gravitational deformation. The operational expectation for the remote microscope is that it will be able to be directed at a target using the altitude-azimuth mount on the top of a rover mast. Clearly, the gravitational stresses are altitude-angle dependent, but mounting strain is due completely to mutual stresses imposed by physically coupling components regardless of environment or orientation. It is nearly impossible to accurately model the deformation induced solely by the

coupling bolts since the localized stress on the mirror is highly dependent upon any variations of the surfaces from the idealized model. The machined surfaces that are assumed to be perfectly flat will have changed shape to a small degree and the real induced strain will be a function of the bolt battling this bulk deformation. In Chapter 4, I describe the measurement of the optical surface with an interferometric tester the use of which allowed me to see surface deformation in real time while adjusting the mounting bolts. I found that even mounting the mirror with nylon bolts to less than finger-tight was sufficient to begin to measurably deform the mirror surface. There's not much that can be done other than make a note that the mounting stress is a significant source of surface error and address it in future iterations of the system design. For the following FEA models, I chose to assume that the manufacturing process of the flat surface of the principle ring was perfect and that the mounting bolts are tightened below the threshold of mirror deformation.

The first model is shown in panel A of Figure 3.2 with a front, back and side view. The primary mirror is mounted with three bolts spaced at 120 degree increments with the orientation that the triangle of the bolts has the apex pointed down to provide as much support for the upper portion of the mirror as possible. The mirror is held vertically and subjected to Earth gravity. The principle ring at 60% of the radius is allowed to deform with the rest of the mirror rather than assume it is bound to a rigid surface. The maximum deformation of any part of the simulated mirror is 71.3 nm from the set zero locations of the mounting bolts. The maximum deformation of the reflective surface is a little more than 50 nm with a maximum deformation over 1 cm^2 anywhere on the optical surface of 7 nm. There is a clear trefoil deformation of the surface as expected, but it is far below the required tolerance threshold.

The second model (panel B) demonstrated the effect of changing the placement of the mounting bolts, where the bolts are no longer equidistant and the upper two bolts are moved two holes closer together and located further up the principle ring. The gravitation stress and orientation is identical to the first model. The total deformation of the mirror was reduced to 60.8 nm and across the optical surface deformation was reduced to a maximum of 32 nm. A portion of the mirror below the central hole and above the lower bolt showed slightly greater deformation than in the

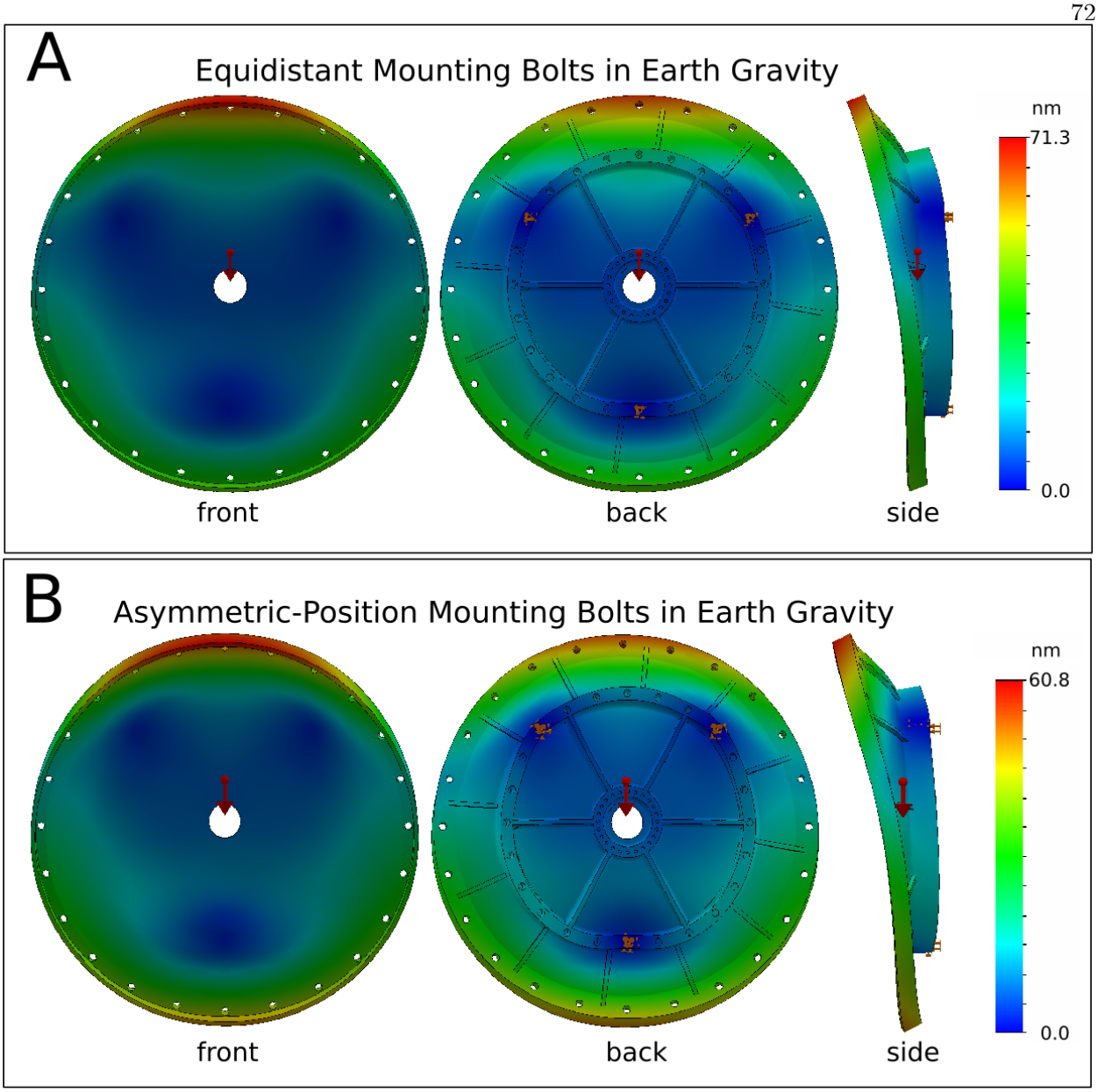

Figure 3.2: Finite element analysis models of deformation of the primary mirror due to gravitational stress. A. Aluminum primary mirror supported by three equidistant mounting bolts shown as orange location markers and deformed by Earth's gravity (the red arrow shows the direction of the gravitational force in the model). The worst deformation occurs in the circumferential ring at the top of the mirror. A trefoil aberration is clearly present from the material strain away from the mounting bolts. B. The same primary mirror supported by three mounting bolts with a reduced physical separation, partially compensating for grativational deformation.

equally spaced bolt pattern. In addition, the support for the sides of the mirror was reduced by placing the upper bolts closer together, but maximum increase in deformation was less than 3 nm.

This model resulted in the best preformance of any bolt pattern containing 3 bolts and was chosen as the actual mounting orientation for the experimental mirror.

3.4.3 Modeled performance of primary mirror to change in gravity

The remote microscope was designed for a nominal operation on the surface of Mars mounted to the mast of a Mars rover. Recently, I've been looking at the possibility of sending this instrument on the possible Europa lander. The lower gravity on Mars in comparison to Earth (and even more so on Europa) will obviously reduce the deformation of the primary mirror and allow a greater degree of lightweighting. To provide an indication of the amount of material that can be removed from a mirror fabricated out of aluminum and still retain optical function for planets with lower gravity, I ran the gravitational sag model using the value for Mars ($g_{MARS} = 3.7 m/s^2$). The results of this model are shown in Figure 3.3. The total deformation was reduced to 27 nm over the entire surface and 16 nm over the optical surface a reduction of 50 percent with respect to Earth. Although operation on the surface of another planet allows the mirror to be lightweighted significantly, the forces experienced during launch and landing are many times that of gravity on Earth and the mirror needs to survive these events as well.

With a total mass of 0.84 kg, the aluminum primary mirror contains a large portion of the mass of the 1.25 kg of the optical assembly. A common solution in space-flight applications is to substitute the aluminum with beryllium. Despite being toxic and having poor reflective qualities, beryllium can act as a substrate that is coated with more reflective materials such as nickel or aluminum. An aluminum coated beryllium mirror under Earth's gravity is shown in panel A of Figure 3.4. The total mass drops to 0.57 kg and the gravitation sag is less than 6 nm across the optical surface. Without changing the design of the lightweighting process, a beryllium mirror on the surface of Mars will sag less than 3.5 nm. My initial attempts at reducing mass for a Mars rover using beryllium indicated a viable mirror mass closer to 0.4 kg, but further work needs to be done.

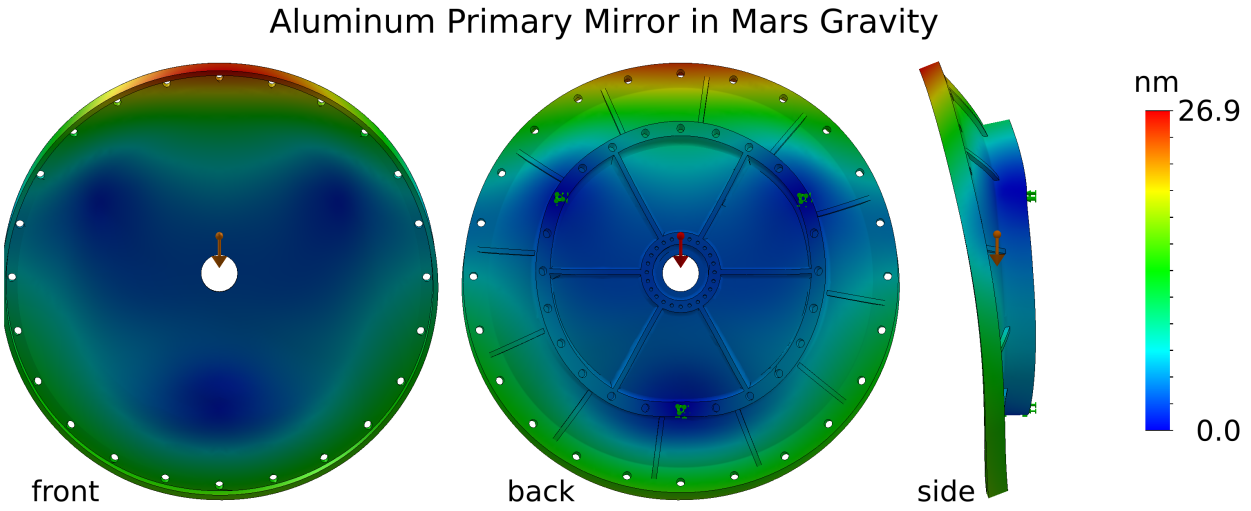

Figure 3.3: Finite-element analysis of the aluminum primary mirror deformation due to Mars gravity - direction represented by the red arrows. The surface deformation is less than half of the deformation on Earth. The green markers on the back show the locations of the bolts used to support the mirror.

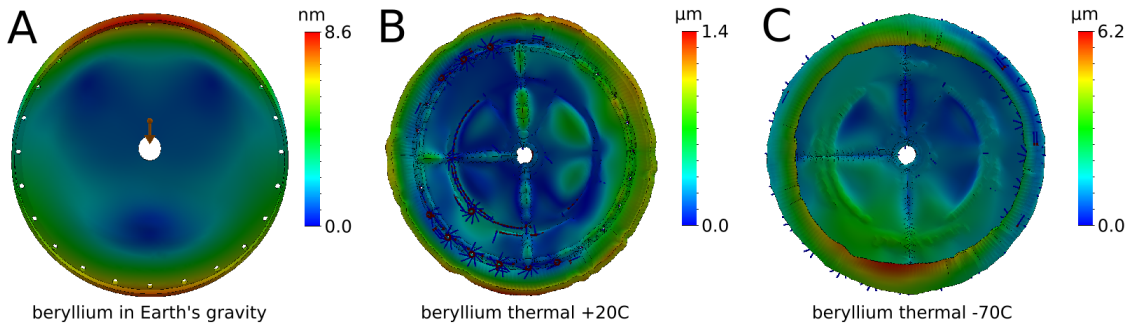

Figure 3.4: The FEA model of the primary mirror made out of beryllium supported in Earth gravity with three ideally placed bolts. A. The front of the mirror shows total optical surface deformation of less than 6 nm. B. The deformation of a beryllium mirror due to an increase in temperature of 20 ^{o}C over ambient (20 ^{o}C). The surface violates the optical constraints over approximately 10% of the mirror surface. Although the total surface deformation is less than 1 μm sharp deformation boundaries can be seen. C. The beryllium mirror in a -70 ^{o}C environment from ambient. Total deformation is 4x the warm scenario, but optical requirements are only violated over an additional 5% of the optical surface.

3.4.4 Modeled performance of primary mirror to change in temperature

The dominant transient deformation of the optical surfaces during operation is material expansion due to temperature changes which will induce gross expansion and deformation gradients

across the optical surface. I felt the only reasonable model to run was a change in ambient temperature with no directional thermal loading either from convection or radiation. It is safe to expect that thermal gradients due to heat vented from the lander can be mitigated during operation on the surface of a planet. The radiative loading from sunlight can be an issue, but it is highly dependent upon the radiative, conductive and convective properties of the atmosphere of the planet in question. In short, any induced temperature gradients are more an operational consideration than a system design failure.

On the surface of Mars, the thermal extremes extend from -150 ^{o}C to 20 ^{o}C and total diurnal cycling of 100 ^{o}C. In the laboratory, the assumption of an isothermal environment holds as long as the air conditioning and cooling fans of electronics aren't directed at the mirror, but the temperature of the entire laboratory can change by many degrees over the course of hours or days. The shape change of the mirror at two temperatures is shown in the following models. Figure 3.5 shows the total surface shape change for a temperature of +20 ^{o}C from ambient (20 ^{o}C) on the top row (A) and -70 ^{o}C from ambient on the bottom row (B). The figure illustrates the absolute value of deformation from the ideal for every point. Total surface deformation of the aluminum mirror is a disastrously large 3.8 μm and 13.2 μm respectively. Even in the +20 ^{o}C environment the localized warping of the surface is so severe that it violates the surface form requirement of $\lambda/4$ over 1 cm over 30% of the mirror. There is buckling along the parallel and perendicular directions to the gravitational vector regardless of the location of ribs, although the rings do seems to act as a boundary for surface buckling. In general, the shape evolution shows a radial expansion of the mirror in the +20 ^{o}C regime so that the conic constant of the mirror will become more positive (or alternatively the radius of curvature increases), and vice versa for the -70 ^{o}C regime. Because the CTE of aluminum is so large in this temperature range, the shape of the aluminum mirror only keeps the optical operational requirements over a $\pm$12 ^{o}C isothermal temperature range.

I ran the same thermal deformation model on the beryllium mirror and the results are shown in panel B and C of Figure 3.4. The pattern of deformation is unsurprisingly similar in morphology, but the amplitude is approximately half of the aluminum deformation. Unlike the aluminum mirror

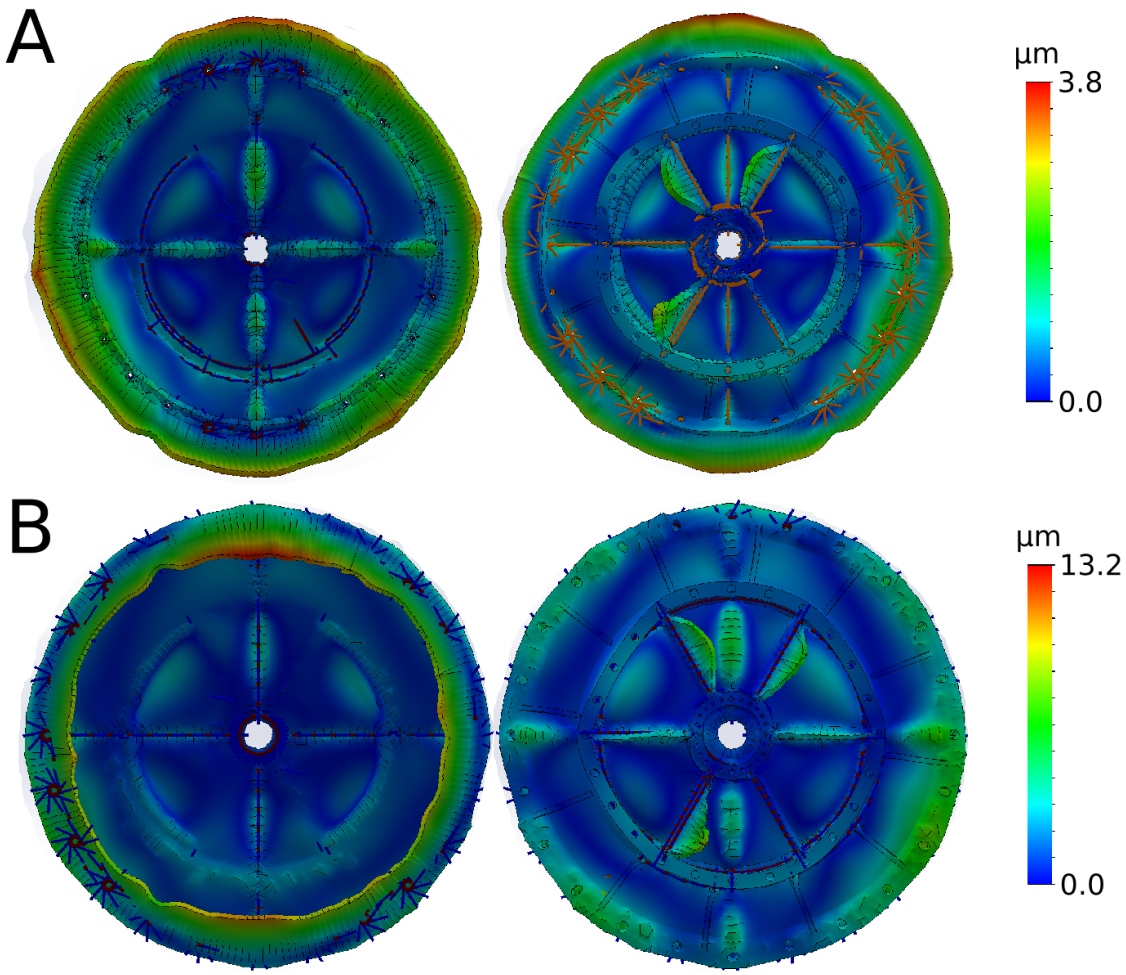

Figure 3.5: A. The FEA model showing front and back surface deformation of an aluminum primary mirror at +20 ^{o}C above the reference temperature. Surface warping is dominated by horizontal and vertical buckling patterns and a general expansion of the surface. B. The same mirror in an environment -70 ^{o}C above ambient. Total deformation is more than 4 times worse than the warm case.

which has severe surface gradients which violate the optical quality constraints, the beryllium is far better behaved and only fails to meet the surface requirements over 10% and 15% of the surface respectively.

3.5 Spider Assembly

As described at the beginning of this chapter, the entire proposed instrumental package that sits on top of the rover mast is best thought of in three component blocks; the acousto-optic pattern

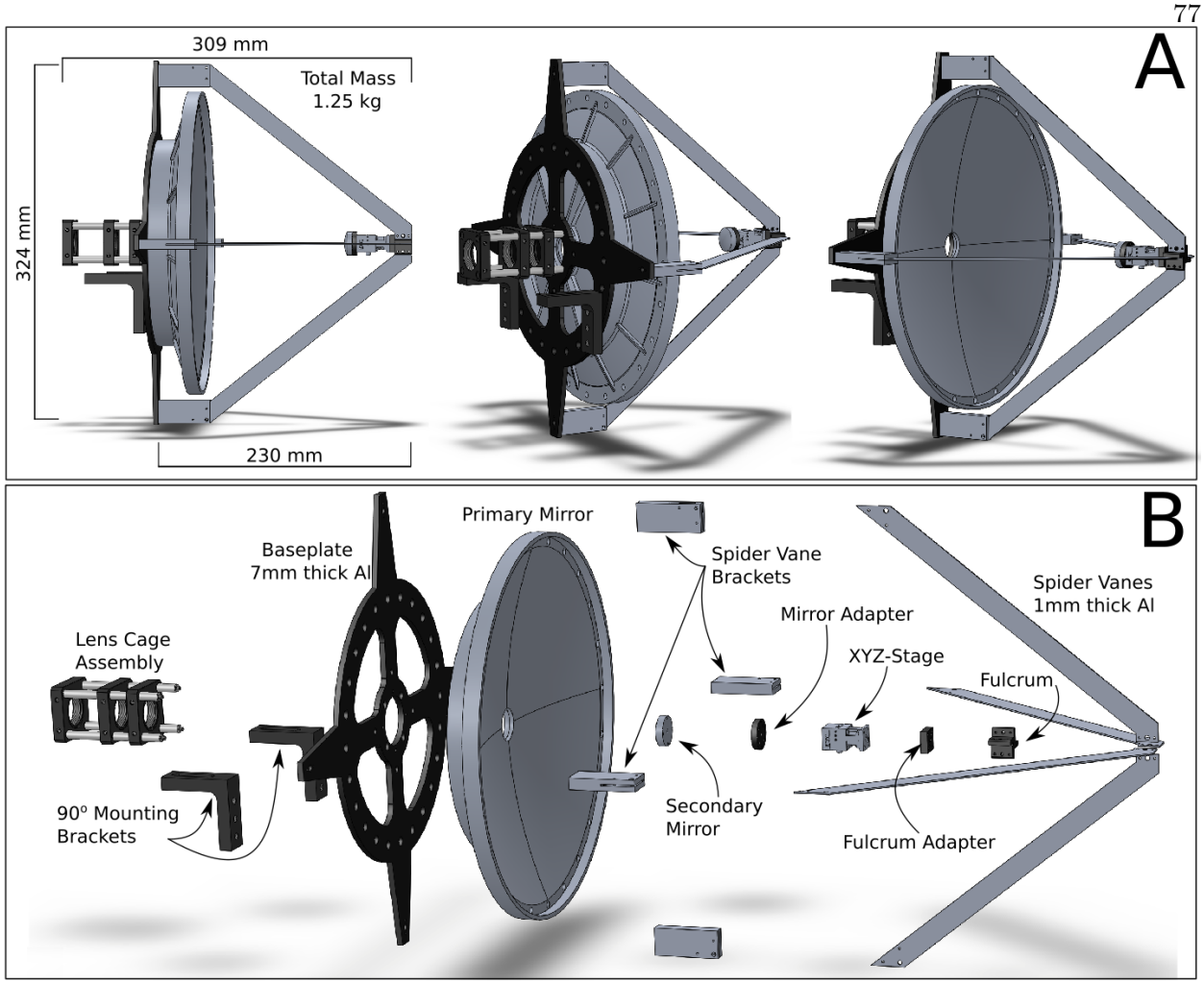

Figure 3.6: A. The optical assembly of the remote microscope shown in three different orientations. The total mass of the entire assembly is 1.25 kg. B. An exploded view of the opto-mechanical assembly. The lens cage assembly was constructed of off-the-shelf components from Thorlabs, the 90^o brackets and miniature XYZ-stage are also commercial products. I designed and fabricated all other components for this thesis.

generator, the relay optics and the RM optical assembly. The pattern generator and the relay optics with the detector are all rigidly mounted to a nominally-inflexible mast platform. The entire mass of the RM optical assembly, shown in panel A of Figure 3.6 was designed to hang off the edge of the mast platform supported only by the two L-brackets mounted to the baseplate just below the optical path. The assembly consists of eleven unique components and has a mass of approximately 1.25 kg, the majority of which is the primary mirror at 0.84 kg.

The baseplate is 7mm thick extruded sheet aluminum and provides the structural rigidity necessary to mount both the primary mirror and the remainder of the spider while retaining optical alignment stability. Three sets of tapped and through-holes provide the coupling of the cage system for the 3-lens set, the primary mirror and spider vanes holding the secondary mirror. The backplate was lightweighted through an iterative design using FEA models and resembles a large throwing star. The cage system for the lens set contains rods with 4-40 threaded studs that screw directly into the baseplate. The mass of the cage system, however is supported directly on the mast-plate with the remainder of the relay optics and so does not need to be considered in deformation studies. The baseplate has 24 matching through holes to the tapped 1/4-20 holes in the principle ring of the primary mirror to allow for any arrangement of mirror mounting. Extending out from these holes at every 90 degrees, the baseplate has four entensions that contain the mounting bolt holes and precision alignment dowel pin hole for the spider vane brackets.

Each spider vane bracket is a two-part rectangular assembly that rigidly couples one spider vane to the baseplate. The spider vane is sandwiched between the two portions of the bracket which are bolted together during assembly. All three components of the sandwich contain one bolt through-hole and two alignment dowel pin holes. There is no adjustability of the assembly. Each spider vane was cut out of 1 mm thick aluminum sheet with a water jet. All four spider vanes are coupled together on the optical axis at the fulcrum.

The fulcrum is an extended '+' shaped piece to which all spider vanes are affixed and which supports the remainder of the secondary mirror positioning mechanism. Just as with the spider vane brackets, the fulcrum has one tapped bolt hole and two precision fit dowel pin holes for each spider vane. Looking back on this design, I'm surprised it worked since there was very little room for error in the manufacture of these components and still allow them to fit together. Up to this point, there is no adjustability, or even flexibility of any of the bolted components. The baseplate, spider vane brackets, spider vanes and fulcrum are merged as a solid piece once they are assembled.

The main components supported by the fulcrum of the spider are the miniature XYZ stage and the secondary mirror. The 15 x 15 x 30 mm Optosigma dovetail XYZ stage can be positioned

± 2 mm in each direction using a 2.5 mm hex-head screw. The XYZ stage has threaded mounting holes on either side, but these holes were inconvenient for mounting directly to the fulcrum and secondary mirror and so adapter components were necessary. The fulcrum adapter and mirror adapter are just 5 mm thick aluminum blocks that contain hole patterns compatible with the two adjacent pieces they are joining. Finally, the secondary mirror has a single 4-40 tapped hole and 4 precision dowel pin holes to couple it to the mirror adapter.

3.5.1 Spider Assembly Finite Element Analysis Results

As with the primary mirror, I used finite element analysis to evaluate the deformation of the opto-mechanical assembly due to gravity and thermal changes shown in Figure 3.7 panel A and B respectively. Although I ran gravitational sag models at a range of angular orientations, the greatest deformation occurred at a horizontal orientation as expected. The deformation is most pronounced in the spider vanes and shows the secondary mirror drooping down approximately 15 microns with negligible rotation about the optical axis. This exceeds the thesholds defined in section **??**, but only in the case where the microscope is used over a wide altitude range without re-calibration. The alignment requirements 6 and 7 relate to a position offset of the secondary mirror from the location used during calibration. A more likely source of deformation that would violate these alignment requirements is the transient motion due to vibration. Regardless, this model shows that the current microscope opto-mechanical design cannot be used looking directly up and then directly horizontal without performing another calibration. In Mars gravity, this maximum offset of the secondary mirror is reduced to 7 microns from center, which means that this opto-mechanical assembly could be used on Mars at any orientation without recalibration to compensate for gravitational deformation.

The thermal analysis shown in panel B is the same +20 and -70 ^{o}C isothermal offsets applied to primary mirror in the section 3.4.4. Due to the isometric expansion of aluminum, the spatial distribution of the deformation caused by the two thermal extremes appears identical between the models but the absolute magnitude is scaled and shown on either side of the color bar. Significant

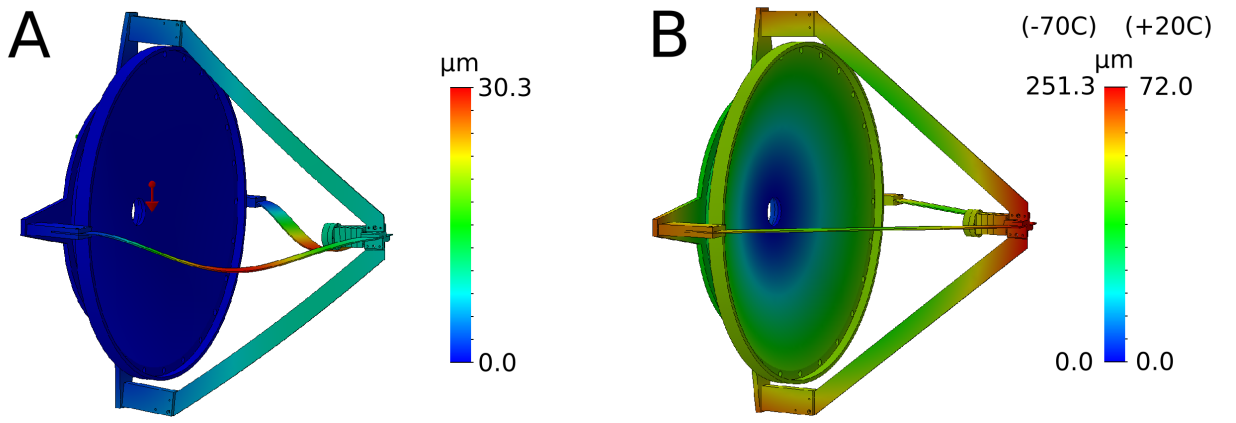

Figure 3.7: A. The entire opto-mechanical assembly and the deformation due to Earth's gravity. The secondary mirror is offset downward from the optical axis 15 microns, well within the required tolerance and correctable with the XYZ stage. B. Expansion and contraction of the assembly due to temperature changes of -70 and +20 ^{o}C result in the secondary mirror moving along the optical axis by -200 μm and 60 μm respectively.

deformation of the primary mirror is still evident, but the overall scale of deformation is dominated by the extreme points of the opto-mechanical assembly. This model was run without gravity being taken into account, and as a result the 60 μm and 200 μm respective offsets of the secondary mirror with respect to the center of the primary mirror occurs solely along the optical axis. Both of these values exceed the optical requirement alignment thresholds, but again, this is only relevant if there is a large enough temperature change after calibration. The position of the secondary mirror can be compensated by the motion of the XYZ stage, but this doesn't alleviate the deformation of the primary mirror surface from the ideal as described in the previous section.

The final FEA model run attempted to ascertain any failure modes of the opto-mechanical assembly due to roto-vibrational modes. The FEA software module is rather rudimentary and doesn't provide the ability to assign specific modes and driving strengths, but instead simply evaluates the modes of the five highest magnitudes. In the case of the remote microscope, these modes corresponded to twisting and train on the spider vanes shown in Figure 3.8. Mode A corresponds to a rotation about the optical axis. Mode B applies a vibration along a 45 degree angle from the optical axis as judged by an observer looking down the optical axis toward the surface

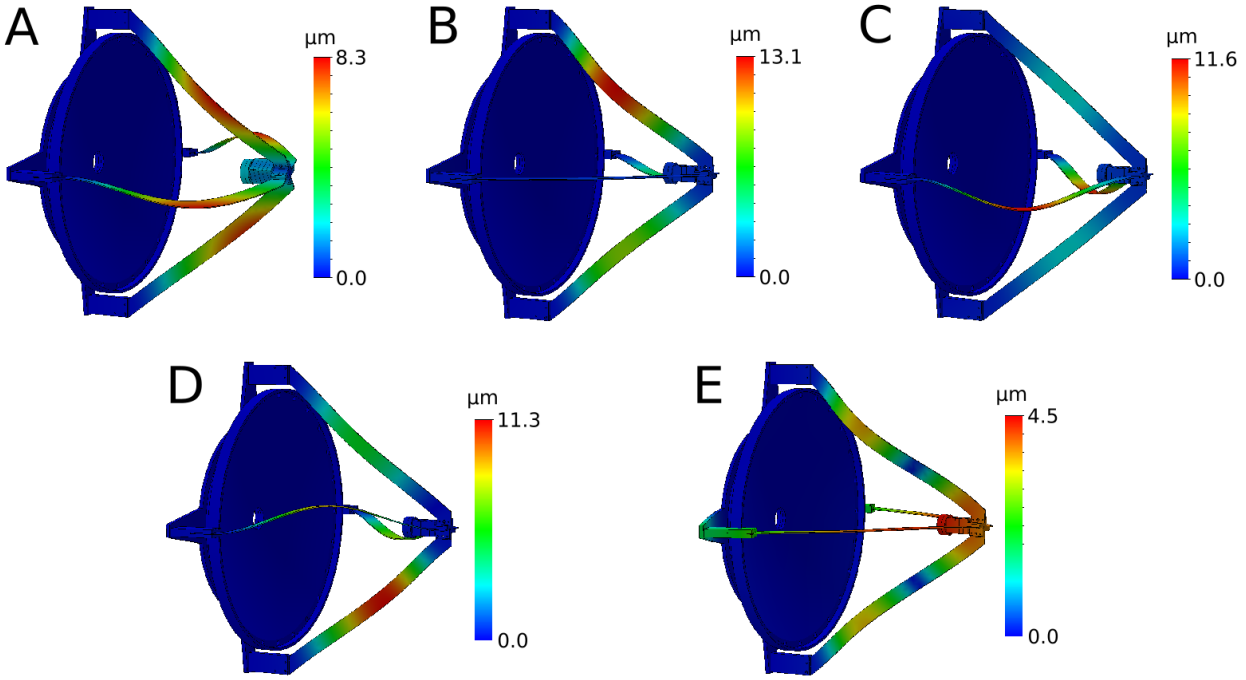

Figure 3.8: The normalized magnitude of the 5 highest vibrational modes of the opto-mechanical assembly (A. - half-sinusoid twist, B. - half-sinusoid horizontal vibration, C. - half-sinusoid vertical vibration, D. - half-sinusoid corner-to-corner vibration, E. - full sinusoid horizontal vibration). All models are dominated by the potentially damaging roto-vibrational modes in the spider vanes.

of the mirror. Mode C showed the greatest amplitude of vane deformation with vibration in vertical direction. Mode D evaluated another angle (unreported) where the spider vanes were significantly deformed. Finally, mode E showed compression and expansion due to vibrations along the optical axis. All of these modes showed that the vast majority of the possible deformation occurred in the vanes, although model A did demonstrate that the secondary mirror can move significantly with a rotation of the spider vanes along the optical axis, and model E similarly showed net motion of the secondary. These models are indicative but not quantitatively useful since they don't couple the induced amplitudes experienced during shake and bake to the modeled deformation. However, these do provide guidance as to what primary structural weaknesses should be investigated before finalizing a spaceflight design.

3.6 Final Opto-Mechanical Evaluation

The finite element analyses of both the primary mirror design and the spider assembly show that this system is sufficiently engineered to reliably function in gravity regimes of any possible rocky body of interest in the solar system. A proposed benefit of this system is that it can use a low-optical quality light-weight mirror cheaply manufactured with a diamond-lathe. Although the aluminum-construction remote microscope can be used in the laboratory and can be optimized to function over a ± 12 ^{o}C temperature range from ambient, it is fatally flawed when considering planets with large temperature swings such as Mars or Earth's moon. The CTE of aluminum simply changes the optical form of the mirror too much to reliably calibrate and use. Beryllium offers a similarly low-cost option for a wider range, but still fails to guarantee function over hundreds of degrees. In addition to this, I've performed no analysis concerning spatially-dependent thermal loads, either radiative or conductive. Sunlight illuminating only a portion of the assembly is almost guaranteed to alter surface forms. One of the solutions for this is to use a more traditional lightweighted material but which still can be allowed to have a low optical quality surface form, although, why would you demand to have a low optical quality if you didn't benefit from it? A good example of this is an ultra-low expansion ceramic or glass substrate. These materials are still able to be diamond turned, but have acceptible coefficients of thermal expansion over the entire range of expected operating environments on other planets. The gravity and thermal finite element analysis shows that the remainder of the opto-mechanical design is sufficient for planetary exploration. The thermal expansion of the assembly that causes the secondary mirror to migrate away (or closer to) the primary mirror is well within the range of the XYZ stage. Finally, the vibration analysis showed that the spider vanes are the most vulnerable portion of the opto-mechanical structure during launch and landing.

Chapter 4

Remote Microscope Optical Design

4.1 Optical Performance Requirements

There are two functions of the remote microscope optical assembly; 1. projection of the structured illumination from the acousto-optic pattern generator onto the target at 5 meters, and 2. collection of the scattered light for delivery to the high-speed bucket detector. These two functions need to be satisfied by a single optical train with the exception of a beamsplitter that directs the return light to the detector rather than returning to the laser source. In the most general (and slightly sloppy) terms, the optical system produces an "image" of near-unity magnification of the superimposed active apertures of the acousto-optic deflectors at the surface of the target. In reality, this is a poor description because we aren't really concerned with an image being formed but rather that collimated beams reach the target. The importance of this difference will be made clear in the following discussion.

The projection system can be described either as a low NA microscope with a very large objective or as a very high NA telescope. There are many finite-conjugate systems produced commercially in the form of microscope objectives and the closely-related near-field camera lenses that are designed to reduce aberrations over some portion of the field of view. These designs almost invariably use refractive optical elements and are consequently disqualified for adaptation to the remote microscope. The nominal functional design of the remote microscope optical assembly consists of relaying the collimated beams from the acousto-optic pattern generator onto the target with an on-axis, two-reflector telescope system that retains beam collimation. The spatial size of

the smallest feature in the image is 10 microns which, along with the pre-supposed working distance of 5 meters, sets the numerical aperture of the optical system to NA = 0.025 via Equation 1.5. This in turn sets the diameter of the primary mirror to 25 cm. One of the most substantial tasks of this PhD was to design and construct the optical assembly that met the performance requirements for both the projection and collection functionalities.

The remote microscope sequentially samples the Fourier components of a target, and in order to meaningfully reconstruct an image requires knowing the relationship of the phase of a spatial frequency sample to all adjacent samples. The representation of the phase of highly spatially complex targets can evolve quickly across the 2D Fourier representation, and good reconstructions require knowing these phases very accurately. As a consequence, it is highly preferable, although not strictly required, to align the optical system to avoid inducing any non-linear 2D phase evolution across the pupil. This means that the optical design should heavily weight the minimization of OPD across the pupil function.

In order to use Fourier synthesis to faithfully reconstruct images of the target, the aberrations induced by the optical assembly should ideally be limited so that any warping of the projected fringes is less than $d/4$ on the target surface, where d is the spatial period of the fringe. In Chapter 2, I claimed that a Fourier component of the target can still be measured even when the illumination fringe curvature exceeds this limit as long as such fringe curvature is known for each pair of interfering beams, but warping of the fringes is only one consequence of optical aberrations. I'll be exploring the effects of aberrations in detail in the following sections. Another expression of this requirement is that the beams interfering at the surface of the target need to be collimated in order to avoid curvature of the fringes due to converging or diverging wavefronts. This is a requirement that is not generally assumed in most imaging systems; there is very little meaning to demanding beam collimation in applications using incoherent illumination, and even in coherent imaging, this is often not required. It is not strictly needed here either; if both beams have identical divergence or even spatially-conjugate wavefront distortion, then those terms cancels in the interferometric product. In practice, however is it nearly impossible to guarantee identical wavefront error, and it

is far better to aim for an ideal collimated beam.

Although it may seem too obvious to state, a somewhat softer design goal is that the magnification of the imaging system should be as constant across the aperture as possible. Variable magnification can be somewhat tolerated with the remote microscope, but only if the variation in the magnification is well behaved and symmetric about the optical axis. Pincushion distortion (which translates to a change in beam magnification with pupil radius) will result in a collimated beam with a greater diameter than at some other radius. However, since the spatial period of the fringes is determined by the angle of the interfering beams, the Fourier component is unchanged but the FOV is larger. So, a change in magnification will pollute the measurement of the Fourier component of the nominal FOV with the surrounding area illuminated by the larger beam. In general, it is far more operationally convenient and it permits a greater flexibility in sampling schemes if the optical system generates a constant magnification, although small deviations might be compensated during image reconstruction.

4.2 Remote Microscope Optical Projection Assembly

The coherent light pattern generator of $\mathcal{F}$-BASIS (panel A of Figure 4.1) employs a crossed pair of slow-shear-mode TeO_2 acousto-optic deflectors (AOD) to diffract the resulting Doppler-shifted laser beams up to a couple of degrees [56]. To first order, all beams exiting the pattern projector are collimated and have identical beam widths and intensity profiles. They share a common overlap plane at the exit port of the projector which coincides with an "image plane" of the active apertures of the AODs. These beams are then injected into a passive optical projection assembly which directs them onto the surface of a target without inducing fringe-corrupting optical aberrations. This passive optical system increases the lateral separation of the beams as would be achieved by allowing the diverging beams to propagate through free space. Collimation is restored for each individual beam as are the inter-beam angular relations, and with a projection-angle-invariant compression factor of the beam width. To probe the Fourier representation of a target at a finite distance requires an infinite-conjugate optical system to map collimated beams from a finite

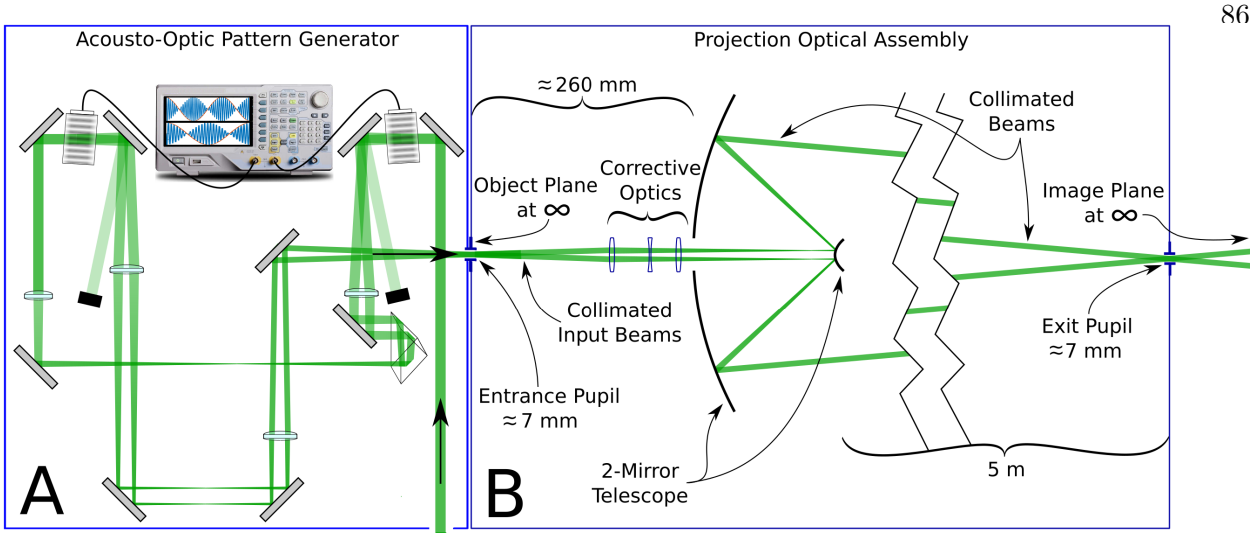

Figure 4.1: A. The acousto-optic pattern generator contains two crossed AODs used to produce Doppler-shifted, spatially-diffracted collimated laser beam pairs. The diffracted laser beams all overlap at a single plane at the exit of the pattern generator which is the mutual image plane of the active apertures of both AODs. B. The exit port of the pattern generator is co-incident with the 7 mm diameter entrance pupil of the projection optical assembly. A 2-mirror telescope and corrective optics expands the lateral separations between beams, recollimates and overlaps the beams at the 5 mm diameter exit pupil of the projection assembly at a distance of 5 meters.

distance entrance pupil to a finite-distance exit pupil. Since the beams enter and exit the projection assembly collimated, as is the case with astronomical telescopes (if the eyepiece is included), it is an afocal imaging system. However, the 1:1 mapping from entrance to exit pupil demands that the optical train also performs as a finite-conjugate imaging system but without design optimization to minimize aberrations. The "object plane" of this finite-conjugate system is the afore-mentioned "image plane" at the output of the pattern generator.

The presented design of the remote microscope projection optical assembly (shown in panel B of Figure 4.1) is most accurately and intuitively described as a fast, two-mirror infinite-conjugate telescope with a small central obscuration and aberration corrective optics. The small entrance and exit pupils of the system are nominally located approximately 5.4 meters apart. The projection assembly has optical performance requirements which are not satisfied by traditional infinite-conjugate telescopes nor any finite conjugate 4-f imaging systems found during an exhaustive literature search. It has the unorthodox characteristic that the two planes that dictate the perfor-

mance requirements of the system are located at neither image nor Fourier planes but rather at the entrance and exit pupils. It is this condition that renders most conventional telescope designs unsuitable for adaptation to the remote microscope. There exist patents for catadioptric (containing reflective and refractive optical compoenents) projection systems that demand collimated input and output beams, but the designs are highly complex with dozens of components and optimized as sub-assemblies of larger devices, making them impractical to adapt to this effort (e.g. [72]).

4.2.1 The Unsuitability of Conventional Telescopes

Although a great number of elegant, aberration-minimized infinite-conjugate catoptric (reflective optical elements only) telescope designs have been developed over the last four centuries, the vast majority of the optimization effort was spent minimizing spherical aberration and coma (to generate aplanatic systems) or to produce anastigmat telescopes (which eliminates astigmatism). Techniques for general analysis and design of aplanatic two-mirror telescope designs were still being published well into the 20th century [74], while the drive to eliminate astigmatism inspired catoptric designs with three and more mirrors [136, 125]. Although aberration-free performance is philosophically preferable for any implementation, the astronomical two-mirror telescopes were optimized for two goals which render them ill-suited for adaptation to $\mathcal{F}$-BASIS remote microscopy. The first design goal is that astronomical telescopes should maximize the light-collection area for all source directions within the field of view. To achieve this, it is preferred to position the entrance pupil both near to and with the same diameter as the primary objective, as in the cases of Gregorian or Newtonian designs, or at a corrective lens in front of the primary mirror for Cassegrain geometries. Reducing the entrance pupil diameter is antithetical to the goal of astronomical light collection, but also the entrance pupil location is one of the design free variables, and moving it alters the third-order aberrations of the system. The second design goal also relates to the minimization of aberrations and has two detrimental consequences for $\mathcal{F}$-BASIS remote microscopy. One of the most effective techniques to reduce the off-axis aberrations of coma and distortion in the image is to reduce the angular field of view (FOV) [97]. As a result, FOV values for astronomical telescopes

are typically significantly less than a degree. The beams exiting the acousto-optic pattern generator and those converging toward the target for $\mathcal{F}$-BASIS span up to 3.4 degrees - far beyond the optical performance of most of the conventional telescopes. The second consequence of reducing the FOV while increasing the collection area is a necessary increase in system length. Significant effort has gone into folding the pathlength in telescopic imagers, but the resulting assemblies are still prohibitively massive for the operational constraints of $\mathcal{F}$-BASIS remote microscopy.

Cassegrain telescopes

Although a true Cassegrain telescope with a parabolic primary and hyperbolic secondary can be designed with sufficiently high FOV angles, typically, aberration corrective optics are needed to reduce agressive off-axis aberrations [21]. Cassegrain telescope derivatives with front corrector plates are prohibitively long, with system lengths often more than three times the diameter of the primary mirror. The corrector plate coincides with the entrance pupil of the telescope which is the defined location of the target of the remote microscope optical assembly. High optical performance derivatives such as the Richey-Chrétien also demand a very restricted FOV, typically to much less than a degree [166]. An afocal, compact two-mirror derivative called the Mersenne-Cassegrain uses two conicoidal parabolas, but again suffers from strong off-axis aberrations.

Maksutov

The Maksutov telescope requires a large, heavy meniscus lens before the spherical reflective components. Although the system length is significantly shorter than other Cassegrain types, it still represents a prohibitive mass for use as a pointable system. Furthermore, the optimized geometry causes the secondary mirror to be a significant fractional obscuration of the primary mirror.

Schwarzschild

An almost deceptively promising finite-conjugate telescope design using all reflective elements is the Schwarzschild objective. The Schwarzschild lens has long been used for broadband illumination, x-ray through the infrared narrow-field industrial inspection systems and to deliver high-powered laser pulses to a diffraction-limited spot on the surface of a target for laser ablation applications [87]. Aspheric variations of the Schwarzschild design have been made to produce objectives with

unit magnification [114] and microscope objectives with 20x the working distance of traditional objectives [151]. The geometry of the objective nearly perfectly cancels 3rd-order aberrations and generates a converging spherical wavefront.

Despite being an all-refective system free of all aberrations but distortion over a wide angular FOV [137], the Schwarzschild objective operates in exactly the opposite geometry as is needed for the remote microscope. The infinite-conjugate is located on the back of the primary mirror while the finite distance of the focal plane is in "front" of the telescope. To add to the sour grapes, the equations that govern the aberration-free design use all of the degrees of freedom of the system, and as a result, the distances between mirrors and to the focal plane are set by the size of the primary mirror [69]. The distance to the target must be $(\sqrt{5}+2)/2$ times the distance from the primary to the secondary mirror [166, 131]. The flawless aberration performance of the Schwarzchild lens quickly degrades as the optical surface parameters deviate from the mathematical ideal, making it impossible to adapt for the remote microscope development effort.

Gregorian

The Gregorian telescope, with a paraboloidal primary, ellipsoidal secondary, no corrector plate, short system length and arbitrarily small central obscuration offers the most promising of standard designs for adaptation to the remote microscope. Like the other infinite-conjugate designs, the entrance pupil is still located at the primary mirror. The Gregorian also suffers from a quick reduction in performance with increased field angle, and so is typically used over a FOV of less than a degree [67], although limited wide-field correctors for Gregorians have been developed [154]. Nevertheless, an inverted conicoidal geometry of the Gregorian is the basis for the design of the remote microscope projection mirror set.

4.3 Remote Microscope Projector Optical Design

The remote microscope projector (Fig 4.2) is double-telecentric (defined as a system where the principal rays are parallel with the optic axis on one side and which converge to a point on the optical axis on the other) catadioptric afocal optical assembly with a 7 mm entrance pupil at the

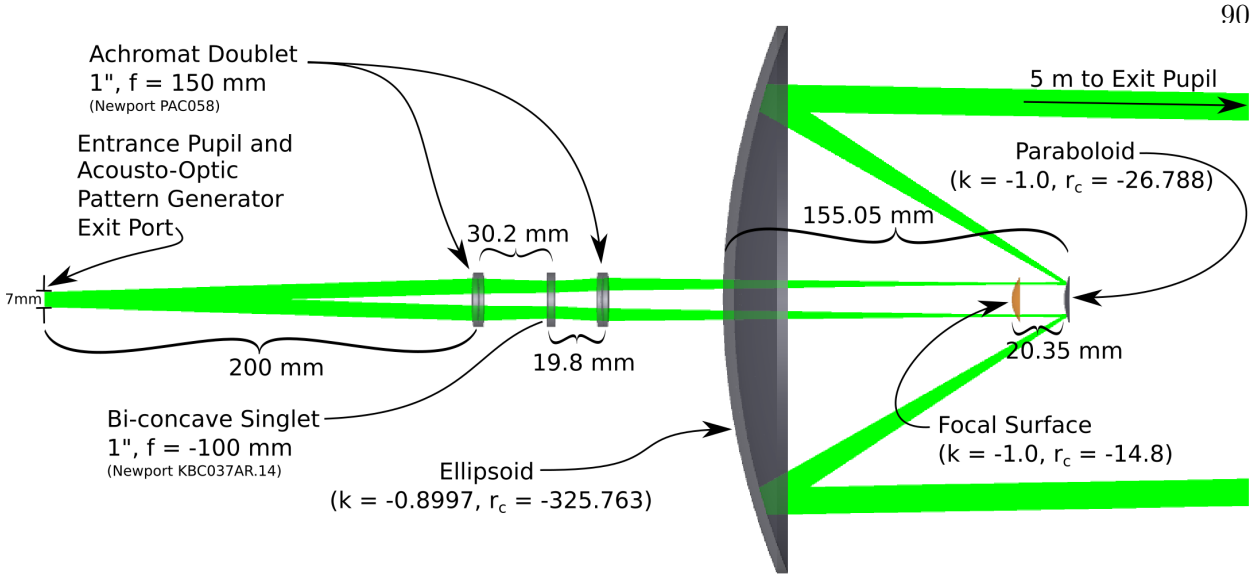

Figure 4.2: The remote microscope projection optical assembly. Beginning at the entrance pupil that coincides with the exit port of the acousto-optic pattern generator, collimated beams are Fourier transformed by a Cooke triplet operating under the conditions of double telecentricity to generate a convex focal surface before the secondary paraboloidal mirror. After the double reflection of the secondary and primary (ellipsoidal) mirrors, collimation is regenerated for every beam and they overlap at the exit pupil at 5 meters from the confocus.

acousto-optic pattern generator and a 5 mm exit pupil at the target of the microscope approximately 5 meters distant, corresponding to a magnification of M=0.71. The relative sizes of the pupils set the compression factor to 1.4 (an expression of the optical invariant). The two-mirror telescope of the remote microscope projector uses a large concave prolate ellipsoid ($k = -0.8997, ROC_e = -325.763$ mm) as the primary and a small convex paraboloidal ($k = -1, ROC_p = -26.788$ mm) secondary mirror in an inverted-Gregorian (IG) conicoidal geometry. Ellipsoidal mirrors have primarily been used in car headlight designs for more than a century [27, 145], but the arrangement of an ellipsoidal-paraboloidal mirror set has negligible appeal for traditional high precision finite-conjugate imaging due to a fixed focal length, substantial aberrations, and the ubiquity of excellent variable focal length refractive optical systems. As a result, there is a paucity of detailed analysis or reported uses of the inverted-Gregorian for imaging in the publication record.

The entrance pupil of the IG telescope is located at a focal surface positioned approximately 20 mm before (to the left of) the secondary mirror. To project collimated beams after reflection

from the primary mirror in the remote microscope projection assembly, the focal surface at the entrance pupil of the telescope must be aberrated with strong field curvature. A Cooke triplet set of corrective lenses focuses the collimated beams of the acousto-optic pattern generator at the entrance to the inverted-Gregorian with the appropriate field curvature derived in Section 4.3.4 below. One of the consequences of the IG conicoidal geometry is that the system is double-telecentric and the Cooke triplet is well known to be able to operate in either a single or double telecentric mode [10].

4.3.1 Third Order Analysis of the Two-Reflector Conicoidal Telescope

A generic derivation of the five Seidel aberrations is standard in most optics texts [43] and expressions relevant to generalized systems of conic mirrors has previously been rigorously derived [102]. There is also a generous selection of publications that have specific analyses of the aberrations of 2-mirror anastigmats [167], two-mirror relay systems [71], and a generalized analysis of the three primary designs of aplanatic 2-mirror telescopes [163]. There is little more to add to these explorations, and so we will apply the analysis presented by [*Korsch, 2012*] to quantify the specific third order aberrations of the inverted-Gregorian telecentric, infinite-conjugate telescope with the additional constraints of set entrance and exit pupils without repeating the derivation of the generalized equations.

Expressed in terms of the angular coordinates of the reflected ray, the third order Seidel ray-aberration equations excluding defocus are:

$$\theta_{xi} = S_1 h^2 x - S_2[h^2\theta_{xo} + 2x(x\theta_{xo} + y\theta_{yo})] + S_3\theta_{xo}(x\theta_{xo} + y\theta_{yo}) + S_4 x\theta_o^2 - S_5\theta_o^2\theta_x \quad (4.1)$$

$$\theta_{yi} = S_1 h^2 y - S_2[h^2\theta_{yo} + 2y(x\theta_{xo} + y\theta_{yo})] + S_3\theta_{xo}(x\theta_{xo} + y\theta_{yo}) + S_4 y\theta_o^2 - S_5\theta_o^2\theta_y \quad (4.2)$$

where the five sequential coefficients represent the spherical (S_1), coma (S_2), astigmatism (S_3), field curvature (S_4) and distortion (S_5) respectively. In this notation, the components of the ray height h and position x, y are defined in pupil coordinates. The computed angle θ_{xi} is the x component of the image-space ray after reflection, while the θ_{xo} is the object-space ray component and θ_0 is the total angular displacement from the axis. For a system of multiple conic mirrors, the total for each

of the third-order aberration coefficients is the summation of the coefficient contributions for each mirror surface. The aberrations of a system with two conic mirrors with conic constants k_1, k_2 and curvature c_1, c_2 can be fully described in terms of any five degrees of freedom [102]. For this system, the most relevant quantities for the design of our system are the distance between the mirrors d_{12}, the ratio of the radii of the primary to secondary mirror R_m (a measure of the maximum paraxial beam height at each surface), the distance between the apex of the primary and the entrance pupil z_{ep}, the distance from the object z_o, and the axial distance to the image z_i.

The generalized expressions for the five Seidel aberrations for conic mirror sets each contain terms that are a function of the ratio between the distance of the exit pupil z_{ep} to the distance to the initial object z_o. Since this optical system is designed with the constraint of collimated input beams, the object distance is infinity and the ratio goes to zero. After significant algebraic manipulation, the system variables (z_{ep}, d_{12}) may be expressed in terms of the mirror figure variables (k_1, c_1, c_2) via the following relations:

$$z_{ep} = \frac{1 + \sqrt{k_1}}{c_1(1 + k_1)} \tag{4.3}$$

$$d_{12} = \frac{1 - \sqrt{k_1}}{c_1(1 + k_1)} - \frac{1}{2c_2} \tag{4.4}$$

The system variable R_m is a practical definition of the fractional central obscuration, but is also a function of the maximum entrance angle θ_0. An expression derived in terms of the mirror variables has little utility to the system designer, since the obvious and most relevant consequence of reducing the size of the secondary mirror is to produce a stronger Petzval curvature. The final system variable z_i (the axial distance to the image) is not easily deduced from geometric inspection and is derived using ray tracing techniques in section 4.3.3.

Using several substitutions, the generalized equations for the aberrations may be expressed exclusively in terms of our chosen degrees of freedom while retaining the mirror form variables for

compactness.

$$
\begin{aligned}
S_1 &= (k_1+1)c_1^3 - R_m^4 c_2^3\Big(k_2 + \Big[\frac{R_m d_{12} - z_i(1-R_m)}{R_m d_{12} + z_i(1-R_m)}\Big]^2\Big) && (4.5)\\
S_2 &= z_{ep}S_1 - c_1^2 - R_m^2\Big[\frac{R_m d_{12} - z_i(1-R_m)}{R_m d_{12} + z_i(1-R_m)}\Big]c_2^2 \\
&+ R_m^2 d_{12} c_2^3\Big(k_2 + \Big[\frac{R_m d_{12} - z_i(1-R_m)}{R_m d_{12} + z_i(1-R_m)}\Big]^2\Big) && (4.6)\\
S_3 &= 2\Big[- z_{ep}S_1(z_{ep} + \frac{d_{12}}{R_m}) + S_2(2z_{ep} + \frac{d_{12}}{R_m}) \\
&+ \frac{d_{12}}{R_m}(c_1^2 - R_m^2\Big[\frac{R_m d_{12} - z_i(1-R_m)}{R_m d_{12} + z_i(1-R_m)}\Big]c_2^2) + c_1 - c_2\Big] && (4.7)\\
S_4 &= \frac{1}{2}S_3 - c_1 + c_2 && (4.8)\\
S_5 &= z_{ep}^2 S_1(z_{ep} + \frac{d_{12}}{R_m}) - z_{ep}S_2(3z_{ep} + 2\frac{d_{12}}{R_m}) \\
&+ S_3(z_{ep} + \frac{d_{12}}{2R_m}) + z_{ep}S_4 - \frac{d_{12}}{R_m}(R_m d_{12} c_2^2 + c_1 + c_2) && (4.9)
\end{aligned}
$$

Each of the coefficients stated above may now be calculated using the terms relevant to the inverted-Gregorian optical parameters.

A system of conic mirrors is free of astigmatism when the principal rays passes through the conicoidal points [21]. Since this is the exact condition that the mirror set is designed for, this sets the value of $S_3 = 0$, defines the condition for zero astigmatism in the IG system, and sets constraints on the relative curvatures of the two mirrors in the system. A two conic mirror set has sufficient degrees of freedom in the design to perfectly eliminate any two aberrations [21]. If we plug the system values shown in Figure 4.2 into the above equations of the Seidel coefficients without optimizing to eliminate coma and spherical aberration, we obtain the following specific coefficient values: $[S_1 = 0, S_2 = 1 \times 10^{-6}, S_3 = 0, S_4 = 7.9 \times 10^{-5}, S_5 = 3.1 \times 10^{-5}]$. The inverted-Gregorian has negligible third order spherical aberration and astigmatism and by setting the S_1 and S_2 terms to zero in the equation for S_3 the following relation is obtained.

$$
\frac{d_{12}}{R_m}c_1^2 + c_1 = d_{12}R_m\Big[\frac{R_m d_{12} - z_i(1-R_m)}{R_m d_{12} + z_i(1-R_m)}\Big]c_2^2 + c_2 \qquad (4.10)
$$

The fourth Seidel coefficient relating to field curvature S_4 contains the astigmatism coefficient as a

contribution, this demands that the S_4 value for this set of mirrors in conicoidal alignment is:

$$S_4 = c_2 - c_1 \tag{4.11}$$

The radius of curvature of the circle of least confusion (c_{clc}) of a focal surface generated by a system of k mirrors has been shown to be related to the third and fourth Seidel coefficients via the following equation [102]:

$$c_{clc} = (-1)^k(S_3 + 2S_4) \tag{4.12}$$

Since the astigmatism, S_3, of the IG is zero, the circle of least confusion has a curvature at twice the S_4 coefficient value, which is the definition of the system Petzval curvature, as expected.

The large contribution of distortion from the primary is very nearly perfectly canceled by the secondary. Operating the system in a geometry that obeys the telecentric condition sacrifices the freedom to eliminate coma, but there isn't much anyway. The strongest aberration is field curvature which we've shown is equal to the Petzval sum of the system ($ROC_p = -14.59mm$). Although the field curvature is very large, the Petzval sum is only one desired quantity regarding the paraboloidally shaped focal surface, the radius of curvature of which is dominated by the influence of the curvature of the secondary mirror after reflection. Furthermore, the non-negligible Seidel coefficients provide very limited insight into the performance of the final catadioptric assembly for the purpose of projecting collimated beams. It is far more useful to calculate the exact location, radius of curvature and cross-sectional diameter of the focal surface of the IG in the reversed surface order. This allows us to evaluate and reverse-engineer with corrective optics the optical field conditions necessary to project collimated beams from the surface of the primary mirror when the IG telescope is incorporated into the full remote-microscope projection assembly.

4.3.2 Calculating the optical prescription of the conic mirrors

The prescription of optical components is traditionally described in terms of the radius of curvature of a surface and its conic constant. The radius of curvature is the length of the radius of the best fit circle to the conic curve at the inflection point. The conic constant k is a real number

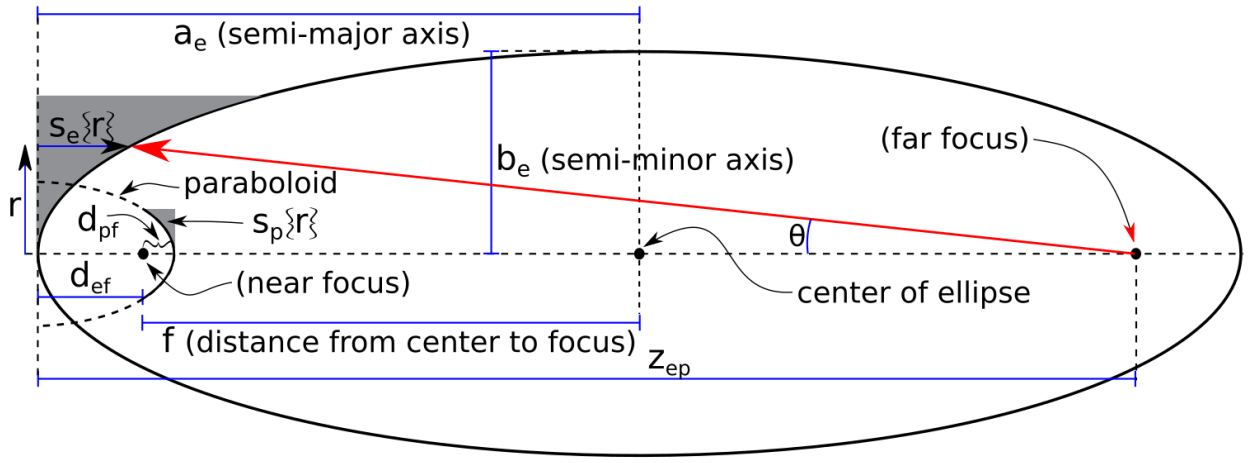

Figure 4.3: The conicoidal ellipse and parabola with co-located foci. The relevant distances between foci and surfaces are shown. The sagitta (the axial distance from the apex of each of the curves to a location on the curve at radial distance r is shaded in gray. The red arrow illustrates an example of a beam leaving the far focus and intersecting the ellipsoidal mirror at a radial distance r. The far focus of the ellipse corresponds to the entrance aperture of the remote microscope when modeled backwards.

numeric value that defines the conic section form of a sagittal cross-section of a 3D surface. The value ranges define the different conic sections with ($k < -1$) designating a hyperbola, ($k = -1$) parabola, ($-1 < k < 0$) prolate ellipse, ($k = 0$) sphere, and ($k > 0$) oblate ellipse.

For the remote microscope, the only optical requirements that are initially defined are the distance to the target (5 meters), the lateral spatial resolution of the microscope which can be expressed as numerical aperture, and a preferred maximum distance from the primary to the secondary mirror (~150 mm). With these values, the relative positions of the mirror surfaces and focal points and the relevant conic values can be calculated. Setting the distance between the foci of the ellipse to 5 m (see Figure 4.3) gives the distance from center of the ellipse to the focus (designated as the focal distance) $f = 2.5m$. The variables we wish to produce are now conic constant (k_e), semi-major axis (a_e) and semi-minor axis (b_e). By geometry, the semi-major axis is:

$$a_e = d_{ef} + f \tag{4.13}$$

where d_{ef} is the distance between the apex of the ellipsoid to the near focus. The semi-minor axis

is then:

$$b_e = \sqrt{(a_e^2 - f^2)} \tag{4.14}$$

These two values then provide the conic constant of the ellipsoid:

$$k_e = \frac{-(a_e^2 - b_e^2)}{a_e^2} \tag{4.15}$$

Similarly, the curvature of the ellipse is defined as:

$$c_e = \frac{a_e}{b_e^2} \tag{4.16}$$

The specified spatial resolution of the microscope at a working distance which is equal to twice the focal length $2f = d_w = 5m$ is $10\mu m$, which is also the spatial period of the required intensity fringes at the target. The electric field spatial period is twice that value $20\mu m$. Using the Abbe equation $d = \lambda/NA$, at an illumination wavelength of 532 nm gives NA = 0.0532. The radius of the primary mirror is then:

$$r_e = \frac{d_w \times NA}{2} \tag{4.17}$$

The maximum surface depth of the ellipsoidal primary mirror s_e is needed to specify the thickness of the substrate in a complete opto-mechanical design is calculated via the sagitta equation [97].

$$s_e\{r_e\} = \frac{c_e r_e^2}{1 + \sqrt{(1 - (1 + k_e)c_e^2 r_e^2)}} \tag{4.18}$$

To define the distances relevant to the paraboloidal mirror, the radial extent r_p must be specified. In practice, this will either be set by a maximum central obscuration requirement, or by the operational limits of the aberration correction lenses described in the sections below. Either way, using the values already calculated allows us to calculate the distance from the paraboloidal mirror to the near focus d_{pf} minus the sagitta of the paraboloid s_p.

$$d_{pf} - s_p = \frac{r_p}{r_e}(d_{ef} - s_e) \tag{4.19}$$

The distance from any point on the parabola to the focus is equal to the distance to the directrix, so d_{pf} is found by setting the sagitta to zero. This value is the definition of one half of the radius of

curvature of the paraboloid, which calculates both the sagitta according to the properly substituted Equation 4.18 and finally the distance from the apex of the ellipsoid to the apex of the paraboloid $d_{mirrors}$.

$$d_{mirrors} = d_{ef} - d_{pf} \tag{4.20}$$

The final design of the primary mirror is an ellipse of conic constant, k_1 = -0.8779 and with a radius of curvature (ROC_1) of 325.7628 mm. The secondary mirror is a paraboloid (k_2 = -1) with ROC_2 = 26.79 mm.

4.3.3 Curvature of the focal surface of the inverted Gregorian telescope

Beams of collimated light that pass through an on-axis entrance pupil in front of the inverted Gregorian telescope will focus to a very-nearly paraboloidal focal surface after reflecting from the two surfaces (Figure 4.4). For this analysis, we assume that the entrance pupil is located at the ellipsoidal focus far from the telescope mirrors and that the mirrors are arranged conicoidally, thereby demanding a telecentric operational geometry. Since the system is free of astigmatism and has negligible spherical aberration, it only requires tracing two rays per beam angle through the system in the sagittal plane to determine the shape of the focal surface assuming that the collimated beams are sufficiently small in comparison to the ellipse. This assumption slowly breaks down as the beam size increases with field angle due to the small amount of residual coma and distortion of the inverted-Gregorian.

The first step is to trace the principal ray through the system. For notational convenience, we define the variable α:

$$\alpha = \sqrt{(1 - (1 + k)c^2r^2)} \tag{4.21}$$

where k is the conic constant, c is the curvature and r is the radial distance from the optical axis. The sagittal function of any conic surface is defined as [97]:

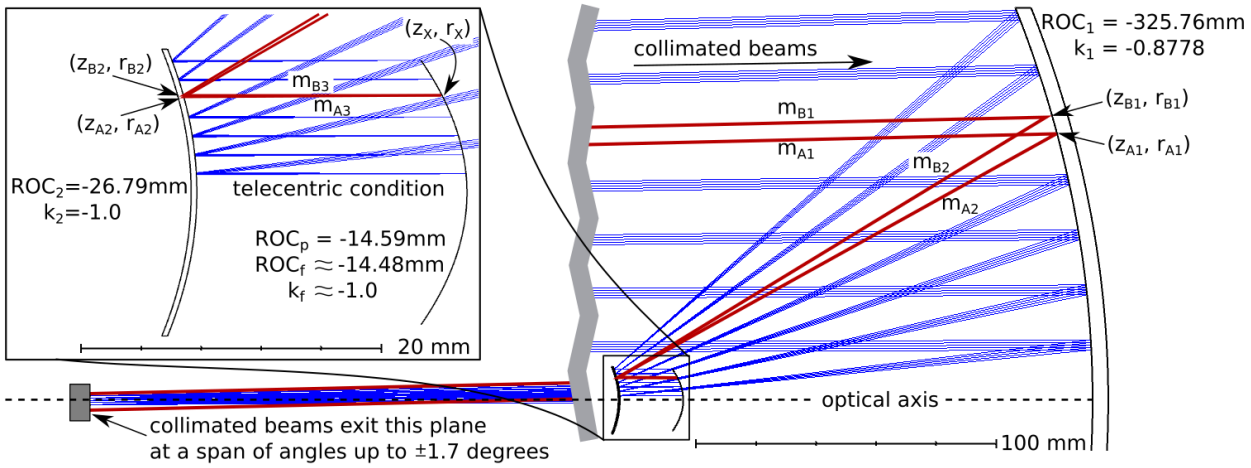

Figure 4.4: Modeling the IG telescope in the traditional direction with finite-width collimated beams originating at the far focus of the ellipsoid and propagating towards the ellipsoidal primary mirror. The beams reflect toward a focus behind the conicoidal paraboloidal secondary mirror. [Inset] Any two reflected rays per beam are sufficient to define the telecentric near-paraboloidal focal surface with the direction of the concavity matching the secondary mirror. The radius of curvature of the Petzval surface ROC_p was calculated using Equation 4.58.

$$s\{r\} = (cr^2)/(1+\alpha) \tag{4.22}$$

A principal ray (denoted with a subscript A in Figure 4.4) leaving the far focus at some slope m_{A1} will reflect from a point on the ellipsoidal surface at a radius r_{A1} and axial-distance z_{A1}. Using the definition of the conic constant:

$$k_e = -\frac{a^2 - b^2}{a^2} \tag{4.23}$$

and the definition of the semi-major (a) and semi-minor (b) axes gives the distance from the near focus to the ellipsoidal surface d_{ef}.

$$d_{ef} = a(1 - \sqrt{-k_e}) \tag{4.24}$$

So that the distance z_{ep} from the entrance pupil at the far focus to the apex of the ellipsoidal reflector is

$$z_{ep} = a(1 + \sqrt{-k_e}) \tag{4.25}$$

and the axial location z_{A1} of the radial point r_{A1} of the principal ray on the ellipsoidal surface with

sagitta s_e is:

$$z_{A1} = z_{ep} - s_e\{r_{A1}\}; \tag{4.26}$$

which then determines the original slope and angle of the principal ray as it left the far focus.

$$m_{A1} = \frac{r_{A1}}{z_{A1}} = \tan(\theta_{A1}) \tag{4.27}$$

In the absence of a secondary mirror, the reflected principal ray would, by definition, intersect the optic axis at the near focus at $(r = 0, z = 2a)$ with a slope m_{A2} of:

$$m_{A2} = \frac{r_{A1}}{z_{A1} - 2a} \tag{4.28}$$

The marginal ray (denoted with a subscript B) leaves the entrance pupil with the same slope as the principal ray since they are parallel. It is sufficient to pick a radial intersection value that differs from the principal ray radial value by some arbitrarily small distance δr.

$$r_{B1} = r_{A1} + \delta r \tag{4.29}$$

which then sets the sagittal value for the intersection of the marginal ray with the ellipsoidal mirror surface.

$$s_e\{r_{B1}\} = \frac{c r_{B1}^2}{1 + \sqrt{\left(1 - (1 + k_e) c_e^2 r_{B1}^2\right)}} \tag{4.30}$$

To calculate the slope of the marginal ray m_{B2} after reflection from the ellipsoid requires calculating the derivative of the sagitta of the mirror with respect to radius.

$$\frac{ds_e}{dr} = \frac{2c_e r}{\alpha(1+\alpha)} - \frac{(1+k_e)c_e^3 r^3}{\alpha(1+\alpha)^2} \tag{4.31}$$

$$= \frac{2c_e r\left(1 + \sqrt{1 - (1+k_e)c_e^2 r^2}\right) - (1+k_e)c_e^3 r^3}{\sqrt{1 - (1+k_e)c_e^2 r^2}\left(1 + \sqrt{1 - (1+k_e)c_e^2 r^2}\right)^2} \tag{4.32}$$

The normal to the ellipsoidal surface $\theta_{e\perp}$ is then:

$$\theta_{e\perp} = \pi + \arctan\left(\frac{ds_e}{dr}\right) \tag{4.33}$$

and the slope of the reflected second ray is:

$$m_{B2} = \tan\left[2(\pi + \arctan\left(\frac{ds_e}{dr_{B1}}\right)) - \theta_{A1}\right] \tag{4.34}$$

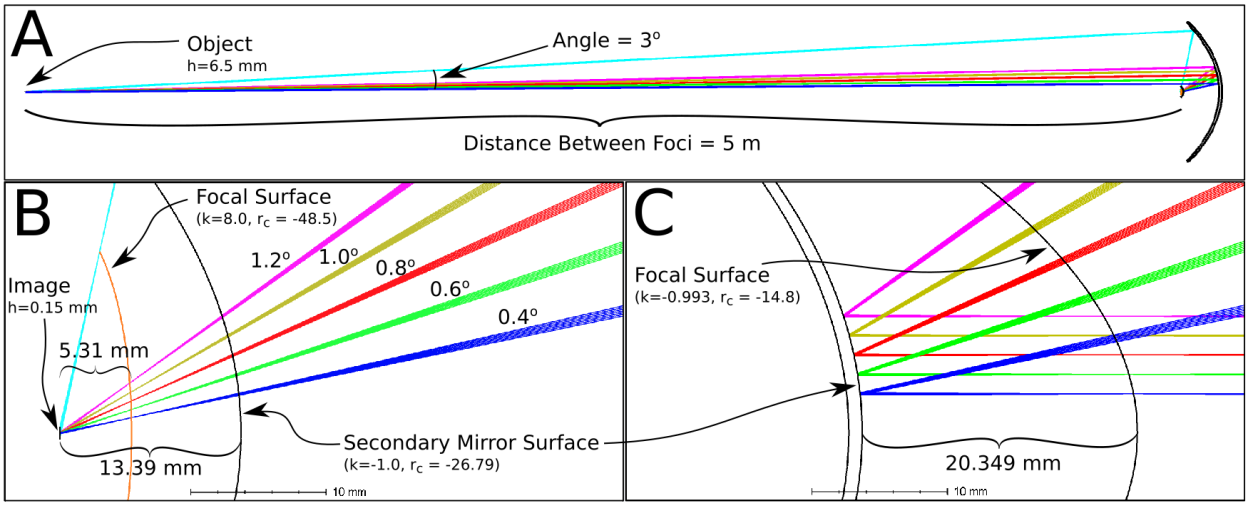

Figure 4.5: The input field curvature needed to flatten the OPD across the full aperture of the optical system is calculated by mapping the system backwards. A. The object being imaged by the remote microscope is now the source of the perfectly collimated beams desired. The primary mirror diameter is doubled to facilitate a illustrative beam directed at a 3^o angle. The height of the object is 6.5 mm, and the distance to the focus near the mirrors is 5 meters. B. A zoom in of the focus and image plane of the single ellipsoidal primary mirror. The beams at the labeled initial angles are shown passing through the surface of the secondary mirror to illustrate where the focus is generated. To first order, the best-fit focal surface of all the rays is a prolate ellipse (k=8.0) with a radius of curvature of 48.5 mm and is 5.3 mm away from the ideal geometric focal position of the primary, labeled as "Image". The image of the object is only 0.15 mm tall for the beams starting at angle 1.2^o or smaller. C. When the secondary mirror is in place, the beams are reflected with their principle rays all parallel with the optical axis. The best-fit focal surface is now nearly a parabola (k=-0.993) and has a 14.8 mm radius of curvature in the same direction as the parabolic mirror.

The coordinates of the intersection of the two rays (z_x, r_x) after reflection from the ellipsoid in the absence of the secondary mirror can now be calculated, shown in Panel A and B of Figure 4.5.

$$z_x = \frac{r_{B1} - r_{A1} + z_{A1}m_{A2} - z_{B1}m_{B2}}{m_{A2} - m_{B2}} \tag{4.35}$$

$$r_x = r_{A1} - m_{A2}(z_{A1} - z_x) \tag{4.36}$$

To compute the curvature of the focal surface after reflection from the secondary surface requires finding the intersection coordinates of the two rays with the paraboloid. First, the distance of the apex of the paraboloid from the conicoidal point needs to be set. Up to this point, the analysis has been general to any arbitrary ellipsoid. To apply this analysis to an IG mirror set will eventually require applying certain restrictions to the design space. In addition to setting the

totally unconstrained ellipsoidal conic constant k_e, the mirror radii (r_e, r_p) and curvatures of the two mirrors (c_e, c_p) must also be chosen and are likewise unrestricted other than the logical limit that the values for the paraboloidal mirror must be smaller than the ellipsoidal mirror. Since the system is designed to work in a telecentric geometry, the choice of r_p and c_p are coupled and set the distance of the paraboloidal mirror from the near focus z_{np}. Although the analysis doesn't demand it, it makes sense to set the diameter of the paraboloidal mirror to be the same aperture stop as the primary mirror to avoid vignetting. Applying this restriction and using similar triangles, the distance from the near focus to the apex of the paraboloid d_{pf} is set by the ratio of the mirror radii $(R_m = \frac{r_e}{r_p})$.

$$d_{pf} = \frac{\left[d_{ef} - s_e\{r_e\}\right]}{R_m} + s_p\left\{\frac{r_e}{R_m}\right\} \tag{4.37}$$

This distance is also 1/2 the radius of curvature of the paraboloid $ROC_p = 1/c_p$. The intersection of both rays on the surface of the paraboloid can now be calculated. Combining the equation for a parabola with axis along z, offset from the origin along the axis and setting the near focus at the origin with the equation of a line defined by (r_{A1}, z_{A1}, m_{A2}), solving the quadratic equation for z_1 for the principal ray and rearranging gives the axial location of the intersection of the principal ray with the paraboloidal surface z_{A2}.

$$z_{A2} = \frac{2a(z_{A1}m_{A2}^2 + r_{A1}m_{A2}) + 1 \pm \sqrt{4am_{A2}(z_{A1}m_{A2} + r_{A1} - z_{np}m_{A2}) + 1}}{2am_{A2}^2} \tag{4.38}$$

Finally, using the equation of a line yields the radial value of the intersection of the principal ray with the paraboloidal surface:

$$r_{A2} = m_{A2}(z_{A1} - z_{A2}) - r_{A1} \tag{4.39}$$

The process for finding the coordinates (r_{B2}, z_{B2}) intersection of the marginal ray with the paraboloidal surface is achieved by simply replacing the principal ray values in Equations 4.26 - 4.39 with (r_{B1}, z_{B1}, m_{B2}). The slope of a ray reflected from the paraboloidal surface again requires calculating the derivative with respect to radius. Luckily, in Equation 4.31 we computed the derivative for any arbitrary asphere. By applying the restriction of $k_e = -1$, the equation for the derivative of a

paraboloid thankfully simplifies to the familiar form:

$$\frac{ds_p}{dr} = c_p r \tag{4.40}$$

The ray slopes after reflection are found by replacing the appropriate values into Equation 4.34.

$$m_{A3} = \tan\left[2(\pi + \arctan(c_p r_{A2})) - \theta_{A2}\right] \tag{4.41}$$

$$m_{B3} = \tan\left[2(\pi + \arctan(c_p r_{B2})) - \theta_{B2}\right] \tag{4.42}$$

The final step is to use the equations of lines to find the intersection of the two rays.

$$z_x = \frac{r_{B2} - r_{A2} + z_{A2} m_{A3} - z_{B2} m_{B3}}{m_{A3} - m_{B3}} \tag{4.43}$$

$$r_x = r_{A2} - m_{A3}(z_{A2} - z_x) \tag{4.44}$$

These are the coordinates of the intersection of the principal and marginal rays after reflection from both mirrors. By evaluating these equations at each of the possible beam slopes m_{A1} defines the paraboloidally-shaped focal surface illustrated in Panel C of Figure 4.5.

4.3.4 Sufficient Aberration Correction using a Telecentric Cooke Triplet

Although it would be possible to optimize surface and material parameters to produce a set of lenses to best produce the desired conjugate aberrations to the IG mirror set, the cost of manufacturing optics with custom surface prescriptions prohibited this effort. However, for sets of lenses it is possible to change the amount of third order astigmatic field curvature by selecting the distances between lenses, thereby specifying the distances to the aperture stop for each element. We selected a Cooke triplet as the basis for the design of the corrective lenses for two reasons. Firstly, the Cooke triplet can be a double-telecentric system [144], defined as having either the exit or entrance pupil at infinity. In practical terms, this means that the chief ray of the system is parallel to the optical axis at the entrance pupil. Secondly, we needed a telecentric system with a negative field curvature which is only possible to obtain with multiple elements. Although the Cooke triplet is generally designed to have a low Petzval sum to generate a flat image, selecting

lenses with different surface curvatures allowed us the freedom to begin the design optimization with a non-zero Petzval curvature of either sign. Furthermore, as is visible in Fig. 4.4, the focal surface is very near to the secondary mirror. In order to place the corrective lens package on the back of the primary mirror, the focal length of the corrective lens system needs to be greater than 155 mm, and triplets can be designed with any focal length desired.

The Cooke triplet focuses the beams exiting the acousto-optic pattern generator to a focal surface that matches the position and radius of curvature needed to generate collimated beams after reflection from the telescope. A Cooke triplet was chosen primarily due to the availability of a large selection of commercially available refractive elements to construct a zoom lens. Zoom systems that use only reflective elements exist but they need a large number of surfaces to correct for aberrations and they often suffer from a large central obscuration or require off-axis operation [91, 153]. As was the case with the telescope assembly, the third-order aberrations of Cooke triplets have been explored thoroughly in other work [10, 144, 139, 159]. This traditional analysis suffers from a lack of determining *sufficiency* of aberration correction for collimated beam generation, and a great amount of effort can be wasted in the pursuit of reducing all aberrations when some subset may be irrelevant. Since the majority of the historical effort in optimization is based upon the quality of images produced by the system (vis-à-vis the PSF or spot diagram), it isn't immediately clear how these quantities should be weighted in the optimization of an axially-symmetric collimated beam compressor.

The beams from the AO pattern generator enter the Cooke triplet collimated and at a low angle, making the paraxial approximation sufficiently accurate for this effort. Interestingly, although it is a Gaussian analysis, the focal curve computed using collimated beams along the sagittal plane is the *tangential* astigmatic field curvature. Since the Petzval sum is unchanged by realignment, we also get a very good approximation of the *sagittal* astigmatic field curvature. We make the further simplification of using the thin lens approximation and set the principal planes of each lens to be co-located. To check the validity of the thin-lens approximation, we constructed a thick-lens derivation for the focal surface and also used the optical modeling software Zemax to compute

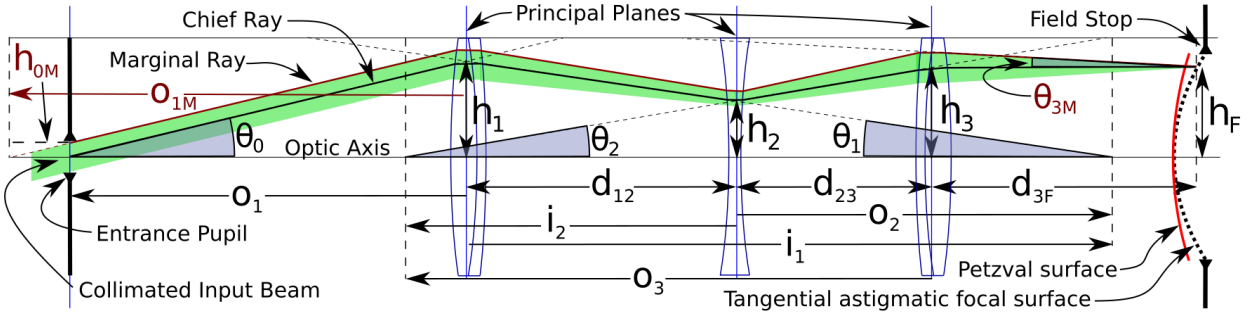

Figure 4.6: Collimated beams entering the Cooke triplet through a small entrance pupil form a forward-convex tangential astigmatic focal surface when restricted to image telecentric geometries. The curvature of the focal surface is uniquely determined by the distance between the first and second lenses of the triplet (d_{12}). The distances to the objects and images for each lens are calculated and denoted with a subscript (e.g. o_1, i_1), and the heights of each ray at the lens and focal plane are denoted as h_1, h_2, h_3, h_f respectively. The distances between each set of successive lenses and the focal plane are simliarly denoted with d_{12}, d_{23}, d_{3F}. The angles of the rays at each interface are also denoted with subscripts $\theta_0, \theta_1, \theta_2$.

the surface at a selection of field angles. All three methods calculated surfaces that were best-fit modeled with a paraboloidal surface of the same curvature. The thick-lens derivation carries a cumbersome number of terms and offers no better calculation than the following derivation using the thin-lens approximation. The chosen approximations generate a sufficiently accurate calculation of the focal surface within the expected functional adjustment range of the Cooke triplet, as is demonstrated in the simulation results.

The generalized Cooke triplet has six full degrees of freedom; the two distances between the lenses, the distance from the object, and the three focal lengths of the lenses[144]. It can be argued that there are actually two more degrees of freedom in the choice of glass for the doublet lenses, but the reasonable range of adjustibility of index of refraction is small in comparison to the other variables, especially when the designer is limited to standard catalog lenses as was the case in this effort. The location and magnification of an ideal sagittal image point is specified by the height of the object point and the angles of the marginal and chief ray.

To compute third order effects, including effects of astigmatism, normally requires parameters for a third ray in the tangential plane. When the Cooke triplet is used with three restrictions, it

allows us to simplify the analysis. The first restriction is that ray bundles pass through the entrance pupil as collimated beams and therefore the object is at infinity. The second restriction is that the triplet must be operated under the conditions of double telecentricity, and thus all chief rays will pass through the aperture stop parallel to the optic axis. The third restriction is that there is an entrance pupil with some "small" aperture located at a finite, but sufficient distance from the first lens to allow the paraxial approximation to apply. Using these limitations, the geometry of all ray bundles passing through the Cooke triplet can be specified in terms of the variables $\theta_0, o_1, d_{12}, f_1, f_2, f_3$ which correspond to the entrant beam angle, the distance to the entrance pupil, the distance between the first two lenses, and the focal lengths of the lenses respectively. In practice, the focal lengths of the lenses of the Cooke triplet will be chosen and the focal surface generated by relative positions of elements will be evaluated, and so these are treated as constants in the analysis. Although it isn't necessary to require a set distance between the entrance pupil and the first lens (o_1), the maximum separation is set by the diameter of the lens, the diameter of the beam and the maximum beam angle entering the system. Reducing this distance any further would crop the high-angle beams. With these additional reductions in variables of freedom, an analysis of the resultant image is fully described by just the angle of the beam (θ_0), and the distance between the first and second lenses (d_{12}). All of the other variables in Figure 4.5, O_2, O_3, d_{23}, d_{3f}, i_1, i_2, h_1, h_2, and h_3 are determined from the given variables.

The chief ray of a collimated beam passing through the entrance aperture at angle θ_0 intersects the principal plane of the first lens located at a specified distance o_1 at a height h_1:

$$h_1 = o_1 tan(\theta_0) \tag{4.45}$$

In the absence of subsequent lenses, Lens 1 would generate an image at a distance i_1. Using the imaging equation:

$$i_1 = \frac{1}{\frac{1}{f_1} - \frac{1}{o_1}} \tag{4.46}$$

The object distance for Lens 2 (positive) is simply the distance to i_1 minus the distance between

the first and second lenses (d_{12}), which is the last degree of freedom of the system.

$$o_2 = i_1 - d_{12} \tag{4.47}$$

When combined with the image height at lens 1, h_1 and d_{12}, this yields the outgoing angle θ_1 and the height of the chief ray as it intersects Lens 2.

$$h_2 = \frac{o_2 h_1}{i_1} \tag{4.48}$$

The value of h_2 can be expressed solely in terms of the variables of freedom of the system by substituting the variables into Equations 4.46,4.47. After a little algebraic reduction:

$$h_2 = \Big[1 - d_{12}(\frac{1}{f_1} - \frac{1}{o_1})\Big] o_1 \tan(\theta_o) \tag{4.49}$$

Using the imaging equation again computes the distance to the virtual image of Lens 2, solely in terms of the free variables:

$$i_2 = \frac{f_2\Big[1 - d_{12}(\frac{1}{f_1} - \frac{1}{o_1})\Big]}{1 - (d_{12} + f_2)(\frac{1}{f_1} - \frac{1}{d_{12}})} \tag{4.50}$$

Adding the distance between Lens 2 and Lens 3 (d_{23}) to this value (paying attention to signs) gives the object distance for Lens 3, o_3.

$$o_3 = \frac{f_2\Big[1 - d_{12}(\frac{1}{f_1} - \frac{1}{o_1})\Big]}{1 - (d_{12} + f_2)(\frac{1}{f_1} - \frac{1}{d_{12}})} - d_{23} \tag{4.51}$$

Using similiar triangles yields the height of the chief ray as it intersects the principal plane of Lens 3:

$$h_3 = \frac{o_3 h_2}{d_{12}} \tag{4.52}$$

$$= \frac{f_2 o_1 \tan(\theta_0)\Big[1 - d_{12}(\frac{1}{f_1} - \frac{1}{o_1})\Big]^2}{1 - (d_{12} + f_2)(\frac{1}{f_1} - \frac{1}{d_{12}})} - d_{23} o_1 \tan(\theta_0)\Big[1 - d_{12}\Big(\frac{1}{f_1} - \frac{1}{o_1}\Big)\Big] \tag{4.53}$$

Enforcing the condition of image telecentricity demands that the chief ray exit Lens 3 parallel to the optic axis which in turn requires the object distance be equal to the focal length of the lens ($o_3 = f_3$). As a result, the chief ray height at the focal surface is h_3. The axial distance to the focal surface is determined by tracing a marginal ray through the system. Most of the calculation for

the marginal ray is identical to the chief ray since the two rays are defined to be initially parallel. The additional distance to object 1 for the marginal ray (o_{1M}) is defined by the half-width of the entrance pupil h_{0M} and the entrance angle:

$$o_{1M} = o_1 + \frac{h_{0M}}{\tan(\theta_0)} \tag{4.54}$$

All of the analogous calculations from Equation 4.46 to 4.53 are computed by substituting this value for the chief ray object distance o_1. Unlike the chief ray, the marginal ray exits Lens 3 at an angle θ_{3M} which must be calculated to find the axial distance to the relevant point on the focal surface. The properly modified Equation 4.51 is:

$$o_{3M} = \frac{f_2\left[1 - d_{12}\left(\frac{1}{f_1} - \frac{1}{\left(o_1 + \frac{h_{0M}}{\tan(\theta_0)}\right)}\right)\right]}{1 - (d_{12} + f_2)\left(\frac{1}{f_1} - \frac{1}{d_{12}}\right)} - |d_{23}| \tag{4.55}$$

Applying the imaging equation once more yields the new theoretical image location on the optic axis that would be generated by marginal ray exiting the third lens:

$$i_{3M} = \frac{o_{3M} f_3}{o_{3M} - f_3} \tag{4.56}$$

where the full substitution for o_{3M} has been left out for readability. This image point on the optical axis is the apex of a similar triangle to the triangle bounded by the intersection of the chief and marginal rays on the focal surface. The distance from the principal plane of Lens 3 to the focal surface (d_{3F}) is then:

$$d_{3F} = \frac{i_{3M}(h_{3M} - h_3)}{h_{3M}} \tag{4.57}$$

The evolution of the sagittal cross-section of the focal surface is most intuitively illustrated with ray-trace plots such as are generated from Zemax, since they also show the relative spacing of the lens elements. The focal surfaces generated by incrementing the spacing between the first two lenses (d_{12}) is shown in panel A of Figure 4.7. Unlike in most zoom lens implementations which seek to retain a flat image plane, the distance d_{12} does not trace out a curve but rather varies linearly over the range of operation. A planar focal surface is generated at one location (bottom trace of panel A) where the system operates both in telecentric mode and where astigmatism

exactly matches the small Petzval curvature of the triplet. Shortening the distance between the first two lenses from this condition produces near-paraboloidal focal surfaces with concave-forward curvatures, while lengthening the distance yields the opposite curvature direction. The slice of the focal surface computed by the ray trace Equations 4.45 - 4.57 is in the sagittal plane, meaning that this curvature is due to the tangential astigmatic field curvatures. Importantly, this then gives us the sagittal astigmatic field curvature for free, since it is defined as $3\times$ the deviation of the tangential field curvature from the Petzval curvature [68]. The Petzval curvature of the Cooke triplet does not change with relative lens positions, but is rather a function only of the index of refraction and curvatures of the optical surfaces.

$$r_{petzval} = \Big(- n_k \sum_{j=1}^{k} \frac{n_j - n_{j-1}}{r_j (n_j n_{j-1})} \Big)^{-1} \tag{4.58}$$

Since this Cooke triplet has symmetric elements, the Petzval curvature is small in comparison to the IG mirror focal curvature ($ROC_p = 325$ mm for the Petzval, and $ROC_c = 14$ mm for the IG focal surface). The conjugate focal surface needed to best correct the IG mirror aberrations is the focal surface of the circle of least confusion of the Cooke triplet. In practical terms, the Cooke triplet should be aligned to produce tangential astigmatic field curvature that is 66% of the Petzval curvature of the IG mirror system.

4.4 Performance of Remote Microscope Optical Assembly

The primary concern of the remote microscope optical assembly is the minimization of the OPD between any two beams at the same cross-sectional coordinate at the intersection plane. Under ideal operation, every beam will be perfectly collimated, have zero radial distortion and therefore have a flat wavefront. The desired result of straight interference fringes will be achieved if each beam has an identical wavefront curvature map, but in reality, any radially-varying axial deviation of the focal surface as the beams enter the IG telescope will result in either converging or diverging beams projected from the primary mirror. Any two beams with different focal point deviations from the focal surface will show radially-dependent OPD at the interference plane resulting in slight,

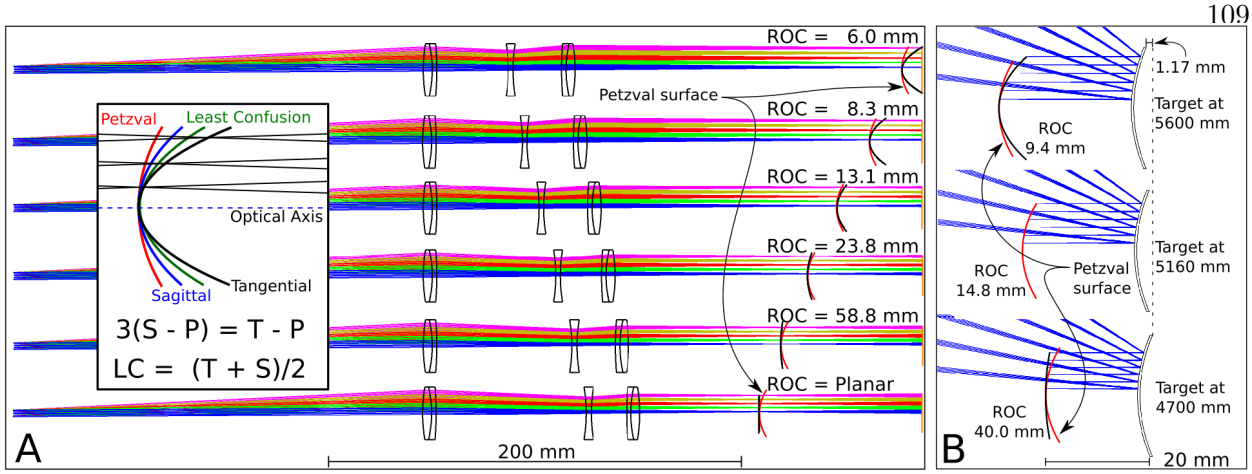

Figure 4.7: A. The Cooke triplet operational alignments when used as a set of corrective optics. When restricted to telecentric operation, the different system alignments of the Cooke triplet produce a near-paraboloidal focal surface of decreasing radius of curvature at increasing distances equal to the tangential astigmatic field curvature. B. A zoom-in of the secondary mirror and focal surface of the IG mirror system in the compatible spatial orientation as Panel A. The mirrors of the inverted-Gregorian can be axially displaced to direct overlapping collimated beams over a range of distances centered at the conicoidal position while retaining sufficient telecentricity. The secondary mirror needs only to be displaced by 1.25 mm to change the overlap position of projected beams from the primary mirror by 1 meter.

unwanted changes to the interference fringe periodicity and curvature. Two-beam OPD maps for uncorrected and corrected optical systems are shown in Panels A-C of Figure 4.8.

Beam pairs were selected to illustrate the three possible degrees of symmetry in the system. Beam pair locations in the normalized pupil function are shown in the first column. Beam pairs positioned symmetrically about the optic axis will show no difference in the OPD in either the tangential or sagittal plane (top row). For these beams, the only result of an uncorrected IG mirror set is an increasing beam distortion with projection angle, which will cause radial non-linear fringe period evolution. The second row of Figure 4.8 shows beams with single lateral symmetry in the interference plane. The tangential OPD now shows significant evolution across the pupil while the sagittal OPD is uniformly zero. As a result, the interference fringes show curvature due to an evolution in period with radial distance from the optical axis. The corrected optical system using the Cooke triplet, shown in the far right, reduces the fringe period evolution to less than $\lambda/8$. The third row shows a beam pair with no axial symmetry. Both the sagittal and tangential OPD are

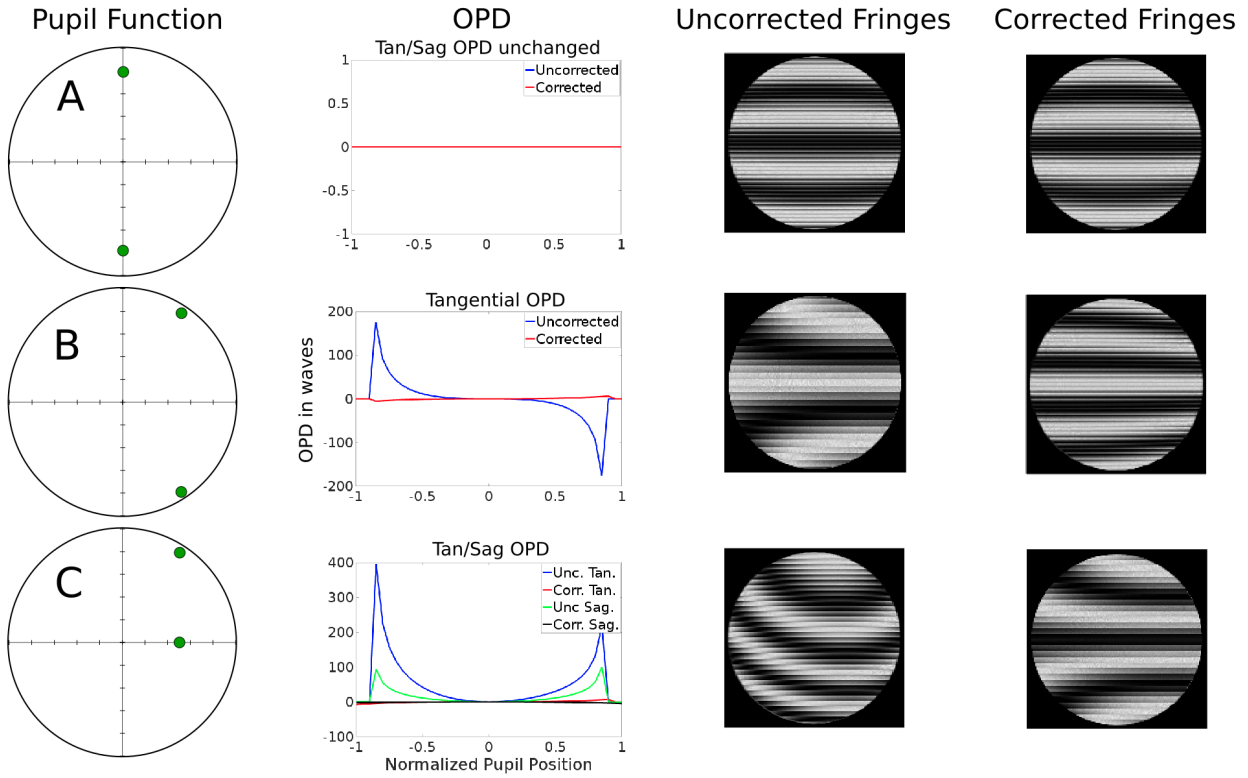

Figure 4.8: The OPD and fringe curvature of three beam pairs of sucessively decreasing symmetry projected from uncorrected and corrected projection optical assemblies. The first column shows the beam locations in the normalized pupil function. The second column plots the relevant sagittal and tangential OPD across the beam at the interference plane. The third column shows Moiré patterns (produced by pixel aliasing) of the interference fringes generated by an uncorrected IG mirror set. The fringes generated by the IG telescope aberration-corrected with a Cooke triplet is shown in the fourth column.

significant for the uncorrected system and are mostly canceled in the corrected optical system. This is illustrated again in the Moiré pattern of the beam interference where the uncorrected system produces fringes with unusable curvature of up to a full wave across the beam. Futhermore, this translates into a fringe pattern with a partial rotation away from optic axis. Since the purpose of this optical system is to measure Fourier components, this rotation will cause the microscope to measure the wrong spatial frequency. The corrected system still shows fringe evolution, albeit with a maximum of $\lambda/4$ deviation across the beam which is the threshold for the system performance.

All radially symmetric beams will have identical axial offsets of beam foci from the focal surface and therefore have similar wavefront curvatures due to beam expansion or contraction at

the intersection plane. Similarly, interference fringe curvature due to astigmatism will be canceled, and coma will have negligible effect. Distortion will induce evolution of the fringe spatial period across the beam radially, but will mostly be limited due to the fact that the beam cross section is small. For radially asymmetric beams, in an uncorrected IG mirror set, coma and defocus will induce fringe curvature and distortion will manifest as fringe period evolution in the radial direction.

4.4.1 Perspective of the Projector as a Finite-Conjugate System

I used an infinite-conjugate analysis for this system because the collimated beams in and out of the projection assembly imply the system uses objects and images at infinity, but in Section 4.2 I said the goal of the projector is to produce an "image" of the active apertures of the AODs at the target. The word "image" is placed in quotes because although there is a 1:1 mapping for every pair of beams, the requirement that beams be collimated demands that the spatial mapping isn't uniform across all sets of beams. In other words, the PSF of a real image at the target would be severely aberrated and as a result the projection assembly is an embarrassingly poor finite-conjugate imager. Simulated images using the system as a finite-conjugate imager are blurry, distorted and nearly unrecognizable. Certainly, the full assembly can be optimized for finite conjugate imaging, but at the cost of collimated beams and radially-dependent aberrations in the infinite-conjugate operational mode.

4.4.2 Improvements to the Optical System

The aberration correction provided by the Cooke triplet is limited to matching the IG focal surface using astigmatic field curvature at the cost of increases to other aberrations, the effect of which can be seen in the previous figure. Over the operational range of the projection optical assembly, particularly at one "focal" position, this correction is sufficient for Fourier-sampling remote microscopy, but the path to immediate improvements is clear. Since there is no astigmatism in the IG mirror set at the ideal working distance, it makes sense to construct a Cooke triplet or other doubly-telecentric zoom lens system that produces the conjugate Petzval sum as the mirror

set and uses the system variables to minimize other off-axis aberrations. This can be achieved with traditional lens bending techniques and using a custom set of lenses with assymmetric surface curvatures, both of which were outside the budget of this study.

4.5 Zoom Alignments for Variable Working Distance

The remote microscope projection optical assembly is nominally designed to operate at some fixed distance between the primary mirror and the location of the exit pupil where the beams overlap (z_{ep} of Equation 4.3) which is defined by the surface constants of the primary mirror. Small axial misalignments (δ_z) of the secondary mirror away from the conicoidal condition with the primary mirror changes the location of the overlap of the beams by a factor of 800 x δ_z (measured in simulations and shown in Figure 4.7). The area of overlap of the beams defines the field-of-view of the Fourier-sampling remote microscope, so aligning the projection optical system to overlap beams at different axial locations represents a "refocusing" of the microscope at different working distances. This only works as long as the beams retain sufficient collimation to not degrade the generated planar interference fringes at the target.

There are three consequences to adjusting the working distance by changing the relative locations of the IG mirrors; 1) the 3rd order aberrations are no longer expressed as functions of the conic variables of the mirrors, 2) the curvature and location of the focal surface changes, and 3) the mirror set is adjustible over a finite range which can be described as operating in a "near-telecentric condition". The third order aberration expressions in Equations 4.5 - 4.9 still hold for an axially misaligned IG system, but the relation between the conic variables (k_1, k_2, c_1, c_2) are no longer strictly related to the system variables (z_{ep}, d_{12}, R_m). One of the primary consequences of misalignment of the IG mirror set is the loss of the anastigmatic operation of the system. As can be seen in panel B of Figure 4.7, the curvature of the focal surface changes with relative position of the secondary mirror, but since the Petzval curvature is unchanged, this curvature is completely due to an astigmatic contribution.

The curvature and location of the focal surface derived in Section 4.3.3 assumed conicoidal

mirror locations to find the intersection of the principal and marginal rays. This analysis can be extended to non-conicoidal geometries by computing both rays of a beam using the equations for marginal rays. In practice, this system is going to be modeled in a ray-trace program like Zemax which calculates the focal surface and makes the impressively laborious algebraic derivation for non-conicoidal geometries ultimately pointless. The non-conicoidal focal surfaces for three target distances are shown in panel B of Figure 4.7. The curvature (expressed as radius of curvature) is shown for the near-telecentric secondary mirror position. Although the secondary mirror need only move 1.25 mm axially to change the position of beam overlap (target position) by 1 meter, the focal surface curvature changes significantly over this range and moves in axial position almost 12 mm.

The collimated beams leaving the AO pattern generator are focused by the Cooke triplet while obeying the telecentric condition. For this lens set to be used for aberration correction of the IG system, the assumption of telecentricity must be sufficiently valid for all usable non-conicoidal positions of the secondary mirror. The ideal angle of principal rays of collimated beams leaving targets at different working distances is calculated using Equations 4.29 - 4.36 of the backwards modeled IG mirror set. Telecentric beams exiting the Cooke triplet are focused to a focal surface with the matching curvature of the non-conicoidally aligned IG system will cause the beams to overlap at a different distances dependent upon the angular deviation at the focus. This is the measure of the maximum angular deviation from telecentricity a beam can have and still be "sufficiently telecentric" to produce usable beams for Fourier sampling remote microscopy.

Chapter 5

Optical Form Testing

5.1 Phase Shifting Interferometry

The surface forms of spherical mirrors and lenses are straightforward to measure using well-established processes using phase-shift interferometry and either planar or spherically symmetric wavefronts, but they have limited utility in practical optical applications due to design inflexibility and inherent aberrations [111]. Aspheric lenses and mirrors provide a much wider solution space in reducing the number of elements and eliminating aberrations in optical designs, but it is significantly more difficult to measure their surface forms. Despite the fact that aspheric optics have been in use for centuries, other than for paraboloids, no standard process has been developed to measure these surfaces. The invention and commercialization of stabilized lasers and phase-shift interferometers provided the community with the basic tools to make the problem tractible but every unique instantiation of an aspheric surface shape required a new measurement procedure and supplementary tools. Consequently, over the last few decades, there has been a considerable amount of work in the development of sophisticated instrumentation and techniques to precisely manipulate the spatial orientation and interferometrically measure the surfaces of various aspheric mirrors and lenses. Not withstanding the subtleties of some of the commercial instruments, the approaches to measuring the surfaces of aspheres fall into two general categories: optical nulls and subaperture stitching.

5.1.1 Optical Nulls

Optical nulls, also known as null correctors, are reflective or transmissive components that are designed to alter the planar or spherical wave of the test beam to match the conjugate wavefront to the surface under test. Upon reflection from the test surface the wavefront deviation due to the test surface errors is measured as variations from a planar wave. The fabrication of optical nulls is expensive and is only practical when an optical component is being mass produced, furthermore optical nulls for aspheres are themselves aspheres which also require testing [111]. One of the solutions to optical testing of aspheres, particularly convex aspheres, which has applicability over some range of surface morphologies, is a variation on phase-shift interferometery that is supplemented with the use of devices called variable optical nulls (VON). These devices induce varying amounts of low-order aberrations to the test beam to better match the wavefront of portions of the surface under test. Rotating prism pairs placed into a converging spherical wave can generate a small amount of spherical aberration, astigmatism, coma and trefoil, but with only two degrees of freedom (tilt and wedge) these aberrations are not independent [158]. The use of a pair of rotating wedge prisms as a variable optical null has been demonstrated in the measurement of aspheric surfaces varying up to 1000 waves from the best fit sphere [118, 149]. It should be noted that the use of VONs to date will only allow the measurement of some subaperture of the tested surface requiring multiple test configurations to cover the full aperture. Computer generated holograms (CGH), a.k.a. holographic test plates, have also been used as supplemental devices to interferometrically test large convex aspheric surfaces [25, 23]. By writing a set of concentric rings onto a concave mirror, full aperture tests of convex mirrors up to 1.15 m in diameter have been achieved [26] and in later work on concave paraboloid mirrors up to 6.5 m [26]. More advanced CGHs containing the recordings of multiple wavefronts have been demonstrated and offer the possiblility of a generalized null-corrector for a wide range of concave and convex aspheric surfaces [7].

5.1.2 Subaperture Stitching

Subaperture stitching is a measurement technique in which the optical surface is tested in multiple spatial subsets that are subsequently assembled algorithmically to obtain the full interferometric map of the surface. It is preferable that the illumination wavefront matches the morphology of the surface (e.g. a spherical wavefront for a spherical surface with identical radii of curvature) as much as possible to maximize the efficiency of each subaperture measurement and reduce the errors that need to be corrected in the stitching process. One of the earliest demonstrations of subaperture stitching used multiple spherical subaperture wavefronts to assemble a spherical full aperture [42]. The technique, however, was primarly developed to allow the measurement of surfaces that had significant deviation from the testing wavefront, as in the canonical case of using spherical wavefronts to measure aspherical surfaces. Nearly the entirety of the experimental implementations reported in the literature use a spherical wavefront generated using a focusing output coupler of a Fizeau interferometer. This wavefront is used to illuminate subapertures of the aspheric surface of interest, each of which have circular 2-D projections. To acquire multiple subapertures, the tested optic must be repositioned relative to the illumination beam, a process with six independent degrees of freedom (x-y tilt, x-y-z translation and rotation) that must be accounted for in the stitching process. Early versions of the technique used non-overlapping subapertures and the complete surface was modeled using Zernike polynomials which yielded inaccurate results in the presence of localized assymmetric phase errors [121, 89]. Overlapping subapertures were used by *Stuhlinger, (1986)* wherein the phase errors were evaluated at discrete points in the intersecting regions using least-squares fitting to minimize x-y tilt and piston. The so-called discrete phase method provided much greater localized precision and was used for apertures up to several meters in diameter. Concurrent and many subsequent implementations returned to Zernike polynomials to parameterize each of the spherical subapertures to compute the coefficients of piston, x-y tilts and defocus resulting from variations in subaperture optical alignment [108, 104, 52, 107, 106]. Strictly speaking, non-axially symmetric subaperture stitching consists of two general problems;

the parameterization of each subaperture, and the algorithm to stitch those modeled subapertures into a full aperture map. The highest precision reconstructions of mild aspheres takes both of these problems into account by either directly measuring all degrees of freedom through significant mechanical expense (e.g. [119, 60]), or through computationally expensive non-linear iterative fitting algorithms that can take many hours to converge to a reconstruction [31, 32, 33, 34]. A common admission reported in the published literature on spherical subaperture stitching techniques is that the geometry allows the testing of only mild aspheres with up to, at most, a few hundred waves of spherical departure.

5.1.3 Annular Subaperture Interferometry

A variant of the subaperture stitching technique called annular subaperture interferometry employs the assumption of rotational symmetry about the optical axis to measure annuli of the aspheric surface that closely match a best-fit sphere [161]. Annuli are selected by changing the axial distance between the asphere under test and the focus of a spherical wavefront. The most popular approach is to parameterize the annuli with an orthonormal set of annular Zernike polynomials to separate geometry-induced phase errors from surface errors. This approach has been demonstrated on concave paraboloidal mirrors as a set of best fit spheres [108, 51, 82, 83, 81]. Recently, the inclusion of a partial null lens in the beam path has been shown to reduce the number of annuli needed to span the full aperture of a paraboloid, although the need to fit to a large number of Zernike polynomials remains [170]. Another implementation that sought to extend the capabilities of annular measurements induced small amount of tilt to the spherical test wave to produce a quasi-elliptical, off-axis annular data set [171]. These off-axis annuli were then stitched together by compensating only for tip/tilt and piston errors. Finally, a ray-tracing method was proposed to measure the OPD between the spherical wave and the annuli of the test surface [156]. The proposed method yielded successful reconstructions in simulations, but retained all of the apparatus of Zernike decomposition.

5.2 Parabolic Parameterization

I have developed another variant on annular subaperture interferometry for the testing of nominally axially-symmetric large-aperture concave aspheres that parameterizes annuli as variances from best-fit paraboloids. Instead of using a spherical wave to test the asphere, a planar wave is emitted out of the Fizeau inteferometer and interacts with the mirror under test in a double pass optical setup. Using a small spherical mirror within the range of foci, the asphere will closely match a paraboloid over an annulus of conformance and will generate resolvable fringes with radially varying phase curvature. The OPD between each aspheric annulus and the corresponding best-fit paraboloid is calculated via geometric ray-tracing without the need to use Zernike polynomials. I describe the experimental setup, derive the OPD calculation, discuss pertinent errors in the measurement scheme and report the experimental results on the primary ellipsoidal mirror described in Chapter 4.

5.2.1 Instrument and Experiment

The instrumental setup in shown in Figure 5.1. A flat output coupler is used on a standard Fizeau interferometer (WYCO 6000) to generate a large test beam. The Fizeau interferometric tester uses a frequency and temperature stabilized Helium-Neon laser to emit a well-collimated laser beam 6-inches in diameter. The mirror under test is aligned with the optical axis parallel to the beam, but it is laterally offset so that the center of the mirror is on the edge of the beam aperture. It is necessary to use at least one flat fiducial either manufactured into the mirror or temporarily affixed to the mirror to retroreflect the light in order to interferometrically align the ellipsoid. The mirror used for the experiments in this effort had an optically flat rim manufactured into the monolithic aluminum body directly abutting the aspheric surface. After reflection from the asphere, the beam becomes a converging wavefront that comes to a rough focus along the optical axis of the mirror. A high-optical-quality concave spherical mirror is placed so that the center of the mirror is co-located within the span of the focused beam. The circle of rays that pass

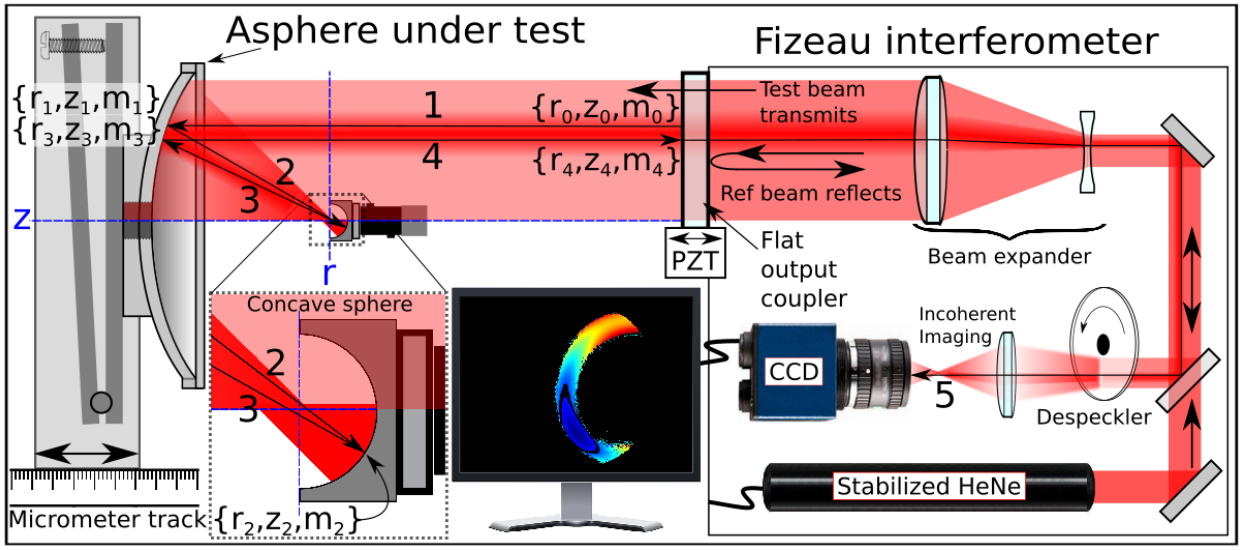

Figure 5.1: Testing an asphere as a paraboloid: A flat output coupler transmits a collimated beam from a standard WYCO 6000 Fizeau interferometer. The beam reflects off of the asphere under test creating an aspherical converging wavefront that focuses approximately at the center of curvature of a small concave spherical mirror. Only rays sufficiently near the paraboloidal-matching condition will retro-reflect into the interferometer and be detected as an annulus of resolvable fringes. The annular portion of the mirror measured is selected by changing the separation between the asphere and the spherical mirror. The OPD is calculated as the sum of all the numbered segments 1 through 5. The radius (r), axial distance (z) and slope (m) of the rays as they intersect the surfaces are calculated in the method.

through the optical axis at the co-location of the center of curvature of the spherical mirror will reflect from that mirror back along the identical path. These rays are indistinguishable from rays reflected from a paraboloid of identical radius of curvature. As the radial distance away from this circle of conformance increases, the rays will accumulate phase until the phase difference is greater than the Nyquist sampling limit of the 2D detector for standard phase-shifting interferometry to resolve resulting in a finite annulus of measurement data. The annulus of resolvable data is selected by changing the separation of the aspheric mirror under test and the spherical mirror. Because the beam exiting the output coupler of the Fizeau interferometer is collimated, the choice of which mirror to move is arbitrary and geometrically equivalent. As with prior implementations of annular sub-aperture interferometric measurement schemes where the number of apertures is related to the amount of departure from a spherical wavefront, the greater the aspheric surface departure is from

the best fit paraboloid, the greater the number of annuli needed to cover the aperture of the mirror. With each change in the separation between the mirrors, the orientation of the mirror under test is tweaked to optimize optical alignment using the flat fiducial. It is beneficial to record the change in separation of the mirrors to enable the calculation of the conic constant and radius of curvature of the mirror under test without prior knowledge; a process described in Sec. 5.2.6. Plotting these measurements against the measured radial distances to the centers of the parabolic-parameterized annuli provides useful information about the mirror quality and surface form. The analysis of the theoretical and measured annuli is presented in the discussion. Once data is acquired across the full aperture of the collimated beam the test mirror is rotated around the optical axis and another series of annuli are acquired using the same procedure. Assuming a single flat fiducial at the center of the test mirror, an optical aperture twice the diameter of the collimated beam can be tested. An additional flat fiducial ring on the circumference of the mirror allows quadrupling of the testable mirror aperture.

The aspheric mirror used in our experiments was a 250 mm diameter ellipsoid with a conic constant of $k = -0.8778$, curvature of $c = 3.07m^{-1}$ and with more than 3000 waves of spherical departure making traditional subaperture testing as an asphere impractical [123]. The mirror was manufactured by Nipro Optics out of a single piece of aluminum and had a central hole 22 mm in diameter. The majority of the mirror had a thickness of 5 mm with 13 light-weighted sagittal support ribs machined out to provide optical rigidity. Mounting holes were drilled into the ribs to support the mirror at approximately 7/10th of the radius. For all tests, the mirror was mounted to the test structure using three nylon 1/4-20 screws at 120 degree intervals. The reflective aspheric surface and a flat ring orthogonal to the optic axis around the circumference was diamond-turned to an optical tolerance of $\lambda/4$ over any 1 cm aperture. The mirror was mounted on a translation platform containing x-y tip-tilt and x-y translation micrometer stages and a 360 degree rotation stage. This platform coupled to an encoded positioning rail with 5 micron precision which was aligned to the laser beam of a WYCO 6000 Fizeau phase-shifting interferometer. We used the manufacturer-supplied software to perform the phase-shifting operation and acquire and store the

data to disk. A high optical quality concave hemispherical mirror with a radius of 5 mm was mounted to the floating optical table approximately 0.5 m from the output coupler on a mechanical x-y positioning stage. The center of the spherical mirror was aligned to the optical axis of the aspheric mirror using the annulus data generated in the test. The ellipsoidal mirror was chosen to move during testing rather than the smaller spherical mirror due to the high-quality encoding rail and platform. The total change in separation between the mirrors required to test the portion of the mirror filling the aperture of the test beam was 1.2 mm and 25 annuli of data. I developed a phase correction and stitching algorithm described in the next section to construct the mirror reconstruction shown in Fig. 5.8.

5.2.2 Parameterization Derivation

The optical test configuration used in this effort assumes that an arbitrary aspheric surface closely matches a paraboloid over some annular extent of the surface and that any sagittal slice will match a parabola. Paraboloidal parameterization differs from all other previous annular sub-aperture techniques which evaluate a surface using best-fit spheres, but it shares the requirements that the annuli of data require phase flattening before they can be stitched together to make a map of the optical surface. In addition to any phase variations due to errors in the surface of the aspheric mirror, each annulus of resolvable data will contain a phase morphology resulting from the geometric variance from a paraboloid. A ring in the middle of each annulus of data called the circle of conformance is mathematically identical to the best-fit paraboloid, while every other point will accumulate phase error as a non-linear function of radial distance from this circle resulting in a quasi-toroidal topology. Rather than model the data using annular Zernike polynomials which inherently suppress high-frequency phase errors, I calculate this toroidal phase curvature for each annulus by tracing rays through the system to compute the optical pathlength difference (OPD) between the test configuration containing the aspheric mirror and the ideal system containing the best-fit paraboloid for the annulus. The appropriate phase curvature can then be subtracted from the annuli of data and they are stitched together using linear least squares minimization of x,y tilt

and piston residuals of overlapping pixels.

5.2.2.1 Aspheric OPL

To begin, we calculate the OPL for every ray traversing the system with an ideal aspheric prescription. As a reminder, the curvature is defined as the inverse of the radius of curvature $c = 1/R$ and the conic constant is defined as:

$$k = \frac{b^2}{a^2} - 1 = -e^2 \tag{5.1}$$

Where the conic sections are $(k < -1)$ hyperboloid, $(k = -1)$ paraboloid, $(-1 < k < 0)$ prolate ellipsoid, $(k = 0)$ sphere, and $(k > 0)$ oblate ellipsoid. For convenience, we define the variable α:

$$\alpha = \sqrt{(1 - (1 + k)c^2r^2)} \tag{5.2}$$

where k is the conic constant, c is the curvature and r is the radial distance from the optical axis. The sagitta of an aspheric surface is defined as:

$$s = (cr^2)/(1 + \alpha) \tag{5.3}$$

Path segment 1 (See Fig 5.1) from an arbitrary reference z-location z_{ref} (nominally the output coupler of the interferometer) is just the distance to the surface of the asphere.

$$L_1 = z_{ref} - s \tag{5.4}$$

To calculate L_2 from the surface of the asphere to the surface of the spherical mirror requires knowing the outgoing slope which requires calculating the derivative of the sagitta with respect to radius of the aspheric surface.

$$s' = \frac{ds}{dr} = \frac{2cr}{1 - \alpha} + \frac{(1 + k)c^3r^3}{(\alpha(1 + \alpha))^2} \tag{5.5}$$

The slope of the outgoing ray (m_1) after reflecting off of the asphere is then

$$m_1 = -\cot(\pi - 2\arctan(s')) \tag{5.6}$$

The pathlength of section 2 requires knowing where a line starting at the aspheric surface (z_1, r_1) with slope m_1 intersects the spherical mirror. Expressed where the definitions of the relevant variables (r, z, m) are consistent with a system spatially oriented so that the optical axis is horizontal, the line defining the traced ray is described by:

$$(r_2 - r_1) = m_1(z_2 - z_1); \tag{5.7}$$

The 2D sagittal cross section of the sphere is just the equation of a circle offset in z by a distance h:

$$R_{sec}^2 = (z_2 - h)^2 + r_2^2 \tag{5.8}$$

Rearranging these equations generates two equivalent expressions for r_2 expressed in terms of the known variables (R_{sec}, z_1, h, r_1) and unknown z_2.

$$r_2 = \sqrt{R_{sec}^2 - (z_2 - h)^2} = m_1(z_2 - z_1) + r_1 \tag{5.9}$$

By applying the quadratic equation and solving for z_2 we obtain a rather lengthy expression for the resulting z value at the intersection of the spherical mirror surface.

$$z_2 = \frac{z_1 m_1^2 - r_1 m_1 + h \pm \sqrt{R_{sec}^2 - r_1^2 + m_1(2r_1 z_1 - 2hr_1) + m_1^2(2hz_1 + R_{sec}^2 - z_1^2 - h^2)}}{m^2 + 1} \tag{5.10}$$

From which r_2 is calculated using Eq 5.9. This radial value is needed for the calculation of the next segment, although it isn't technically required to calculate the pathlength of segment 2 which can be computed with:

$$L_2 = (z_2 - z_1)\sqrt{1 + m_1^2} \tag{5.11}$$

To calculate the next section, the process outlined from Eq 5.5 to Eq 5.11 is repeated from the surface of the secondary to the surface of the primary. The calculation of the outgoing slope from the spherical surface does not require solving for the derivative of the surface function since the slope is easily obtained from simply geometric analysis. The slope of the normal line connecting the spherical surface to the center of curvature is:

$$\theta_{norm} = \cos^{-1}(\frac{r_2}{R_{sec}}) \tag{5.12}$$

In these coordinates, the slope and the angle of the incoming ray are related by:

$$\theta_{in} = \cot^{-1}(m_1) \tag{5.13}$$

Since the incoming and outgoing angles with respect to the surface normal must be equal, the difference between the incoming ray and the normal may just be doubled:

$$\theta_{out} = \theta_{norm} - (\theta_{in} - \theta_{norm}) \tag{5.14}$$

and by applying the inverse of Eq. 5.13, the outgoing slope is:

$$m_2 = \cot\left(2\cos^{-1}\left(\frac{r_2}{R_{sec}}\right) - \cot^{-1}(m_1)\right) \tag{5.15}$$

Following the same logic as was used in the computation for Eq 5.10, the ray beginning at (r_2, z_2) on the spherical surface intersects the aspheric surface at the new location (r_3, z_3). Unfortunately, attempting to use the quadratic equation to compute this intersection with the equation of a line and Eq. 5.3 yields no closed form solution. A solution for the new locations can be found if we define the surface of the asphere using the equation of a conic. For convenience we use the semi-major axis:

$$a = 1/(c^2(1+k)) \tag{5.16}$$

and semi-minor axis

$$b = 1/(c\sqrt{1+k}) \tag{5.17}$$

where c and k are the curvature and conic constant of the aspheric surface respectively. Although the interpretation of the semi-major and semi-minor axis is most geometrically relevant for an ellipse, these values are still calculable for all aspheres. In the case of a axially-symmetric ellipsoidal surface, the specific equation for our ellipse offset in one dimension from the origin by a distance equal to the semi-major axis is:

$$\frac{r_3^2}{b^2} + \frac{(z_3 - a)^2}{a^2} = 1 \tag{5.18}$$

Rearranging to solve for r_3 and using the appropriately subscripted version of Eq. 5.7, we get the equality:

$$r_3 = b\sqrt{1 - \frac{(z_3 - a)^2}{a^2}} = m_2(z_3 - z_2) - r_2 \tag{5.19}$$

This equality can be solved in closed form using the quadratic equation. After substantial algebraic manipulation, we obtain the z position at the second interface with the aspheric surface.

$$z_3 = \frac{a(b^2 + az_2m_2^2 - ar_2m_2 - b\sqrt{2az_2m_2^2 + 2z_2r_2m_2 - z_2^2m_2^2 - 2ar_2m_2 + b^2 + r_2^2}}{a^2m_2^2 + b^2} \tag{5.20}$$

The radial position is generated by plugging this value in Eq. 5.19,

$$r_3 = (z_3 - z_2)/m_2 + r_2 \tag{5.21}$$

which allows the pathlength of segment 3 to be expressed in z-positions and the incoming slope:

$$L_3 = (z_3 - z_2)\sqrt{1 + 1/m_2^2} \tag{5.22}$$

Inserting the r_3 values into Eq. 5.2, Eq. 5.3 and Eq. 5.5 gives the outgoing slope at the second interface with the aspheric surface (m_3). The values of the slope for all rays within the resolvable annulus will all be near zero, but will contribute a non-negligible component to the total OPD. The sectional pathlength back to the output coupler ($z_4 = z_0 = z_{ref}$) is then just:

$$L_4 = (z_{ref} - z_3)\sqrt{1 - 1/m_3^2} \tag{5.23}$$

The pathlength outside of the interferometer of all rays in the measurement annulus is the sum of sectional optical pathlengths:

$$L_{ann} = L_1 + L_2 + L_3 + L_4 \tag{5.24}$$

5.2.2.2 Parabolic OPL

The optical pathlength of rays in a system with an ideal axially-aligned paraboloid is far easier to compute. The condition that all rays are entering the system parallel to the conic axis provides two simplifications to the calculation. The first simplification is that all rays passing through the system will have the same pathlength, so the OPL need only be calculated for a single ray. The second is that all rays will pass through the co-located focus of the paraboloid and center of curvature of the sphere. This guarantees that the ray will back-reflect on the same point on the paraboloid. It is important to note that this pathlength must be independently calculated for each annulus which is best-fit with a different paraboloid. By definition, the paraboloid surface matches the ellipsoidal surface at the center of the annulus (circle of conformance), and it is at that circle that the pathlength must be calculated.

We can divide the pathlength of any ray into three sections. The first section L_{p1} is from the output coupler (z_{ref}) to the mirror surface at radial distance r_{ac} and axial distance $z+_{r_{ac}}$ where the origin is defined at the apex of the mirror.

$$L_{p1} = z_{ref} - z_{r_{ac}} \tag{5.25}$$

The next section is from the mirror surface to the center of curvature of the spherical mirror. By definition, the distance from every point on the parabola to the focus (center of curvature of the spherical mirror) is equal in length from the same point on the parabola to a line on the opposite side of the origin called the directrix (see the blue lines in Figure 5.2). To calculate the z-location of the directrix requires knowing two values that define the geometric prescription of the paraboloid, typically the conic constant k and the curvature c. The only information we know about the best-fit parabola is the coordinate location (z, r) of where it matches the ellipse - which is insufficient by

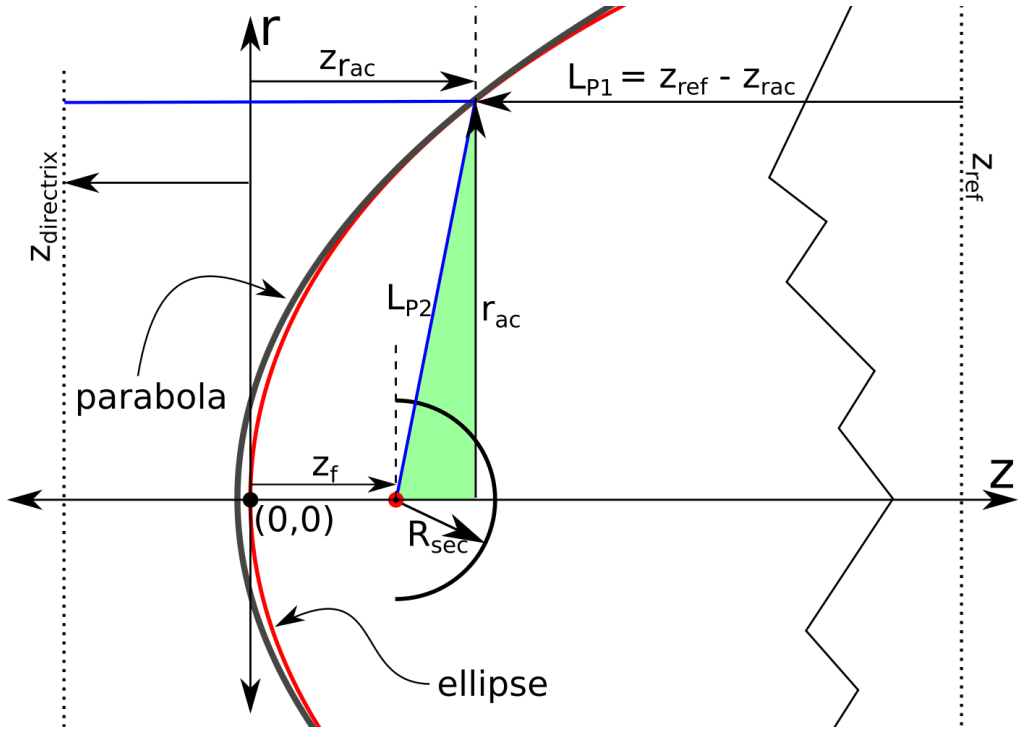

Figure 5.2: The ellipsoidal mirror (red) is matched in the (z, r)-plane at the circle of conformance of a chosen annulus at the coordinates $(z_{r_{ac}}, r_{ac})$. The pathlength of all rays within the annulus equal the pathlength of the ray at this location. The two blue lines are equal length due to the definition of the directrix. The center of the coordinate system is the apex of the ellipse which does not equal the apex of the parabola.

itself to calculate the location of the focus, apex or directrix. Luckily, the location of the focus can be calculated from already known values. The laser beam is oriented along the z-axis and the slope m_1 of the surface at the circle of conformance is defined by Equation 5.6. Using the coordinates on the mirror and the slope of the reflected ray allows us to calculate the location of the focus where the ray crosses the z-axis (at z_f) via the following equation:

$$z_f = z_{r_{ac}} + r_{ac} m_1 \tag{5.26}$$

The length of the hypotenuse L_{p2} of the green triangle in the figure is calculated directly from the coordinates of the focal point $(z_f, 0)$ and the location of (z_{rac}, r_{ac}) of the ray at the circle of conformance.

$$L_{p2} = \sqrt{(z_{r_{ac}} - z_f)^2 + r_{ac}^2} \tag{5.27}$$

By definition, this length is equal to the distance to the directrix, so that for any ray in the same annulus, a change in pathlength from z_{ref} to the surface will be offset exactly by an opposite change in pathlength from the surface to the directrix.

The final pathlength section traversed by a ray is the distance from the focus to the secondary mirror which is just the radius of curvature of the spherical mirror R_{sec}. Since each of these paths are traversed twice for every ray, the parabolic pathlength (L_p) is:

$$L_p = 2\Big[L_{p1} + L_{p2} + R_{sec}\Big] \tag{5.28}$$

$$= 2\Big[z_{ref} - z_{r_{ac}} + \sqrt{(z_{r_{ac}} - z_f)^2 + r_{ac}^2} + R_{sec}\Big] \tag{5.29}$$

Finally, the parabolic-parameterized OPD is the difference between the pathlengths of the ideal tangentially-matched parabola and the ideal aspheric surface.

$$OPD = L_{ann} - L_p \tag{5.30}$$

The OPD is the function that defines the toroidal curvature of the measured annulus and must be removed from the measured data to obtain the wavefront error of the mirror with respect to the ideal aspheric presciption. However, the OPD is somewhat more complex than a linearly separable offset function, and is further affected by complications inherent in annular Fizeau measurements which must be accounted for and are discussed in the following section.

5.2.3 Errors and OPD Completion

The errors and resulting limitations of stitched annular subaperture interferometry using spherical waves to test aspheres has been examined in detail [104, 52]. Two of these errors, namely magnification and retrace errors, are present in paraboloidal parameterization, but have significantly different manifestations due to differences in the optical train and beam geometry. To understand the effects of these errors on our measurement technique, it is useful to illustrate their sources and compare them in both geometries.

Magnification error

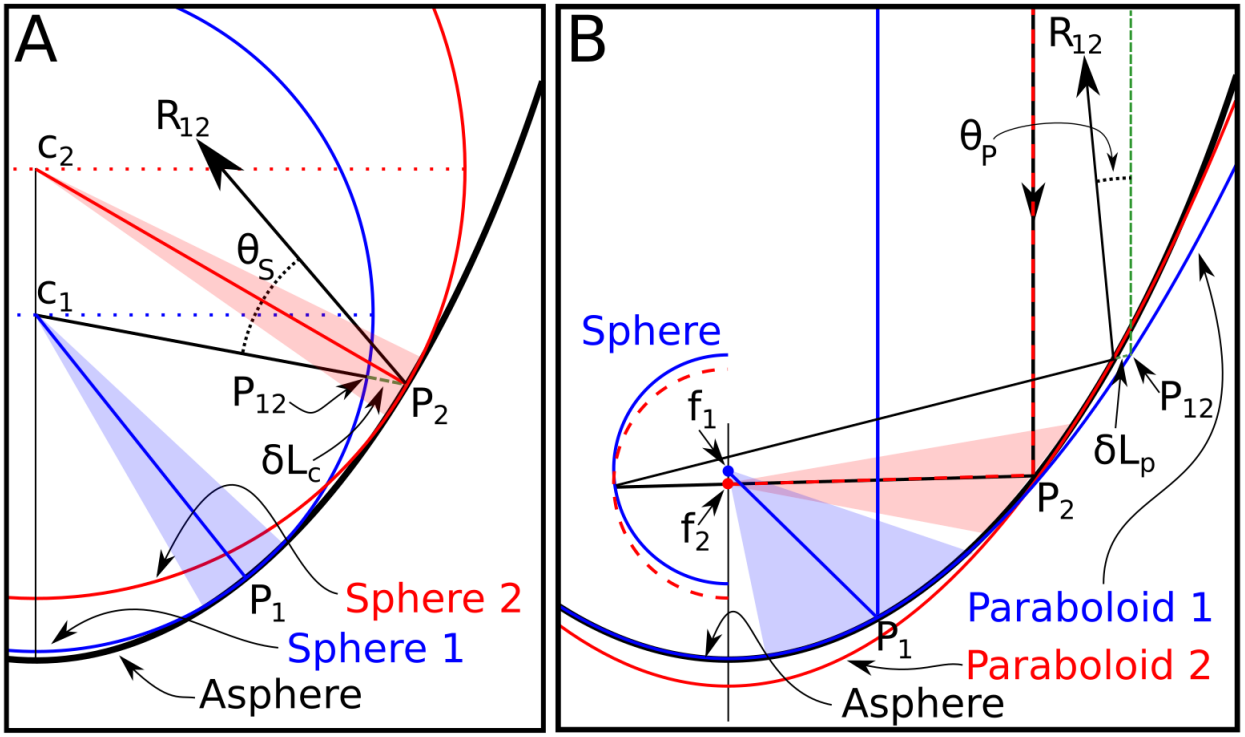

Figure 5.3: Magnification and retrace errors: (A) Standard spherical annular subaperture interferometry models an asphere using closest fit spheres. Sphere 1 (blue) matches the asphere (black) at P_1 and Sphere 2 (red) matches at P_2. Best fit spheres get larger with increased aspheric radial distance, and the centers of those respective spheres c_1 and c_2 increase in distance away from the apex of the asphere. The blue and red shaded areas represent the measurable radial range of the annulus. (B) In paraboloidal parameterization, the asphere is modeled as deviations from the best fit paraboloid. Paraboloid 1 (blue) matches the asphere at location P_1 while Paraboloid 2 (red) matches at location P_2. As the radial distance increases, the focus of the best-fit paraboloid gets closer to the apex of the asphere. The manifestation of magnification error in paraboloidal parameterization is shown by the lateral offset of the input and output beams parallel beams. Retrace errors in paraboloidal parameterization are due to the angular deviation θ_P from the normal.

The fitting of an aspheric surface to spheres and parabolas as well as several illustrative rays are shown in the two panels of Figure 5.3. In panel A, two example spheres centered at c_1 and c_2 on-axis have matching tangents to the asphere at P_1 and P_2 respectively. The light blue and red areas designate the angular range over which annuli of resolvable fringes may be generated with each sphere. In the standard annulus technique, a planar wave in the Fizeau interferometer is converted to a converging spherical wave via the output coupler and the returning wavefront, which is spherical barring the optical surface errors, will be back-converted into a plane wave. As

a result, the distance on the detector from the pixel that images the center of the asphere to other pixels will be a 1:1 map of angle of the diverging spherical test beam, not a scaled mapping of the distance away from the optical axis. The spherical wavefront c_1 will have a ray that extends to the center of annulus-2 ($\overline{C_1P_2}$) and will be reflected about the surface normal defined by the line $\overline{C_2P_2}$ at an angle θ_S away from the ideal spherical wavefront ray $\overline{P_2C_1}$. Since pixels on the detector are 1:1 mappings of return angle, this ray will be mapped to a different detector pixel than the outgoing ray defines. This represents a non-linear magnification away from the annulus center. Magnification errors manifest when attempting to stitch the data from different annuli far away from the center of an annulus. To allow for the unaberrated stitching of successive annuli, the detector mapping of the reflected ray of $\overline{C_1P_2}$ needs to co-locate with $\overline{P_2C_2}$, which cannot happen by definition. In general, when stitching algorithms are applied, the overlapping pixels of successive annuli will be averaged; a process that blindly blends two locations on the mirror and throws away high frequency surface errors.

In paraboloidal parameterization a plane wave reflects from segments of the asphere to the foci [f_1, f_2,...] of the best-fit paraboloids (panel B). Perfectly retro-reflected rays from the spherical mirror co-located with a paraboloidal focus are shown emanating from f_1 and from a shifted sphere from f_2 as solid blue and dashed red rays respectively. In the case that the spherical mirror is co-located with the blue focus f_1, the angular range of the annulus of resolvable fringes is shown as the light blue triangle. However, for illustrative clarity we will inspect a high-departure incoming ray intersecting the asphere at point P_2 that reflects from the sphere towards the second point on the asphere surface P_{12}. This ray will reflect through point R_{12} on its way back to the interferometer at an angle θ_P from normal. We will investigate the effect of the angular deviation in the next section, nevertheless, the ray returning to the interferometer is laterally offset from the original emitted ray position. The radial offsets for our ellipsoidal mirror are illustrated in Figure 5.4. Panel A shows a trace of one incoming (solid red) ray significantly separated from the location of the paraboloidal matching condition and the resulting radially offset reflected ray (dashed red). This offset (panel B) on the surface of the ellipsoid is a function of distance from the circle of conformance (black

vertical line) where the offset is zero for this spherical mirror position.

Unlike in traditional annular testing where the pixels are linearly tied to angle, pixels in paraboloidal parameterization are, to first order, mapped to linearly-scaled x-y locations on the aspheric surface. The good side of this is that annuli may simply be stitched together without concern about magnification distortion. The obvious complication is that every pixel in the 2-D measured wavefront data matrix (w_{meas}) that deviates from the circle of paraboloidal conformance is the summation of the combined real wavefront error of 2 locations (w_i, w_j) on the surface of the asphere (Fig 5.4 panel A) plus the parabolic-parameterizerization-induced toroidal wavefront curvature (OPD_{ij}) derived in Eq. 5.30 :

$$w_{meas(i,j)} = \frac{1}{2}(w_i + w_j) + OPD_{ij} \tag{5.31}$$

The coupled locations on the surface $i = 1, (r_1, z_1)$ and $j = 3, (r_3, z_3)$ were derived in the paraboloidal parameterization equations 5.19,5.20 above.

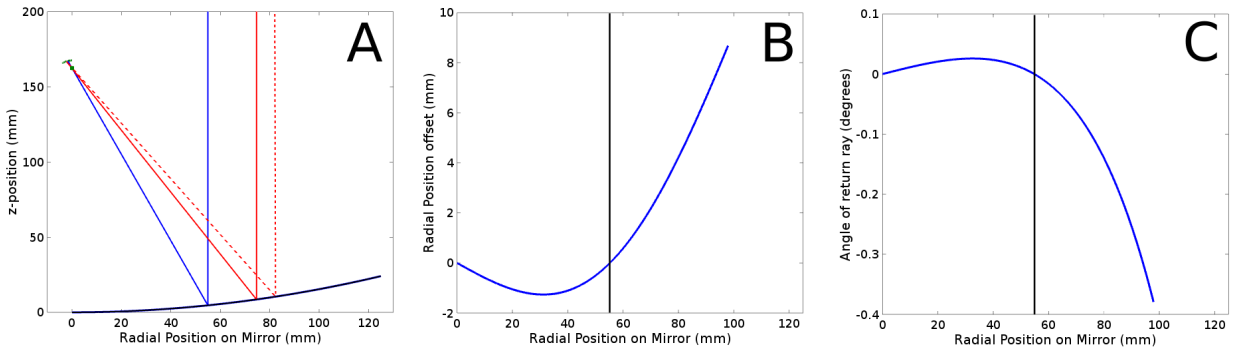

Figure 5.4: (A) - An incoming ray (solid red) reflects off of the asphere (black) at a point far from the parabolic-matching condition (blue). The reflected ray from the spherical mirror (dashed red) intersects the asphere surface at a lateral offset. (B) The lateral offset of every ray incident upon the asphere under paraboloidal parameterization geometry for a chosen axial separation between the mirrors. The black line designates the parabolic-matching radial distance for that separation. (C) The angle θ_p with respect to the test beam of the reflected rays from the asphere after the triple reflection.

At each radial distance from the circle of conformance a ray will adhere to the relationship in Eq. 5.31 but with a unique radial separation between surface reflection points shown in Figure 5.4, panel B. The black line designates the chosen radius of the circle of conformance, while the

blue curve specifies the radial offset of the second reflection point from the initial point. It should be noted that all second reflection points will be farther from the circle of conformance than the original reflection point. The next annulus will have measurements of the surface that overlap with points in the previous annulus (Figure 5.5), but where the initial reflection point of a ray in the second annulus coincides with the second reflection point of a ray in the prior annulus.

$$w_{meas(j,k)} = \frac{1}{2}(w_j + w_k) + OPD_{jk} \tag{5.32}$$

This generates a set of two coupled equations with three unknowns (w_i, w_j, w_k). Solving for the wavefront error at location w_j in terms of the measured and calculated quantities:

$$w_j = 2(w_{meas(i,j)} - OPD_{ij}) - w_i \tag{5.33}$$

$$= 2(w_{meas(j,k)} - OPD_{jk}) - w_k \tag{5.34}$$

This process is repeated for every overlapping set of points within or across annuli of measured data that do not lie upon the circle of conformance. In the generalized case, this provides a set of N measurements with N+1 unknowns. Fortunately, in every annulus of data there exists a subset that contains measurements of points on the surface where the incoming and outgoing rays sample the identical location (along the circle of conformance) and points on the surface that are within the spatial resolution threshold of the interferometric detector. This is illustrated as the green ray in Figure 5.5. In this case we obtain a direct measurement of one point on the surface without coupling in another and where the OPD is zero by definition. With sufficient amount of overlap between successive annuli, this reduces the number of unknowns to N or fewer and the set of linear equations can be solved to give the independent wavefront error at every point within the set of coupled annuli.

Retrace error

Retrace errors are a change in OPL due to the local surface slope with respect to the idealized spherical wavefront and they are responsible for an erroneous change in the measured surface figure [52]. If a surface tilt exists without an increase in surface depth, the initial ray and return

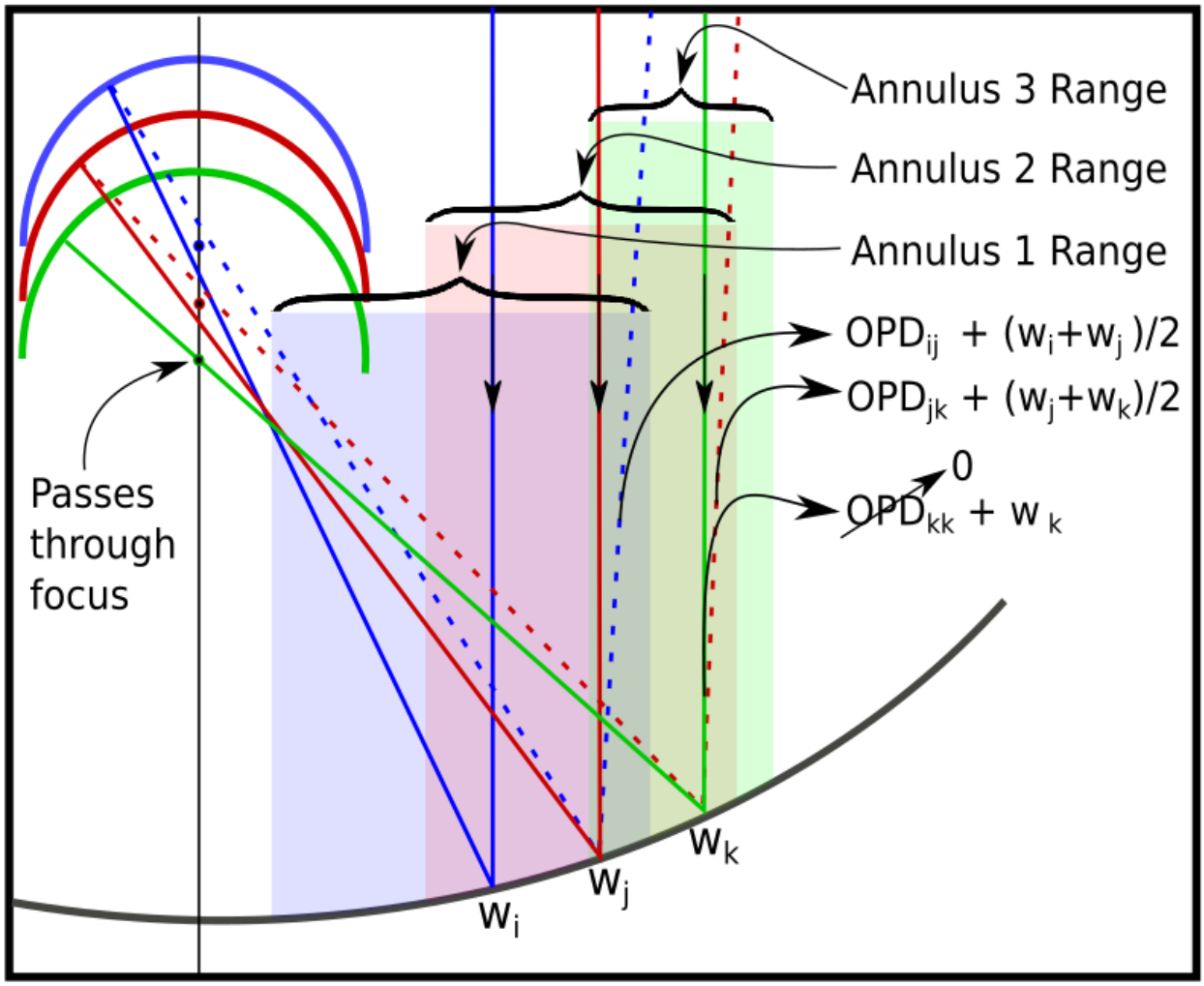

Figure 5.5: Overlapping annuli will contain multiple measurements of a subset of points on the surface of the ashere. The three color shaded rectangles designate the radial limits of three annuli. A ray (solid blue) in Annulus 1 with initial incidence at w_i which does not lie on the circle of conformance will not pass through the focus of the best fit parabola as it reflects from the spherical mirror (blue). This ray will have a second reflection from the aspheric mirror (dotted blue) at w_j that overlaps with the initial incidence of a ray (solid red) in Annulus 2. If the red ray also does not lie on its circle of conformance then after a retro-reflection from the spherical mirror (red) it will reflect from another point on the surface w_k. With sufficient sampling of the aspheric surface, this coupling of measurements across annuli will include rays (green) that do pass through the circle of conformance for their best fit parabola (w_k) where the OPD due to paraboloidal parameterization wavefront curvature is exactly zero.

ray are no longer traveling common path and must therefore measure an OPD. Returning to the standard spherical annulus technique in figure 5.3 panel A, the ray $\overline{C_1P_2}$ intersects the ideal spherical wavefront matching the surface point P_1 at point P_{12}. There is an extra pathlength δL

that constitutes a real component to the OPD. Upon reflection, the ray passes through point R_{12} at angle θ_S and will return to the detector via a different path than the retro-reflected ray $\overline{P_{12}C_1}$. In addition to the simple geometry of the increase in OPD which can be calculated via ray tracing and calibrated out of the system with enough care, there are figure imperfections and misalignments in the internal optics of the Fizeau interferometer which contain much higher spatial frequency errors. In the common-path operation of a nulled optical system these misalignments all cancel.

The paraboloidal parameterization geometry suffers from retrace errors with the same proportion to surface tilt as traditional annulus techniques. In figure 5.3, panel B an incoming ray reflects from point P_2, through f_2 offset from the center of the blue sphere f_1. This line continues on the path toward point P_2 but reflects off of the surface of the mirror and reflects toward R_{12} at an angle θ_p with respect to the test beam. Like with the lateral offset, the angular deviation is a non-linear function of radial distance from the circle of conformance (Figure 5.4 panel C). As in the spherical geometry, there is a contribution to the OPD δL_p that originates from the geometric mis-match. However, just as annuli are much wider in paraboloidal parameterization as the aspheric prescription steepens and the conic constant approaches -1, the angular tilt between the reference wave and the asphere also lessens proportionally, reducing the retrace error phase accumulation. For simplicity, we look at a ray generated from the focus of the blue paraboloid intersecting with the asphere surface far away from the annulus ($\overline{f_1P_2}$). For this ray to be reflected in a parallel path to the illumination beam the ray would have to extend past the asphere surface a distance of δL_p to point P_{12}. In addition to this real contribution to the pathlength difference, the ray reflects at an angle θ_P with respect to the common-path condition. Retrace errors are difficult to alleviate in the standard annular technique, but in paraboloidal parameterization this retrace error only affects the L_4 portion of the OPD, the one relating to the second sampled location on the asphere. Accounting for this angular error in the return beam requires altering Equations 5.30

and 5.31-5.34 to the form:

$$w_{meas(i,j)} = \frac{1}{2}(w_i + w_j) + OPD^*_{jk} \tag{5.35}$$

$$OPD^*_{jk} = L_p - \left(L_1 + L_2 + L_3 + \sec(\theta_p)(z_{ref} - z_3)\sqrt{1 - 1/m_3^2}\right) \tag{5.36}$$

Rather than being an obfuscating error, if it is properly accounted for, this angular dependence on the measured OPD is used to determine the effective OPL between the output coupler of the Fizeau interferometer and the detector (path segment 5 in Figure 5.1). This will be discussed in the Section 5.2.5.

5.2.4 Circle of conformance location and annulus topology

As the difference between two axially-symmetric conic sections, the topology of the annulus of phase error as a function of radius is a 4th order polynomial. However, it is unnecessary to perform a polynomial fit to the measured data to determine the appropriate "radius" of the annulus. It is geometrically fortuitous that the circle at the "bottom" of the trough where the radial derivative of the phase curvature goes to zero is equal to the circle of paraboloidal conformance. A simple geometric analysis shows that an axially-parallel incident ray, which after reflection passes through the center of curvature of the spherical mirror, takes the shortest optical path of all rays hitting the surface. Due to Nyquist limitations of the Fizeau interferometric measurement which cannot calculate phase curvature that surpasses $\lambda/2$ between subsequent pixels, the slowly varying trough of the annulus is the only portion that will be measured and appears quasi-toroidal in shape. A sagittal cross section of one annulus and the calculated curvature using paraboloidal parameterization is shown in Figure 5.6 panel A. The full 2D annulus of raw experimentally measured data with the uncorrected quasi-toroidal phase curvature is shown in false color in Figure 5.6, panel B and the corrected annulus is shown in panel C.

The red region of the curve shows the extent of the measured annular data, the blue curve is the calculated OPD via the parabolic parameterization, and the black line designates the circle of conformance. In order to calculate the location of the annulus to subpixel accuracy, the separation

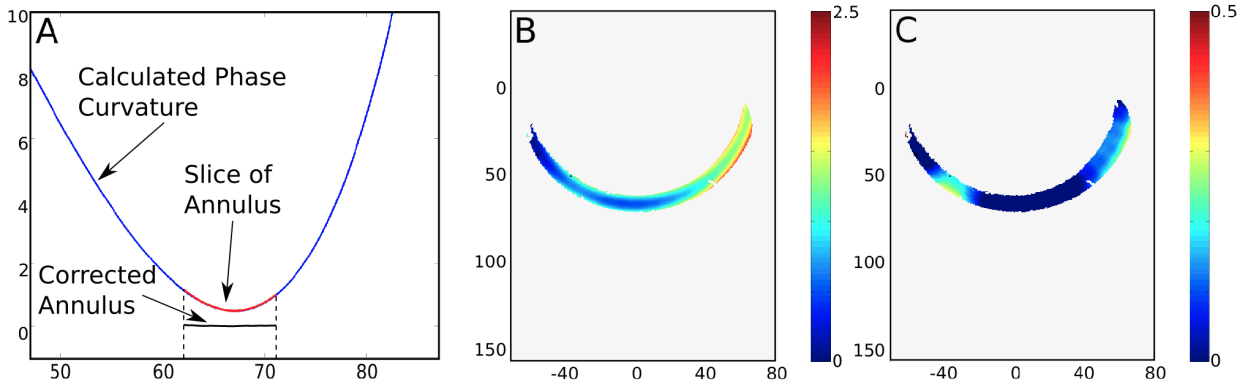

Figure 5.6: (A) A sagittal cross section of the annulus (red) overlays the calculated OPD (blue). Subtracting the two gives the phase flattened data (black). (B) The full annulus of raw data showing the quasi-toroidal phase curvature and tilt up to 2.5 λ. (C) The annulus of phase flattened data showing a maximum variation across the annulus of 0.3 λ.

between the aspheric and spherical mirrors must be known to micron precision. Fortunately, the separation between each successive measurement of the mirror need not be directly measured with this level of precision (although it provides a useful reality check) since the ideal conic prescription values provide the appropriately delicate mathematical lever arm to determine these positions and accurately calculate the annular phase curvature. In the case where the conic parameters are assumed and the radii of the annuli are measured, the locations of the focus are uniquely determined without measuring the z-step between data acquisitions (as in Figure 5.7 panel A).

5.2.5 OPD completion

Up to this point, the discussion of the calculation of the phase curvature of the measured annuli has been limited to the OPD outside of the Fizeau interferometer (segments 1-4 defined in Figure 5.1). From Eq. 5.36, it has been shown that all rays other than those lying on the circle of conformance will have an angle with respect to the test beam which must result in a contribution to the total OPD that is a function of distance to the detector. In terms relevant to the experiment, if the beam has a return angle at the output coupler, the optical invariant demands that it have non-zero angle on the inside of the interferometer. However, the operating principle of the Fizeau interferometer demands that regardless of the transfer optics, a plane wave at the

output coupler is a plane wave at the detector. This allows us to simplify all of the OPL inside the interferometer into an equivalent OPL that is just tracing the rays some extra unknown distance on their trajectories at the output coupler. Once this distance is determined, it is used for all paraboloidal parameterization calculations of annuli.

The OPL of segment 5 is responsible for a non-negligible portion of the phase curvature of the annulus. The simplest method to measure this equivalent pathlength is to use a mirror of known prescription and to set the OPL of section 5 to the value necessary to null the fringe curvature. In the experimental mirror surface reconstructions, the equivalent pathlength inside the WYCO 6000 was slightly less than 3.5 meters. This length is then added to the distance to z_{ref} in Eq. 5.36. Once this OPL is found, it applies for all future paraboloidal parameterization measurements. The curvature of an annulus is then a unique function of only the aspheric prescription and can be used to determine the conic constant and radius of curvature of a mirror.

5.2.6 Blind aspheric prescription determination

Accurate phase-flattening of annuli requires matching the calculated phase curvature from the paraboloidal parameterization to the measured phase curvature of the interferometric data. This is predicated upon accurate knowledge (or an assumption) of the conic constant and radius of curvature of the asphere, the pixel mapping of the optical axis onto the interferometric detector, and to a lesser extent, the z-translation between each of the successive interferometric measurements. It turns out that the precision of the values from which the technique benefits the most are the spatial-pixel mapping to the detector (x-y offsets and scaling), and the measured OPD. With these quantities known to high precision, the mirror form can be tested against any arbitrary ideal aspheric prescription, but it is also possible to determine the aspheric parameters without prior knowledge.

During the testing procedure it is beneficial to precisely measure and record the change in the separation of the mirrors between successive interferometric measurements. Although not linearly dependent, these values are related to the location of the focus of the best-fit paraboloid for every

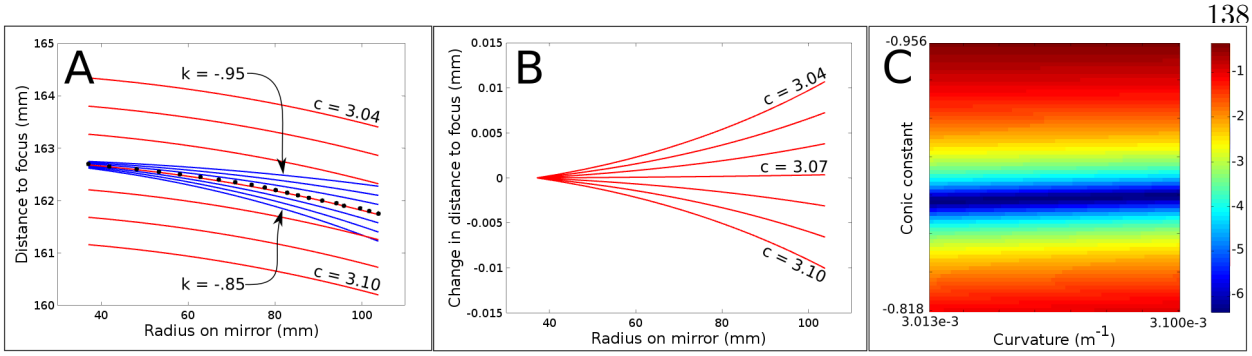

Figure 5.7: (A) The measured values of the radius of the annulus and the δz values between annular measurements are shown as black dots. The entire set is shifted in z by a single offset value to bring it into range of the expected z-values of the focal points. The blue lines show the family of curves due to changes in conic constant k while the red lines show different values of curavture c. (B) The red curves from the previous plot after subtracting the curvature and offset of the center red line. This shows that the red curves are changing shape as well as z-position. (C) A subset of the 2-D solution space of linear least-squares fitting of the measured curve to theoretical curves over the k-c ranges shown (logarithmic scale).

annulus. By coupling Δz values with the k and c of the ideal mirror using Eq. 5.5 - 5.10, a plot of focal distance vs radial position of the center of the annulus can be generated (Figure 5.7 panel A). The black dots are the measured radial locations and have the recorded δz beween measurements plus a single offset to match the theoretical z-values from the k-c mirror prescription (the red line directly below the black dots). This shows the surface of the tested ellipsoidal mirror matches the expected aspheric prescription very well.

In the case where a mirror of unknown conic constant and radius of curvature is tested, the aspheric prescription can be determined using paraboloidal parameterization. A series of annuli spanning the full aperture of the mirror is collected. The annular centers and the z-step between interferometric measurements are extracted and produce a plot just as would be the case if the prescription is known, but without the absolute offset necessary to define a unique conic prescription. The foci separations as a function of radial position on the mirror is an equivalent expression of the 1:1 functional relationship between conic constant and radius of curvature of the mirror. In short, the curve consisting of the radial distance vs the change in focus (black dots in Figure 5.7) uniquely defines both the conic constant k and the curvature c. As the radius of curvature increases, the

Step Number	Algorithmic step
1	Designate a k and c of expected mirror prescription to test against
2	Calculate the center pixel and radius of the annulus on detector plane
3	Convert from pixels to mm using detector scaling factor
4	Using k and c calculate expected 3D annular curvature
5	Convert from mm to pixels
6	Subtract calculated curvature from annular data plane
7	Step through annuli and subtract sequential piston (tip/tilt) error
8	Weight annuli as distance from circle of conformance
9	Add annuli together according to weighting function

Table 5.1: The simple stitching algorithm used for the reconstruction in Figure 5.8. The annuli are flattened and added together using a normalized weighting function based on the distance from the circle of conformance.

conic constant becomes more negative and the absolute offset increases. The blue lines show the family of curves resulting from small changes in k, while the red lines are the family of curves when c is changed. The red lines are not identical curves offset in z however, Figure 5.7 panel B plots the relative change between them. The entire solution space is continuous and contains no local minima and is illustrated in panel C. The function changes rapidly with c and slowly with k, but there exists a global minimum at a single aspheric prescription that is easily found using parabolic interpolation minimation or other minimization algorithms. One of the most important advantages of paraboloidal parameterization is that there is no need to colocate the center of curvature of the mirror with the focus of a converging wave - a particularly onerous requirement if the prescription is unknown. Aspheres are measured at any convenient distance from the interferometer that accommodates a sufficient separation betyween the test mirror and the spherical mirror.

5.2.7 Mirror figure reconstructions

The simplest algorithm used to generate a surface reconstruction from paraboloidal parameterization data is described in Table 5.1. The paraboloidal parameterization technique computes the mirror surface morphology difference from a chosen geometric (aspheric or spherical) surface defined by a conic constant and curvature at the beginning of data processing. There are nine conceptual steps to the simplest algorithm. 1. Select the k and c values to evaluate against. 2.

Using a standard circle-fitting algorithm, the center of the annulus and the radius of the circle of conformance is found in pixel space on each data plane. 3. These pixel locations and lengths are converted into millimeters by applying a previously measured scaling factor of the image on the detector plane (mm/pixel). 4. The curvature of the annulus is calculated according to the equations derived in Sections 5.2.2.1 and 5.2.2.2. 5. This derived ideal curvature of the annuli is scaled back into detector pixel space. 6. The curvature is then subtracted from the raw annuli to produce paraboloidal parameterized annuli that have the toroidal curvature removed but retain the morphology due to mirror surface deformation (Figure 5.8 Panel B). 7. Once these annuli are flattened, they retain some arbitrary relative piston offset and possible tip-tilt offset depending upon the diligence and accuracy of the operator during data collection. All annuli are piston-corrected to one chosen annulus. Using pixels containing surface values in both of the two adjacent data planes, the piston error and possible tip/tilt are computed and applied to the entire data plane before advancing to the subsequent annulus. 8. Before stitching these annuli together, it is important to note that the quality of the data varies as a function of distance from the circle of conformance due to increasing retrace error. In order to select the highest quality data in the reconstruction, I generate a spatial weighting function for each annulus that is 1 at the circle of conformance and decreases linearly with distance. Pixels with values from multiple data planes are multiplied by their plane-dependent weighting factor, summed across all planes and then divided by the summation of all weighting factors used. A cross section of 13 stitched annuli is shown in Panel C of Figure 5.8 and the entire reconstructed quandrant in Panel D. Holes in the surface data (black pixels in Panel D) are the result of surface damage on the spherical mirror.

I used paraboloidal parameterization to measure the surface of the 250 mm diameter ellipsoidal primary mirror with conic constant ($k = -0.8778$) and curvature ($c = 3.07m^{-1}$) described in Chapter 4. It has a spherical departure of more than 3000 waves over the full aperture. The mirror diameter was too large to collect as a single data set, so the measurements of the surface were collected in 4 quadrants at every 90 degrees with 25 annuli per quadrant. One quadrant of the surface figure reconstruction of the ellipsoidal mirror is shown in Panel D of Figure 5.8. Although

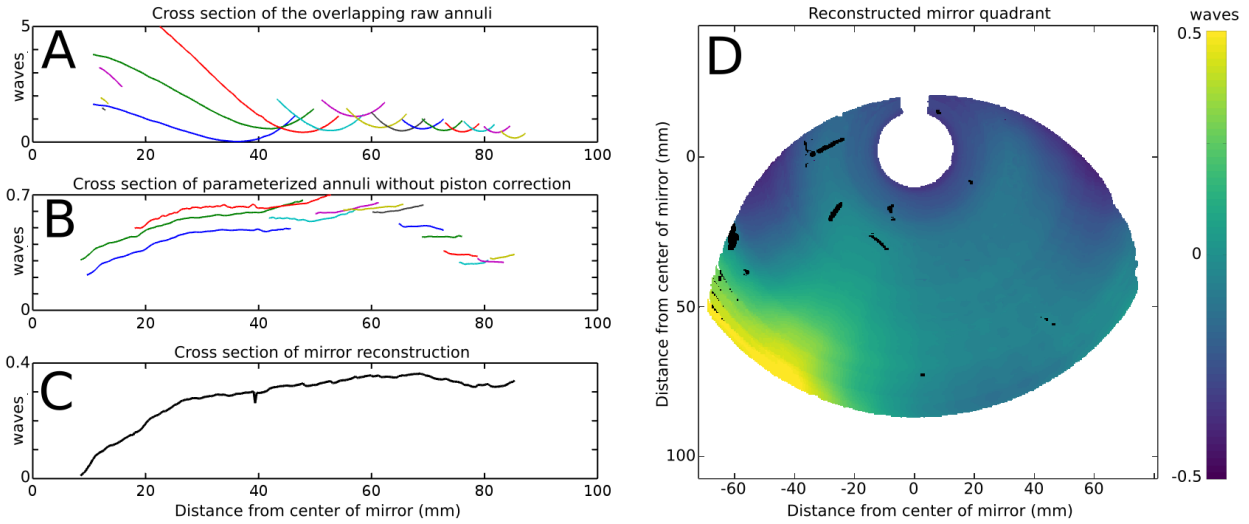

Figure 5.8: The paraboloidal parameterization interferometric measurements and data products of one quadrant of the ellipsoidal mirror with conic constant ($k = -0.8778$) and curvature ($c = 3.07m^{-1}$). A. A cross section through the raw annuli collected showing the annular toroidal shape before paraboloidal parameterization. The larger annuli show several waves of curvature from the center to the edge. B. The same cross sections after parameterization. No piston offset between the annuli has been applied. The slopes are now due to evolution of the surface of the mirror. C. The cross section of the reconstructed mirror using the annuli from (B). The total mirror shape evolution over 13 annuli spanning 75 mm is less than 0.4 waves. D. One quadrant of the mirror reconstructed using the parameterized annuli. Variation over the measured area is less than 1 wave peak to trough.

I collected 25 annuli per mirror quadrant, only the first 13 consecutive annuli were usable for this reconstructed quadrant. In order to calculate the tip/tilt and piston error between annuli, there must be a sufficient number of pixels that contain data in both annuli. During the measurement of the mirror, I moved the primary mirror too far in the axis to contain overlapping pixels between the 13th and 14th annulus. The map shows the dominant error is trefoil mirror deformation due to stresses induced by the three back-mounting bolts and a small amount of turn-down (darker blue) in the center. Over this quadrant the mirror far exceeds the required specifications of less than $\lambda/4$ over 1 cm aperture since this measured a maximum variation of less than one wave across this 100 x 150 mm. This reconstruction used the simplest algorithm (from Table 5.1) and didn't attempt to solve the linear equations to decouple the OPD measurements from multiple locations on the surface of the ellipse across multiple annuli. I calculated the error between measurements of annuli

after correcting for piston and tip/tilt offsets. I measured the difference for every pixel in each independent annulus from the reconstructed quandrant data which used weighted pixel averages. Only pixels co-existing in multiple annuli were calculated since those in only one annulus would have a zero error by definition. The standard deviation of the wavefront error was 0.04 waves for all of the overlapping pixels in this quadrant. Unfortunately, I think this is a rather deceiving analysis. It would be better to compute the mean error for every annulus as a function of radial distance away from the circle of conformance, or even better as a function of the waves of toroidal curvature due to the paraboloidal parameterization. Future work will include this analysis, a comparson to another measurement technique and implementing the solution of the coupled linear equations.

5.3 Full System Double Pass Optical Test

To simultaneously test the full surface of the primary mirror entails installing both the ellipsoidal and paraboloidal mirrors mounted into the optomechanical structure. In place of the collimated output coupler on the WYCO, I used a converging lens pass through focus to generate an expanding spherical wave. By using two 6-inch aperture flat folding mirrors placed at opposite sides of a 10-ft optical table I folded a five meter pathlength onto a single floating surface. I mounted the opto-mechanical assembly onto the adjustible rail in order to adjust the relative position of the assembly to the WYCO so that the conicoidal focus of the mirrors could be precisely located at a 5 meter distance from the focus generated by the WYCO output coupler. The laser light leaves the WYCO, is focused at a distance of 25 cm and expands in a cone of light. A central portion of the expanding beam is reflected by the first folding mirror toward the second folding mirror. Again, a small portion of the expanding beam is reflected toward the optomechanical assembly where it reflects from the primary mirror. When the optomechanical assembly is precisely aligned, the laser light is focused exactly toward the conicoidal focus, reflects from the paraboloidal secondary as a perfectly collimated beam pointing toward the central hole of the primary mirror. I placed a 1-inch flat mirror on the far side of the primary and aligned it to back-reflect the collimated light through the optical assembly and folding mirrors to the WYCO where it meets the output/input coupler

as a spherically expanding beam that is converted into a collimated beam inside the WYCO. This reflected beam has a much smaller lateral extent than the test beam due to the unreflected lost light at each of the folding mirrors and must be zoomed in on the detector to maximize the number of pixels used during measurement. The data collected from this experiment are shown in Figure 5.9.

The surface error measured by the phase-shifting interferometry must be halved to account for the double-pass in the optical test geometry. This technique suffers from the fact that it is also a measurement not just of the mirror, but of the optical alignment of the two mirrors in the set. As a result, this test contains a large number of variables of freedom and it is impossible to determine whether small errors in the bulk location of the opto-mechanical assembly are being compensated for with small axial mis-alignments of the secondary mirror with respect to the primary (as I described in the zoom ability in Chapter 4). All that can be said with absolute certainty is the total mirror evolution along a single radial value. Looking at the figure, it is clear that the full system measurement shows fast evolution with radius totaling nearly 1.5 waves near the central obscuration. This surface form error isn't visible in the paraboloidal parameterization quadrant shown in Figure 5.8, which suggests that the secondary mirror was placed in a non-conicoidal position and the computed error of the reconstructed surface contains a mixture of mirror form error and system geometry error.

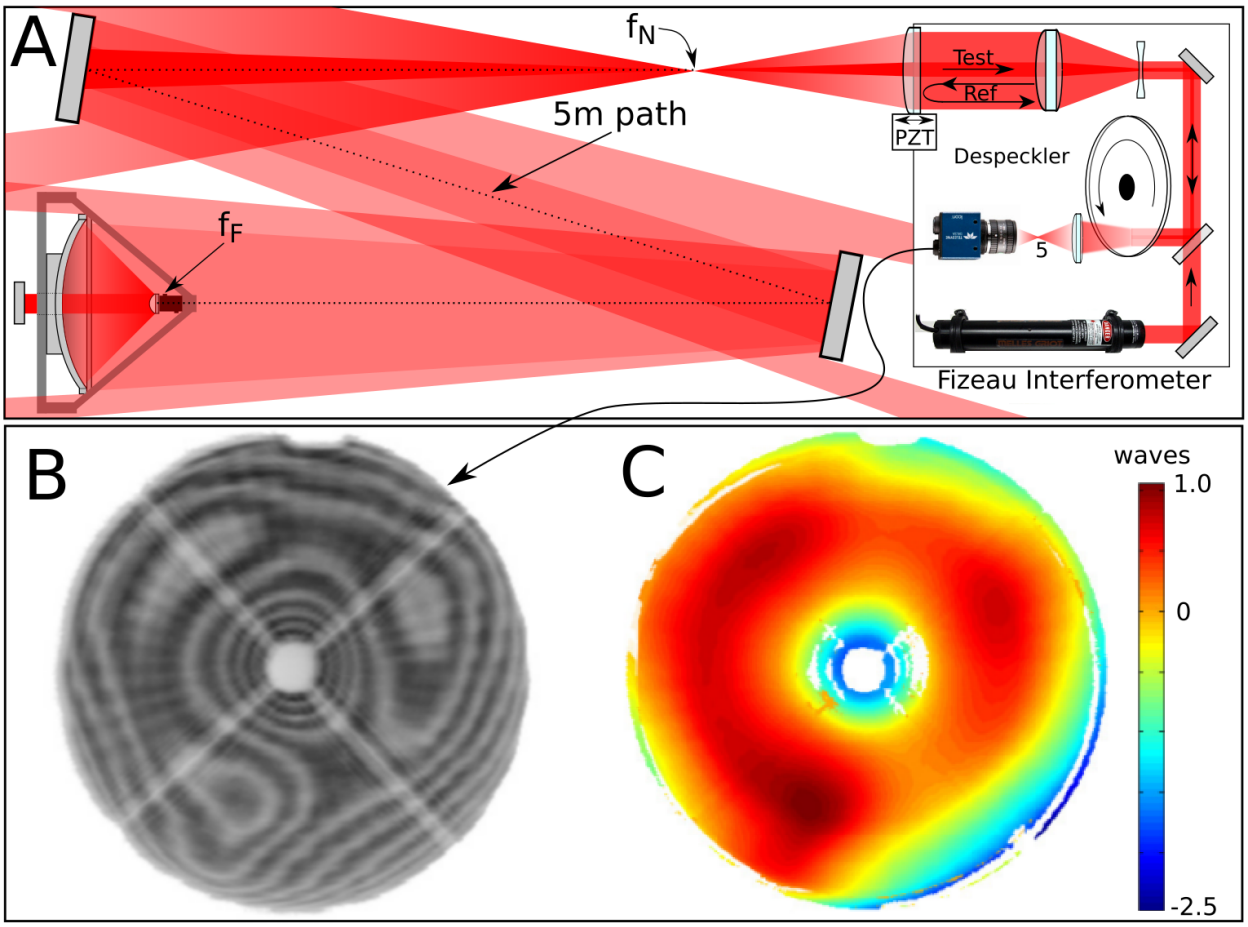

Figure 5.9: A) The measurement scheme of the full aperture of the two-mirror optical assembly using a double pass geometry. From the output coupler, a converging beam passes through focus and expands. Two flat mirrors fold the optical path but also angularly limit the cone of light so that only a central portion reaches the ellipsoidal mirror. The separation between the focus near the WYCO f_N and the focus far from the WYCO f_F is 5 meters matching the ellipsodial prescription. The beam then converges towards the focus and reflects off of the paraboloidal secondary mirror as a collimated beam which is retro-reflected down the entire system using a flat mirror behind the optical assembly. B) The instantaneous interferogram as imaged in the WYCO. C) The measured surface error of the double pass system shows a maximum surface error of 1.5 waves. The evolution of the surface error in the radial direction is likely the result of mis-alignments between the primary and secondary mirrors and the visible trefoil deformations are due to the mirror mounting bolts.

Chapter 6

Remote Microscope Laboratory Experiment

I use the schematic of the principal experimental setup as shown in figure 6.1 as the visual guide for my detailed description of the relevant optical, electrical and physical characteristics of the remote microscopy implementation. For clarity, the system is most efficaciously described by breaking it into the following six conceptual blocks; the Laser Source, Acousto-Optic Pattern Generator, Relay Optics, Remote-Microscope Optical Assembly, Control Electronics, and Data Acquisition and Analysis. The most natural narrative progression of the system operation is accomplished by following the laser light through the system.

I begin at the laser source in the bottom right hand corner of the figure. The laser beam is conditioned and directed toward the entrance pupil of the acousto-optic pattern generator (AOPG) which amplitude-subdivides the input beam and diffracts a MxN 2D array of beams that pass through the exit aperture. This 2D set of beams is transferred to the remote microscope optical assembly (RMOA) via a set of relay optics which re-image the exit aperture of the AOPD to the input aperture of the RMOA. The remote microscope projector redirects the beams to overlap at the target and collects the resulting scattered light, redirecting it back through the optical train. A polarizing beam splitter sends the back-reflected light to the avalanche photodiode detector and the signal is collected by a digitizer and stored for processing and image reconstruction. In the following sections, I delve into the details of each subgroup.

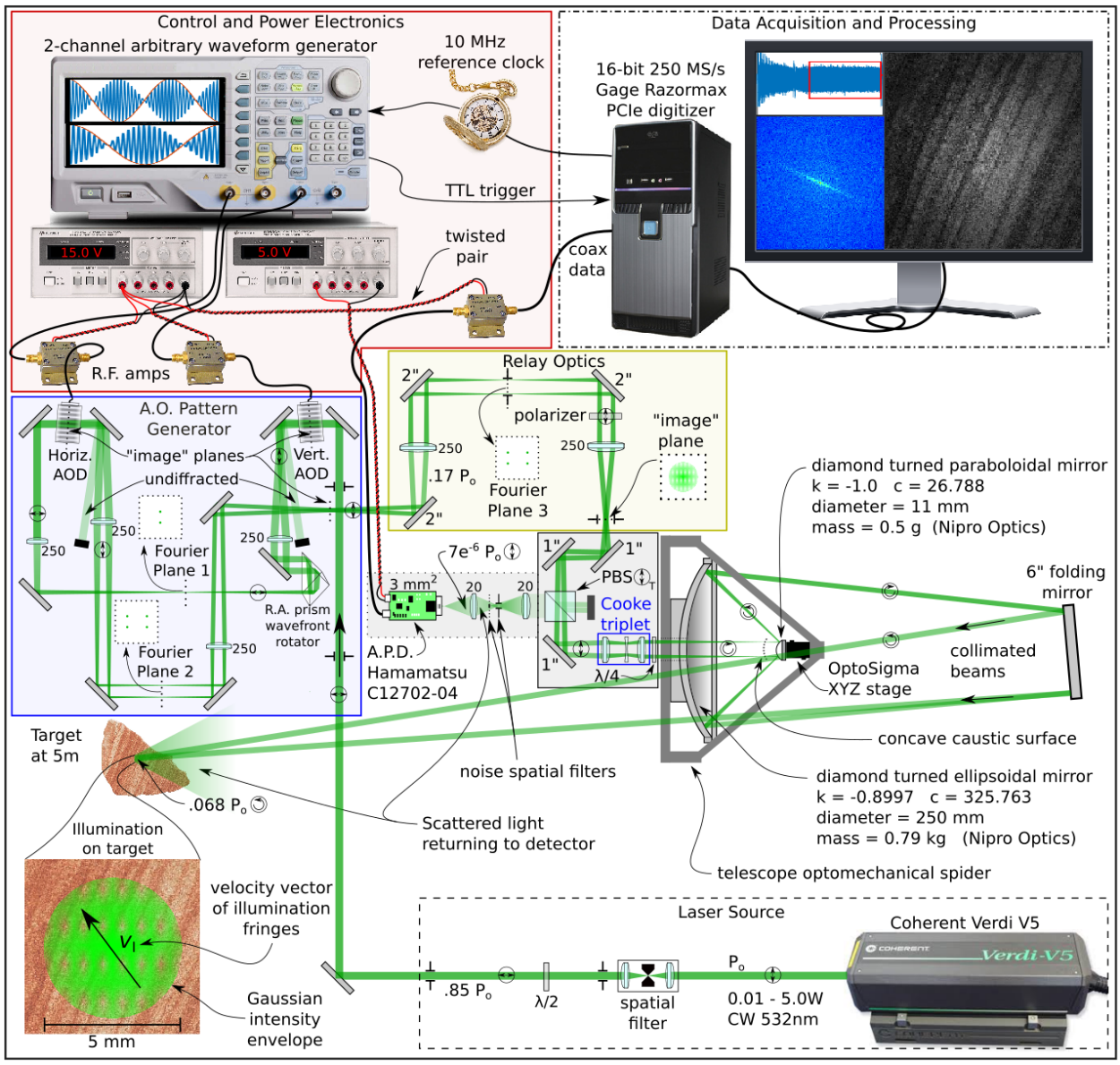

Figure 6.1: The laboratory experimental setup of the $\mathcal{F}$-BASIS remote microscope. A laser is amplitude-divided into multiple, symmetric pairs of Doppler-shifted and spatially diffracted by the acousto-optic pattern generator. The multiple pairs of beams of roughly equal amplitude are directed by the microscope optical projection assembly onto the target where they recombine to generate the traveling interference fringes. A portion of the scattered or specularly reflected light is collected by the same optical assembly and spatially integrated on an avalance photodiode. The experiment is described according to the six subgroups designated in the figure: the Laser Source, AOPG, Relay Optics, Remote-Microscope Optical Assembly, Control Electronics, and Data Acquisition and Analysis.

6.1 Laser Source Group

During the experimentation and development effort, I used two commercial laboratory laser sources in the optics-table implementation of the remote microscope: a low-power Coherent Compass and the Coherent Verdi V5 for high power and variable fluence experiments. It is tempting to naively claim that all that is needed is a TEM00, single longitudinal mode CW laser source with the appropriate amount of optical power to achieve a desired SNR for $\mathcal{F}$-BASIS remote microscopy, but the reality is that both of these lasers have operational trade-offs and failure modes that are worth calling out since they are subtle, difficult to detect and diagnose, and catastrophic for Fourier synthesis.

The Coherent Compass C315M-100 produces 100 mW of CW 532 nm laser light in a very compact laser head package ($8 \times 4 \times 3$ cm). The small form factor, modest electrical power requirements (< 25 W), and stable beam operation make this laser an attractive solution for a portable laser source for the remote microscope instrument. It uses a neodymium doped yttrium aluminum garnet (Nd:YAG) gain medium to produce a 1064 nm fundamental wavelength and a potassium titanyl phosphate $KTiOPO_4$ (KTP) crystal for second harmonic generation (532 nm) in a Fabry-Perot linear cavity configuration [3]. The laser is powered by a small controller box which performs an enigmatic, undocumented and wholely mysterious 5-minute-long start up and temperature/lasing stabilization procedure, during which, the laser slowly ramps up the optical power of the beam, but also evolves in wavelength following a ramping sawtooth function. Ideally, after warm-up, the laser emits a low-divergence (< 3 mrad) nearly circular, TEM00 (Gaussian) beam with long-term optical power stable to $< \pm 5\%$. Unfortunately, this laser has two character flaws that make it unsuitable for a wide range of $\mathcal{F}$-BASIS remote microscopy targets. The first is the low optical power. I'll provide details regarding the optical power losses through the components of the experiment in Section 6.11, but suffice to say that for most scattering surfaces, the required optical power for meaningful remote microscopy reconstructions far exceeds the 100 mW provided by the Coherent Compass laser. The second flaw of the C315M is an unstable operational mode where the

laser control module seems to spontaneously get caught in the wavelength and power oscillation cycle long after the completion of the warm-up procedure. The oscillation of both the power and wavelength follows the sawtooth waveform and is surprisingly subtle making it difficult to notice by casual inspection until long after time has been wasted collecting useless data. The only solution I found to eliminate this oscillation was to power cycle the laser and hope. Unfortunately, I was unable to find a root cause, but lowering the emitted optical power via the flathead-screw potentiometer on the laser controller seems to lower the odds of the onset of the oscillation failure mode. In a few locations within the remote microscope experiment optical elements generate unintended low-angle interferometers easily observed by the user. I used these serendipitous interference fringes to look for oscillations during the laser failure mode and attempt to address it. I found that these interferometers were the easiest method to monitor the laser stability. Fundamentally, however, the primary reason I chose to abandon the Compass was due to optical power limitations wherein I upgraded the laser source to the Verdi V5.

The majority of the successful experiments performed with the remote microscope used the Coherent Verdi V5 laser [2], which can be considered a larger, more powerful Compass. It is much larger with a laser head ($10 \times 14 \times 46$ cm) connected to the controller ($23 \times 45 \times 50$ cm) via a beefy umbilical, requires water cooling, and consumes up to 700 W of electical power. Instead of a Nd:YAG, the Verdi uses a diode pumped neodymium-doped yttrium orthovanadate ($Nd:YVO_4$) medium and a Type I, non-critically phase-matched Lithium triborate (LBO) crystal for second harmonic generation to get to 532 nm. The Verdi employs a single frequency ring cavity design with an etalon as a guarantee of single frequency operation. As with all ring cavities, bi-directional operation is possible, the Verdi cavity incorporates an optical diode to force unidirection operation. Thermoelectric heaters/coolers regulate the temperature of the vanadate and etalon and must be slowly ramped to operational temperature during the warm up procedure which can take more than 30 minutes. The LBO crystal temperature is regulated with a resistive heater and must reach a temperature of nearly 150 °C, while the optical bench inside the laser head must reach 55 C. Once lasing has been established, the system runs in one direction at a single longitudinal mode

with vertical linear polarization (100:1). The beam divergence is less than 0.5 mrad, the M^2 (a standard measure of the quality of the beam) is less than 1.1 and the beam pointing stability is claimed to be $< 2\mu rad/^{\circ}C$.

A major benefit of Verdi is the control of the optical power output from 0.01 - 5.0 W in 10 mW increments via a manual control knob on the power supply. The upper range of this optical power is needed to compensate for the span of reflectivities of objects and the low percentage of optical power that is collected as scattered light. In the case of specularly reflecting materials, the total optical power returned to the detector can be nearly 15% of the transmitted light, while the most challenging remote microscopy experimental conditions of scattering targets with low reflectivity result in throughput efficiencies as low as 10^{-8}. In Section 6.11, I quantify the measured laser power, sources of losses and polarization state at each major component group, but suffice to say that every photon counts, and the Verdi provides a substantial power increase over the Compass.

Unfortunately, the failure mode of the Verdi is even more crippling than that of the Compass. The manufacturer-suggested operational procedure for the Verdi directs the user to place the Verdi into "standby mode" wherein the LBO crystal and optical bench remain heated, but the diodes are not flashing. The laser can nominally stay in standby indefinitely without damage, but there are unadvertised rare failures of the control circuitry in some of the models of the Verdi. During long periods of remaining in standby mode, the temperature control circuitry can destabilize after which the only recourse is to power cycle the laser. The destabilization of the Verdi is only manifested during active lasing where the output power oscillates according to the curve shown in Figure 6.2. The oscillation cycle is on the kilohertz time scale and so is too fast for a human to see, but it produces extreme amplitude oscillations in the collected sinusoidal waveforms. In addition, the time scale of the oscillation is linearly dependent on the output power of the Verdi, where higher powers yield faster oscillations up to approximately 10 kHz. The only method I found to eliminate the failure mode oscillation is to power cycle the laser system. This entails slowly cooling down the LBO crystal to below 40 C which can take up to 40 minutes, after which the main power to the laser must be turned off and back on. The laser must then go through the entire warm up cycle

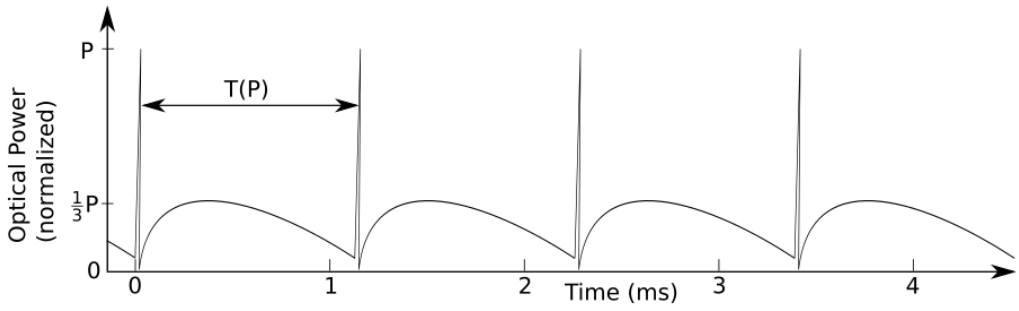

Figure 6.2: The Coherent Verdi V5 failure mode induces a ms-time scale (T) oscillation that is a function of the output power (P). Each cycle begins with a spike up to the set power of the laser followed by a sharp drop to zero and then a long curve that reaches a maximum of P/3 before collapsing back to near zero. Power measurements were taken using a fast photodiode directly after the laser output shutter.

for the LBO which takes another half hour or so. In addition to the time lost to power cycling the laser, there is an additional risk to power cycling. A small number of the Verdi lasers produced by Coherent have exhibited a catastrophic failure wherein power cycling the laser will cause it to lose all firmware and calibration settings, necessitating sending the laser head and power supply back to Coherent for an expensive complete calibration refurbishing. So, in short, the laser can spontaneously degrade and the solution has the possible side effect of rendering the laser dead.

To first order, the laser beams of both the Compass and the Verdi are well-behaved with clean Gaussian intensity distributions, however to generate as clean of fringes as possible in the AOPG, it is necessary to remove residual high spatial frequency residues in the beam profile and remove all non-vertical polarization. To condition the beam, the laser source is directed through a vertical linear polarizer and a standard laboratory spatial filter. The collimated TEM00 linearly polarized beam is polarization rotated using a halfwave plate to obtain horizontal linear polarization to be compatible with the first AOD of the AOPG which is discussed in the next section.

6.2 Acousto-Optic Pattern Generator

I introduced the pattern generator in Chapter 1, but now I'll revisit the description to include output power, polarization and details concerning the Fourier planes that are relevant to the remote

microscope experimental setup. The active optical element upon which the technology of the AOPG depends is the acousto-optic deflector. The physics of AODs is far more involved than I have time to present here, but I would direct the reader to see any of the excellent and thorough publications on acousto-optics, e.g. [13]. A basic and practical description of the function of the AOD is shown in Figure 6.3. The piezo-electric transducer mounted to the AOD with center frequency of 80 MHz is driven by two RF tones $f_1 = 78.5$ MHz and $f_2 = 81.5$ MHz. These generate a beat frequency of 3.0 MHz, which is expressed in the TeO_2 as a traveling sinusoidal power modulation of the acoustic shear-wave centered at 80 MHz. The spatial period of this sound wave (Λ) is equal to the acoustic velocity $c_A = 617$ m/s divided by the beat frequency f_b. When a collimated beam of light is directed through the AOD at the Bragg angle, a portion of the intensity of the beam is diffracted by the traveling volumetric holographic grating. The angle of deflection of the beam of light is easily calculated using the geometric k-space representation of wave vectors of the incident light beam, acoustic grating and the deflected ray. The undiffracted light is treated as waste and represents a significant portion of the optical losses in the projection function of the remote microscope.

The AOPG consists of a 4-f imaging system that places the AODs into conjugate "object" planes to doubly diffract the laser beams in orthogonal axes with no axial spatial offset. In other words, the beams are diffracted in two-dimensions in such as way that the principal rays of all the collimated beams intersect the optical axis at the same axial point. I place "object" and "image" in quotes because a real image isn't actually formed due to the fact that the beams are collimated at the planes of overlap, although a 1:1, 2D spatial mapping is perserved amongst "image" planes. The laser enters the AOPG (outlined box in Figure 6.4) as a single Gaussian beam with horizontal linear polarization. It passes through the first AOD (denoted as the "vertical" AOD for reasons that will become clear shortly), which diffracts a portion of the amplitude of the single beam into multiple positive 1st order beams that are switched to vertical polarization and angularly dispersed in the horizontal plane. The zeroth order beam of undiffracted light is directed into a beam dump. The positive first diffracted order beams for each RF tone driving the AOD are focused (Fourier transformed) by the first F = 250 mm lens. These horizontally dispersed beams are then spatially

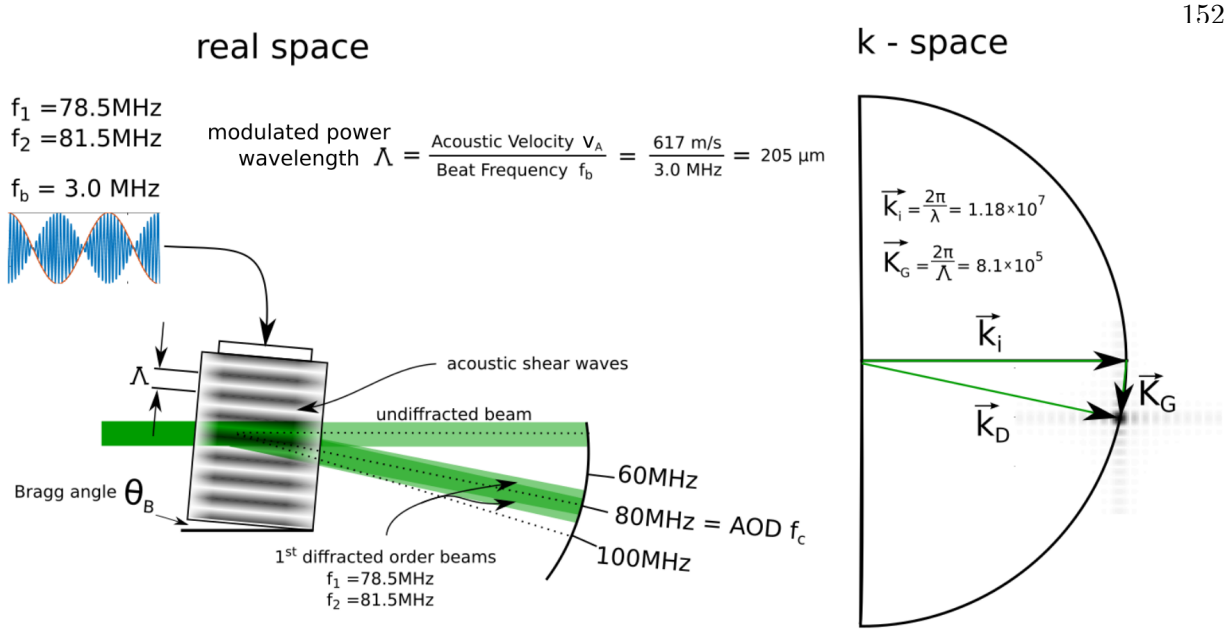

Figure 6.3: A real space and k-space simplified overview of the function of an AOD. In real space, the AOD is driven by two RF tones f_1 and f_2 which produce a sinusoidal power modulation of the traveling acoustic wave in the TeO_2. The period of the power modulation grating Λ is determined by the acoustic velocity v_a and the beat frequency f_b. A laser enters the AOD at the Bragg angle θ_B and a portion is diffracted into two first order beams. The angle of those beams is easily calculated in k-space (right). On a k-circle, the length of the k-vector of the laser is $2\pi/\lambda$, while the K-vector of the power modulation grating is $2\pi/\Lambda$, and the diffracted laser k-vector follows simple vector addition.

rotated into a vertically-oriented angular dispersion using a right angle prism oriented at a 45° angle to vertical. This also rotates the polarization to linear horizontal (ignoring the small spread of the polarization state due to focusing of the beam which is canceled later). As the beams pass through focus at Fourier Plane 1, the spots are located along a line and their spatial positions from an "origin" at 80 MHz are proportional to the Doppler shift imparted by the AOD.

After passing through focus, the beams expand for another 250 mm to the next lens that re-collimates them, thereby demanding that they reconverge and overlap again. Coinciding with the fourth full focal length in the 8-f system, the beams overlap within the active aperture of the "Horizontal" AOD (with a center frequency of 86 MHz). From each input beam, first-order diffracted beams are again produced and dispersed angularly in the horizontal plane and vertically polarized, and the undiffracted light is beam dumped. Following the same steps as for the first

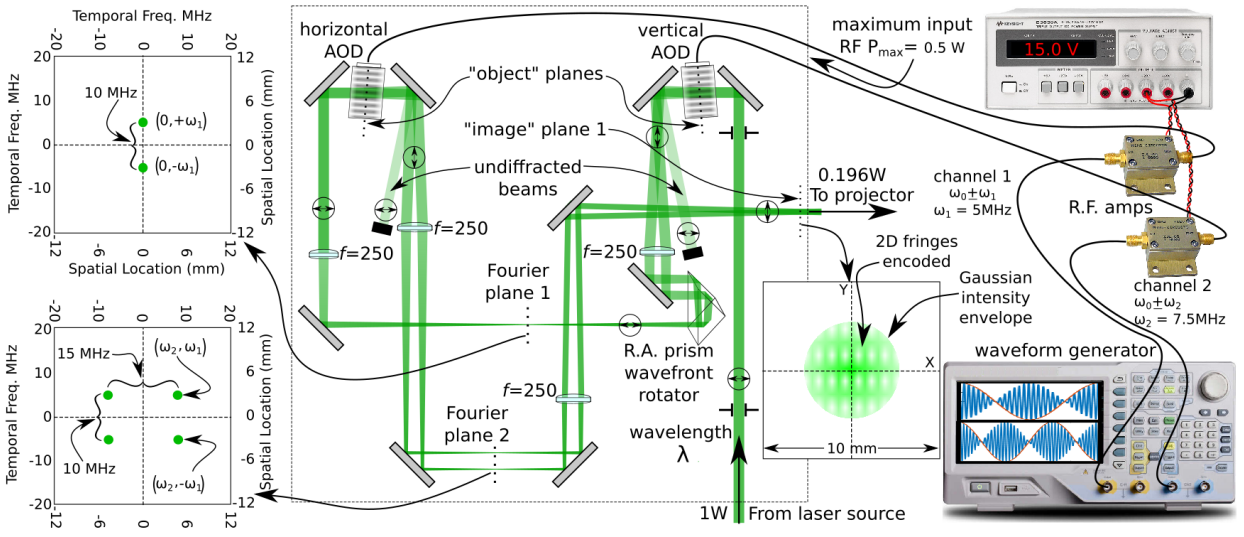

Figure 6.4: Acousto-optic pattern generator schematic. The laser enters the AOPG from below as a collimated, spatially-filtered Gaussian beam of approximately 1W. After passing through the "vertical" AOD two first-order diffracted beams are generated while the undiffracted light is dumped. These beams are rotated 90 degrees by a right-angle prism and re-imaged into the horizontal AOD. For each input beam, two output beams are generated. The beams are then re-imaged again to the output port of the AOPG.

AOD, the beams are focused using another 250 mm *fl* lens. As the beams pass through focus again at Fourier Plane 2, the spot distribution is now spread across a 2D plane. The spatial coordinates of this plane are rotated 90 degrees from Fourier Plane 1 and have an origin at the center frequencies of the horizontal and vertical AODs. All beams are re-collimated again with horizontal linear polarization and overlap in both planes at the last "image" plane just before the exit aperture of the AOPG.

6.2.1 Frequency Addition

Each of the AODs are oriented to Doppler upshift the frequency of the laser light by the RF tones driving the piezo-electric transducer. A sample interaction is shown in Figure 6.5. The first diffracted order of each beam coming out of the first AOD is upshifted by the frequencies $f_1 = 78.5MHz$ and $f_2 = 81.5MHz$. Spatially recombining these beams would produce a temporal frequency of 3 MHz. When these two beams are passed into the second AOD driven by 82 MHz

and 78 MHz, they are again upshifted by the frequency of the RF tones. The two cross products will have two different temporal frequencies. The diagonal with the largest cross products contains the beam upshifted by 81.5 MHz (AOD 1) and 82 MHz (AOD 2) for a total frequency shift of 163.5 MHz, and the other beam shifted by 78.5 MHz and 78 MHz for a total of 156.5 Mhz. The difference between these two beams is 7 MHz as shown in the bottom left of the figure. The other diagonal has the first beam upshifted by 81.5 + 78 = 159.5 MHz and the other by 78.5 + 82 = 160.5. The difference between those beams is only 1 MHz (bottom right). Although the temporal frequencies are different, the angular separation between these beams is identical and both diagonals therefore have the same spatial period, albeit with different wavevector orientation of their interference.

6.3 Relay Optics

A goodly portion of the effort of designing the $\mathcal{F}$-BASIS remote microscope was to engineer it such that it could be used for field work - in particular, field work that was demonstrative and analogous to a planetary exploration operational modality. The initial concept of this device was that all components depicted in Figure 6.1 with the exception of data processing would be designed and constructed in form and fit for use on top of the mast of a planetary rover. To this end, the optical bench containing the remote microscope optical assembly was designed to accept the beams generated from a compact, field-capable AOPG. Unfortunately, the field unit was never delivered to the university by the subcontractor. As a result, all of the operational tests, performance characterization, and algorithm development were performed within the confines of an optics laboratory crammed into an existing experimental architecture on a floating optical table.

As described in subsection 6.2, the AOPG generates beams that have a maximum angular separation of 1.98° (corresponding to the limits of the ±20 MHz bandwidth of each AOD). In order to couple the remote microscope optical assembly to the optical bench version of the AOPG, I used two 250 mm *fl*, 2-inch diameter achromat lenses to relay the beams across the table to the input of the remote microscope optics. The deflection angle and beam diameters are coupled via the optical invariant, so in order to conserve these quantities, the 4-f system has to induce no

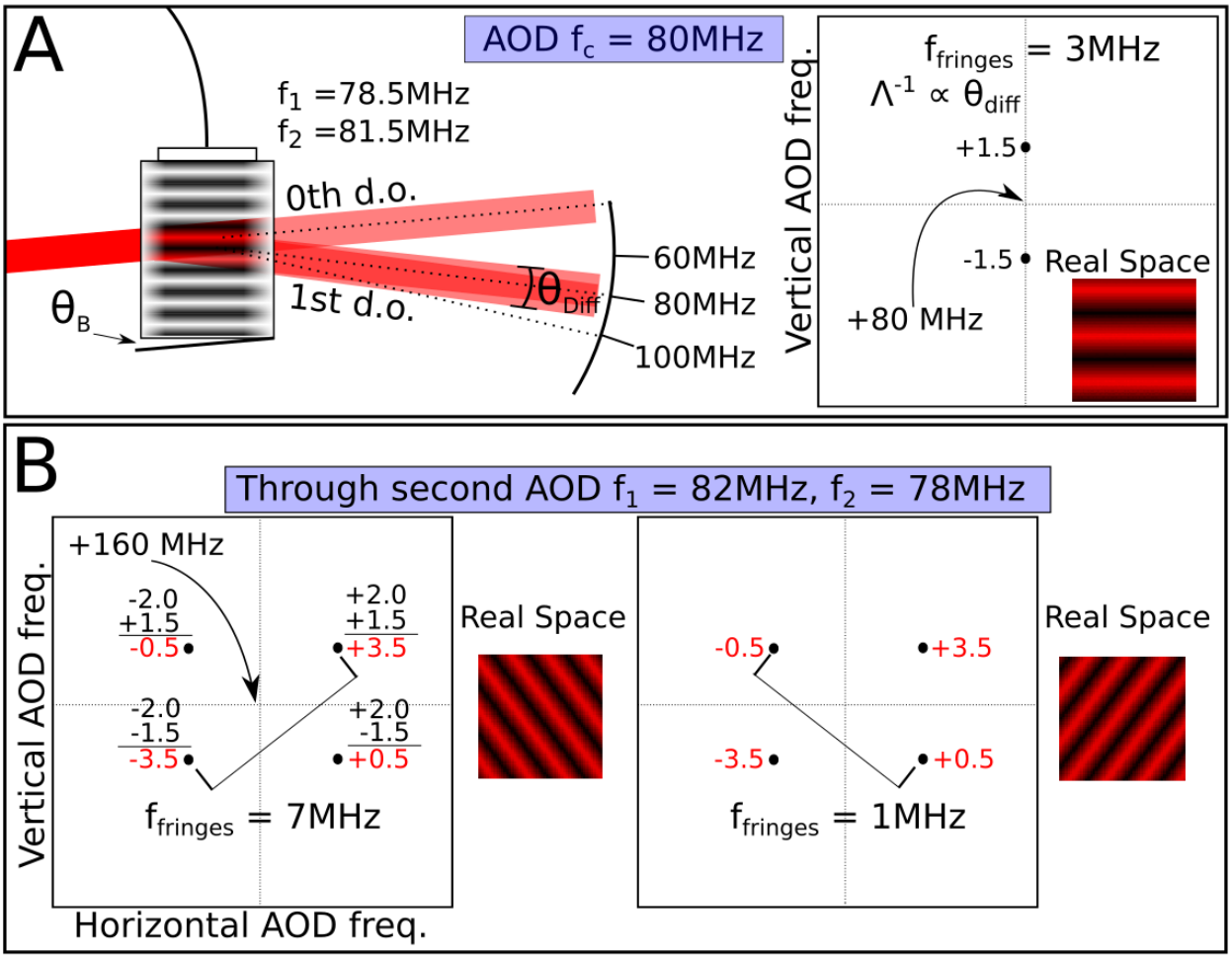

Figure 6.5: Demonstration of the temporal and spatial frequencies genenerated from two crossed AODs. A) The laser enters the first AOD at the Bragg angle θ_B and is Doppler shifted according to the two RF tones at 78.5 and 81.5 MHz driving the AOD. The box on the right shows the separation of the two tones from a 80 MHz center frequency and the real space illumination field. B) When two crossed AODs are used the beams are now all uniquely Doppler shifted. The second AOD is driven with two tones at 82 and 78 MHz. After passing through two AODs, the two diagonal cross products have different temporal frequencies but the same magnitude of the interferometric spatial frequency, but at a different orientation.

magnification which along with the focal lengths of the optics, defines the optical pathlength on the table. I used two 2-inch turning mirrors to fold the extra 1 m of pathlength in available space on the table. Halfway through the relay, at Fourier Plane 3, the beams pass through the first of two irises for use during system alignment. Residual polarization contamination is suppressed with another polarizer. The final "image" plane in the relay optics is located at the entrance pupil of

the remote microscope projection assembly.

Although the relay optics seem to be relatively benign and beneath consideration for inclusion into the description of the experiment, the extra meter of pathlength represents a substantial contribution to the total interaction pathlength of the lasers with the atmosphere and therefore induced phase error due to turbulence. There are many heat exhaust fans blowing in the vicinity and eddy-inducing surfaces and obstructions surrounding this falsely innocuous relay path. The effects of turbulence dominate the system performance, and I'll explore this topic in detail in subsection 7.1.3.

Another reason that the relay optics restrict the system is that it locks the location and orientation of the remote microscope assembly on the optics table. The remote microscope was designed with the assumption of a set relative location and orientation of the input "image" from the AOPG, and is intolerant of pointing error. Any amount of re-positioning of the primary mirror would entail a laborious and precise realignment of at least three of the relay optics components.

6.4 Remote Microscope Projector Optical Group

The remote microscope optical assembly contains all of the components in the laser path forward of the relay optics as depicted schematically in Figure 6.1. The assembly is mounted to a small (100 x 150 x 10 mm), light-weight Delrin optical bench for mounting to the rover mast as was done during the fit test in the Jet Propulsions Laboratory (JPL) Mars yard. Delrin is the Dupont trademark for the acetal resin thermoplastic polyoxymethylene known to be relatively stiff with accompanying low density (1.41 g/cm^3). I chose this material primarily because it was cheap, easily machinable and had similar rigidity performance to far more expensive laminated honeycomb breadboard constructions used in spaceflight missions. The total mass of the Delrin mast-bench is a little under 200 g. Mounted to this platform is a Thorlabs cage system containing all the optical components leading up to the mirror assembly. The four rods of the Thorlabs cage are screwed into the support plate in the back of the telescope optomechanical spider providing good mechanical coupling but limited optical adjustment flexibility. A CAD rendering of the realistic

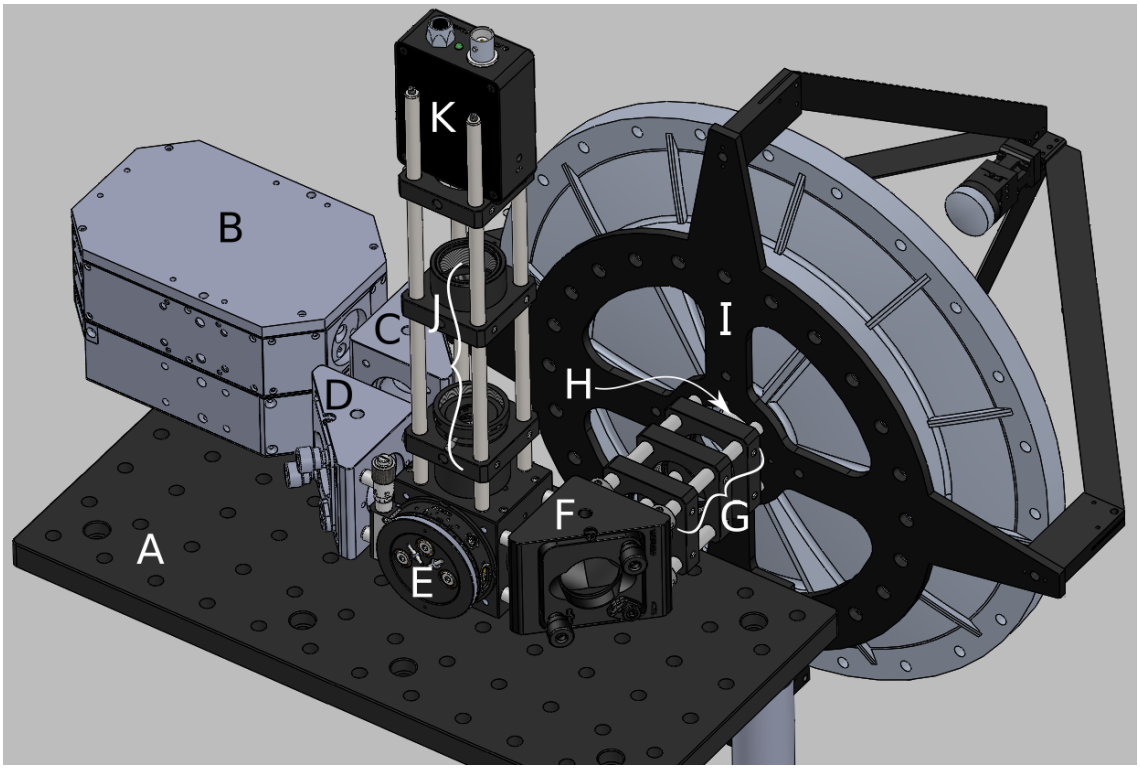

Figure 6.6: CAD drawing of the 1/2-inch thick Delrin optical bench (A) with Thorlabs components. B) The LambdaMetrics AOPG field unit. C, D, F) Turning mirrors in X-Y kinematic cage mounts. E) 1-inch polarizing beam splitter cube in a rotation mount oriented to send the reflected polarization light out of the plane of the bench. G) The Cooke triplet lenses in fixed-orientation cage holders. H) Quarter-wave plate to convert linear to circular polarization. I) Mirror opto-mechanical spider assembly. J) Focusing lenses and spatial filters for sample-scattered light. K). Hamamatsu avalanche photodiode module.

opto-mechanical structure including the LambdaMetrics AOPG field-unit is shown in Figure 6.6. In the laboratory experiment, I use the optical laboratory AOPG and place the last "image" plane produced by the relay optics at the location where the output aperture of the field AOPG would be.

Two flat 1-inch turning mirrors are mounted in Thorlabs KCB1 right-angle kinematic mounts to z-fold the OPL before entering the mirror set. These z-fold mirrors provide the largest adjustability for the gross pointing of the beams entering the telescope. The vertically-oriented diverging beams pass through a 50/50 polarizing beam splitter (PBS) that transmits vertical polarization and reflects the orthogonal polarization vertically down through a hole in the Delrin ending in a

beam dump. The PBS is mounted in a Thorlabs B4CRP 30 mm cage cube precision kinematic rotation platform with micrometer to precisely rotate the orientation of the beam splitter cube. The platform mounts into C6W cage cube into which the cage rods are threaded. The cage cube acts as the structural anchor for the entire 4-way cage system on the optical bench. Continuing through the system following the beams, another 1-inch turning mirror in a Thorlabs KCB1 mount turns the cage system 90 degrees toward the telescope assembly. This turning mirror is mounted a fixed 6-inch distance from the baseplate of the telescope spider via the cage rods. The three lenses of the Cooke triplet are mounted into Thorlabs CP09 cage plates to allow for independent axial positioning. A quarter wave plate is the last component before the telescope and converts the linear polarization into circular for projection toward the target. I describe the logic of using circular polarization in section 6.11. The cage rods are threaded into the baseplace of the telescope assembly, but are supported by the PBS cage cube to avoid any possible torque on the optical surface of the mirror.

Before moving on to the description of the detector arm of the optical assembly, I want to specifically call out some of the design flaws and important experimental observations. The first and foremost weakness of the design is the lack of being able to adjust the position of the input pupil to the remote microscope optical assembly. The Thorlabs cage system allows for the design to be compact, rigid and easy to purchase and construct, but this implementation requires the relay optics or the portable AOPG to be adjustable in X, Y, Z, tip and tilt.

Another drawback of this design entails the necessity to remove the lenses for the initial alignment procedure, but retain alignment of the turning mirrors in the cage system. This flaw is mostly alleviated by using a new product by Thorlabs (CP09) that allows a segment of the cage system to be removed and repeatably replaced without alignment error. The blocky nature of the cage components makes checking alignment, beam offsets and symmetries functionally impossible. While on the subject of commercially available solutions to optomechanical problems, I put a great deal of effort into light-weighting the primary mirror. This effort was nearly completely negated by the added weight of the cage system components.

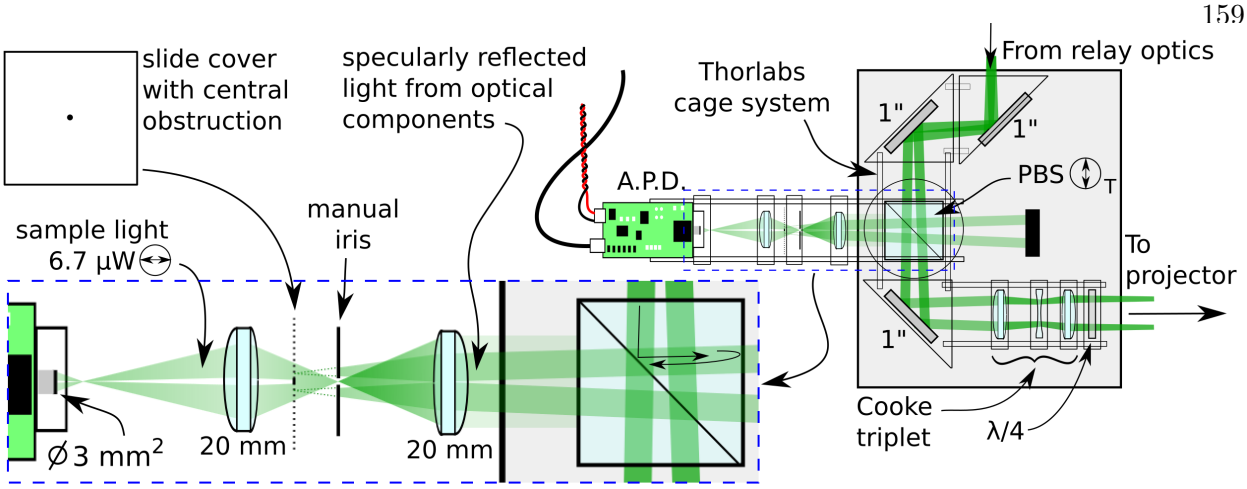

Figure 6.7: A flattened schematic of the benchtop optical assembly of the remote microscope with a zoom-in of the optical receiver section. The scattered light returning from the target is directed by the polarizing beam splitter into the detector arm. The first lens focuses the scattered light through a constricted iris. Residual back-reflected off-axis light from the microscope components are partially blocked by the closed iris. A telescope slide cover with a central obscuration dot completes the filtering of the back-reflected light contibuting to the noise and partially blocks a small portion of the desired light from the target. Another lens re-images the iris to the 7 mm^2 surface of the avalance photodiode for collection.

During the initial system integration and alignment I made several paper masks with central holes that could sit between the components and be removed easily. These paper tools were absolutely crucial in the alignment procedure, but were rather delicate. Machined metal alignment masks with arrays of holes matching the locations of patterns of beams generated by the AOPG would have provided a level of precision not attained during these experiments. The hardest aspect of alignment was attempting to determine the position of the beams at the threshold of the central hole of the mirror after passing through the quarter wave plate. A central plastic plug, again with indexed holes would have solved this hitherto unresolved difficulty.

6.5 Optical Filtering of Received Light

The detector arm of the remote microscope optical assembly is shown in Figure 6.7. Scattered light returning from the sample will either be in an unpolarized state or in the opposite circular polarization as the outgoing beams. As it passes through the quarter wave plate in the cage system,

the light will be converted into horizontal polarization which will be reflected by the PBS toward the detector. I explore the various polarization outcomes with respect to target construction in section 6.11. Even though the laser light enters the microscope optical assembly in vertical polarization a small portion of back-reflected can make it toward the detector. The PBS has an expected extinction ratio between 500:1 and 1000:1. A small portion of the power of the beams can be reflected off of any of the eleven optical surfaces after the PBS boundary. The curved surfaces of the lenses in the Cooke triplet are unlikely to cause much interference due to the divergence and angular offset of residual beams after reflection, however the quarter wave plate and the flat surfaces of the cube beamsplitter do provide specular back-reflection. Assuming the worst case scenario of 4% reflection off of the far face of the beam splitter and the lower end of the extinction ratio of the PBS, a 1 W beam could possibly send 80 μW down the detector arm towards the detector. These are obviously worst case values, and measured powers of back-reflected light from the outgoing laser beams with 1 W of power results in multiple reflection artifact light in the detector arm of less than 2 μW.

Luckily there is a way in which the back reflected light differs from the desired scattered light from the sample that allows us to separate the two and eliminate unwanted stray beams that may swamp the detector through optical means. The laser beams projected toward the target come to a focus at a surface derived in section 4.3.3 before expanding to the size of the "pencil beams" that illuminate the target. Scattered light returning from the target can be considered a point source producing a spherically expanding wavefront. This wave fills the entire primary mirror aperture and is reflected and focused toward the secondary mirror which converts the light into a mostly collimated beam. This returns back to Chapter 4 where I described the optical system as an infinite-conjugate imaging system for the projected beams and a finite-conjugate system during the light collection mode. The returned light is collimated where the projected beams are focused and vice versa. As a result, returning to the zoom-in of the detector arm in Figure 6.7, the first focusing optic will generate a closer focus for returned scattered light than for the back-reflected light of the outgoing laser beams. I placed a mechanical iris with an approximately 500

micron aperture at the focus of the scattered light. The multiply reflected artifact beams from the beamsplitter with sufficient angular deviation from the center are blocked by the iris. This however, only works for highly deflected beams for high spatial frequencies. Beams will low deflections from the optical axis will still at least partially get through the manual iris, however they still form a focus nearly a centimeter away from the scattered light focus. I placed a microscope slide cover with a 500 μm-diameter opaque dot at the focus of the back-reflected light and reduced the detectable multiple reflection artifact light to below the noise threshold of the optical power meter. This central obscuration does slightly reduce the amount of sample light getting to the detector, but the loss was unmeasurably low. Luckily, all photons are created equal with respect to containing information regarding the time-series amplitude oscillation of the returned scattered light from the sample, and a small obscuration will only reduce all measured spatial frequency components equally. The second focusing lens re-images the iris onto the avalanche photodiode. I provide values for the optical power of detected light from the targets used in section 6.11.

6.6 Si Avalanche Photodiode Detector

The detector I use is a Hamamatsu Si Avalanche Photodiode, model # C12702-12. According to the datasheet provided by the manufacturer, it has a 3 mm^2 detection area, 40 MHz bandwidth with a 4 kHz low frequency cutoff response. The NEP is 1 pW/$\sqrt{Hz}$ with a 6.3 nW rms detection limit at full bandwidth. The APD is spectrally responsive from 200 - 1000 nm with 10 A/W photosensitivity at 532 nm. It consumes 60 mA at 5 V. The maximum amount of incident light the APD can handle without damage while powered is 10 mW. Electrically, it has a 50 Ω internal impedance. At only 80 x 50 x 22 mm, the APD is approximately the size of a credit card, although weighing 37 g. It has a preset gain of M=30 with gain temperature stability of $\pm$ 2.5 % between 15 and 35 ^{o}C. Its amplified response is 20kV/W up to 10 MHz and thereafter dropping to 10kV/W at 40MHz [20], [48], [53]. The photocurrent signal produced by the APD is transmitted via a 50 Ω coaxial cable terminated with BNC connectors to a 24 dB R.F. amplifier before being digitized and stored.

6.7 Analog to Digital Converter

My choice of digitizer evolved during the years of experiments due to a range of factors including the iterative improvement of data measurement schemes, object reflectivity ranges, attempted compensation for the short-comings of several components of the equipment, and a constantly improving understanding of the difficulties, errors and noises of the experiment. I describe the data measurement schemes used during system alignment studies and for the final image reconstructions in following sections adjoining the results they produce. Although it is arguably some of the most important information to give the reader, it would be unmanageable for me and unpalatable for you if I were to provide a comprehensive list of failed schemes and technical dead-ends that led to the final data-management solutions.It makes sense for me to provide a narrative that calls out the digitizers used, their relevant technical specifications and limitations, and the reasons why they were inevitably replaced.

The first digitizer I used was the Tektronix MDO 4034-3 mixed domain oscilloscope. It is a low-cost, stand-alone oscilloscope with 8-bit vertical resolution. It acquires up to 2.5 billion samples per second (2.5 GS/s) with 350 MHz bandwidth. It is capable of storing 20 M-samples onboard and averaging up to 512 waveforms. For strong SNR data, such as produced by the specularly-reflecting resolution targets, the 8-bit resolution was sufficient especially when beating down noise with averaging of many waveforms. I abandoned this oscilloscope for two reasons. The first is that the 20 M-sample for waveform storage length was a critical limiter for Fourier-sampling schemes. For proper sampling of an arbitrary set of Fourier components (which I'll define in section 7.4), a 80 μs waveform at 250 MS/s must be collected, which results in 20k samples per measurement. The 20 M-sample waveform limit represents only 1000 unique Fourier measurements of the sample, while the remote microscope supports a maximum measurement of 160k unique samples. So, a complete sample acquisition would entail the collection of an absurd 160 separately stored waveforms. The second reason that this oscilloscope was ultimately unusable was the comically slow data transfer mechanisms. The best option for waveforms being saved onboard is as an ascii csv file. Each

numeric digit of the waveform sample is converted into a 2-byte UTF-16 ascii character. The data waveforms could only be removed from the oscilloscope via slow USB 2.0 or ethernet protocols. The upshot is that a 20 M-sample waveform takes over a half-hour to transfer off of the oscilloscope. At this rate, a full data acquisition, transfer and processing to generate an image would take slightly under 99 hours.

The second digitizer I used was the Keysight Infiniium S-Series oscilloscope. This scope is a professional-quality mid-range device with 10-bit resolution and capable of 20 GS/s. It has a 500MHz bandwidth and provides 200 M-samples of onboard storage. Although it is capable of averaging up to 256 traces for waveforms smaller than 10-Msamples, it is unable to average at all for waveforms longer than this. The Infiniium has a high resolution mode which collects data at the 500 MHz bandwidth and does the appropriate sample averaging to generate waveforms with lower bandwidth but with higher bit depth. This scope offers many benefits over less expensive oscilloscopes in that waveforms are stored and transferred as binary files. This facilicated transferring a full data file in less than 4 minutes via USB 3.0. The 200 M-samples maximum was obviously still insufficient for a full data acquisition with the remote microscope, but it did lower the number of required files to a more manageable 16 per reconstructed image. Under these conditions, full acquisition, transfer and image construction would take approximately 1 hour and 40 minutes per image, a 59× improvement over the Tektronix. The primary reason that I gave up this oscilloscope was because we didn't own it. Although, to be honest, the bells and whistles provided by this oscilloscope and its industry equivalents come at a high monetary cost and no practical benefit to the remote microscope digitization needs. The most important qualities for my purposes are data storage length, transfer rates and bit depth.

I completed the experiment using a Gage Razormax PCI-ex digitizer card mounted in a desktop computer borrowed from the Southwest Research Institute. The Razormax is a 16-bit, 1GS/s, 8-channel device with 700MHz of bandwidth. It contains 4 G-samples of onboard storage, and as a computer-mounted card is capable of using the PCIe bus to transfer data directly to the computer hard drive. However, more importantly, this card allows access to the onboard memory

buffer via a software-development-kit (SDK) and drivers for Matlab or LabVIEW programming environments. This functionally provides full programmatic access to what can be considered slow RAM already loaded with the waveform data. Rather than transfer the entire waveform from the digitizer to a computer where the data processing software would have to read the full waveform into computer RAM before processing segments of it, the Razormax allows the user to download a small segment of the waveform at a time for processing. This eliminated all time spent in transferring and loading the file as was required for all other oscilloscopes. Another reason that this digitizer card was an ideal solution is that an acquisition of a full set of data using the aforementioned 20 k-samples for 160k measurements generates 3.2 G-samples which is fully accommodated by the 4 G-samples of onboard storage. At 250 M-samples/sec this waveform is collected in 12.8 seconds. The processing of the data, which was a small percentage of the overall data acquisition process with other digitizers, takes a little over 2 minutes with 4 computing cores operating. In all, the full data acquisition and image reconstruction takes approximately 2 minutes and 30 seconds per image, a 40× increase over the Infiniium and a 2340× increase over the Tektronix. The Razormax does not support any native waveform averaging, but instead provides the user the ability to average by storing many waveforms onboard and using post-processing. Although I explored using this functionality, I found that averaging in voltage-space was less useful than Fourier-component-space, and as a result onboard averaging wasn't used in any of the final data because of length of the waveform files.

6.8 Control Electronics Group

The final set of components I need to describe are the control and power electronics group, highlighted in the upper left hand corner in red in Figure 6.1. This group is responsible for producing the RF waveforms that drive the transducers on the AODs, amplification of the RF signals to and from the experiment, and powering the APD. The control electronics are also relatively straight-forward in their function; however a great deal of care must be taken in constructing an operating procedure for the experiment due to opaque and pernicious performance limitations of

the equipment.

The RF waveforms used to drive the piezo-electric transducers on the AODs are produced by two linked Tektronix arbitrary waveform generators model # AWG520. The AWG is a large, desktop-computer-sized piece of laboratory equipment that the user programs to generate discretely sampled waveforms of arbitrary real-valued functions with no limitations regarding continuity. The user is able to designate the time-step between samples, the amplitude at every sample point and the waveform length up to the memory limit of the device. In the case of the AWG520, the maximum waveform length (which I'll be revisiting a few times in the following discussion) is 4,194,048 ($2^{22} - 2^8$) samples. The AWG outputs waveforms with amplitudes up to $\pm 1V$ with a 50 Ω output impedance. A single waveform can be output in a continuous loop with no latent delay between cycles, and more than one waveform can be output in sequences where the total number of elements of all waveforms that make up a repeated cycle is less than the 4 M-samples mentioned above. In modern models of arbitrary waveform generators, each output channel contains its own sequencer, but in the AWG520 one sequencer handles both output channels. This was the reason that I was unable to use a single AWG, and I'll go into the necessary sequence of the waveforms in the next section. For each output channel, the AWG has two associated marker channels that output a bimodal TTL signal (0 - 2 V, 50 Ω) used for triggering and timing purposes. Each AWG has an internal 10 MHz clock source which is upsampled to generate waveform time-bases up to 1 GHz. The AWG520 allows the option to sync this internal clock to an external 10 MHz reference clock (1 V_{PP}) to facilitate timing accuracy across devices to 1 ns. Finally, the AWG can run in either a "continuous mode" where the waveform cycles without stopping, or in "triggered mode" which requires an external signal to begin the waveform sequence. I use all of these qualities in the experimental setup.

The wiring and timing diagram for the control electronics group is shown in Figure 6.8. The Razormax digitizer acts as the master clock wherein the 10 MHz reference clock out signal is connected to both of the AWG "clock-in" recepticals via a BNC-T connector to split the signal. In order to sync these devices, it is necessary to change selections in an internal menu system. .

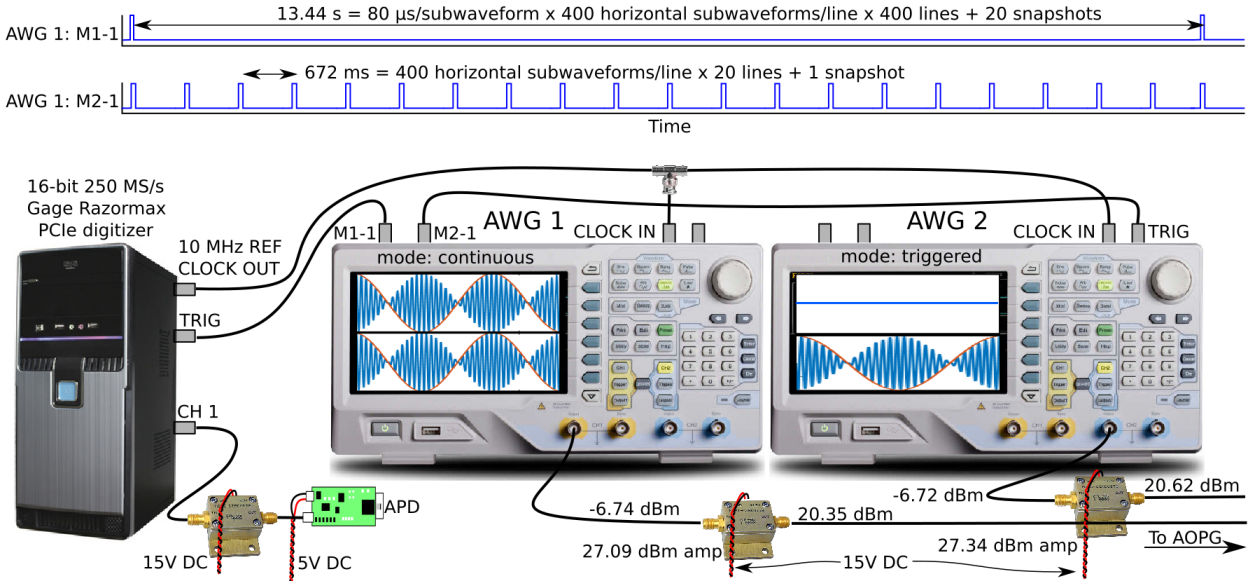

Figure 6.8: Timing and wiring diagram for the control electronics group. The digitizer is mounted in the desktop computer and acts as the master clock outputing a 10 MHz reference used to sync the clocks of the arbitrary waveform generators. The left AWG produces the RF tone for the "horizontal" AOD, and outputs this waveform to both channels to enable the use of both markers. The first marker M1-1 contains a pulse every 13.44s and is used to send a trigger back to the digitizer to begin data acquisition. The second marker M2-1 repeats every 672 ms sending a trigger to the second AWG to begin its frequency step sequence. The right AWG produces the RF tone for the "vertical" AOD and steps through the waveforms every 80 μs.

In the timing menu, I selected the "reference sync" while also keeping another setting to use the "internal clock".

The waveform generator labeled AWG 1 produces the waveforms going to the vertical AOD, and also acts as the principal sequencer for the data acquisition cycle. The first marker for channel 1, labeled M1-1 in the figure, contains a trigger pulse sent to the digitizer that starts the 13.44 s data acquisition cycle. For reasons that can't possibly be immediately obvious, the waveforms on channels 1 and 2 of AWG 1 only differ by 20 of the 820 waveform sequence. The markers are written with the waveform, and in order to send two separate triggers with distinct periods to AWG 2 and the digitizer requires making copies of certain waveforms with and without triggers and sending them to different channels. The first marker for channel 2 of AWG 1, labeled M2-1, sends a pulse every 672 ms to AWG 2 to trigger a "horizontal block sequence" which I'll describe in section 6.10.

The AWG 2 is set into "triggered" operational mode which forces it to wait for the next trigger pulse before executing a horizontal block sequence.

After setting the output range to $\pm 1V$, I measured the total RF power at the output of each signal channels of AWG 1 and 2 with an RF power meter. The values were -6.74 dBm and -6.72 dBm respectively, which corresponds to 0.211 mW and 0.213 wM. After passing through the RF amplifiers I measured outputs of 20.35 dBm and 20.62 dBm (108 mW and 115 mW). The maximum RF power that can be sent to the AODs without inducing harmonic side-lobes is approximately 0.5 W, which demands that no more than 1 mW leave the output of the AWG channel. Each of the RF amps are powered via twisted pair wires with a standard Agilent adjustable $\pm 25V$ DC power supply set to 15V.

6.9 Data Acquisition and Processing Software

I wrote all of the data acquisition and processing software in LabVIEW, a programming environment that specializes in easy communications with an extensive range of laboratory instruments allowing for integrated data reduction during experiment operation. LabVIEW implements the concept of the "virtual instrument" (VI) in which the "front panel" of a synthetic laboratory device provides the user control of all adjustable aspects of the experiment. The front panel of the standard data acquisition VI for the remote microscope is shown in Figure 6.9.

The conjugate of the front panel is the "block diagram" (one frame of which is shown in Figure 6.10) which contains all of the code defining the mathematical and algorithmic operations of the VI. The code of LabVIEW is written in a GUI with icons representing functions and wiring layouts defining the interoperation of those iconographic functions. Timing and event-dependent operation is handled using an array of built-in programming structures that are nested like pages of a book that can only be viewed one frame at a time. The nesting aspect of LabVIEW makes the code cumbersome to publish and a little frustrating to try to translate into words. It is far easier to explain the processing by expressing the relevant conceptual blocks of the code in a flow chart which I explore in depth in section 6.10.

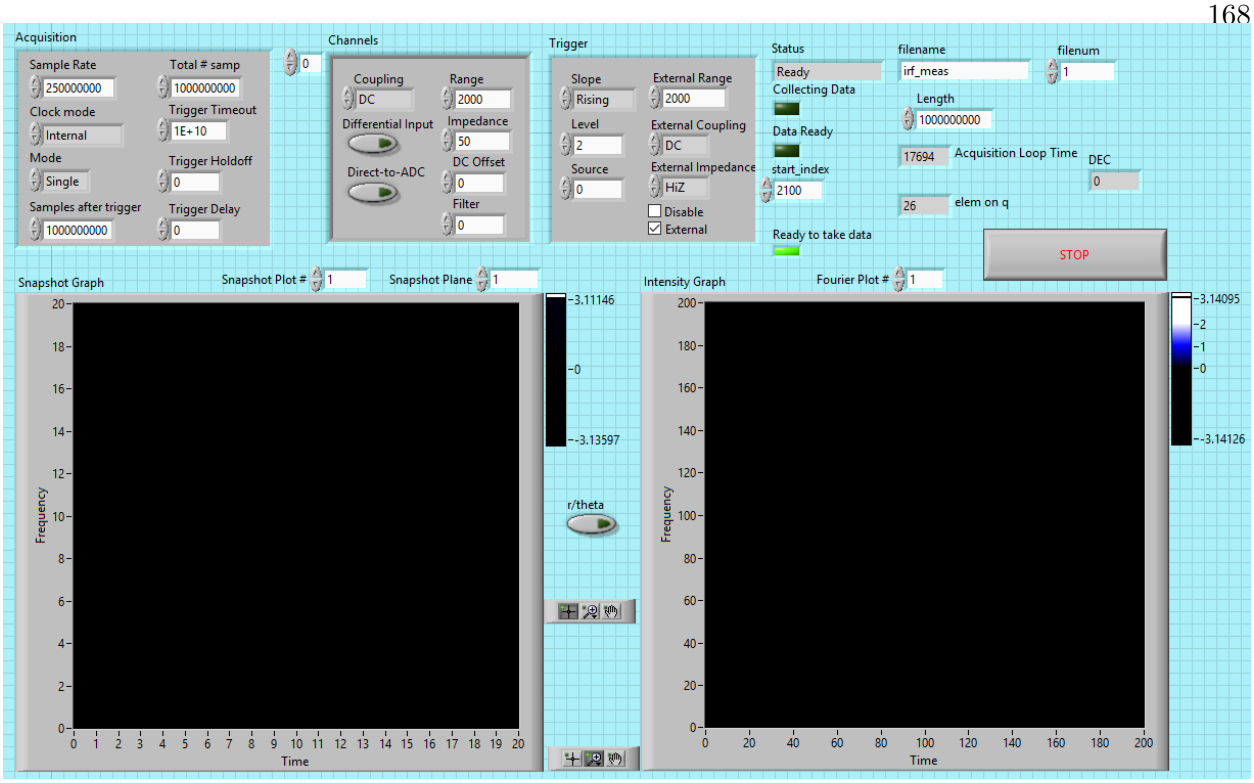

Figure 6.9: The front panel of the virtual instrument used to collect data. The grey settings boxes in the upper left labeled Acquisition, Channels and Trigger adjust the settings of the digitizer. The file name to be generated, data length to be recorded, and other indicators of variable values are shown in the upper right. The two large graphs update with planes of acquired data from the snapshot and standard data.

In best-practice coding techniques, the LabVIEW code is modular, allowing for multiple instantiations of code to operate at the same time. A substantial benefit of the LabVIEW language is the well-developed and seemless multi-processor parallel processing ability. This provides the user with the ability to assign specific processors to data acquisition tasks without allowing them to be used in other processes thereby mitigating timing errors or resource conflicts often resulting from more rudimentary code bases built by users from primary languages like C, Matlab or python. A good part of the time-savings obtained by using the Razormax digitizer PCIe card over stand-alone oscilloscopes was the ability to set four of the host computer processors working at once. Using the parallel processing capability of LabVIEW allowed me to ensure that at all times during the reduction sequence a processor was always requesting data subwaveforms from the onboard

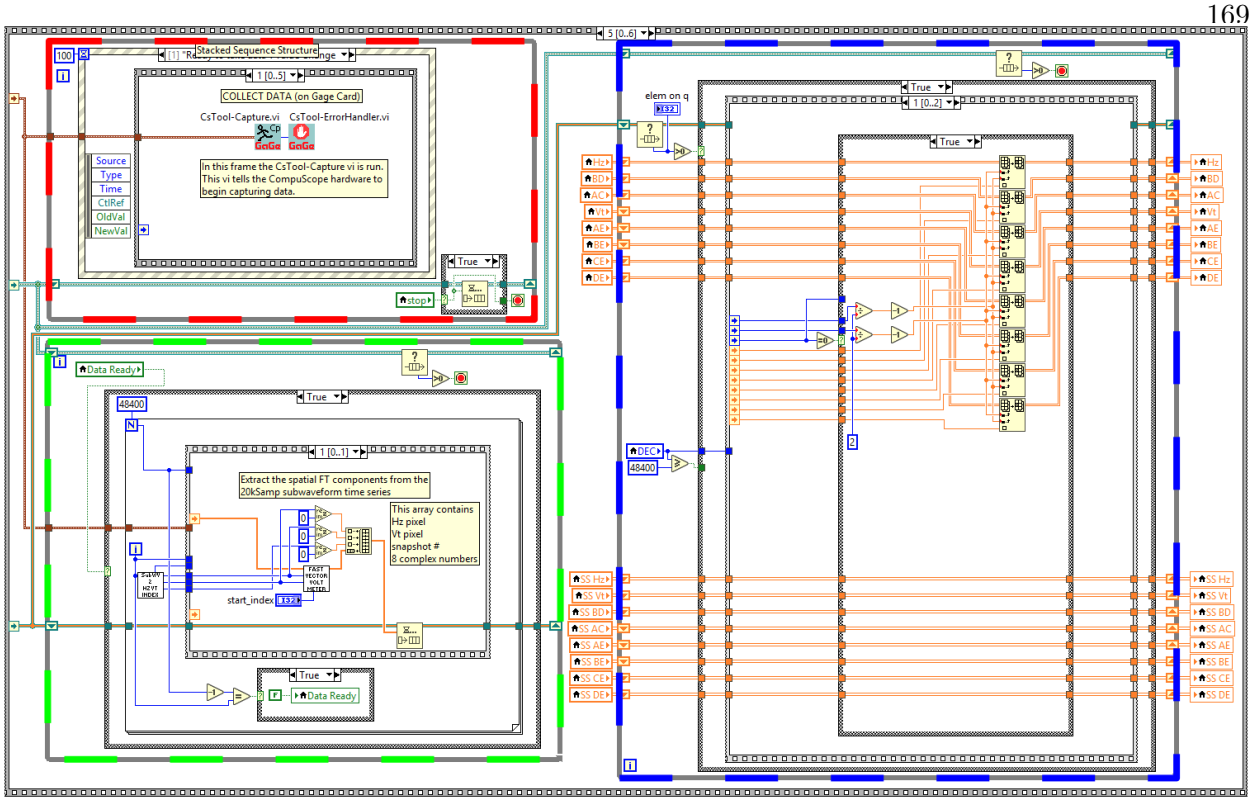

Figure 6.10: One frame of the acquisition VI code for the remote microscope. The three boxes outlined in dashed colored lines represent a looped process assigned to a single processor. The red dashed box circumscribes the processor loop to set the Razormax digitizer to collect data. The green box contains the code that computes and extracts the Fourier component from each 20 k-sample subwaveform. The blue box surrounds the code loop that organizes the measured Fourier components into 16 arrays and writes them to data files. Each of the small square icons represent subroutines containing their own graphical code.

memory of the digitizer while the other processors were operating in a staggered work flow.

The majority of the data collection task for the VI is organizational in nature. The only mathematical operation performed is a 1D Fourier transform on each collected subwaveform. The bulk of the work lies in calculating and book-keeping each of the components since each subwaveform contains four independent spatio-temporal frequencies (horizontal, vertical and two diagonal terms). In addition, peppered throughout the data acquisition process are planes of data used to track the bulk phase evolution during the 13 seconds of acquisition. These "snapshot" planes need to be identified and properly separated. The code contains three loops assigned to dedicated computing cores in order to avoid resource conflicts. Although the code has many non-sequential aspects

with varying frame depths, the principal loops provide the best overview of the process. The upper left hand corner of the code contains a rectangular box outlined in dashed red. This loop establishes that a data acquisition trigger has occurred, sets the acquisition parameters on the digitizer and sets it collecting data. The green-outlined box contains a loop which extracts each of the 168,400 subwaveforms, performs a 1D Fourier transform, calculates the indices of the desired Fourier components, extracts them and places them into a linear container. The blue box extracts those complex values out of the linear container and organizes them into multiple 2D data for the target and 3D data for the snapshot planes, and plots the values to the cscreen as it updates. With 4 computing cores running on a 2.5 GHz intel processor, 3.2 GBytes of data is reduced to approximately 1.5 Mbytes of extracted data in 2.5 minutes. In all, the data acquisition and processing VIs contains over 70 subroutines and 15 loops.

6.10 RF Waveforms, Sequences and the Measurement Scheme

In section 2.2.10, I claimed that the AODs used in this work have a bandwidth of 40 MHz and an illuminated time aperture of 20 μs which gives a time bandwidth product TB = 800 and corresponds to a resolvable frequency separation of 50 kHz. The minimum waveform length necessary to Nyquist sample 50 kHz is 10 μs. However, it's never wise to sample near the Nyquist limit. Furthermore, the 20 μs illuminated time aperture is a theoretical maximum for these devices, and 10 μs corresponds to the illuminated 6 mm aperture with $v_c = 0.617$ mm/μs, which gives a TB = 400. The 20 μs acousto-optic access time defines a period of transition between two adjacent acoustic frequencies wherein both would contribute to the diffracted light field. In order to avoid these periods of frequency confusion and acquire a waveform with sufficient length to guarantee good sampling in the presence of variable noise, I set each subwaveform that measures a set of Fourier components to 80 μs long.

The full data acquisition cycle consists of snapshots, horizontal frequency blocks and vertical frequency blocks. A snapshot is a fast set of 20 x 20 temporal frequencies evenly spaced at every ± 2 MHz throughout the horizontal and vertical bandwidth as shown as the array of red dots in Figure

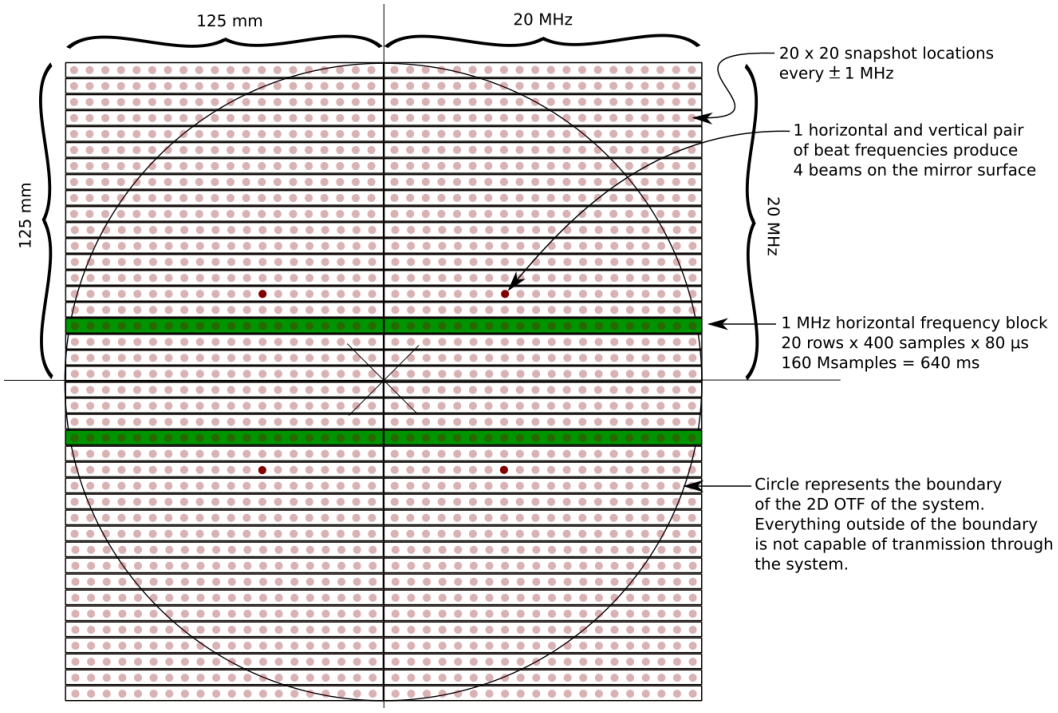

Figure 6.11: The basic construction of the measurement scheme, mapped as locations of the beam on the primary mirror. The red dots represent locations of the snapshot measurements where a dot in one quadrant is coupled with three symmetrically located dots in the other quadrants. The green bars represent a single row of frequency measurements where the vertical frequency is held steady and the horizontal frequencies are stepped by 100 kHz every 80 μs. The beams that fall outside of the circle are outside the 2D OTF of the remote microscope and are lost.

6.11. The purpose of a snapshot is to measure the same subset of Fourier samples periodically throughout the measurement in order to track time-varying offsets in magnitude and phase and use these to correct the full acquisition data in post processing. A shapshot takes 20 x 20 x 80 μs = 32 ms to acquire. A horizontal frequency block consists of 20 iterations of a full set of 400 80 μs-long measurements in the horizontal frequencies from 100 kHz to 40 MHz. At the end of each line completing 400 horizontal measurements, the vertical frequency is stepped, so that a horizontal frequency block contains measurements of 2D spatial Fourier components for 20 vertical and 400 horizontal frequencies, shown as green bars in Figure 6.11. A vertical frequency block is a set of 20 increments of the vertical frequency by 100 kHz held for 80 μs x 400 = 32 ms during which the horizontal frequencies are iterated and measured.

The full data acquisition cycle consists of the following steps. A trigger pulse is sent from AWG 1 to AWG 2 to initiate a snapshot and horizontal frequency block. At the end of each frequency block that contains 20 vertical steps another trigger pulse is sent to AWG 2 to initiate another cycle beginning with a shapshot. It is clear from the figure that this measurement scheme contains a sizable set of spatial frequencies that lie outside of the OTF of the system (the beams fall off of the mirror and are not used to illuminate the target). As the vertical frequency climbs, the portion of unusable frequencies increases. As a result, this measurement scheme guarantees a time loss equal to the ratio set by the measurement square and the inscribed circle (21.5 % = 2.9 s).

The reason I settled on this scheme was due to the memory limits of the AWG520. I set the AWGs to produce waveforms with temporal sampling every 4 ns = 250 MHz. To be better than Nyquist sampled, the sampled subwaveforms need to be at least 5000 samples in length = 20 μs. A set of 400 subwaveforms then consists of 400 $\times$ 5k = 2M samples, or half the memory limit of the AWG. In addition to the set of 400, the horizontal sequencer also needs to hold the 20 subwaveforms for a snapshot, bringing the total number of points in the waveform to 2,100,000. Although it would be more efficient to reduce the number of horizontal samples as the pattern marched up the mirror to remain within the OTF of the system, to do so would require creating copies of waveforms in the sequence. At most, one more foreshortened set of horizontal frequencies could be added to the sequence before running out of memory, but the gains in measurement speed would be more than offset by the added effort required to maintain proper book-keeping during the data reduction process. In short, I chose to lose efficiency in measurement to gain simplicity in processing. In the sequencer, each of the 5 k-sample subwaveforms are repeated to produce the 80 μs (20k) subwaveforms used to probe the surface.

The LabVIEW data acquisition and storage cycle is shown as a flowchart in Figure 6.12. After the 13.4 s data collection is complete, the 3.2 G-sample waveform consisting of 168,400 subwaveforms is stored on the buffer of the Razormax digitizer onboard memory. For each index, a subwaveform is transferred from the Razormax memory to a RAM buffer. The first 5 k-samples

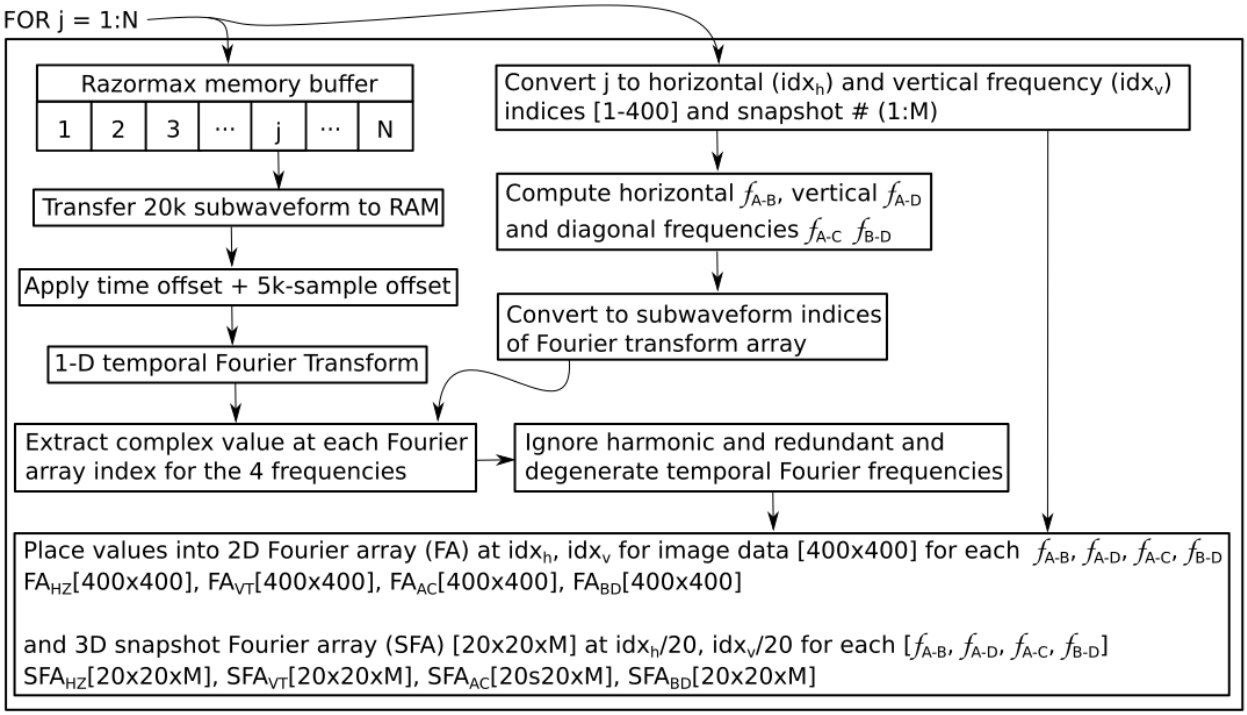

Figure 6.12: The flow diagram for the data acquisition for remote microscope image reconstruction. Looping through N waveforms, the relevant indices of the Razormax memory buffer are accessed to transfer only 20k samples to the computer RAM. After applying the measured time offset, the correct indices for the measured Fourier components are extracted from the 1-D FFT. These two complex values are placed into the correct location in a 2D array. The same process is performed for snapshot data, but into a smaller 20x20 data plane.

which contain measurements during the acoustic frequency transition are removed. In addition, I subtract a sample offset needed to begin each subwaveform at the same relative time-position. This index value depends upon electronic and acoustic delays and I explain how to find this offset empirically using collected data in section 7.1.3. Starting from the combined index offset, a 10 k-sample (40 μs) 1D portion of the subwaveform is Fourier transformed. I convert the index of the subwaveform to the equivalent horizontal and vertical frequency step indices (1 - 400) according to the sequencing of the AWGs. From these indices, the horizontal, vertical and cross-product temporal frequencies are computed as discussed in section 6.2.1. These frequencies are converted into the 4 subwaveform indices within the Fourier transform array which contain the measured Fourier components during that time period and the values are extracted. Redundant spatial

frequencies and measurements that are second harmonics of another temporal frequency are ignored. Finally, these values are placed into (400 x 400) 2D arrays, or (20 x 20 x 21) 3D arrays for snapshot planes, and written to file. At this point, the full waveform is dumped from memory and another waveform is collected. All information concerning noise in the waveform is condensed to a contribution to the four complex values, and all other Fourier components in the spectrum are ignored.

6.11 Laser Power and Polarization at Fiducials

One of the drawbacks to the $\mathcal{F}$-BASIS remote microscope is the low system efficiency from the initial laser source to the collection of light at the APD. In the worst case Lambertian scattering target, for every million photons emitted by the laser only 7 make it to the detector. Beginning at the laser source in Figure 6.1 the typical output of the Verdi V5 beam is set to 1 W. I measured the total beam power at locations through the system to determine losses at each major block. The beam loses approximately 15 % in the spatial filter, apertures and half wave plate and enters the AOPG with 0.85 W. Each of the AODs are approximately 50 % efficient, but with additional losses to optical components, the AOPG as a whole is 19.5 % efficient and only 166 mW passes through the exit port. By using all possible AR coated lenses and surfaces in the relay optics and remote microscope assembly, 68 mW, 41 % of the light leaving the AOPG reaches the target. The total system efficiency for beam projection is 6.8 %.

The amount of light returned to the detector strongly depends upon the reflectivity of the target. In the case of flat specular reflectors such as the mirrored portion of resolution targets, up to 90 % of the incident beam can be reflected back through the system and 41 % of that light can reach the detector for an upper detection efficiency of 36 %. In that case, the total system efficiency is 2.4 %. The other side of the performance scale is a strongly absorbing or transmissive Lambertian scatterer. From a theoretical standpoint, assuming one third of the incident light is scattered from a surface, an isotropic hemisphere of light is generated. At 5 meters distance, the total surface area of the hemisphere is 31.4 m^2. The 250 mm diameter primary mirror collects

0.05 m^2 (0.15 %). With totally unpolarized light as would be expected from an ideal Lambertian scatterer, only 50 % of this will pass through the polarizing beam splitter in addition to losses from the other optical components transmitting only 40 %. All told, with 68 mW illuminating the target, the amount of light reaching the detector is 6.7 μW. This calculated value matches well with the system efficiency found empirically by measuring the light with a power meter. For 108 mW of initial optical power from the compass laser and a fiberous paper target with black lettering on it, only 700 nW reached the detector.

In the system I use polarization rotation techniques to attempt to maximize the detected signal irregardless of the target construction. The light leaving the AOPG is linearly polarized in the vertical direction, and it remains in this polarization through relay optics and polarizing beam splitter. After the Cooke triplet, the beams pass through a quarter wave plate to rotate the polarization into right hand circular. The swap to left-hand circular due to reflection from the secondary mirror is reversed by the primary mirror. One more inversion to left-hand circular occurs after leaving the 6" folding mirror.

The polarization state and degree of polarization of the returning light depends upon the sample. In the case of specularly reflecting targets such as the linear gratings and Air Force resolution targets (AFRT), the polarization reverses just as it would from any mirror surface. Tracing this backwards through the system, the quarter wave plate will rotate the polarization to linear horizontal which will then be reflected by the polarizing beam splitter toward the detector. In the case of an ideal Lambertian scatterer such as paper fiber, the return light will be completely depolarized and the detected signal will be less by half, just as in the case of a 50/50 beam splitter.

The most interesting case is when the polarization of the scattered light depends upon the surface structure of the material. The clearest example of this is black laserjet print on white paper stock. The paper stock is high reflectance, but completely depolarizes the incident light, while the ink retains a good part of the specular nature of glossy surfaces but with much lower reflectivity. Several of my test targets were constructed via printing on white paper to develop the system and I observed strong differences in the strength of the Fourier components due to the presense

of the quarter wave plate with respect to its absence. The characterization of geologic materials is often explored using polarimetry, and the remote microscope could be adapted to explore this investigation space with the inclusion of either an easily removable or tunable wave plate.

Chapter 7

Remote Microscope Alignment, Errors and Image Reconstructions

In this chapter I describe in detail the use of the remote microscope laboratory instrument. I provide detailed alignment procedures and metrics for system characterization in section 7.1. An analysis of phase errors due to atmospheric sources is provided in section 7.2. I describe the measurement scheme and provide a tour of the hidden pitfalls and contributions to the measured signal in section 7.3. I show the first image reconstruction in section 7.4 and conclude with the inevitable optical losses and limits, that need to be addressed, and possible routes for further improvements in future work.

7.1 Alignment Procedures

One of the downfalls of using an optical system that you've designed from scratch is that you've only yourself to blame when you discover that it is offensively difficult to align. There are six degrees of freedom in the positions of the optical components and a family of solutions that will allow the system to be used outside of the ideal alignment. There are five axial (z) distances between the optical components that must be set, some of which are more sensitive to misalignment than others, and the lateral position (x,y) of the secondary mirror which has micron-tolerances. In section 4.3.4, I showed that the distance from the entrance pupil to the first achromatic lens was only relevant to the determination of the maximum lateral field width of the beams, and not of the distance to or curvature of the focal surface. As a result, this requires the user to measure the distance between the final "image" plane to the first lens of the triplet only to the accuracy of a ruler, or to use

the first lens in the Cooke triplet as the limiter of maximum lateral extent. The intercomponent distances for the alignment of the Cooke triplet will set the curvature of the focal surface, while the distance between the triplet and the mirrors will define the divergence/convergence of the individual pencil beams as they propagate toward the axial overlap location at the target. The alignment and accurate relative placement of the Cooke triplet is the task over which I have the least amount of leverage to determine with precision. I'll discuss the best alignment procedure I was able to invent in section 7.1.2. The axial separation between the mirrors sets the distance to the focus, however I showed in section 4.5 that the telescope was capable of operating in a near telecentric condition over a wide range of target distances. To accurately specify the distance to the target to within 1 cm requires setting the axial position of the mirror to a precision of 12.5 microns. I explain how to achieve rough alignment of the mirror set in section 7.1.1. Finally, the x-y alignment of the secondary has the greatest effect over erroneous phase evolution across the aperture of the mirror assembly and also needs to be accurately placed to within a 10 micron tolerance. I give the secondary mirror precision-alignment procedure and some of the serendipitously useful results in section 7.1.3.

7.1.1 Rough Alignment of Telescope

During the full-aperture interferometric test described in section 5.3, I aligned the two mirror telescope by adjusting the position of the secondary mirror to best match the spatial orientation of the primary mirror with respect to the WYCO beam. That final test displayed residual surface curvature that didn't exist in the subaperture measurement technique and therefore could only be present due to misalignments between the two mirrors. Once the telescope is coupled to the rest of the remote microscope experiment, the absolute alignment of the mirrors needs to be verified. Figure 7.1 shows the experimental setup required to "rough" align the two telescope mirrors within the frame of reference of the optics table. Immediately after the turning mirror that directs the spatially-filtered laser towards the AOPG, I installed a beam expander to bring the beam diameter to 1 inch. The collimation of the beam was guaranteed with a standard collimation tester. I used

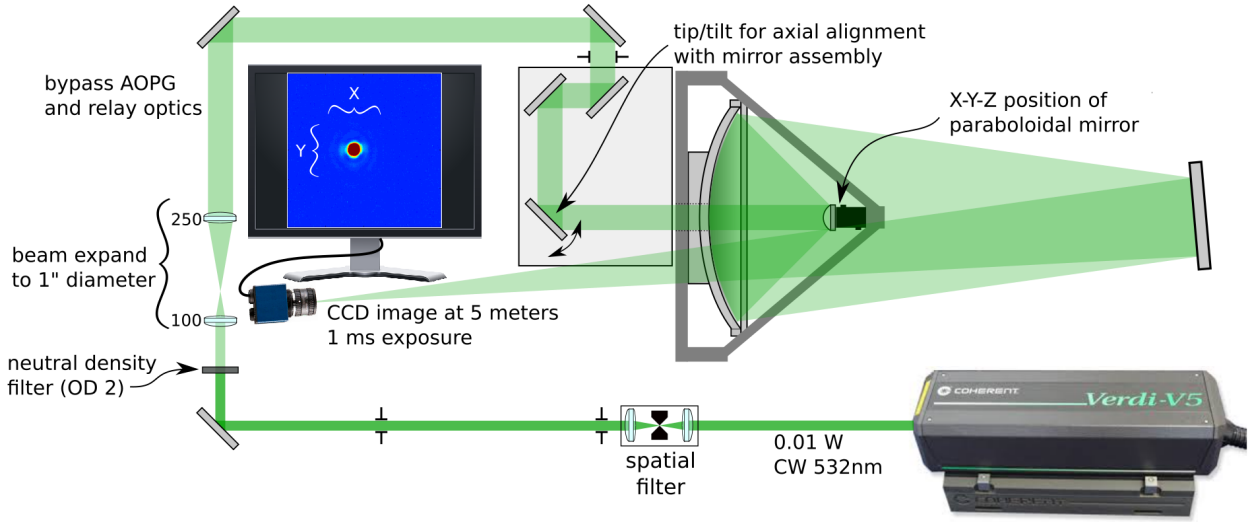

Figure 7.1: The experimental setup for rough alignment of the telescope. After spatial filtering, the collimated laser diameter is expanded to 1". Turning optics are used to bypass the AOPG and relay optics. The enlarged beam passes through the turning optics on the remote microscope optical assembly where the Cooke triplet is removed to avoid focusing the beam before the secondary. After reflection from the secondary, the beam fills the primary and converges toward the focus at 5 meters.

two flat turning mirrors to bypass the AOPG and the majority of the relay optics. I fed the beam directly into the entrance pupil of the remote microscope optical assembly cage system mirrors and removed the polarizing beam splitter, Cooke triplet and quarter wave plate. The collimated beam is large enough to illuminate the entire secondary mirror. If the system is perfectly aligned, every ray reflects from the paraboloidal mirror as if it was emitted from a point source at the conicoidal focus. The beam expands to fill the entire aperture of the primary mirror and then refocuses to a point at 5 meters distance. A CCD camera placed at the focus of the light takes images of the focused spot. Since the total optical power is concentrated to a small point, I turned the laser power to its minimum, placed a OD 2 neutral density filter into the beam path and set the exposure length to the minimum setting of the camera (approximately 1 ms). The CCD shows a saturated central spot with a low-constrast halo. To align the telescope, the secondary mirror position is moved axially which changes the location of the far focus. The camera is moved to the new focus and measurements of the diameter of the saturated spot and diameter of the halo are taken. This process is best when it progesses in one direction, and adjustments of the secondary

mirror are as even as possible. Near the ideal alignment, the spot size and halo will change very little with position and accuracy is limited to approximately ±3 cm of camera z-motion. Once the relative axial separation of the primary and secondary is found, the optomechanical spider, Delrin optical bench, and Thorlabs cage rods are fixed both together and in reference to the optical table containing the AOPG for precision alignment.

7.1.2 Cooke Triplet Alignment

The Cooke triplet is particularly hard to align both independently and with respect to the telescope. There are two goals that the Cooke triplet alignment procedure must achieve, the first is telecentric operation and the second is to generate the desired curvature and distance of the focal surface so that it corrects for the field curvature of the telescope. Typically, with any zoom lens system, an opto-mechanical housing dictates the inter-component separations at every zoom setting using precision cut grooves that express the mathematical relationship needed to properly operate the lens. As I described in section 4.3.4, the Cooke triplet for the remote microscope operates with different assumptions than typical zoom lenses in that it demands telecentric operation and high amounts of induced field curvature, and as a result, no commercial lens package exists that would serve the purpose. The ideal solution to the alignment problem is to fabricate the housing necessary for proper operation, but that was far outside the reach of the budget of the remote microscope effort.

The best solution that I could find was to approach the alignment in two procedures. The first aligns the triplet based on the mathematical coupling of the focal surface width to field curvature. I began with focusing the single enlarged beam from Figure 7.1 to a diffraction limited point with a 250 mm lens outside of the restrictions of the remote microscope platform and cage system. Each of the three triplet cage mount plates are set on independent optical posts and post holders on the optics table. I placed the first lens on axis at a 200 mm distance from the laser beam focus and used an iris (and some cardboard) to restrict the beam to only fill the first lens of the Cooke triplet. This diverging wave contains all possible principal rays of the beams produced by the AOPG, and as such,

the telecentric condition demands that this expanding wave needs to be converted into a planar wave after passing through the triplet. The equations derived in section 4.3.4 specify the shape and position of the focal surface where the curvature is directly coupled to the width. The second lens in the triplet defines an open parameter that, once set, places demands upon the placement of the third lens. I placed the second lens closer to the first lens than I believed appropriate, positioned the third lens to produce the best collimated beam possible and measured the distances between the edges of the cage plates using a ruler. I performed this operation three times across the ideal focal position as calculated by the optical models and equations. This provided me a measurement with respect to the opto-mechanical cage system rather than the difficult-to-locate principal planes or centers of the lenses themselves. Optical models suggest that the elements of the Cooke triplet needs to be aligned to within 500 μm to achieve sufficiently accurate curvature. This distance is admittedly on the edge of the accuracy of a ruler. Unlike most zoom lenses, the triplet separations are linear functions (Figure 4.7), and with these empirical measurements any needed separation for the cage plates of lenses 2 and 3 can be easily calculated from the separation of lenses 1 and 2.

Once the measurements of the lens alignment were complete, I remounted the lenses into the cage system in the remote microscope assembly. One of the failings of this alignment procedure is the large uncertainly of the relative location of the entrance pupil of the triplet when it is mounted in the cage system with folding mirrors. Unfortunately, this is another example where the proper solution is to manufacture the cage system as a portion of the triplet assembly for precision alignment and then place the demand of the input "image plane" at the mechanically-designated entrance pupil. It would have been better to align the triplet using the cage system with a pupil designation aperture and proceding with the same alignment procedures described in the prior paragraph.

After mounting the triplet elements back into the cage system and aligning them using the free-standing measurements, I removed the beam expander and AOPG bypass optics from the table. I programmed the AOPG to produce three sets of axially-symmetric beams with low, medium and high spatial frequencies so that the beams emerged from the surface of the primary

mirror at progressive radial distances. Under the conditions of proper alignment every beam will be collimated and overlap at the same axial location. I estimated the size of each beam along the entire path to determine whether the beam passed through a focus or changed diameter. Over the course of a couple of days, I iterated on the locations of the triplet to achieve the best collimation for each beam.

7.1.3 Phase Flattening and Precision Alignment

After the rough alignment of the telescope and the best effort alignment and placement of the Cooke triplet, the lateral position of the secondary mirror needs to be precision-aligned with the optical axis of the system to remove erroneous non-linear phase curvature across the aperture of the system. Since there are numerous spatio-temporal phases associated with this system, it requires a greater degree of specificity to understand this error, how it needs to be addressed, and consequently what additional information is gained from the process. A single spatial Fourier components of the target is probed using the traveling sinusoidal light field described at length in prior chapters. However, coupling one spatial Fourier component to the adjacent component (which is probed by another set of beams emitted at some previous or future time) requires knowing the systemic spatio-temporal phase offset between the two samples. In the ideal case, with perfect mirrors and optical components in perfect alignment, there are no phase errors between any two samples, or stated another way, the optical pathlength is identical for all beams passing through the system. Without knowing the 2D map of the relationship amongst all Fourier components, the 2D assemblage of sinusoids in the real-space reconstruction will result in an image that is blurry at best and completely garbled at worst. I'll go into all of the contributions to the phase errors of the system in section 7.3, but a lateral offset of the secondary mirror from the optical axis of the system will result in strong phase curvature (OPD) across the aperture of the system. Optical models tolerance analysis implied that the secondary mirror must be placed on the optical axis to within 10 microns in order to achieve diffraction-limited imaging performance and limit the OPD to $\lambda/4$ between any two radially-symmetric beams. What follows is a procedure that provides the

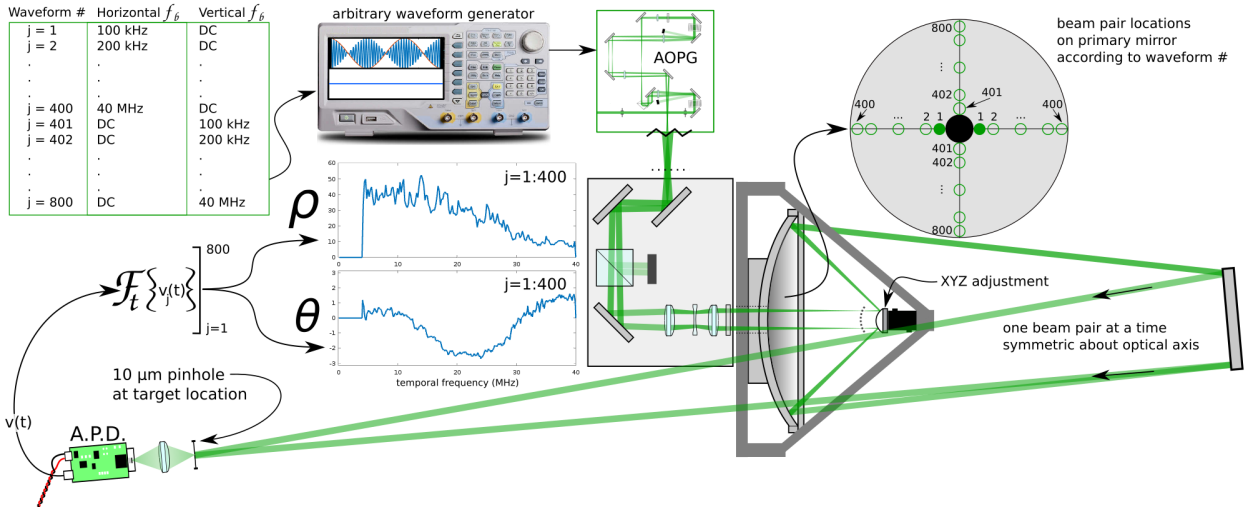

Figure 7.2: The experimental setup used to align the secondary mirror to flatten the phase across the full aperture of the optical system. A set of 800 waveforms (upper left) are sent to the AODs containing a sequential series of two tones that step across the horizontal and vertical temporal frequencies range. These waveform pairs map out a t-pattern on the primary mirror (upper right). The beams interfere on the surface of a 10 μm pinhole and the light that passes through is collected with an avalanche photodiode (bottom left). The time series waveforms are Fourier transformed and converted into amplitude (ρ) and phase (θ) for analysis.

accuracy and precision necessary to align the secondary to within this tolerance.

The phase-flattening experimental setup is illustrated in Figure 7.2. For this procedure, I use the completed opto-mechanical experimental setup that is used for the full remote microscopy efforts but with a different operational procedure. The arbitrary waveform generators are programmed to produce two RF tones at a time for a period of 80 μs. The sequence of the tones begins with a pair of horizontal RF tones that are separated by 100 kHz and with a DC tone in the vertical AOD so that only two beams in the horizontal plane are produced. After 80 μs the horizontal tones are changed to produce a pair of beams with a 200 kHz separation. This sequence progresses until the 400th step when the horizontal temporal frequencies reach their maximum bandwidth separation of 40 MHz with the beams at the edge of the primary mirror. The 401st set of tones switches from horizontal beam pairs to vertical beam pairs, beginning again at a 100 kHz frequency separation and ending at 40 MHz separation at the 800th subwaveform. Representative locations of these beam pairs is shown in the figure as they are mapped onto the primary mirror in a t-pattern. I

placed a 10 μm pinhole at the convergence of the beams at 5 meters distance from the telescope set. The light passing through the pinhole is reimaged onto the surface of the avalanche photodiode using a 25 mm focal length lens. The photocurrent waveform is digitized and sent to LabVIEW for processing as per the process described in Figure 6.12. Each 80 μs subwaveform containing a probed spatial frequency is 1D Fourier transformed and the relevant index of the complex 1D array is extracted and converted into magnitude and phase (ρ, θ). The magnitude and phase values of the entire sequence are assembled into a 1D array and displayed to the user in a real-time plot. Each cycle of data acquisition takes 80 μs $\times$ 800 subwaveforms = 64 ms. A small lateral offset of the secondary mirror will result in steep and non-linear phase accumulation in the direction of offset that will dominate the calculated unwrapped progressive phase in the plot. The lateral position of the secondary mirror with respect to the primary mirror is adjusted using the manual XYZ stage at the fulcrum of the optomechanical spider until the unwrapped phase is as flat as possible. After completion, the system is fully aligned and ready to be used for full data acquisition.

The data taken in order to precision-align the secondary mirror also holds a trove of critical information relating to time-varying phase error due to thermal drift and turbulent eddies. In the following section, I provide some historical perspective on the study of turbulent eddies and the instrumentation developed to measure them. I dissect the data that was just taken and explain how the remote microscope is an unintentional and serendipitous advancement in the field of high frequency atmospheric dynamics.

7.2 Phase Error due to Temperature, Turbulence, and Timing Offsets

7.2.1 Prior Art of Turbulence Measurements

The effects of atmospheric turbulence on a transmitted electromagnetic wave include scintillation, time-dependent optical pathlength variation, fluctuations in the angle-of-arrival of wavefronts, distortions leading to beam divergence and image degradation, and depolarization [164]. Various consequences of scintillation, which is defined as irradiance fluctuations due to turbulence, have

been studied for many decades [152] and a plethora of models exist to predict and compensate for turbulence for applications ranging from long-distance laser communication [6], information transfer time-delay [103], precision in lithographic processing [15], astronomical adaptive optics, and even using the scintillation for diffraction-limited speckle imaging for distant objects [105]. Most of these studies concentrate on characterizing the time-averaged effects of turbulence, and as a result the vast majority of the published literature describes statistical methods, models and experiments.

The standard approach to modeling turbulence is to treat the atmosphere as obeying one of several statistical models, the most canonical of which was established by Kolmogorov [36]. Kolmogorov theory is predicated upon the assumptions that the turbulent nature of the atmosphere is isotropic and that the statistics of turbulent eddies is scalable from the largest mesoscale turbulent structure to the microscale. In this work, Kolmogorov derived the famous mathematical expression for the turbulence structure functional dependence on $r^{2/3}$ (the so called 2/3 law), where r is the spatial scale. Near the planetary boundary layer, the outer scale of the largest relevant eddy (a measure of the size of the turbulent feature) is approximately the same size as the height of the measurement above the ground. Turbulence is almost exclusively modeled as fluctuations in eddy velocity or temperature rather than pressure. The argument supporting this assumption is that pressure fluctuations at some fixed altitude will be small in magnitude and will quickly relax to equilibrium due to the high thermal velocity of atmospheric constituents, whereas temperature diffusion is dependent upon particle collisions. The perturbations in the index of refraction that leads to scintillation are thus caused by pockets of air with a different local semi-stable temperature than the surrounding atmosphere. Standard derivations of Kolmogorov turbulence prove that fluctuations in the index of refraction follow the same structure function law as velocity turbulence and can be handled with the same statistical apparatus [164].

A typical approach for quantifying the turbulent energy is to take the Fourier transform of the temporal oscillations to compute the power spectrum. In certain atmospheric energy transfer models this provides the most valuable metric of turbulent energy, but like all temporal-averaging values, it provides no insight into the instantaneous turbulent field. There are far more involved

models which calculate the higher moments of the field [147], and others that use Zernike polynomials to decompose the Kolmogorov turbulence spectrum [122]. This is now a standard approach used to quantify the error of a wavefront at a telescope after propagating through the entire atmospheric column [37]. More recent efforts have shown the Kolmogorov statistical model does not well match propagation through the entire atmosphere where turbulent layers are bounded by tropospheric-scale anisotropies producing a so-called non-Kolmogorov regime [172], [40], [46], which should be analyzed using two different power spectra relating to the isotropic and anisotropic turbulence [132].

The instruments and experimental measurements used for characterizing atmospheric turbulence have typically concentrated on investigating only one aspect of turbulence; namely optical pathlength fluctuation, accumulated time-delay, image degradation or angle-of-arrival of aberrated wavefronts, with the first topic being the most useful metric for most applications. A study of the turbulent fluctuations resulting from high velocity air-flows passing through a heterodyne Michelson interferometer used for lithographic measurements showed that typical OPL variance was less than 10 nm over a 15 cm long arm [15]. In another study, they constructed an interferometer with two 1 m long arms separated in height to study variations in the optical path at different vertical distances from the ground and measured OPD of up to 200 nm [63]. By mixing the two frequencies of a Zeeman-split HeNe, they produced a 2 MHz reference beat. The two beams from the vertically-separated arms were recombined to produce a beat frequency which was compared to the 2 MHz reference and changes in pathlength as small as 16 nm were measured on an 8 Hz cadence. Similar instruments have been used for long baselines, measuring time-averaged OPD at distances up to 350 m [76]. It has been suggested in the literature that using different wavelengths of light over long distances would provide two different indices of refraction from which the OPL could be calculated and the error of optical measurements over long baselines could be significantly reduced [155] [49]. This technique was demonstrated to improve the accuracy of microwave measurements of distance by an order of magnitude [12].

For some applications, this OPL variance is converted into signal path delay fluctuations,

with one study showing up to 3 ps of arrival delay over a 4.3 km horizontal free space propagation [103]. A recently published technique uses frequency combs to measure the optical phase noise and free-space optical time-frequency transfer to femtosecond resolution [142]. Whereas measurements using CW source interferometry are limited in time by the uncorrelated non-Kolmogorov phase evolution due to slow environmental changes, the coherence of the frequency combs allows comparisons of pathlength over many hours and long distances. Due to this extra stability in turbulent measurements, [142] found that the turbulent OPD over a 2 km horizontal path follows the Kolmogorov scaling with no roll off at the outer scale from 100 μHz to 10 Hz. This is in conflict with prior models and experiments that had shown that phase power spectral density should be subdivided into four distinct temporal regimes.

Several studies examine Kolmogorov and anisotropic turbulence from the perspective of fluctuations of the angle-of-arrival (AoA) of the wavefront [157], [110]. In most long-distance atmospheric progagation studies, the reciever is much smaller than the lateral spatial extent of the wave and so a change in AoA is interpreted as a slope of the normal of the incoming wavefront and therefore just an aperture-integrated temporal phase error.

One of the few instantaneous AoA experimental techniques is called the small aperture beam technique (SABT) [112]. A small-diameter collimated laser beam propagates across a turbulent flow and the lateral position offset was measured using an autocollimator as a means to determine the wavefront slope, which when integrated yields the OPD. This technique has been successfully used for calculating the OPD for far-field adaptive-optics applications [35]. This instrument design was improved by using multiple beams up and downstream in a turbulent flow in order to calculate the slope of the wave front over a finite aperture [92], [85]. From this wavefront spatial sampling the OPD of the entire wavefront can be calculated by integration. This is the identical calculation used in traditional Hartmann wavefront sensors, but at much higher sampling frequencies than was available at the time (approximately 1 kHz). Recently 100 kHz 2D Hartmann wavefront sensors have been developed [4]. Additional improvements to SABT employed fast turning-mirror scanned beam systems for cross-stream wavefront measurements [59], and incorporation of polarimetry

components enabled high cadence measurements of turbulence-induced weak depolarization [146]. In all of these cases, the fast measurements of wavefront sensing is used to provide experimental data for time-averaged statistical models.

7.2.2 Turbulence Measurements Using the Remote Microscope

The measurement scheme described in section 7.1.3 that is used to provide fast visual feedback for optical alignment phase flattening, not only provides measures of the limits of practical resolution for Fourier sampling remote microscopy in the presense of turbulence, but also serendipitously contains a wealth of information that can be used to measure and uniquely characterize small-scale low-velocity eddies. The coupling between temporal and spatial frequencies vis-a-vis the separation angles of the Doppler-encoded beams can be exploited to differentiate OPL fluctuations in the direction of beam travel from AoA fluctuations which result in lateral offsets of one or both beams in an acousto-optic-generated pair. This differentiation is important for remote microscopy because in-line OPL differences are simply phase errors of a spatial Fourier sample of the target while an AoA fluctuation will include a lateral shift of the FOV of the microscope on the target and can not be corrected and incorporated into the Fourier-basis data set for a remote-microscope image reconstruction. What's surprising is that the degree of decoupling of these two related components of turbulence is not achieved by any previous turbulence characterization instrument where all of the induced errors resulting from the various turbulent processes are reduced to one of the desired calculated values, traditionally phase error or OPD. The remote microscope has a sensitivity advantage for AoA unmatched in prior turbulence studies which I will explore. I'll first describe the data collected and the processed products and then I'll present a mathematical justification for separating in-line OPD from AoA fluctuations.

I used the data measurement scheme described in section 7.1.3 to collect 2000 contiguous 64 ms t-pattern complex Fourier component data cycles for a total of 128 s. Each subwaveform contains the 80 μs time-series measurement of a single horizontal or vertical spatio-temporal traveling sinusoidal illumination pattern passing over a 10 μm pinhole in front of the APD. The sequence

of spatial frequencies is stepped every 100 kHz from 100 kHz to 40 MHz. I converted the complex values for each time subwaveform into magnitude and phase, the latter on which I used a standard phase unwrapping algorithm. For both the magnitude and phase of the horizontal and vertical subwaveforms I computed the temporal mean and standard deviation values. The mean horizontal magnitude and phase and their standard deviations are shown in Figure 7.3 and the same values for vertical phase are shown in Figure 7.4.

The mean horizontal magnitude, which is just a time-averaged horizontal slice of the OTF, shows a relatively linear drop from low frequencies to high frequencies but contains a significant amount of variation off of the trend line which must be accounted for during the construction of the instrument response function. The linear drop off of the OTF with higher frequencies is consistent with the OTF of a traditional optical system, as was illustrated in Figure 2.4, rather than the theoretical OTF of the $\mathcal{F}$-BASIS system shown in Figure 2.5. Similarly, the standard deviation of the horizontal magnitude shows the same trend decreasing linearly with frequency. The cause for this also has a diagnostically useful effect on the phase measurement which I'll get to in a moment. When the standard deviation is normalized to the mean value (not explicitly plotted, but evident from panel A and B of Figure 7.3) it shows that the lower spatial frequencies have lower amplitude variation than higher frequencies. I'll return to this observation later. What is surprising is that the time-averaged magnitude errors for two adjacent frequencies (two adjacent samples in Panel B) can vary by more than a factor of 2. This suggests that some spatio-temporal frequencies have a greater degree of amplitude instability than others. I honestly have no explanation for this result.

The mean horizontal phase shows a maximum absolute phase deviation of less than 1/6th of a spatial period - functionally phase flat across the full temporal frequency range of the system. The quartic or sextic polynomial evolution of phase across the aperture is very likely attributable to a small axial misalignment of the secondary mirror and a minor contribution due to gravitational deformation of the primary mirror. Finally, the most intriguing result is the standard devation of the horizontal phase which clearly matches an increasing linear trend toward high frequencies (shown in blue). This is coupled to the linear decrease in magnitude with increasing temporal

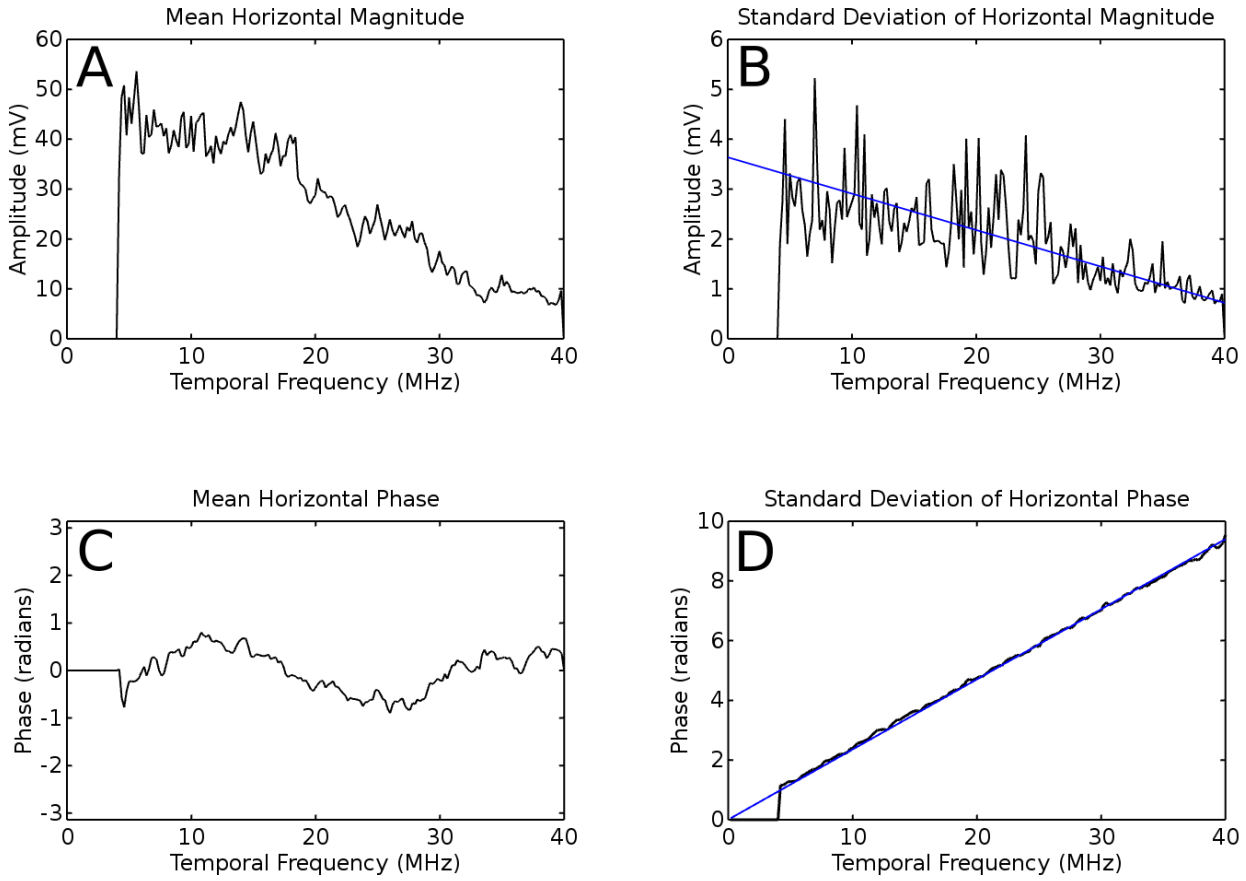

Figure 7.3: The time-averaged horizontal magnitude and phase of 128 seconds of t-pattern phase-flattening alignment data and their associated standard deviations. A) The time-averaged mean value for each targeted temporal frequency extracted from the Fourier transform of the time-series waveform. The magnitude exhibits a diagnostic linear drop-off from low to high frequencies. B) The standard deviation of the magnitude of the time-averaged data plotted in Panel A. Adjacent frequency measurements show up to 2x differences in errors, but the trend shows an expected linear drop off of error with amplitude magnitude. C) The phase of the same time-averaged mean values. The phase exhibits a flat response across the slice of the OTF. D) The standard deviation of the calculated phase shows a linear increase with increasing temporal frequency.

frequency and is the primary bit of evidence that allows us to separate OPD from AoA fluctuations and to which I'll return shortly.

Figure 7.4 shows the equivalent results in the vertical magnitude and phase measurements. As with the horizontal magnitude, the mean vertical magnitude exhibits a linear decrease with increasing frequency. The standard deviation of these values shows a linear drop off, but the normalized standard deviation shows much more amplitude-stable lower frequencies in comparison

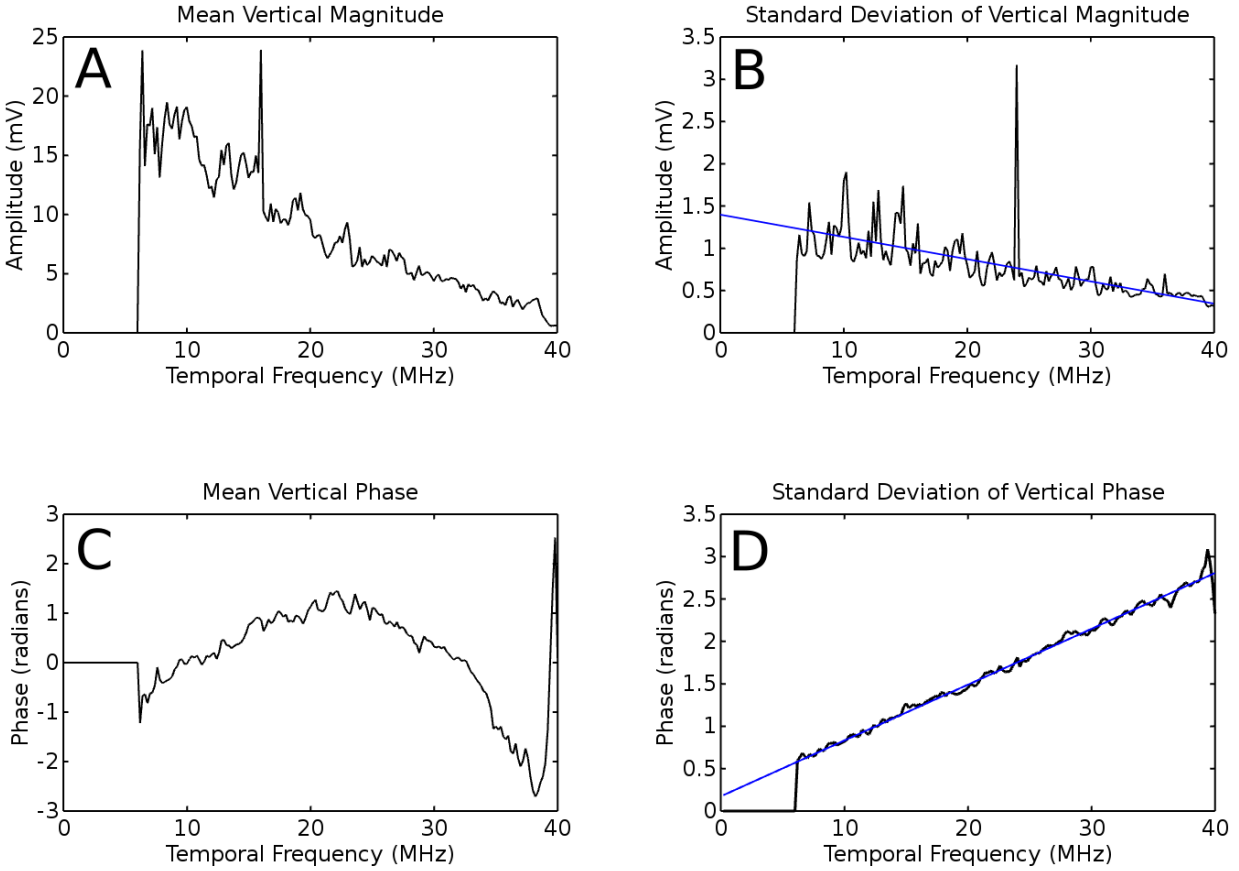

Figure 7.4: The time-averaged vertical magnitude and phase of 128 seconds of t-pattern phase-flattening alignment data and their associated standard deviations. A) The time-averaged mean value for each targeted temporal frequency extracted from the Fourier transform of the time-series waveform. B) The standard deviation of the magnitude of the time-averaged data plotted in Panel A. The anomalous spike at 24 MHz is ignored in the trend line calculation. C) The phase of the same time-averaged mean values shows a curvature consistent with a mirror shape sagging due to gravity. D) The standard deviation of the calculated phase shows a linear increase with increasing temporal frequency.

to the higher frequencies than does the horizontal data. Other than a spike near 24 MHz, the variance of standard deviation between adjacent frequencies is approximately 3/4 of the same metric in the horizontal measurements. In short, it seems that the vertical temporal frequencies are more amplitude-stable than the horizontal. The amplitudes of the vertical measurements at any frequency are approximately 42% of the horizontal. Since the waveforms all had the same temporal length and measurement and processing technique, I can only attribute this to differences in the diffraction efficiencies of the two AODs in the AOPG. The mean vertical phase exhibits a

quartic polynomial form with a maximum divergence from the mean of less than 1 spatial period, and again is attributable to a combination of telescope misalignment and gravitational deformation of the optical surface. Finally, the standard deviation of the phase shows a similar, well-behaved linear dependence with frequency as with the horizontal data.

7.2.2.1 Longitudinal OPD fluctuations

The interference pattern generated by two intersecting collimated plane waves at an arbitrary angle was expressed in Equation 2.18 and illustrated in panel A of Figure 7.5. By rotating the coordinate system to the plane of the two beams (XY), the interference equation simplifies to the one dimensional form:

$$\vec{I}_{12}(x,t) = I_o\Big[1 + \frac{m}{2}\cos\big((\omega_1 - \omega_2)t - (\vec{k_{x1}} - \vec{k_{x2}})x + (\phi_1 - \phi_2)\big)\Big] \tag{7.1}$$

The difference in the temporal frequencies $(\omega_1 - \omega_2)$ defines the temporal beat frequency of the pattern, the difference in the wave-vectors defines the spatial period, and the differences in the phases of the individual beams defines the spatial phase shift of the interference pattern.

Assume a uniformly thick parcel of air denser than the surrounding atmosphere is placed in the path of beam 2 and induces a longitudinal OPD of 266 nm without inducing any change in the propagation direction of the beam, i.e. k_{x2} is unchanged after the beam exits the air parcel. At a nominal laser wavelength of $\lambda = 532$ nm, this represents a phase shift of the beam by -π. The total phase shift of the interference pattern is then $(\phi_1 - \phi_2 - \pi)$. Unsurprisingly, a shift in the phase of a beam results in the exact same phase shift in the interference pattern.

The AODs Doppler shift the frequency of the laser light by up to $\pm$ 40 MHz. Laser light at 532 nm has a temporal frequency of 564 THz, so the Doppler frequency shift represents a fractional change in laser wavelength of 7e-8. So, the 266 nm of OPD induced by the parcel of dense air will represent an identical phase shift of the beam regardless of the acousto-optic frequency/wavelength shift in the system. Longitudinal OPD fluctuations will therefore *identically* affect all temporal frequencies used by the remote microscope, and by extension, we would expect that all of the

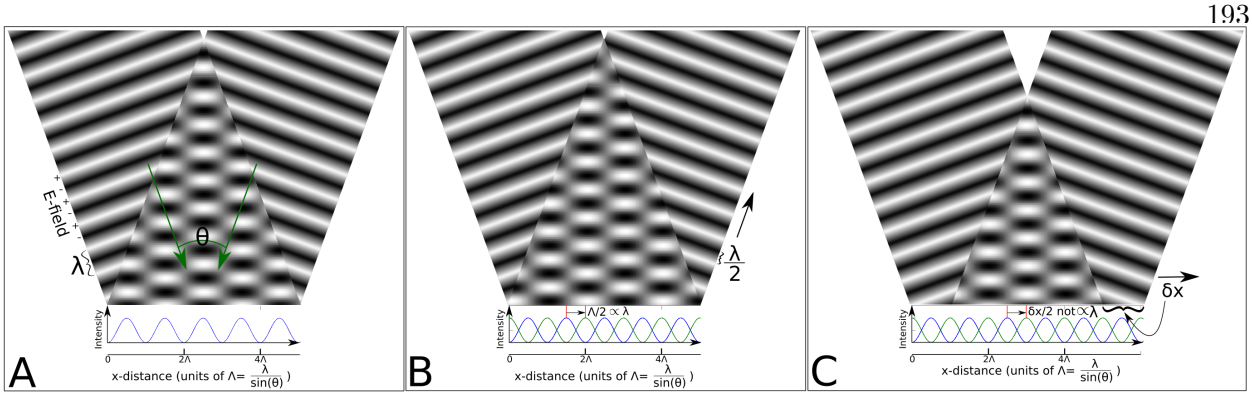

Figure 7.5: A) Two collimated beams of wavelength λ arrive at an intersection plane with a full separation angle of θ within the plane of the paper. The bright and dark sinusoidal pattern illustrates the electric field value at an instant of time. The triangular area of overlap shows the summation of the field while the blue sinusoidal waveform below plots the intensity of the illumination field. B) An offset of the right beam along the direction of the beam travel by an OPD of $\lambda/2$ generates a shift in the illumination intensity (green sinusoid) of one half the period of the fringes $\Lambda/2$ regardless of the separation angle. C) A lateral shift of $\delta x = \Lambda$ parallel to the plane of interference produces an illumination fringe shift of $\delta x/2$ (green plot) and is not proportional to the period of the fringes Λ.

spatial frequencies probed would have the same phase error response from turbulence, i.e. the standard deviation of phase should be best fit with a line with zero slope. By examining the standard deviation of phase plots in the last two figures, this is obviously not the case.

7.2.2.2 AoA fluctuations

Angle-of-arrival error induces a completely different phase error response than longitudinal OPD fluctuations (illustrated in panel C of Figure 7.5). Assume a parcel of dense air with a OPL wedge spatial distribution is placed across beam 1. The gradient in the OPL across the beam acts like a prism and induces a wavefront tilt which changes the beam propagation direction. Even a miniscule change in k_{x2} will cause a significant lateral shift of beam 2 at an observation plane sufficiently far away.

For example, a generous value for the time-bandwidth product of the AOD is TB=400. With 40 MHz of bandwidth, the minimum resolvable frequency step is 100 kHz. For the remote microscope, every 100 kHz step is separated in angle by 0.0036°. The angular equivalent of a 10

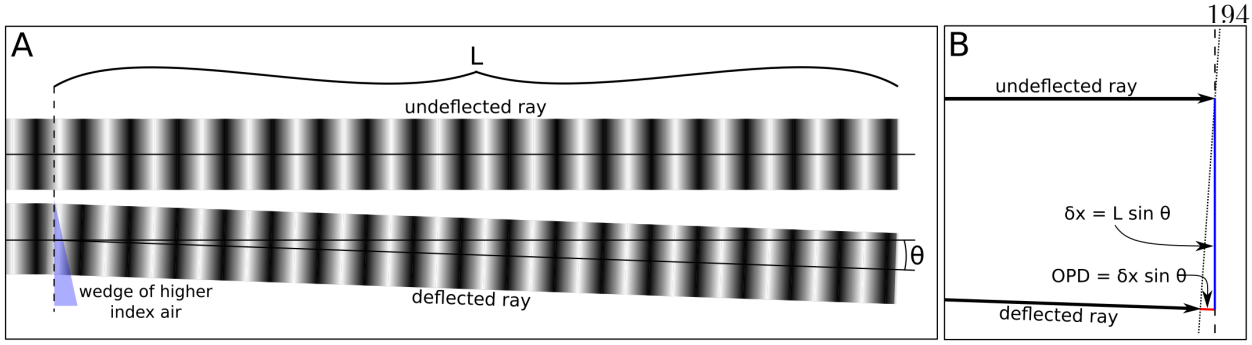

Figure 7.6: A) An undeflected ray travels a distance L to the interference plane. At some future time a wedge parcel of air deflects this beam by some angle θ. B) A zoom-in of the plane of interference. The dashed line designates the original OPL of the undeflected ray wavefront. The dotted line is new tilted wavefront. The lateral beam displacement shown in blue is δ_x and the OPD produced by this angular deflection is shown in red.

kHz step (1/10th of this theoretical resolvable step) is therefore 0.00036°. If the wedge-parcel of air is located 5 meters away from the interference plane (the maximum possible distance for the remote microscope), this change in propagation angle produces a lateral spatial shift of the beam by $\delta x = 31\mu m$ which is a small fraction of the 5 mm beam width. An illustration of an undeflected ray and a ray deflected by some higher index parcel of air is shown in Figure 7.6. The optical pathlength difference for the deflected beam to reach the same plane as the undeflected beam is just OPD = $\delta_x \sin\theta = 0.193$ nm, or a fractional change of less than $4e^{-}11$ (0.193nm/5m). The miniscule angle of deflection produces negligible OPD, and instead an angular deflection due to a turbulent parcel of air can just be modeled as a lateral translation of the beam in the plane of interference.

Returning to Equation 7.1, a lateral shift of beam 2 won't effect the temporal frequency ω_2 and is too small of a shift in wave vector k_{x2} to resolve, but will induce a phase shift of beam 2, and thus also a phase shift in the interference pattern equal to:

$$\Delta\phi_{\delta x} = \frac{K_x \delta_x}{2} = \frac{\pi \delta x}{\Lambda_x} \tag{7.2}$$

where K_x is the k-vector of the interference fringes, not the beams, δ_x is the shift in position of the beam in units of distance (e.g. mm), and Λ_x is the spatial period of the interference fringes. The division by two is due to the fact that the illumination field has twice the spatial frequency

than the electric field of the beams, so a shift in δ_x that generates a shift in illumination field phase of π will only cause a change in electric field phase of one beam by $\pi/2$. This shows that for a lateral spatial shift δ_x the induced phase error $\Delta\phi_x$ is proportional to the illumination spatial frequency K_x. Since the remote microscope couples spatial frequencies to temporal frequencies via a 1:1 relationship, lateral spatial shifts will manifest as a linearly increasing phase error in the time-averaged temporal frequency measurements. For the highest spatial frequency with a period of $\Lambda_x = 10$ μm, a 31 μm lateral offset represents a 6π phase error, while it is only a $2\pi/3$ for fringes with a 100 μm spatial period. This linear increase in phase error is exactly the behavior we see in Figures 7.3 and 7.4. On average, the turbulence causes beam displacements equally for all beams, and any particular beam displacement represents a phase error dependent upon the spatial frequency of the interference fringes.

In addition to producing frequency-dependent phase error, the lateral spatial shifts produced by AoA fluctuations cause the remote microscope to illuminate and probe the Fourier component of a different location on the target. Unlike the phase errors induced by longitudinal OPD fluctuations, this induces erroneous signal that cannot be corrected by a phase shift, and for which there is no indicator in the data. If a strongly reflective dot lies 10 microns outside of the nominal FOV of the microscope, AoA fluctuations will cause this dot to randomly get sampled during data acquisition, ruining the reconstruction process.

Prior studies of OPD fluctuations are all in good agreement with reported values in Kolmogorov turbulence consistently around 200 ppb [63], [142]. This value is well above the measured values made by the remote microscope. Ostensibly, this could be attributed to the fact that the remote microscope experiments were performed on an optical table in a protected laboratory environment. Unfortunately, that has dire consequences for using a $\mathcal{F}$-BASIS remote microscope in natural environments with a thick atmosphere where OPD fluctuations could be 3 orders of magnitude worse. This is less of a concern on Mars where the atmospheric pressure is less than 1% of that on Earth and no concern at all on airless bodies.

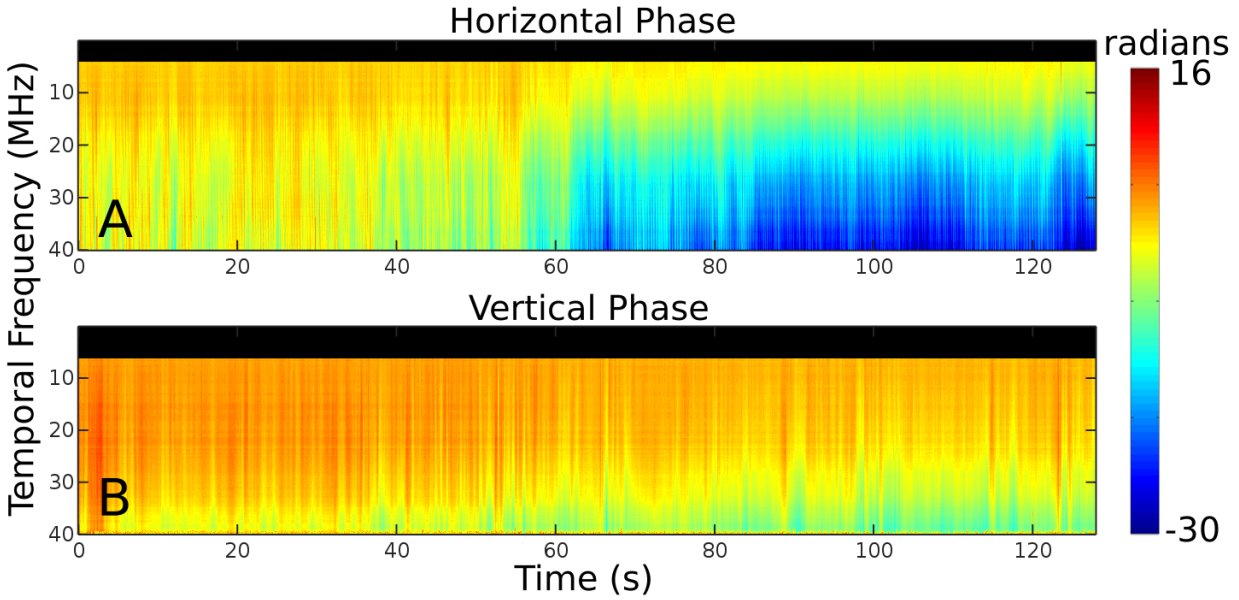

Figure 7.7: The complex Fourier component of the 128 s of t-pattern data for each temporal frequency was converted into magnitude (not plotted) and phase. A) The phase of the horizontal sequence exhibits a trend of higher phase at low temporal frequencies (redder color higher on the plot). The absolute phases of the Fourier components generally decrease with time, showing a significant step down at 62 s. B) The vertical phase also shows the general behavior of lower temporal frequencies having higher phase, but the decrease in average phase per time unit is much less pronounced than in the horizontal sequence.

7.2.3 Decomposition of the Turbulent and Thermal Drift Error

I've shown that the two forms of turbulent fluctuations will manifest differently in the phase error of the measurements, and by examining the results of the phase-flattening t-pattern data it is clear that AoA fluctuations are by far the dominant form of error. In addition to these high-speed fluctuations, long time-constant thermal changes in the laboratory lead to progressive phase drift. I processed the 128 seconds of t-pattern data to separate these effects, and the results are shown in the following figures. The raw phase data for horizontal and vertical measurements are illustrated in Figure 7.7 with phase measured in radians. The frequency from 0 to 40 MHz is plotted on the y-axis, while the x-axis is the time index. The large black sections contain no useful data because of obscuration by the secondary mirror, and so have been nulled. These time-series plots contain short time-constant variations that are strongly correlated across all frequency measurements generating

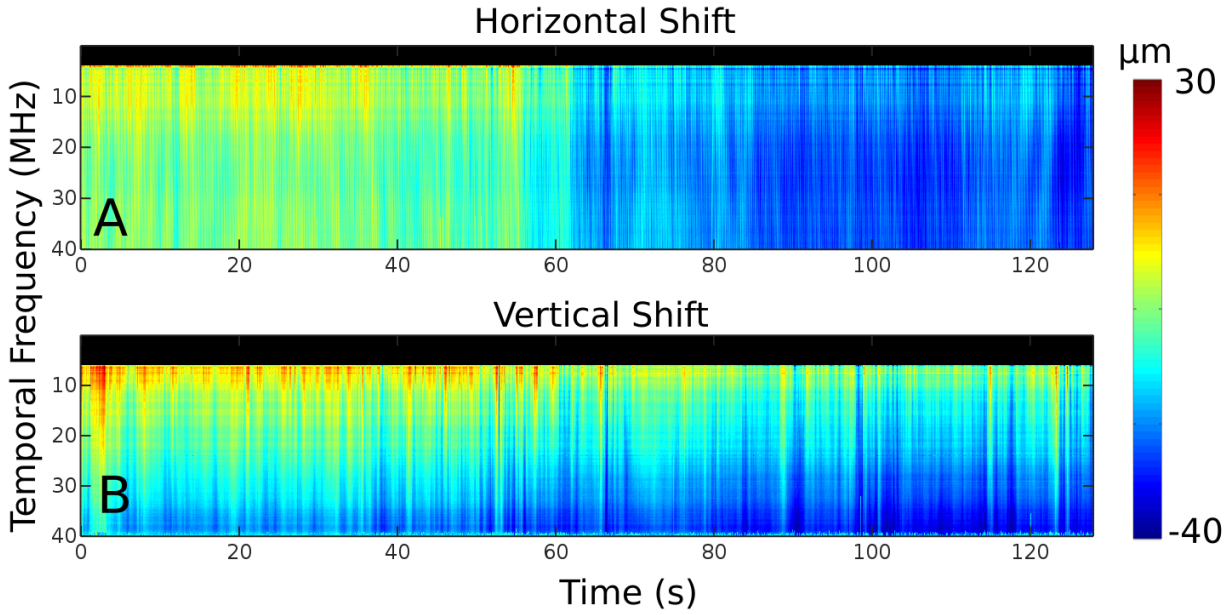

Figure 7.8: The equivalent lateral shift of one beam for each measurement to achieve the measured phase offset described above for the 128s of t-pattern data. The phase offsets were converted into lateral offset for the horizontal (A) and vertical (B) portions of the t-pattern using Equation 7.2. A) After conversion to beam offset, the trend of higher phase offsets for lower frequencies displayed in Figure 7.7 has largely disappeared for the horizontal data suggesting that all beams are equally displaced averaged within a single time-sample. B) The vertical beam shift exhibits a bias of beam displacement from low to high temporal frequencies - an effect consistent with primary mirror deformation due to gravity.

the overall vertical streakiness in the plots. The data also shows a strong general trend toward lower phase measurements as time goes on, as is indicated by bluer colors. The last important trend to note is the overall large peak-to-peak constrast for higher frequencies while the variations in phase for low frequencies are much more subdued. This is the same trend expressed in the standard deviation of phase plots in Figures 7.3 and 7.4.

I processed this data under the assumption that the phase error was dominated by the AoA fluctuations as implied by the previous section, with the expectation that if the data obeyed different statistics then the resulting analysis would produce incongruent results. I computed the lateral distance offset of one beam required to account for the shift in phase for every frequency-time point in the set according to Equation 7.2. These results are shown in Figure 7.8. The general trend toward lower lateral offset values as time goes on shows that there is slow temperature evolution

in the laboratory (although it was not explicitly measured). The implications of a system-wide temperature change aren't immediately clear, but if we apply some logic, there are only a limited number of reasonable consequences. A general rise in temperature due to heat build up in the laboratory from the electronics exhaust fans could result in physical expansion of materials which translates to increased distances between optical components or a deformation of the aluminum mirror set. In Chapter 3, I showed that small changes in temperature for the mirrors would result in roughly-isothermal expansion of the optical surfaces, and that the deformation would be preferentially radially symmetric. Distortions and misalignments of the optical system would result in non-linear effects with position on the mirror and thus with temporal frequency of the waveforms. The slow beam migration during t-sample data is visible during data acquisition and is completely corrected by the user by slightly re-directing the beam to the center on the pinhole by adjusting the 6" turning mirror on the optics table. This tells us that the lateral offset of all beams is exactly identical - there is no optical deformation occuring, it is simply a pointing migration. So, this thermal drift can be modeled as a frequency-independent slow beam position shift. I also claim that static deformation of the mirror would manifest as a beam offset, and so, along with acousto-optic diffraction efficiency variations the frequency, it is reasonable to expect that any constant deformation of the beams would show up regardless of the temperature of the system. I averaged the lateral shift with respect to time and define this as the instrument reponse function (IRF) - a static beam position offset that must be applied for all acquisitions. The horizontal and vertical components of this are shown in Figure 7.9. Any temperature or turbulence induced offset will be added to the offsets caused by the IRF. As was done by [172], I fit the long time-constant evolution of the horizontal lateral-shift data in the last figure with a 3rd order polynomial to account for time-dependent thermal gradients. The result is shown in panel A of Figure 7.10. Subtracting this shift as a function of time from all frequencies results in panel B, where the short time-constant lateral distance offsets are of comparable size for all frequencies. A zoom-in of a small time subset of this series is shown in panel C. An identical analysis was performed for the t-pattern vertical data, the results of which are shown in Figure 7.11.

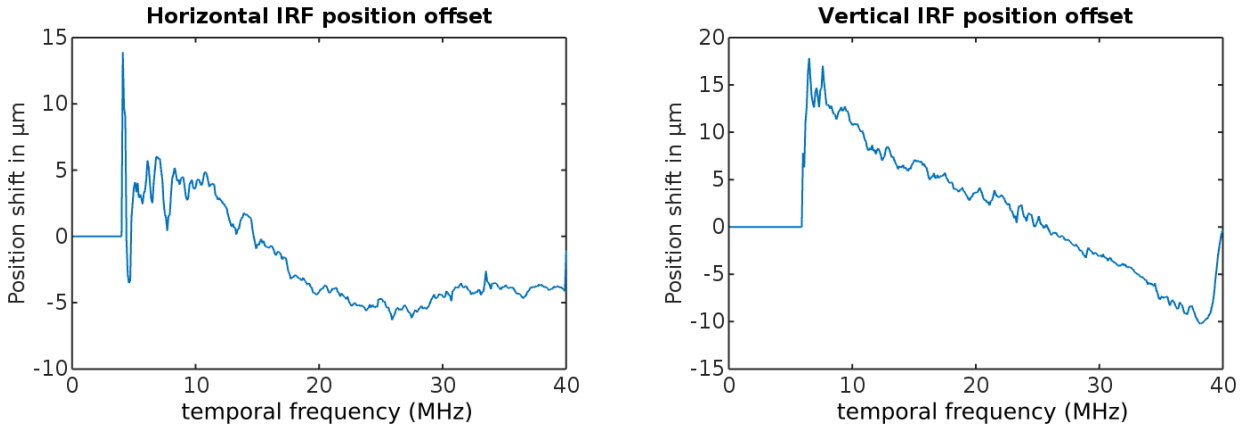

Figure 7.9: The horizontal and vertical instrument response function (IRF) derived from the 128 s of t-pattern data. The IRF is the time-averaged calculated relative beam position offset necessary to cause the measured phase errors. As the time-averaged value, the IRF quantifies the static beam offset due to mirror deformation and system mis-alignment. The horizontal IRF shows quartic curvature characteristic of optical misalignment of the primary and secondary aspheric mirrors. The vertical IRF exhibits a linear trend from low to high temporal frequencies consistent with beams that are displaced more the further they are from the center of the mirror and the support fixtures.

The turbulent eddies can be seen moving horizontally across the mirror as well as clearly moving in and out of the plane of the distributed laser beams. If there had been a significant contribution of OPD due to longitudinal pathlength contributions such as would be the case if a uniform slab of air was placed in front of the beams, there would be a frequency-independent longitudinal phase shift which would not be removed linearly in lateral offset space. In short, it is safe to conclude that the phase errors due to turbulence are almost exclusively determined by AoA fluctuations and this effect is far greater than the longitudinal OPD differences. This observation provides the basis to propose instruments as a new type of small aperture beam technique (SABT) atmospheric measurement instrument. In all other turbulence-measurement instruments, OPD differences are computed using standard multi-beam interferometic fringe counting techniques which are inherently limited by detection certainty, measurement speed and instrument cost. The standard techniques have used single wavelength light sources which leads to an inevitable convolution of the two effects (longitudinal OPD and AoA) when restricting the measurement to overall OPD or AoA (e.g. [63]). In the case of the recent frequency comb experiments, their apparatus used a plethora

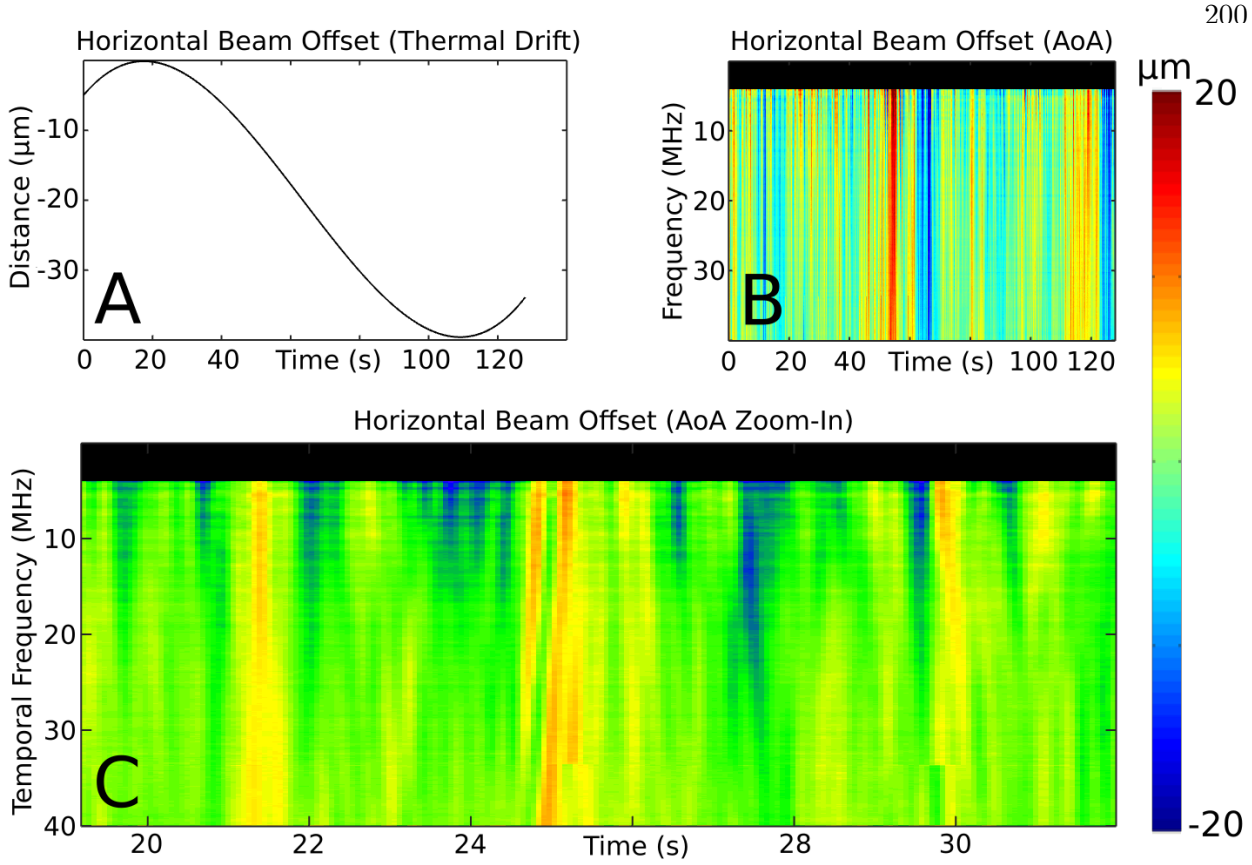

Figure 7.10: Decomposition of the horizontal beam offsets responsible for the measured phase errors of t-pattern data into the separable components of long time-scale thermal drift and short time-scale angle-of-arrival (AoA) variation. A) The 3rd order polynomial best-fit to the slow change in beam pointing due to thermal drift of the optical system. B) The 128 seconds of horizontal beam displacement from Figure 7.8 after subtracting the IRF and the thermal drift from panel A. The beam displacement magnitude is flat across all temporal frequencies and only short-time constant variations due to AoA fluctuations are seen. C) A zoom-in of 13 seconds of the AoA fluctuations showing beam displacement resulting from parcels of turbulent eddies passing across the mirror (red and blue non-horizontal streaks).

of laser wavelengths, but the measurement was fundamentally a single beam-path and therefore had no lateral spatial information [142]. By coupling illumination laser frequency shift to spatial location and transforming the detection of pathlength differences to an incoherent measurement, the remote microscope is ideal for use as a high-speed atmospheric 2D turbulence mapper.

The relevant frequency-dependent time constants can be extracted from the t-pattern data to tell us how long we can expect the atmospheric and system phase errors to remain effectively constant. To compute the time constant for the slow thermal drift, the lateral position function of

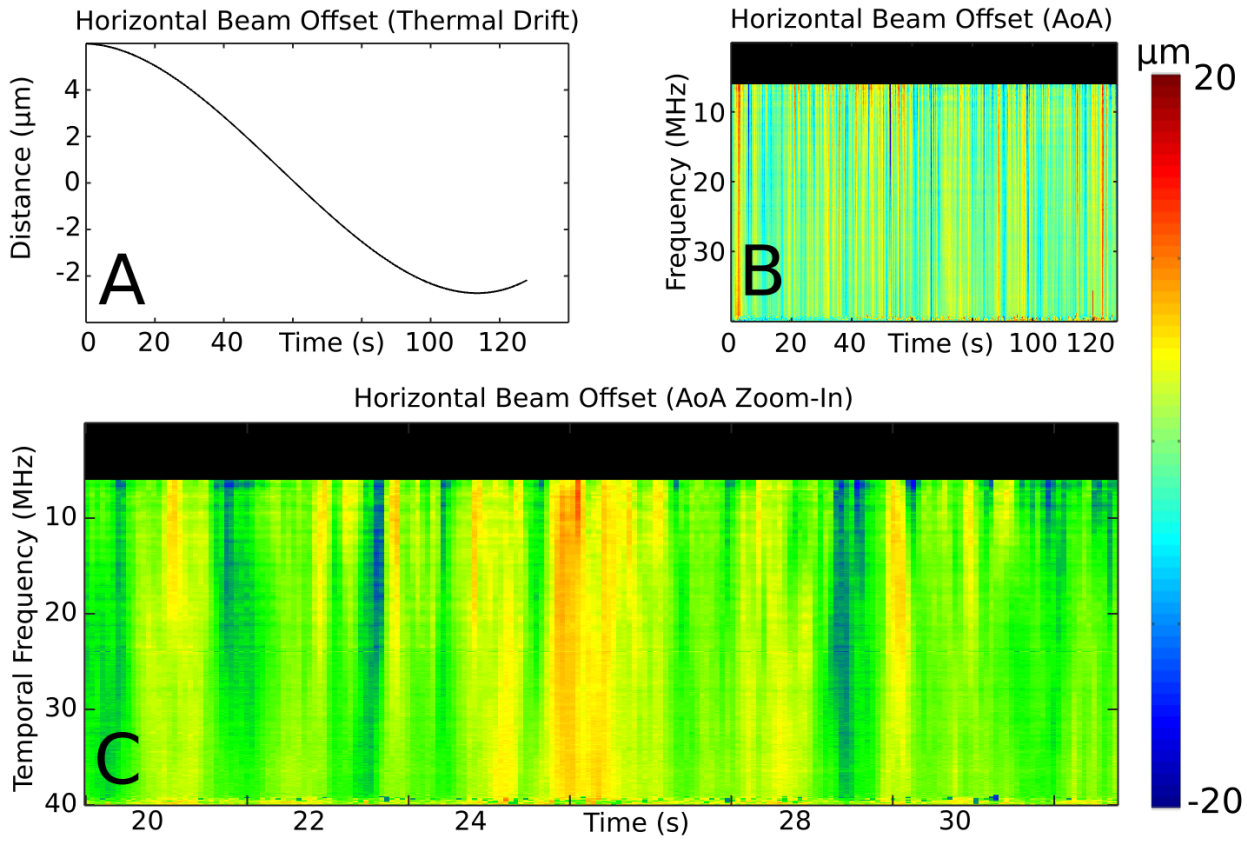

Figure 7.11: Decomposition of the vertical beam offsets responsible for the measured phase errors of t-pattern data into the separable components of long time-scale thermal drift and short time-scale angle-of-arrival (AoA) variation. A) The 3rd order polynomial best-fit to the slow change in beam pointing due to thermal drift of the optical system. The thermal drift is significantly smaller than in the horizontal components. B) The 128 seconds of horizontal beam displacement from Figure 7.8 after subtracting the IRF and the thermal drift from panel A. As with the horizontal data, the beam displacement magnitude is flat across all temporal frequencies and only short-time constant variations due to AoA fluctuations are seen. C) A zoom-in of 13 seconds of the AoA fluctuations showing fewer effects from turbulent eddies passing across the mirror the horizontal AoA plot (Figure 7.10). This is consistent with the expectation of near zero net vertical eddy velocities.

panel A in Figures 7.10 and 7.11 is converted back into phase via equation 7.2 and the average time (per frequency) for a phase shift of $\pi/2$ is measured. For the horizontal data the thermal drift time constant $\tau_{TD_H} = 71.54s \cdot MHz$ or 0.177 s per micron of resolution. For example, the phase remains constant to within $\pi/2$ for 3.57 s for 20 μm resolution images. The vertical data is more stable with a time constant $\tau_{TD_V} = 469s \cdot MHz$ or 1.17 s per micron of resolution. The horizontal and

vertical thermal drift time constants are different by nearly an order of magnitude, suggesting that one of the AODs in the AOPG has a larger thermal load and thus changing temperature faster than the other. A slightly more complicated process is performed for the short time-constant data since the time-local derivative changes drastically with turbulent conditions. The AoA lateral offsets are converted back into phase without the thermal drift contribution, and the instantaneous phase step at every frequency-time point is calculated. For every frequency row, I step through the array and calculate the time ellapsed until a phase shift of $\pi/2$ is accumulated. The mean time constant value of the horizontal and vertical AoA phase error are almost identical at $\tau_{AoA} = 6358ms \cdot MHz$ or 1.08 ms per micron of resolution.

7.2.3.1 Angle of Arrival CMOS Measurement

The t-pattern data attributing the phase errors to short time-constant AoA variations is convincing, but does not constitute absolute proof. I performed an additional experiment, similar to standard published AoA measurement techniques using fast 2D arrays [4], shown schematically in Figure 7.12. The AOPG is programmed to emit a single beam offset from the optical axis to avoid the central obscuration. This beam passes through a constricted iris at the input pupil (the nearest "image" plane) to reduce the beam diameter to around 300 μm. This narrow beam is projected to the target location using the standard remote microscope optical assembly. I placed a Pt. Grey Flea II CMOS camera at the location of the target and acquired 4.6 seconds of 60 Hz video. Using a simple 2D Gaussian peak fitting algorithm I located the centroid of the projected spot and plotted the time series of this data (shown in panel B). The maximum horizontal position range (x) is approximately 130 microns while the maximum vertical range is 80 microns. This difference in horizontal and vertical variance is in good agreement with the results found using the t-pattern data. Although the t-pattern data provides a valuable high-cadence measure of the component of the beam wander in the Cartesian axes orthogonal to the beam propagation, the majority of the standard remote microscope data contains measurements of Fourier components with both horizontal and vertical projections. As a result, it is a better indicator of statistical error

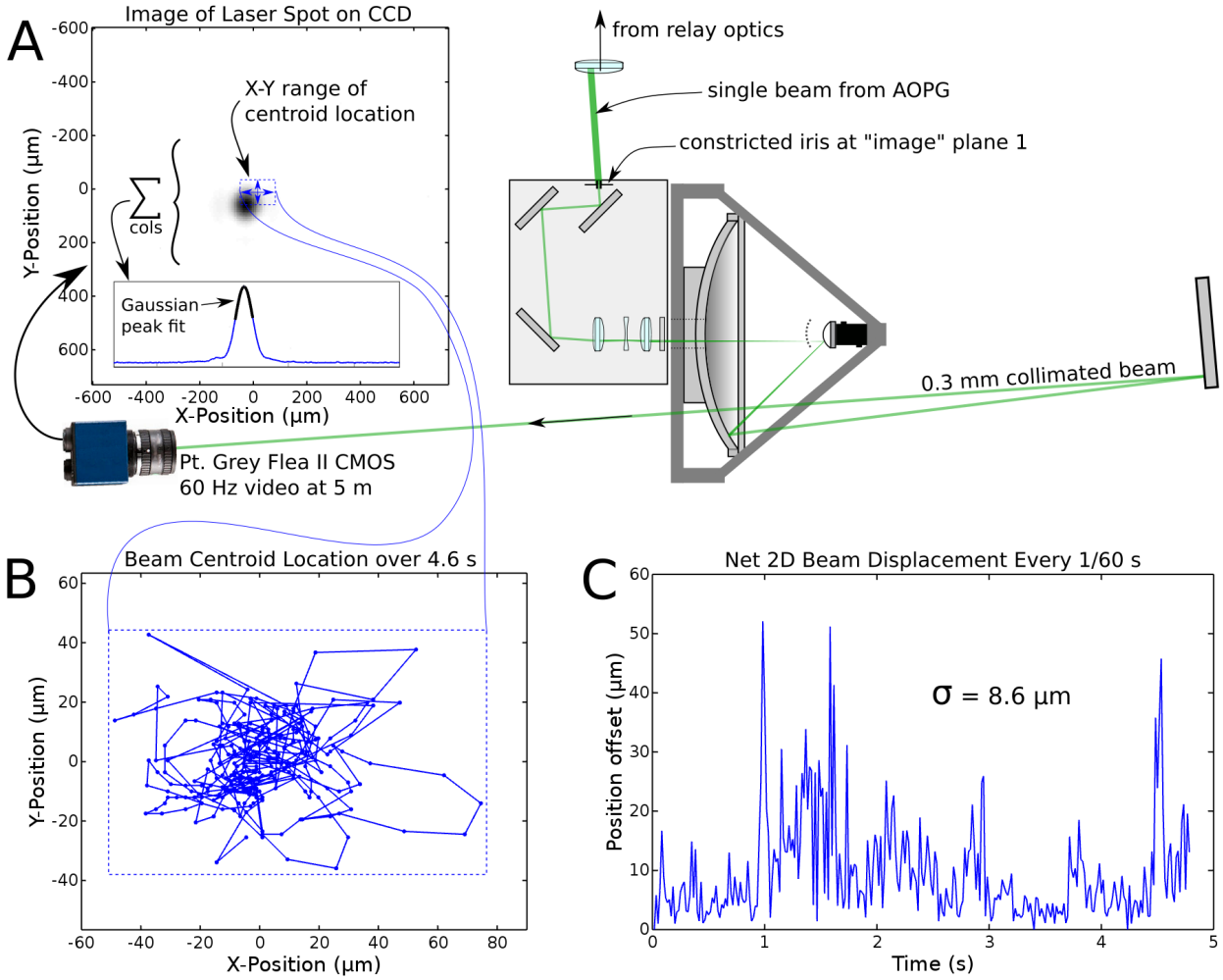

Figure 7.12: A) A single laser beam is passed through a maximally constricted iris before projection by the remote microscope optical assembly. A CMOS camera placed at target acquires 4.6 s of 60 Hz video of the beam wander. B) Using a centroid location algorithm the position of the beam is mapped out in time. C) The absolute value of the 2D beam displacement from the previous measurement is plotted versus time, showing beam jumps of up to 50 microns in 1/60th of a second.

to compute the total 2D difference in position as a function of time (shown in Panel C). The mean 2D position difference for a 16.6 ms interval was 9.5 μm with a standard deviation of 8.6 μm.

7.2.4 Timing Offsets

All of the subwaveforms written to the AWGs begin the beat frequency between two RF tones at phase zero, meaning that both sinusoids cross the x-axis zero value and proceed into positive

voltages in the subsequent time samples. It takes some time for any arbitrary subwaveform to transmits the RF tones to the AODs and for the acoustic wave to fill the active aperture. There is some arbitrary timing offset between the beginning of the first AWG subwaveform and the beginning of the digitizer data acquisition collection. This timing offset must be found to set the time of "phase-zero" for every subwaveform in the collected data stream. Without knowing this value, each of the subwaveforms will be "started" at some arbitrary time which represents a phase offset of the temporal waveform that is dependent upon the temporal frequency of the RF tone driving the AODs. Basically, we need to find the periodic locations of phase zero for every subwaveform. Luckily, this time offset is just a single value for all subwaveforms and can easily be found using the t-pattern data. An incorrect phase-zero time value will induce a linear tilt in phase for the horizontal and vertical frequency measurement sets, i.e. the mean phase plot shown in panel C of Figure 7.3 would contain a linear tilt with slope not equal to zero. All that will occur if this value isn't properly found is that the reconstructed image of the object will be offset from the center according to the shift theorem. This effect is shown in a 2D partial image reconstruction in Figure 7.13. Five time offsets are illustrated, with the phase of the Fourier components shown on the top row and the image reconstruction shown on the bottom row.

Still, it is easy to find this timing offset during t-pattern data acquisition, and as long as no other system variables are changed, this value will remain constant for all future data taken with the remote microscope. All that is required is to change the beginning time sample of an acquired subwaveform with which to evaluate the phase of the Fourier component, and to move this value until the phase plot (like in Figure 7.3) is as flat as possible. Algorithmically, this value could be found automatically via the 2D phase plots as in Figure 7.13 by simply locating the time offset where the total phase accumulation in an image is minimized. At that time offset, the reconstructed image (which is also the illuminate FOV of the remote microscope) will be centered in the 2D image array.

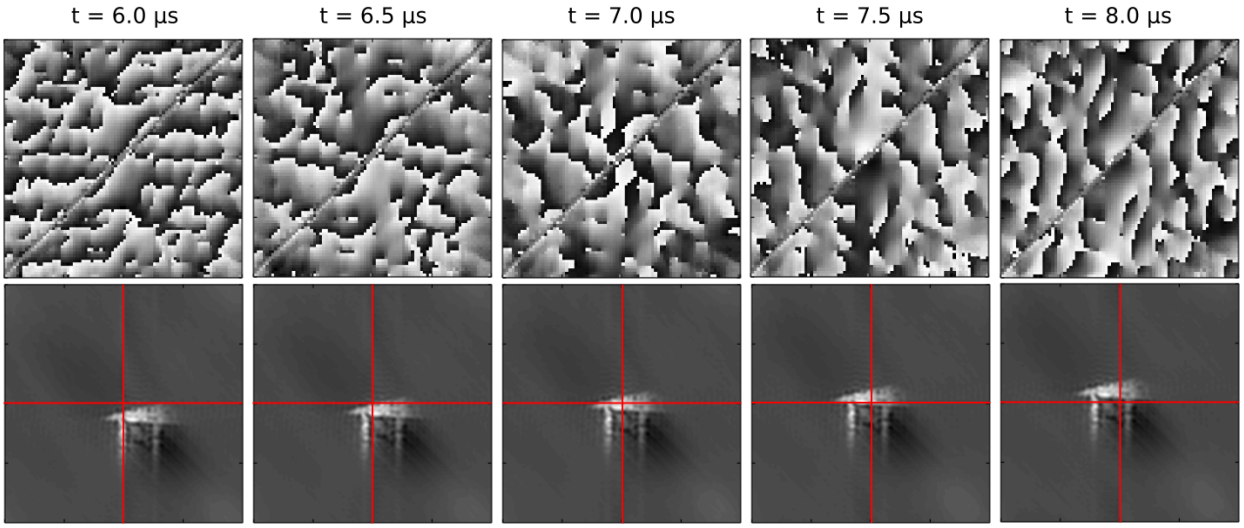

Figure 7.13: Phase evolution due to changes in the timing offset value. The top row shows the phase of the low spatial frequency components for the stated timing offsets used to determine the "phase zero" index in the temporal waveform. The bottom row shows the relative position of the reconstructed image of the object within the calculated array. The red crosses are used to provide a visual reference to the reader. As the time-offset increases, the 2D phase evolution changes from net vertical phase wrapping (horizontal structure to the 2D phase map) to net horizontal phase wrapping (vertical structure).

7.3 Detection Equation and Phase Error Terms

At any instant in time, the 2x2 array of diffracted and Doppler-shifted beams of light interfering at the sample produce four unique spatio-temporal interference patterns due to each non-degenerate pair of beams of which there are two degenerate horizontal, two degenerate vertical and two unique diagonal terms. The intensity measured at the detector $I(t)$ is a function of the system efficiency ($\eta(\omega_p, \omega_q)$) that quantifies both efficiency of transmitted light and the amount that is collected by the system during data acquisition. The system efficiency is the solid angle of light passing through the limiting aperture Ω_{aper} times the frequency-dependent transmittance function of the optical train $\eta(\omega_p, \omega_q)$ as shown in following expression.

$$\xi = \eta(\omega_p, \omega_q) \cdot \frac{\Omega_{aper}}{2\pi} \tag{7.3}$$

The intensity at the detector is the two dimensional integral of the FOV of the interaction of the light field with the position-dependent reflectivity function of the object (R_{obj}) times this system

efficiency term.

$$I(t) = \xi \cdot \iint_{FOV} R_{obj}(\vec{r}) \sum_{p=1}^{4} \sum_{q>p}^{4} \cdot \Big[1 + \frac{m}{2} \cos\Big((\vec{k}_p - \vec{k}_q)\vec{r} - (\omega_p - \omega_q)t + \Gamma_{tot}(\omega_{(p,q)}, \vec{r}, t)\Big)\Big] d\vec{r} \quad (7.4)$$

where k_p, k_q are the wave vectors of the two beams, ω_p, ω_q are the temporal frequencies, $\vec{r}$ is the spatial position in the FOV, and Γ_{tot} is the summation of the phase errors at any instant in time. The total phase error in the spatio-temporal light field contains the terms that I've described in previous sections. The first is the sum of the systematic frequency ω-dependent and spatially $\vec{r}$-dependent phase errors due to optical misalignment, acousto-optic frequency heterogeneity and the surface deviations from the ideal optical shape $\phi_p(\omega_p, \vec{r})$ and $\phi_q(\omega_q, \vec{r})$. These phase errors are dependent upon temporal frequency (ω) because there is a 1:1 mapping of position in the optical aperture to temporal frequency, but they are also a function of position ($\vec{r}$) in the FOV since the interferometric fringe distortion is position dependent. This phase error is a constant in all measurements and is quantified and corrected for in the instrument response function (IRF). The temporally-dependent contributions to the total phase error include the two frequency-temporal terms due to OPL and AoA fluctuations from short time-constant turbulence in the air ($\theta_p(\omega_p, t), \theta_q(\omega_q, t)$) and a slower thermal drift constribution to the phase of the entire optical system ($\beta_p(\omega_p, t), \beta_q(\omega_q, t)$). I can now explicitly state those phase errors and their time constants (τ) for the horizontal t-pattern data.

$$\begin{aligned} \Gamma_{tot}(\omega_p, \omega_q, \vec{r}, t) &= \big[\phi_p(\omega_p, \vec{r}) - \phi_q(\omega_q, \vec{r})\big]_{constant} \\ &+ \big[\theta_p(\omega_p, t) - \theta_q(\omega_q, t)\big]_{\tau_{AoA}=1.08ms/micron} \\ &+ \big[\beta_p(\omega_p, t) - \beta_q(\omega_q, t)\big]_{\tau_{TD}=0.177s/micron} \end{aligned} \quad (7.5)$$

where the time constants will be replaced with the appropriate values for the vertical t-pattern data.

7.4 Microscopic Image Reconstructions

This final section describing the development and testing of the $\mathcal{F}$-BASIS remote microscope contains the produced images of targets using the time-waveform data collected. The first set

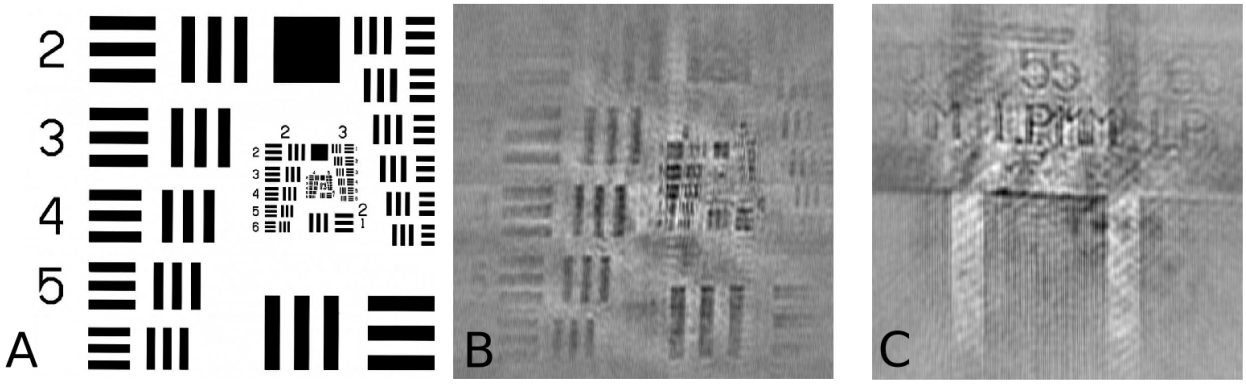

Figure 7.14: A) 1951 Airforce resolution target (AFRT) image. B) Reconstruction of the AFRT using our remote microscope. The spatial frequencies of group 3 are resolvable with features of 35μm visible. C) A reconstructed image of a resolution target showing 55 and 60 lines per mm features which correspond to 18.2 and 16.7 μm features.

of images shown are the preliminary 2D reconstructions using a brute force, turbulence-ignorant technique. The spatial resolution of the images is significantly worse than the theoretrical limit, but they are the first successful reconstructions at five meters of two reflective targets and one scattering target. I provide a description of the final data acquisition technique and some of the tricks that can be played with the remote microscope to avoid low spatial frequency losses due to obscuration by the secondary mirror. I conclude with possible improvements to the system that could be accomplished with future work.

The first reconstructions at 5 meters are shown in the following figures. The three targets used were the US Airforce resolution target (AFRT), a reflective grating target with increasing lines per millimeter and the printed portions of a business card. Figure 7.14 shows the reflective targets. I tested the performance of the microscope under specular reflective conditions using two spatial resolution targets lithographically printed on glass. To prevent damage to the APD during the experiments, the total optical power of the laser was reduced to 15 mW. The image reconstructions showing the resolution target and gratings are shown in Figure 7.14. The reconstruction of the Airforce resolution target (AFRT) is shown in Figure 7.14B. The AFRT Group 3, with features ranging from 35.1 to 62.5 μm are resolvable. The reconstruction of the linear gratings is shown in

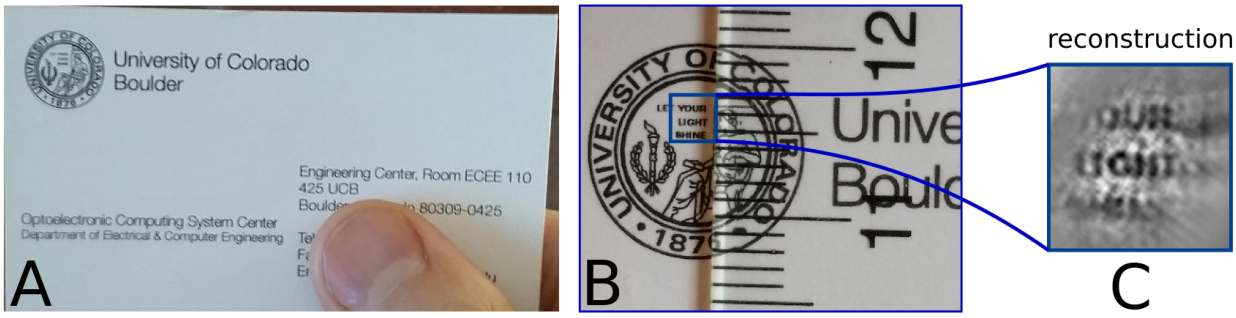

Figure 7.15: A) The business card used as a scattering target at 5 meters. B) A zoom-in of the University of Colorado logo in the upper left hand corner of the business card with a blue box delimiting the FOV of the microscope containing the words "LET YOUR LIGHT SHINE". The letters are 300 μm tall and the "I" is approximately 100 μm wide. C) The full FOV of the first reconstruction of a scattering target showing the words "YOUR LIGHT SHINE" with a resolution of 40 μm.

Figure Fig 7.14C, the 55 and 60 LPMM (18.2 and 16.7 μm) features are just resolved.

I also tested the funtionality of the remote microscope at 5 meters using the fine print on a business card. Panel A of Figure 7.15 shows the business card and my thumb. A zoom-in of the university logo is shown with a ruler for scale. The entire logo is contained within a 12 mm wide circle. The FOV of the microscope only contained the three words "YOUR LIGHT SHINE". The reconstruction of those words using the remote microscope data taken at 5 meters. Only 6.5% of the data containing the low spatial frequencies was used in this reconstruction which is why the resolution is only approximately 40 μm. The additional high spatial frequency data only added noise to the reconstruction due to the turbulent phase randomization.

7.5 Final Spatio-Temporal Sampling Scheme

The brute-force, slow march through every temporal frequency step in a horizontal line before iterating on the vertical frequency illustrates two serious drawbacks which can be addressed in $\mathcal{F}$-BASIS remote microscopy by applying slightly more forethought into the data acquisition scheme. The first involves compensating for low spatio-temporal frequencies lost due to the central obscuration. The second relates directly to the accumulated residual phase errors inherent in a

sparse temporal sampling with regard to slow thermal drift and the mostly stochastic turbulent eddies.

7.5.1 Center Frequency Offset

I've already stated several times that there is a 1:1 mapping between spatial frequencies probed on the target and temporal beat frequencies in the illumination waveform used. Although this is true, it provides an unfortunately deceptive and confusing mental image to the reader, so I need to be more explicit. Recall that to construct a light field with a chosen spatial frequency/period the two beams used must be separated by a set angle described by the equation 1.14. For this discussion, I'm going to set the 2D surface of the target at some axial distance z_t where the z-axis is the normal vector to the target's surface, and the two beams illuminating the surface are restricted to the X-Z plane. For a two-dimensional target, any two such collimated beams inside the X-Z plane with this angular separation can be used to generate the identical pattern. Although the locations of the intersection of the two beams with the primary mirror will change, and thus the RF tones used to deflect those beams will change, the angle between them and the temporal beat frequency generated by the RF tones will be the same for any valid set of beam pairs. The volumetric interference fringes will be stacked sheets of high and low intensity light that have a surface normal in the X direction, and so it is natural to assume that we must restrict the plane of interference of two beams to contain the Z-axis. However, the same interference pattern will be generated by any set of beams that have the same angular separation so long as they are equally distant from the Z-axis. For example, a set of beams whose plane of interaction is rotated in Y will still produce the same interference pattern on the unrotated 2D target whose normal direction is Z.

I keep emphasizing the two-dimensional nature of these targets, and that's because I'm only exploring the 2D projection of the 3D optical transfer function (OTF) of the $\mathcal{F}$-BASIS system. The 3D OTF of $\mathcal{F}$-BASIS systems to image 3D targets is outside of the body of this work, but it is partially addressed in [53] and subsequent $\mathcal{F}$-BASIS publications. The 1D OTF and coherent

transfer function (CTF) were introduced in Figure 2.5. It is clear from the CTF that any two beam frequencies with separation $2f_1$ that both obey the condition that they are contained within the passband defined by the cutoff frequency f_c will produce the same autocorrelation peak and sidebands in the OTF. If the OTF could only be generated using symmetric tones in the CTF (as implied in the Abbe theory of imaging), meaning the beams reflecting from the mirror had to be equidistant from the optical axis, then the OTF of the remote microscope would have a missing passband at the low frequencies where the central hole is cut. In this case, the best image produced would be a high pass filter of the ideal image. I also keep referencing the "plane wave" nature of the illumination beams. If the beams are converging or diverging at all, my previous claims concerning beam tilt ambiguity are no longer true. In Chapter 4, I describe my efforts to design an optical system that had identical OPL at every location in the optic pupil. This is important because in that design I attempted to ensure that beams generated by the AOPG would reflect from the primary mirror as plane waves with less than $\lambda/4$ fringe distortion and allow diffraction limited performance.

This brings me, finally, to the technique that allows the $\mathcal{F}$-BASIS remote microscope to recover the lost low-frequencies. By shifting the position of the low-angular-separation beams on the primary mirror I can probe the low-spatial frequency components of a target and "fill in" the lost donut-hole in the center of the Fourier space representation. This is achieved by offsetting the center frequency of the RF tones, as shown in Figure 7.16 panel A. In the AOPG, the vertical AOD has a center frequency of 80 MHz and the horizontal AOD is 86 MHz. In order to probe the horizontal spatial frequencies, the vertical AOD is driven with a single tone at 80 MHz while the horizontal frequencies are shifted symmetrically from the 86 MHz center. By setting the vertical tone to 85 MHz, the pairs of horizontally-separated beams are shifted up on the mirror; this is illustrated as the blue box above the center circular obscuration. This center-frequency offset would still probably work well enough for the horizontal frequency measurements, but only the aberration correction effort of optical design allows the low vertical frequencies to be measured even with a vertical offset. The interferometric fringe curvature is suppressed well enough in this slightly off-

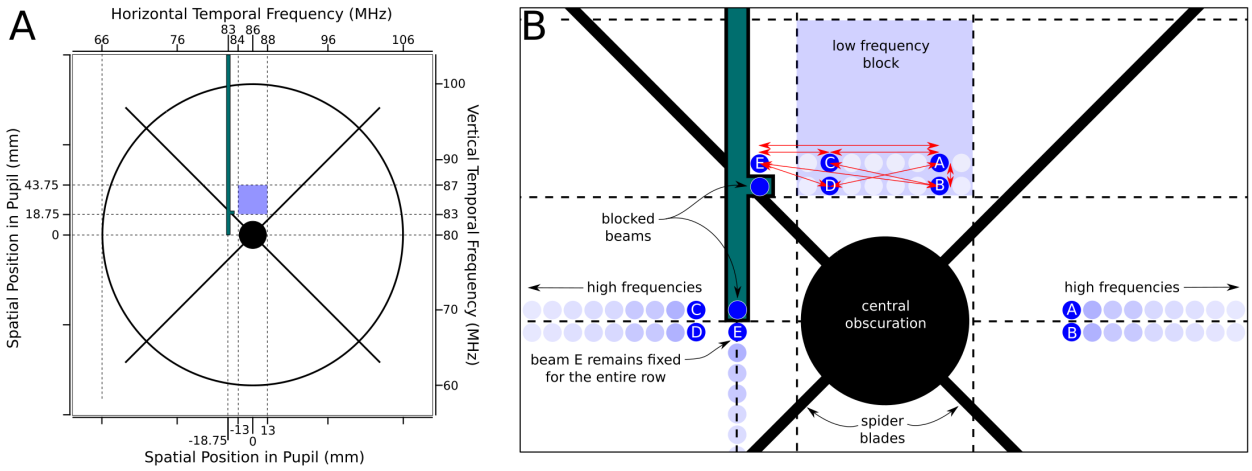

Figure 7.16: The final proposed data acquisition scheme uses 5 tones, one which acts as a "peg point". A) The pupil boundary of the system is shown as the large circle while the small dark central circle is obscuration due to the secondary mirror. The mapping of driving AOD frequency to spatial location within the pupil is shown on opposing axes. B) A zoom-in of the central region of the pupil function. The light blue block illustrates the portion of the pupil which is used to probe low spatial frequency components of the target by offsetting the "center" of the mirror and bypassing the central obscuration. For each measurement, four beams (A, B, C, D) probe the four Fourier components shown as red arrows, and a fifth "peg point" (E) remains fixed on the mirror across measurements. The off-center physical pupil mask, shown in green, blocks the necessary sixth beam from reaching the target. After probing the low spatial frequencies, the five beams are moved to the axially-symmetric location shown.

axis orientation to have no detrimental effect on the spatial Fourier samples collected. What will result from this offset is a discontinuity in the residual optical phase error between measurements inside the blue box and those following which do not have a vertical center frequency offset. The correction for this is to collect the ideal image of a pinhole with the same setup as the t-pattern data and use this instrument response function (IRF) to calibrate out the phase discontinuities. I describe this process in 7.6. As long as the IRF is measured using the same beam locations on the mirror and no optical adjustments have been made, the image reconstructions won't suffer from low-frequency phase error nor the high-pass filter effect from the central obscuration, which this technique effectively removes.

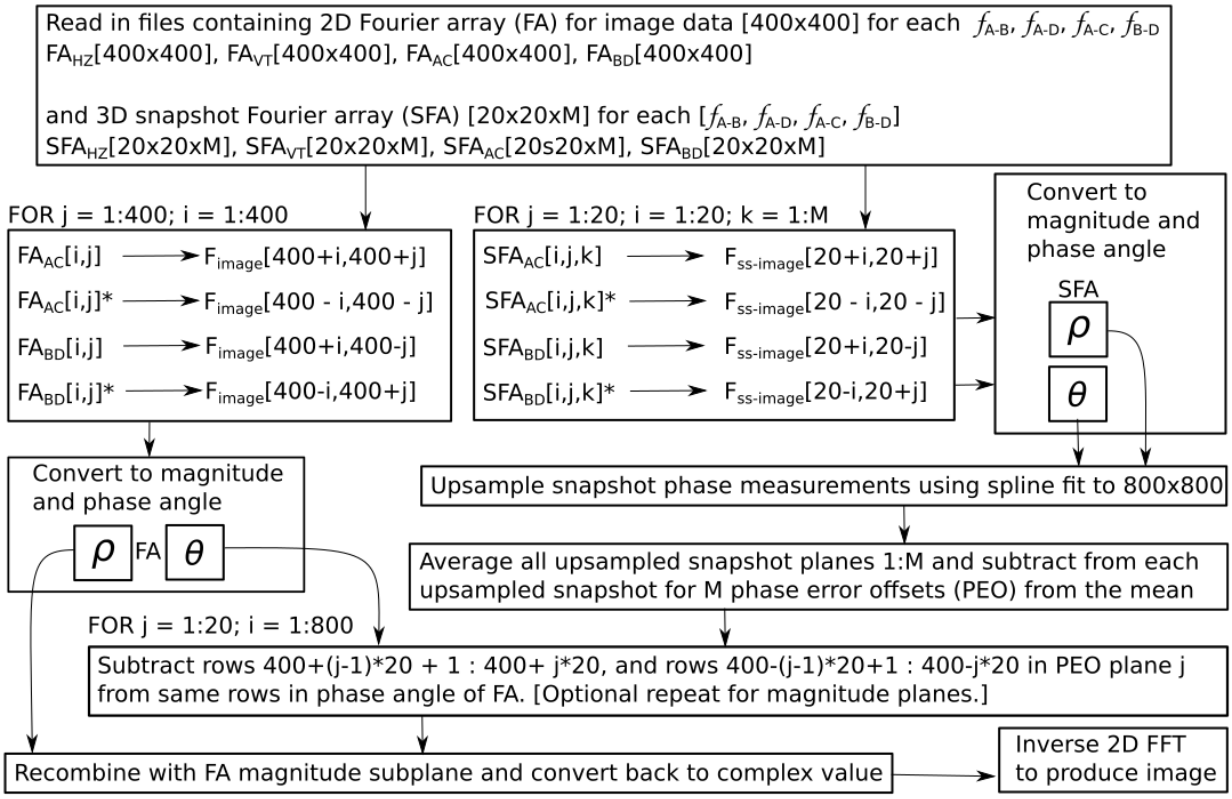

Figure 7.17: The flow diagram in pseudo-code for the final attempted data processing for remote microscope image reconstruction. This algorithm uses thorough data that slowly marches through all desired Fourier components of the object but takes up to 12 seconds to obtain, and snapshots which contain small, fast measurements of 20x20 Fourier components of the object taken at close intevals. Every snapshot data plane is redundant, and is used to construct a rough phase evolution map against which the regular data may be corrected. The regular data is read in and the relevant Fourier components are extracted and converted to magnitude ρ and phase θ. The phase is differenced with an upsampled version of the snapshot plane and recombined with the original magnitude before being converted back into complex values. A single 2D FFT is used to generate the image reconstruction.

7.6 Final Reconstruction Algorithm

A flowchart of the final attempted reconstruction algorithm is shown in Figure 7.17. This algorithm is the continuation of the process that generated the data files written out and described in section 6.10. I read in the data containing the complex Fourier component measurements for the 4 spatial frequencies of the 4 beam interferences, and the multiply-sheeted snapshot array containing multiple 20 x 20 4-beam frequency measurements spread evenly across the Fourier plane. This data

is organized into full Fourier planes by placing the measured cross products into the positive array locations and the complex conjugate of the measured values in the opposite quadrant. A similar process is completed for the snapshot data, but with 21 redundant data planes per image. The snapshot data is converted into magnitude and phase, and the phase is unwrapped. The amplitude and phase planes of this 20x20 array are then independentaly upsampled to 400x400 (per quandrant) by spline fit. The average of the snapshot phase data planes is computed and stored as the true signal. For every snapshot, the deviation from this time average is then subtracted from the phase of the portion of the full data set taken just before that snapshot. The magnitude of the full data is recombined with the "corrected" phase, converted back into a complex value and 2D Fourier transformed to obtain a reconstructed image. Unfortunately, this process doesn't work due to the fact that the snapshots are too far separated to track the turbulence. I describe the possible solutions in the next section.

7.7 Fourier-Sampling Schemes

In an attempt to get a fast selection of regularly spaced samples across the aperture, I devised the "snapshot" set of 20 x 20 horizontal and vertical frequencies that could act as peg points which I tried to use as a way to correct for the turbulence-induced phase evolution. This technique assumes that the phase varies as a continuous, smooth, integrable function, and that the time separation between snapshots is sufficiently small to accurately track the evolution in time. All of the published literature concerning turbulence claims that the first assumption has been shown to be true for the structures of atmospheric eddies so long as spatial sampling is on the order of the "inner scale", the smallest relevant eddy feature size [147, 36, 157].

The combined results from the video data set and the t-pattern data are fairly damning for the prospects of using $\mathcal{F}$-BASIS remote microscopy on any planet with a turbulent atmosphere - especially this one, although it may be successful in a dilute atmosphere on a planet like Mars or even more so the Moon. The basic sampling scheme described in section 6.10 scans the 2D frequency samples one horizontal row at a time to build up a full scan of Fourier space. Since each sample

requires 80 μs and there are 400 samples in a row, adjacent vertical frequency samples will be separated by 32 ms. The video data showed that the correlation time constant of beam position, and by extension Fourier component phase is in the milliseconds. The t-pattern data exhibited AoA variations on two different time-scales. The slow thermal drift with a time-scale measured in seconds is easily tracked, and even the mid-range eddies with time-scales in the hundreds of milliseconds might be sampled and compensated for with sufficient care. The turbulence with the shortest measurable time scale in the single milliseconds contained enough randomization of the phase to make any turbulence-tracking measurement scheme too onerous in data volume to implement. As far as I can see, this leaves three possible options for full data acquisition with sufficient compensation for turbulent phase error.

The first possible data acquisition scheme that can account for turbulence is to take many data sets exactly as previously discussed. A full set of complex Fourier measurements are acquired by marching through one horizontal line at a time, with each set taking 13.4 seconds. The long time-scale thermal drift is modeled and removed for each image using the snapshot data planes, but the short time-scale phase errors are ignored. When a sufficient number of data sets are collected, the complex data is converted into magnitude and phase and each of these components is time averaged to construct a single "corrected" data set from which an image is reconstructed. The main drawback of this technique is obviously a severe degradation in system efficiency in what is already a very inefficient imaging process. In each image we gather 1.2 MB of information by recording over 6 GB of data for a system imaging data efficiency of 0.02%. On top of this, to average out phase variations from AoA fluctuations to a maximum of $\pi/2$ requires an increasing number of measurements as the desired resolution increases. This is clearly uneconomical from a resource utilization perspective.

The second possible acquisition scheme is to acquire subsets of the full Fourier space with more frequent snapshots to track the progress of the turbulence. A significant tradeoff study in data volume and reconstruction quality still needs to be performed, but one possible data management option would be to take a *partial* snapshot after every row of data. Partial snapshots would only

contain 10 samples per row for 2 rows. This would provide row-to-row stitching tie ins and would consume less than 1.6 ms to acquire (80 μs x 20 samples). In addition to this, only acquiring some subset of the row would decrease time between each two-line snapshot. For example, each row could be broken into 5 sets of 80 samples and a 2-row snapshot is taken between each of the 5 subsets. This allows the snapshots to sample phase evolution at a rate of 100 Hz. This data scheme would require the full 4 G-samples of the Gage digitizer, but would contain too many waveform datapoints to fit on a single sequence on the AWG520, and so would take at least two data acquisition sequences. Using a more modern arbitrary waveform generator with a larger memory buffer would resolve this problem, but the total time required for a full image would increase to 20 seconds. This technique should also only be pursued if all other avenues end in a scientific cul-de-sac.

The third acquisition scheme takes a different tack for data collection, and abandons the complete reliance on snapshots to track phase evolution. Instead of slowly marching through subwaveforms where sets of 4 beams illuminate the target and each measurement is only weakly coupled to the subsequent waveforms by the (poor) assumption that the turbulence is frozen for 160 μs, each of the subwaveforms are tied together using a single, constant peg-point beam. This scheme is shown in Panel B of Figure 7.16. The AOPG generates a (MxN) array of beams given M RF tones to the horizontal AOD and N tones to the vertical AOD. Although it may be obvious to point out, this means that every row in the beam pattern has to have the same number of beams. For this peg-point technique, I desire a beam pattern with 5 beams; 4 symmetric beams (A,B,C,D) and one asymmetric beam (E). For all sets of 4 symmetric beams with stepped vertical and horizontal frequency separations, the asymmetric beam remains in constant. The reason I want five beams instead of the natural six that are generated, is that the sixth beam provides no useful information for the reconstruction and its presense would increase the number of redundant interferences as the frequencies are stepped through the sequence since the crossed AOD can only generate a separable array of beams. To eliminate this sixth beam, I place a physical aperture mask in front of the primary mirror to block the beam (shown as the green object in Figure 7.16). The low frequency set requires a different masked location (the small tab shown) than the rest of

the frequency samples due to the vertical offset. For this low frequency set, the lower frequency row remains at the bottom of the blue square while the upper row is incremented higher by 100 kHz each step. This requires the center frequency to be stepped higher by 50 kHz between each row. Upon reaching the end of the blue box, the center frequency drops back to the native central frequency of the vertical AOD and the sample steps progress as with the original sampling scheme. The green beam block extends down one sample-frequency column to the half-way point down the mirror so that every regular row of high spatio-temporal frequencies contains a stable location on the lower half of the mirror. This sampling scheme uses the same peg-point frequency measurement for all samples in a row, allowing me to set the location of the peg point as a set "zero phase" for all measurements. Each of the interbeam phases can then be referenced to this peg point. Each of the desired temporal frequencies, namely the two unique cross products (A-D, B-C) can now be referenced to the E beam location. This technique requires no more time to acquire than the original measurement scheme and only causes two redundant frequency tones with the desired cross products per row.

7.8 Towards Phase Closure Using the 5-tone Scheme

The standard phase closure technique for multi-arm interferometers uses 3 measurements to uniquely determine the phase of complex measurements of the same object by linearly canceling out the errors [88], and I developed a variant of this technique for the remote microscope 5-tone data. The standard approach assumes the errors in the complex measurements are phase linear. I'll present the phase closure mathematics using beams A, D and E in the blue square in panel B of Figure 7.16 as a visual aid. Assuming the instrument reponse function contains the static phase errors as a function of location on the mirror and has been subtracted, the only phase error left to be accounted for is due to thermal drift and AoA fluctuations. From geometric reasoning, the beam position offsets add as vectors such that AE = AD + DE. Furthermore, the phase of a recorded waveform is:

$$\phi_{meas} = \theta_{obj} + \xi_{turb} \tag{7.6}$$

where ϕ is the measured phase of the Fourier transform of the detected waveform, θ is the unknown true phase of the object's spatial Fourier component, and ξ is the phase error contribution due to turbulence. However, I showed in Section 7.2.3 that ξ is equal to the lateral spatial offset of the beam δ times the wave vector $k = 2\pi/\text{period}$ of the fringes per Equation 7.2.

With three measurements taken during three unique turbulent states the phases of the three Fourier components of the object can be perfectly separated from the phase error due to turbulence. The first measurement provides a combined phase measurement described by:

$$\phi_{AE1} = \theta_{AE} + (\delta_{AD1} + \delta_{DE1})k_{AE} \tag{7.7}$$

$$\phi_{AD1} = \theta_{AD} + (\delta_{AD1})k_{AD} \tag{7.8}$$

$$\phi_{DE1} = \theta_{DE} + (\delta_{DE1})k_{DE} \tag{7.9}$$

From this set of equations, we have three measured values but five unknowns: the 3 θs and 2 δs. The beam offsets δ_{AD1} and δ_{DE1} are the only beam offsets relevant to this calculation and are the only two contributors to these three equations. By taking two more measurements under different turbulent conditions, we obtain the following equations:

$$\phi_{AE2} = \theta_{AE} + (\delta_{AD2} + \delta_{DE2})k_{AE} \tag{7.10}$$

$$\phi_{AD2} = \theta_{AD} + (\delta_{AD2})k_{AD} \tag{7.11}$$

$$\phi_{DE2} = \theta_{DE} + (\delta_{DE2})k_{DE} \tag{7.12}$$

Again, there are only two new beam offsets relevant to the three measurements, δ_{AD2} and δ_{DE2}. Finally, the third measurement gives another set of similar equations.

$$\phi_{AE3} = \theta_{AE} + (\delta_{AD3} + \delta_{DE3})k_{AE} \tag{7.13}$$

$$\phi_{AD3} = \theta_{AD} + (\delta_{AD3})k_{AD} \tag{7.14}$$

$$\phi_{DE3} = \theta_{DE} + (\delta_{DE3})k_{DE} \tag{7.15}$$

These three sets of equations provide 9 measured phase values to disentangle 9 unknowns: 3 phases belonging to the Fourier components of the object and 6 spatial distances from the A and D beams

to beam E. This process is computed in tandem for the beams B and C, since those phase values will be collected at the same time. Once the spatial offsets of the beams A-D are subtracted for every subwaveform in a row, the entire row will have phase errors tied to a single beam (E) and I move on to the next row with a new static location for beam E.

Chapter 8

Conclusions

In the course of this project, I had to explore and use several disciplines to produce the remote microscope, with the major tasks concentrating on opto-mechanical engineering and analysis, optical surface testing and atmospheric turbulence modeling. Each of the chapters gave a narrative of how I arrived at my particular solutions to problems along the way, but describing the lead up to the accomplishments can sometimes bury the take away lessons from the tasks. Below, I condense and present the salient points I learned for each of the tasks I undertook and give a description of where it stands and where future work would be valuable.

8.1 Opto-mechanical

There were several lessons learned during the manufacture of the remote microscope optical assembly and after it was assembled. Unfortunately, several of these lessons are well known in the mechanical engineering and material physics communities, but I was ignorant and stymied by inter-disciplinary communication barriers. So, it makes sense to explicitly call some of these out specifically for the computational optics community.

Perhaps the most expensive lesson learned was that the residual stresses in the aluminum after standard machining would relax long after the optical surface was cut. It is important to guarantee the release of these stresses using a thermal treatment of the roughed out mirror blank. Furthermore, to guarantee a flat surface after the initial machining step would require iterative heat-treatment to remove locked-in material stress and re-machining, a process that is prohibitively

expensive. One of the reasons that we didn't pursue a rigorous heat-treatment in the initial fabrication of the mirror was because of the cost of processing. The mirror itself was fabricated for a few thousand dollars, and a quote from a shop to heat treat the mirror was over a thousand dollars. Since we expected to make multiple versions of the mirror, heat-treatment seemed to be an unbudgeted expense. The only reason we were able to iterate on a design with heat-treatment after realizing that the first mirror failed, was that I had access to a research-grade environmental chamber at the Southwest Research Institute. Still, machining any mirror with a light weight rib design requires executing at least a single heat-treatment before cutting the optical surface.

The tradeoff between lightweighting and deformation of the primary mirror required many trial-and-error designs and testing with finite element analysis software to come to a conclusion. The preponderance of the published literature uses assumptions about optical surface quality that far exceeds the requirements of the remote microscope. The solutions also are varied and not well compared. By that I mean, there's a description of *what* a research group did to lightweight a mirror but almost no discussion of *why* they chose any particular geometric philosophy rather than another. The reason I used a rib-ring lightweight configuration was mostly because of the machining costs that would be involved in structures like rectangular thin-walled grid patterns, or even worse, triangular grids. The radial position of the principle ring was anecdotal in nature, and a full analysis of changing the radial position was too costly in CAD model alterations. To be honest, I did change the radial position to two other locations without the rib structure supporting the shell and I found that an adjustment of ring width compensated the gravitational deformation response of the models. The ribs were absolutely necessary, but the height and the number of them were a tradeoff between surface rigidity and difficulty of machining. In short, the biggest lesson concerning the lightweighting process was that the solution space did not immediately reveal a global optimum.

Aluminum was the only reasonable choice for the primary mirror construction, and in fact, was the assumed material in the proposal before I even applied to graduate school. Although it was a successful material for the laboratory prototype, the aluminum substrate is unsuited

for temperature ranges greater than a 24 °C spread. Even inside these thresholds, the CTE of aluminum can sufficiently change the shape of the primary mirror to have a measurable effect on the quality of the microscopic image reconstructions. If the mirror truly did simply expand or contract isometrically, the shape change could be addressed through an appropriate dynamic re-alignment procedure, but unfortunately that's not the case. The lightweighting structure on the back of the shell causes non-uniform strain across the mirror surface when heated or cooled in an isothermal manner.

The common space-flight replacement material for aluminum in optical mirrors is beryllium. In simulations, it provides a significantly better response with respect to temperature induced surface deformations, but only by a factor of two. As a humorous side note, beryllium also produces high-energy neutrons in the presense of gamma radiation, which is not uncommon in planetary exploration and which could adversely impact nearby electronics. An appropriate material choice for planetary exploration would need to limit the expansion of the optical surface over 100 °C. The only materials that I found that are relevant are the more standard ceramics and glasses, which leads to a completely new set of lightweighting techniques not explored here.

We discovered that an optically flat ring should always be included on the circumference of the optical surface and preferably with a normal vector that is parallel to the optical axis of the mirror set. I had placed the ring on the outer edge mostly because I expected to have to mount some portions of the spider assembly to the mirror and needed the 1/4-20 bolt holes. I also figured that the ring and lip would provide structural rigidity, since hollow cylinders are famously stiff geometries. It was only due to a miscommunication that Nipro Optics used the diamond lathe on the flat ring surface producing a planar mirror reference. This fiducial reference surface was vital to the testing of the optical surface. As an anciliary lesson that I wish I had known, a flat ring around the central hole would have been likewise useful to the optical alignment process of the instrument later on. Finally, the vibration analysis shows that the current design of the spider vanes is likely to fail in shake and bake testing.

8.2 Optical Design

I reported the design of a catadioptric optical assembly capable of projecting collimated beams at angles of up to $\pm 1.5^\circ$ onto a target for use in Fourier-sampling remote microscopy. The optical system consists of a conicoidal inverted-Gregorian two mirror set operated in an infinite-conjugate geometry and an aberration-corrective Cooke triplet lens set. The fringes generated by any two interfering beams deviate from linearity by less than $\lambda/4$ over the angular range of the microscope. I derived the curvature of the focal surface necessary to produce collimated beams and reported the operational constraints of the Cooke-triplet needed to generate the conjugate curvature. The working distance of the microscope can be set through the adjustment of the projector elements allowing the location of the target of the microscope to be moved up to ± 0.5 m. Interference patterns of pairs of beams are simulated and shown to be sufficiently corrected for Fourier-sampling remote microscopy.

The real lesson learned during the optical design effort was how to apply the proper infinite-conjugate analysis to the optical system in order to optimize it for the purposes of collimated beam projection. The concept of objects and images when applied to this system are severely misleading and caused me many months of wandering down paths enticed by phastasmagorical promise. One of the failings of the current system is the lack of assurance of absolute alignment. Since the inverted Gregorian telescope zoom capability is able to overlap beams at different axial distances, the proper location and alignment of the Cooke triplet is miserably finicky. Looking forward, the designs of future systems can concentrate on finding the next iteration of aberration corrective lenses to eliminate all aberrations and engineer techniques to guarantee alignment.

8.3 Optical Testing

The vast majority of the literature dedicated to testing the prescriptions of optical components concentrates on techniques that would have been prohibitively expensive or unattainable for this effort. Standard circular subaperture testing was functionally impossible, and annular sub-

apertures using the industry standard spherical departure measurements would have required many hundreds of annuli to compute the surface of our mirror.

The annular-stitching phase-shifting interferometry technique I derived is capable of measuring large-aperture, high-departure aspheres without the use of null optics. The technique uses ray tracing to parameterize the annuli as variances from best fit paraboloids and uses the calculated OPD to eliminate the erroneous phase curvature of the measured interferometric data. I derived the OPD for each annuli and provided a geometric analysis of the relevant errors which dominate loss of information in traditional stitching schemes. A method to decouple additive measurements of two locations on the surface is presented but not implemented in experimental verification. The reconstruction of a portion of an ellipsoidal mirror with more than 3000 waves of spherical departure across the full aperture was produced via paraboloidal parameterization to experimentally verify the mathematical model of the technique. Future work will include full aperture surface reconstructions of large aspheric mirrors and implementing an optimized algorithm to solve the linear equations coupling multiple points on the surface to generate a map that contains higher spatial frequency surface errors.

8.4 Remote Microscope Status and Possible Future Work

Using a low-precision aspheric mirror pair I designed and constructed a microscope that uses axially-symmetric sequential Fourier sampling to probe the spatial Fourier components of distant targets. With this microscope I reconstructed images of resolution targets with a record 17 μm lateral spatial resolution at a distance of 5 meters through turbulent air for a specular target and 40 μm for a scattering target.

The axially-symmetric $\mathcal{F}$-BASIS remote microscope suffers from several disadvantages that must be overcome to achieve the goal of high resolution imagery at 5 meters, especially when considering sending this to another planet on an exploration rover. The three most significant being:

(1) The instrument is currently contained within a laboratory where temperature isn't controlled nor really predictable. The instrument is currently contained on the surface of a optics table where exhaust fans and convective heating is actively working against stability of measurement. The atmospheric turbulence in the optics lab was shown to be sufficient to cause irreparable phase randomization, and all studies suggest that the turbulence in an operational environment would be significantly worse, although vacuum or low pressure atmospheres would be beneficial.

(2) A sample of two simultaneous spatial Fourier components consumes at least 40 μs and up to 80 μs, and with the desire to populate a large number of the Fourier samples, this quickly leads to a long acquisition time for a very small amount of data. The use of the microscope on another planet makes sense only if the distance from the rover can not be overcome by another instrument.

(3) The system's optical efficiency is incredibly low. The optical losses during projection and collection result in a significant waste in the energy budget of the instrument, and limit the SNR that can be achieved due to limited laser power.

Luckily there are some possible routes to address these problems. Chapter 7 provided detail into the real challenges of a turbulent atmosphere, but also that there is sufficient information to plausibly eliminate these errors through a new phase closure technique. This is an obvious route for future researchers looking to develop the next generation of this system. To address the length of acquisition time, there is little one can reasonably expect to achieve. During this effort, there was some discussion of using non-redundant arrays to shorten the acquisition time, but in my opinion this is a doomed road. The number of Fourier components being measured at one time is limited by the laser power and the number of tones going into the AOD. With an increasing number of tones, the total power in each must drop proportionally to remain below damage thesholds for the AOD. Reducing the RF power leads to increasing the amount of time necessary to achieve the same SNR of the measured Fourier component. The *last* thing you would want to do is increase the amount

of time spent on a sample since turbulence is going to scramble the phase of the measurement.

After 5 years of designing, building and using the system, I think that the best option for future development is in scaling down the scope to avoid many of the problems associated with large data sets, long acquisition times, and marginal environmental conditions. From the first reconstructions, it is clear that an imager capable of obtaining 30-40 μm resolution in images at 5 meters is straight forward and achievable, perhaps scaling back to 25 microns is a far more reasonable resolution goal. For myself, I intend to pursue a variant of this for atmospheric research. This instrument is incredibly successful at measuring turbulent eddies.

Bibliography

[1] The anatomy of a microscope. https://micro.magnet.fsu.edu/primer/anatomy/components.html. Accessed: 2017-05-11.

[2] Operator's manual verdi v-8/v-10 diode-pumped lasers.

[3] Sam's laser faq: Commercial solid state lasers. http://www.repairfaq.org/sam/laserscl.htm#sclcpsm. Because this is the real reference people use.

[4] Shaddy Abado, Stanislav Gordeyev, and Eric J Jumper. Designing and testing a high-bandwidth 2-d wavefront sensor for aero-optics. In Advanced Wavefront Control: Methods, Devices, and Applications VII, volume 7466, page 746602. International Society for Optics and Photonics, 2009.

[5] Ernst Abbe. Beitrage zur theorie des mikroskops und der mikroskopischen wahrnehmung. Archiv fur mikroskopische Anatomie, 9(1):413–418, 1873.

[6] Larry C Andrews, MA Al-Habash, CY Hopen, and RL Phillips. Theory of optical scintillation: Gaussian-beam wave model. Waves in Random Media, 11(3):271–291, 2001.

[7] Jean-Michel Asfour and Alexander G Poleshchuk. Asphere testing with a fizeau interferometer based on a combined computer-generated hologram. JOSA A, 23(1):172–178, 2006.

[8] WILLIAM P BARNES Jr. Optical materials reflective. Applied Optics and Optical Engineering, 7:97, 2012.

[9] João Pedro Barreto and Helder Araujo. Issues on the geometry of central catadioptric image formation. In Computer Vision and Pattern Recognition, 2001. CVPR 2001. Proceedings of the 2001 IEEE Computer Society Conference on, volume 2, pages II–II. IEEE, 2001.

[10] Michael Bass. Handbook of optics. Vol. 2, Devices, measurements, and properties. McGraw-Hill, 1994.

[11] Michael Bass, Casimer DeCusatis, Jay Enoch, Vasudevan Lakshminarayanan, Guifang Li, Carolyn Macdonald, Virendra Mahajan, and Eric Van Stryland. Handbook of optics, Volume II: Design, fabrication and testing, sources and detectors, radiometry and photometry. McGraw-Hill, Inc., 2009.

[12] Peter L Bender and James C Owens. Correction of optical distance measurements for the fluctuating atmospheric index of refraction. Journal of geophysical research, 70(10):2461–2462, 1965.

[13] Norman J Berg and John N Lee. Acousto-optic signal processing: theory and implementation. In New York, Marcel Dekker, Inc.(Optical Engineering. Volume 2), 1983., volume 2, 1983.

[14] J-P Bibring, P Lamy, Y Langevin, A Soufflot, M Berthé, J Borg, F Poulet, and S Mottola. Civa. Space Science Reviews, 128(1):397–412, 2007.

[15] Norman Bobroff. Residual errors in laser interferometry from air turbulence and nonlinearity. Applied optics, 26(13):2676–2682, 1987.

[16] F Boddeke, IT Young, R Zagers, LJ Van Vliet, J Mullikin, and H Netten. Depth-of-focus in microscopy. In 8th Scandinavian Conference on Image Analysis, Tromso, Norway, 1993.

[17] Murk Bottema and RA Woodruff. Third order aberrations in cassegrain-type telescopes and coma correction in servo-stabilized images. Applied optics, 10(2):300–303, 1971.

[18] W Boyle and G Smith. Buried channel charge coupled devices, February 12 1974. US Patent 3,792,322.

[19] Ronald Newbold Bracewell. The Fourier transform and its applications, volume 31999. McGraw-Hill New York, 1986.

[20] Kevin F Brennan. The physics of semiconductors: with applications to optoelectronic devices. Cambridge university press, 1999.

[21] HP Brueggemann. Conic mirrors. Focal Press, 1968.

[22] CR Burch. Reflecting microscopes. Proceedings of the Physical Society, 59(1):41, 1947.

[23] James H Burge. Fizeau interferometry for large convex surfaces. In Proc. SPIE, volume 2536, pages 127–138, 1995.

[24] James H Burge. Measurement of large convex aspheres. In Optical telescopes of Today and Tomorrow, pages 362–373. International Society for Optics and Photonics, 1997.

[25] James H Burge and David S Anderson. Full-aperture interferometric test of convex secondary mirrors using holographic test plates. In 1994 Symposium on Astronomical Telescopes & Instrumentation for the 21st Century, pages 181–192. International Society for Optics and Photonics, 1994.

[26] JH Burge, D Murgiuc, and SC West. Null correctors for 6.5-mf/1.25 paraboloidal mirrors. Technical Digest Series - Optical Society of America, 7:164–167, 1996.

[27] Yang C. Car headlight system development, 1998.

[28] Lyndon B Johnson Space Center and John D Figert. Process specification for the heat treatment of aluminum alloys. 2011.

[29] IC Chang. Acoustooptic devices and applications. IEEE transactions on sonics and ultrasonics, 23(1):p2, 1976.

[30] Peter C Chen, Charles W Bowers, Marzouk Marzouk, and Robert C Romeo. Advances in very lightweight composite mirror technology. Optical Engineering, 39(9):2320–2329, 2000.

[31] Shanyong Chen, Shengyi Li, and Yifan Dai. Iterative algorithm for subaperture stitching interferometry for general surfaces. JOSA A, 22(9):1929–1936, 2005.

[32] Shanyong Chen, Shengyi Li, Yifan Dai, and Ziwen Zheng. Iterative algorithm for subaperture stitching test with spherical interferometers. JOSA A, 23(5):1219–1226, 2006.

[33] Shanyong Chen, Shengyi Li, Yifan Dai, and Ziwen Zheng. Testing of large optical surfaces with subaperture stitching. Applied optics, 46(17):3504–3509, 2007.

[34] Shanyong Chen, Chunyu Zhao, Yifan Dai, and Shengyi Li. Stitching algorithm for subaperture test of convex aspheres with a test plate. Optics & Laser Technology, 49:307–315, 2013.

[35] James M Cicchiello and Eric J Jumper. Far-field optical degradation due to near-field transmission through a turbulent heated jet. Applied optics, 36(25):6441–6452, 1997.

[36] SF Clifford. The classical theory of wave propagation in a turbulent medium. In Laser beam propagation in the atmosphere, pages 9–43. Springer, 1978.

[37] Rodolphe Conan. Mean-square residual error of a wavefront after propagation through atmospheric turbulence and after correction with zernike polynomials. JOSA A, 25(2):526–536, 2008.

[38] Lacy G Cook. Wide field of view three-mirror anastigmat (tma) employing spherical secondary and tertiary mirrors. In Recent Trends in Optical Systems Design and Computer Lens Design Workshop, volume 766, pages 158–163. International Society for Optics and Photonics, 1987.

[39] EL Cuellar, James Stapp, and Justin Cooper. Laboratory and field experimental demonstration of a fourier telescopy imaging system. In Optics and Photonics 2005, pages 58960D–58960D. International Society for Optics and Photonics, 2005.

[40] Linyan Cui. Analysis of angle of arrival fluctuations for optical waves propagation through weak anisotropic non-kolmogorov turbulence. Optics Express, 23(5):6313–6325, 2015.

[41] Joseph R Davis et al. Aluminum and aluminum alloys. ASM international, 1993.

[42] Robert D Day, Thomas A Beery, and George N Lawrence. Sphericity measurements of full spheres using subaperture optical testing techniques. In 1986 Quebec Symposium, pages 334–341. International Society for Optics and Photonics, 1986.

[43] Richard Ditteon. Modern geometrical optics. Wiley, 1998.

[44] Charles H Downey, Randal S Abbott, Phillip I Arter, Dale A Hope, Dan A Payne, EA Roybal, Daniel F Lester, and James O McClenahan. The chopping secondary mirror for the kuiper airborne observatory. In 33rd Annual Technical Symposium, pages 329–342. International Society for Optics and Photonics, 1989.

[45] Keith B Doyle, Victor L Genberg, and Gregory J Michels. Integrated optomechanical analysis, volume 58. SPIE press, 2002.

[46] Wenhe Du, Siyuan Yu, Liying Tan, Jing Ma, Yijun Jiang, and Wanqing Xie. Angle-of-arrival fluctuations for wave propagation through non-kolmogorov turbulence. Optics Communications, 282(5):705–708, 2009.

[47] Kenneth S Edgett, R Aileen Yingst, Michael A Ravine, Michael A Caplinger, Justin N Maki, F Tony Ghaemi, Jacob A Schaffner, James F Bell, Laurence J Edwards, Kenneth E Herkenhoff, et al. Curiositys mars hand lens imager (mahli) investigation. Space science reviews, 170(1-4):259–317, 2012.

[48] Farzin Emami and M Ferdosian Tehrani. Noise in avalanche photodiodes. In WSEAS International Conference. Proceedings. Mathematics and Computers in Science and Engineering, number 12. World Scientific and Engineering Academy and Society, 2008.

[49] Kent E Erickson. Long-path interferometry through an uncontrolled atmosphere. JOSA, 52(7):781–786, 1962.

[50] Richard R Ernst, Geoffrey Bodenhausen, Alexander Wokaun, et al. Principles of nuclear magnetic resonance in one and two dimensions. 1987.

[51] J Fausto Escobar-Romero, Alejandro Cornejo-Rodr, et al. Testing parabolic surfaces with annular subaperture interferograms. Optical review, 11(2):82–86, 2004.

[52] CJ Evans and JB Bryan. Compensation for errors introduced by nonzero fringe densities in phase-measuring interferometers. CIRP Annals-Manufacturing Technology, 42(1):577–580, 1993.

[53] Daniel Feldkhun. Doppler encoded excitation patterning (deep) microscopy. PhD. Dissertation, 2010.

[54] Daniel Feldkhun and Kelvin H Wagner. Doppler encoded excitation pattern tomographic optical microscopy. Applied optics, 49(34):H47–H63, 2010.

[55] Daniel Feldkhun and Kelvin H Wagner. Deep-dome: Towards long-working-distance aberration-free synthetic aperture microscopy. In Computational Optical Sensing and Imaging, pages CM3B–5. Optical Society of America, 2012.

[56] Daniel Feldkhun and Kelvin H Wagner. Single-shot afocal three-dimensional microscopy. Optics Letters, 41(15):3483–3486, 2016.

[57] Daniel Feldkuhn and Kelvin Wagner. Fourier analysis and synthesis tomography.

[58] Robert Edward Fischer, Biljana Tadic-Galeb, Paul R Yoder, and Ranko Galeb. Optical system design. Citeseer, 2000.

[59] Edward J Fitzgerald and Eric J Jumper. Two-dimensional optical wavefront measurements using a small-aperture beam technique derivative instrument. Optical Engineering, 39(12):3285–3294, 2000.

[60] Jon Fleig, Paul Dumas, Paul E Murphy, and Greg W Forbes. An automated subaperture stitching interferometer workstation for spherical and aspherical surfaces. In Optical Science and Technology, SPIE's 48th Annual Meeting, pages 296–307. International Society for Optics and Photonics, 2003.

[61] Joseph Fourier. Theorie analytique de la chaleur, par M. Fourier. Chez Firmin Didot, pere et fils, 1822.

[62] CS Gardner. Effects of horizontal refractivity gradients on the accuracy of laser ranging to satellites. Radio Science, 11(12):1037–1044, 1976.

[63] George N Gibson, James Heyman, John Lugten, Walter Fitelson, and Charles H Townes. Optical path length fluctuations in the atmosphere. Applied optics, 23(23):4383–4389, 1984.

[64] Joseph W Goodman. Introduction to Fourier optics. Roberts and Company Publishers, 2005.

[65] EIj Gordon. A review of acoustooptical deflection and modulation devices. Applied optics, 5(10):1629–1639, 1966.

[66] Ronald Greeley, Robert Sullivan, James Klemaszewski, Kim Homan, James W Head, Robert T Pappalardo, Joseph Veverka, Beth E Clark, Torrence V Johnson, Kenneth P Klaasen, et al. Europa: initial galileo geological observations. Icarus, 135(1):4–24, 1998.

[67] James Gregory. Optica promota. 1663.

[68] John E Greivenkamp. Field guide to geometrical optics, volume 1. SPIE Press Bellingham, WA, 2004.

[69] David S Grey. Computed aberrations of spherical schwarzschild reflecting microscope objectives. JOSA, 41(3):183–192, 1951.

[70] David S Grey and Paul H Lee. A new series of microscope objectives: I. catadioptric newtonian systems. JOSA, 39(9):719–722, 1949.

[71] Paul G Hannan. General analysis of two-mirror relay systems. Applied optics, 31(4):513–518, 1992.

[72] Eric C Haseltine and Helene H Jones. Catadioptric projector, catadioptric projection system and process, April 2 1991. US Patent 5,004,331.

[73] William M Haynes. CRC handbook of chemistry and physics. CRC press, 2014.

[74] AK Head. The two-mirror aplanat. Proceedings of the Physical Society. Section B, 70(10):945, 1957.

[75] KE Herkenhoff, SW Squyres, JF Bell, JN Maki, HM Arneson, P Bertelsen, DI Brown, SA Collins, A Dingizian, ST Elliott, et al. Athena microscopic imager investigation. Journal of Geophysical Research: Planets, 108(E12), 2003.

[76] R Bruce Herrick and Jurgen R Meyer-Arendt. Interferometry through the turbulent atmosphere at an optical path difference of 354 m. Applied optics, 5(6):981–983, 1966.

[77] Peter Hidnert and HS Krider. Thermal expansion of aluminum and some aluminum alloys. Journal of research of the national bureau of standards, 48(3):209–220, 1952.

[78] RB Holmes, S Ma, A Bhowmik, and C Greninger. Analysis and simulation of a synthetic-aperture technique for imaging through a turbulent medium. JOSA A, 13(2):351–364, 1996.

[79] Richard B Holmes and Timothy J Brinkley. Reconstruction of images of deep-space objects using fourier telescopy. In SPIE's International Symposium on Optical Science, Engineering, and Instrumentation, pages 11–22. International Society for Optics and Photonics, 1999.

[80] William F Hosford. The anisotropy of aluminum and aluminum alloys. JOM, 58(5):70, 2006.

[81] Xi Hou, Fan Wu, Baiping Lei, Bin Fan, and Qiang Chen. Testing large aspheric surfaces with complementary annular subaperture interferometric method. In SPIE Astronomical Telescopes+ Instrumentation, pages 70183K–70183K. International Society for Optics and Photonics, 2008.

[82] Xi Hou, Fan Wu, Shibin Wu, and Qiang Chen. Annular subaperture interferometric testing technique for large aspheric surfaces. In Photonics Asia 2004, pages 992–997. International Society for Optics and Photonics, 2005.

[83] Xi Hou, Fan Wu, Li Yang, Shibin Wu, and Qiang Chen. Full-aperture wavefront reconstruction from annular subaperture interferometric data by use of zernike annular polynomials and a matrix method for testing large aspheric surfaces. Applied optics, 45(15):3442–3455, 2006.

[84] JH Hubbell. Common volume of two intersecting cylinders. J of Research (National Bureau of Standards) C, 69:139–43, 1965.

[85] Ronald J Hugo and Eric J Jumper. Experimental measurement of a time-varying optical path difference by the small-aperture beam technique. Applied optics, 35(22):4436–4447, 1996.

[86] Richard A Hutchin. Microscope for producing high resolution images without precision optics, April 22 1986. US Patent 4,584,484.

[87] Yoshinori Iketaki, Motohiro Atsumi, Haruo Kamijou, Masaaki Shibuya, Yoshiaki Horikawa, Shouichirou Mochimaru, and Koumei Nagai. Evaluation of the optical characteristics of the schwarzschild x-ray objective. Optics letters, 19(22):1804–1806, 1994.

[88] RC Jennison. A phase sensitive interferometer technique for the measurement of the fourier transforms of spatial brightness distributions of small angular extent. Monthly Notices of the Royal Astronomical Society, 118(3):276–284, 1958.

[89] Stephen C Jensen, Weng W Chow, and George N Lawrence. Subaperture testing approaches: a comparison. Applied optics, 23(5):740–745, 1984.

[90] R Barry Johnson. Wide field of view three-mirror telescopes having a common optical axis. Optical Engineering, 27(12):121046, 1988.

[91] R Barry Johnson and Allen Mann. Evolution of a compact, wide field-of-view, unobscured, all-reflective zoom optical system. In Infrared Technology and Applications XXIII, volume 3061, pages 370–376. International Society for Optics and Photonics, 1997.

[92] Eric J Jumper and Ronald J Hugo. Quantification of aero-optical phase distortion using the small-aperture beam technique. AIAA journal, 33(11):2151–2157, 1995.

[93] Avinash C Kak and Malcolm Slaney. Principles of computerized tomographic imaging. SIAM, 2001.

[94] Serope Kalpakjian and Steven R Schmid. Manufacturing engineering and technology. Pearson Upper Saddle River, NJ, USA, 2014.

[95] Hank H Karow. Fabrication methods for precision optics. Fabrication methods for precision optics, by HH Karow. Hoboken, NJ: Wiley-Interscience, 2004.

[96] HU Keller, W Goetz, H Hartwig, SF Hviid, R Kramm, WJ Markiewicz, R Reynolds, C Shinohara, Peter Smith, R Tanner, et al. Phoenix robotic arm camera. Journal of Geophysical Research: Planets, 113(E3), 2008.

[97] Michael J Kidger. Fundamental optical design, volume 92. SPIE press Bellingham, 2002.

[98] Hagyong Kihm and Ho-Soon Yang. Design optimization of a 1-m lightweight mirror for a space telescope. Optical Engineering, 52(9):091806–091806, 2013.

[99] C-J Kin and JC Wyant. Subaperture test of a large flat or a fast aspheric surface. J. Opt. Soc. America, Vol. 71, p. 1587, 71:1587, 1981.

[100] Rudolf Kingslake. Optical system design. Academic Press, 2012.

[101] Viking Press Kit. Nasa-release 75–183, 1975.

[102] Dietrich Korsch. Reflective optics. Academic Press, 2012.

[103] Lukas Kral, Ivan Prochazka, and Karel Hamal. Optical signal path delay fluctuations caused by atmospheric turbulence. Optics letters, 30(14):1767–1769, 2005.

[104] Michael F Küchel. Interferometric measurement of rotationally symmetric aspheric surfaces. In SPIE Europe Optical Metrology, pages 738916–738916. International Society for Optics and Photonics, 2009.

[105] Taylor W Lawrence, J Patrick Fitch, Dennis M Goodman, Norbert A Massie, Robert J Sherwood, and Erik M Johansson. Extended-image reconstruction through horizontal path turbulence using bispectral speckle interferometry. Optical Engineering, 31(3):627–637, 1992.

[106] Po-Chih Lin, Yan-An Chen, Hung-Sheng Chang, Chao-Wen Liang, and Yi-Chun Chen. Aberration compensation and position scanning of a subaperture stitching algorithm. In SPIE Optical Engineering+ Applications, pages 84940L–84940L. International Society for Optics and Photonics, 2012.

[107] Po-Chih Lin, Yi-Chun Chen, Chung-Min Lee, and Chao-Wen Liang. A subaperture stitching algorithm for aspheric surfaces. In SPIE Optical Metrology, pages 80821G–80821G. International Society for Optics and Photonics, 2011.

[108] Ying-Moh Liu, George N Lawrence, and Christ L Koliopoulos. Subaperture testing of aspheres with annular zones. Applied optics, 27(21):4504–4513, 1988.

[109] Roberto Machorro, Jesús M Siqueiros, and Shu Wang. Optical properties of mg, from uv to ir, using ellipsometry and reflectometry. Thin Solid Films, 269(1-2):1–5, 1995.

[110] J Maire, A Ziad, J Borgnino, and F Martin. Comparison between atmospheric turbulence models by angle-of-arrival covariance measurements. Monthly Notices of the Royal Astronomical Society, 386(2):1064–1068, 2008.

[111] Daniel Malacara. Optical shop testing, volume 59. John Wiley & Sons, 2007.

[112] Michael M Malley, George W Sutton, and Nancy Kincheloe. Beam-jitter measurements of turbulent aero-optical path differences. Applied Optics, 31(22):4440–4443, 1992.

[113] JR Matijevic, DB Beckler, DF Braun, HJ Eisen, LH Matthies, AH Mishkin, HW Stone, LM van Nieuwstadt, L-C Wen, BH Wilcox, et al. The pathfinder microrover. Journal of Geophysical Research, 102:3989–4002, 1997.

[114] Klaus D Mielenz. Spherically corrected reflecting objective for unit magnification. Applied optics, 13(11):2580–2584, 1974.

[115] Peter G Morris. Nuclear magnetic resonance imaging in medicine and biology. 1986.

[116] Pantazis Mouroulis and John Macdonald. Geometrical optics and optical design. Oxford University Press, USA, 1997.

[117] DR Mulville. Payload vibroacoustic test criteria. Technical report, NASA-STD-7001, 1996.

[118] Paul Murphy, Gary DeVries, Jon Fleig, Gregory Forbes, Andrew Kulawiec, and Dragisha Miladinovic. Measurement of high-departure aspheric surfaces using subaperture stitching with variable null optics. In SPIE Optical Engineering+ Applications, pages 74260P–74260P. International Society for Optics and Photonics, 2009.

[119] Paul Murphy, Jon Fleig, Greg Forbes, Dragisha Miladinovic, Gary DeVries, and Stephen O'Donohue. Subaperture stitching interferometry for testing mild aspheres. In SPIE Optics+ Photonics, pages 62930J–62930J. International Society for Optics and Photonics, 2006.

[120] Shree K Nayar and Simon Baker. Catadioptric image formation. In Proceedings of the 1997 DARPA Image Understanding Workshop, pages 1431–1437, 1997.

[121] James E Negro. Subaperature optical system testing. Applied optics, 23(12):1921–1930, 1984.

[122] Robert J Noll. Zernike polynomials and atmospheric turbulence. JOsA, 66(3):207–211, 1976.

[123] Keith Nowicki, Kelvin H Wagner, and Daniel Feldkhun. Optical design and testing of a remote microscope. In Aerospace Conference, 2015 IEEE, pages 1–7. IEEE, 2015.

[124] Keith Nowicki, Kelvin H Wagner, and Daniel Feldkhun. Computational microscopy at 5 meters using axially-symmetric sequential fourier sampling. In Computational Optical Sensing and Imaging, pages CTh3B–4. Optical Society of America, 2017.

[125] Abe Offner. Catoptric anastigmatic afocal optical system, July 4 1972. US Patent 3,674,334.

[126] Natalia Ostroumov, Jeffrey M Gordon, and Daniel Feuermann. Panorama of dual-mirror aplanats for maximum concentration. Applied optics, 48(26):4926–4931, 2009.

[127] Roger A Paquin. Selection of materials and processes for metal optics. In 19th Annual Technical Symposium, pages 12–19. International Society for Optics and Photonics, 1976.

[128] William R Patterson, FO Huck, SD Wall, and MR Wolf. Calibration and performance of the viking lander cameras. Journal of Geophysical Research, 82(28):4391–4400, 1977.

[129] Michael B Prime and Michael R Hill. Residual stress, stress relief, and inhomogeneity in aluminum plate. Scripta Materialia, 46(1):77–82, 2002.

[130] Lord Rayleigh. Xxxi. investigations in optics, with special reference to the spectroscope. The London, Edinburgh, and Dublin Philosophical Magazine and Journal of Science, 8(49):261–274, 1879.

[131] Max J Riedl. Optical design fundamentals for infrared systems, volume 48. SPIE press, 2001.

[132] Clélia Robert, Jean-Marc Conan, Vincent Michau, Jean-Baptiste Renard, Claude Robert, and Francis Dalaudier. Retrieving parameters of the anisotropic refractive index fluctuations spectrum in the stratosphere from balloon-borne observations of stellar scintillation. JOSA A, 25(2):379–393, 2008.

[133] Bahaa EA Saleh, Malvin Carl Teich, and Bahaa E Saleh. Fundamentals of photonics, volume 22. Wiley New York, 1991.

[134] RS Saunders, AJ Spear, PC Allin, RS Austin, AL Berman, RC Chandlee, J Clark, AV Decharon, EM De Jong, DG Griffith, et al. Magellan mission summary. Journal of Geophysical Research: Planets, 97(E8):13067–13090, 1992.

[135] Manish Saxena, Gangadhar Eluru, and Sai Siva Gorthi. Structured illumination microscopy. Advances in Optics and Photonics, 7(2):241–275, 2015.

[136] DH Schulte. Anastigmatic cassegrain type telescope. Applied optics, 5(2):309–311, 1966.

[137] Karl Schwarzschild. Untersuchungen zur geometrischen Optik. 2. Theorie der Spiegeltelescope. Weidmann, 1905.

[138] GE Seibert. Design of lightweight mirrors. SPIE Short Course Notes, 243:244, 1990.

[139] David R Shafer. The triplet: an embarrassment of riches. Optical Engineering, 27(12):121035, 1988.

[140] Simon CF Sheng. Lightweight mirror structures best core shapes: a reversal of historical belief. Applied optics, 27(2):354–359, 1988.

[141] Charles Patten Shillaber. Photomicrography in Theory and Practice. 1944.

[142] Laura C Sinclair, Fabrizio R Giorgetta, William C Swann, Esther Baumann, I Coddington, and Nathan R Newbury. Optical phase noise from atmospheric fluctuations and its impact on optical time-frequency transfer. Physical Review A, 89(2):023805, 2014.

[143] Peter H Smith, Martin G Tomasko, D Britt, DG Crowe, R Reid, HU Keller, N Thomas, F Gliem, P Rueffer, R Sullivan, et al. The imager for mars pathfinder experiment. Journal of Geophysical Research: Planets, 102(E2):4003–4025, 1997.

[144] Warren J Smith. Modern optical engineering. Tata McGraw-Hill Education, 1966.

[145] Edward A Snyder and Michael P Teter. Automotive headlight having optics in the reflector, November 6 1984. US Patent 4,481,563.

[146] J Strohbehn and S Clifford. Polarization and angle-of-arrival fluctuations for a plane wave propagated through a turbulent medium. IEEE Transactions on Antennas and Propagation, 15(3):416–421, 1967.

[147] JW Strohbehn. Modern theories in the propagation of optical waves in a turbulent medium. In Laser Beam Propagation in the Atmosphere, pages 45–106. Springer, 1978.

[148] Tilman W Stuhlinger. Subaperture optical testing: experimental verification. In 1986 International Symposium/Innsbruck, pages 350–359. International Society for Optics and Photonics, 1986.

[149] Christopher Supranowitz, Chuck McFee, and Paul Murphy. Asphere metrology using variable optical null technology. In 6th International Symposium on Advanced Optical Manufacturing and Testing Technologies (AOMATT 2012), pages 841604–841604. International Society for Optics and Photonics, 2012.

[150] Rahul Swaminathan. Focus in catadioptric imaging systems. In Computer Vision, 2007. ICCV 2007. IEEE 11th International Conference on, pages 1–7. IEEE, 2007.

[151] Jiubin Tan, Chao Wang, Yuan Wang, Weibo Wang, Jian Liu, Richard Leach, and Ling Hao. Long working distance microscope with a low obscuration aspherical schwarzschild objective. Optics letters, 39(23):6699–6702, 2014.

[152] Valerian I Tatarski, Richard A Silverman, and Nicholas Chako. Wave propagation in a turbulent medium. Physics Today, 14:46, 1961.

[153] Berge Tatian and Richard Wientzen. All-reflective zoom optical imaging system, December 25 2001. US Patent 6,333,811.

[154] V Yu Terebizh. Wide-field corrector for a gregorian telescope. Astronomy reports, 51(7):597–603, 2007.

[155] Moody Chalmers Thompson and HB Janes. Radio path length stability of ground-to-ground microwave links, volume 219. Superintendent of Documents, US Govt. Print. Off., 1964.

[156] Chao Tian, Yongying Yang, Tao Wei, and Yongmo Zhuo. Nonnull interferometer simulation for aspheric testing based on ray tracing. Applied optics, 50(20):3559–3569, 2011.

[157] Italo Toselli, Larry C Andrews, Ronald L Phillips, and Valter Ferrero. Angle of arrival fluctuations for free space laser beam propagation through non kolmogorov turbulence. In Atmospheric Propagation IV, volume 6551, page 65510E. International Society for Optics and Photonics, 2007.

[158] M Tricard, A Kulawiec, M Bauer, G DeVries, J Fleig, G Forbes, D Miladinovich, and P Murphy. Subaperture stitching interferometry of high-departure aspheres by incorporating a variable optical null. Cirp Annals-Manufacturing Technology, 59(1):547–550, 2010.

[159] Darko M Vasiljevic. Optimization of the cooke triplet with various evolution strategies and damped least squares. In Optical Design and Analysis Software, volume 3780, pages 207–216. International Society for Optics and Photonics, 1999.

[160] David George Voelz. Computational fourier optics: a MATLAB tutorial. SPIE press Bellingham, WA, 2011.

[161] Xiaokun Wang, Lihui Wang, Longhai Yin, Binzhi Zhang, Di Fan, and Xuejun Zhang. Measurement of large aspheric surfaces by annular subaperture stitching interferometry. Chinese Optics Letters, 5(11):645–647, 2007.

[162] GD Wassermann and E Wolf. On the theory of aplanatic aspheric systems. Proceedings of the Physical Society. Section B, 62(1):2, 1949.

[163] WB Wetherell and MP Rimmer. General analysis of aplanatic cassegrain, gregorian, and schwarzschild telescopes. Applied Optics, 11(12):2817–2832, 1972.

[164] Albert D Wheelon. Electromagnetic Scintillation: Volume 1. Geometrical Optics. Cambridge University Press, 2003.

[165] J-P Williams, DA Paige, BT Greenhagen, and E Sefton-Nash. The global surface temperatures of the moon as measured by the diviner lunar radiometer experiment. Icarus, 283:300–325, 2017.

[166] Raymond N Wilson. Reflecting telescope optics II: manufacture, testing, alignment, Modern Techniques. Springer Science & Business Media, 2013.

[167] CG Wynne. Two-mirror anastigmats. JOSA, 59(5):572–578, 1969.

[168] TSUNG-SHOU YEH and Michael D Sacks. Low-temperature sintering of aluminum oxide. Journal of the American ceramic society, 71(10):841–844, 1988.

[169] Paul R Yoder Jr. Opto-mechanical systems design. CRC press, 2005.

[170] Lei Zhang, Chao Tian, Dong Liu, Tu Shi, Yongying Yang, Hanshuo Wu, and Yibing Shen. Non-null annular subaperture stitching interferometry for steep aspheric measurement. Applied optics, 53(25):5755–5762, 2014.

[171] Zixin Zhao, Hong Zhao, Feifei Gu, Hubing Du, and Kaixing Li. Non-null testing for aspheric surfaces using elliptical sub-aperture stitching technique. Optics express, 22(5):5512–5521, 2014.

[172] Arkadi Zilberman, Ephim Golbraikh, Norman S Kopeika, Alexander Virtser, Igor Kupershmidt, and Yuri Shtemler. Lidar study of aerosol turbulence characteristics in the troposphere: Kolmogorov and non-kolmogorov turbulence. Atmospheric Research, 88(1):66–77, 2008.